EIS Investigation of Corrosion Mechanisms of Iron in Acidic Solutions

A dissertation presented to

the faculty of

the Russ College of Engineering and Technology of Ohio University

In partial fulfillment

of the requirements for the degree

Doctor of Philosophy

Negar Moradighadi

December 2022

This dissertation titled

EIS Investigation of Corrosion Mechanisms of Iron in Acidic Solutions

by

NEGAR MORADIGHADI

has been approved for

the Department of Chemical and Biomolecular Engineering

and the Russ College of Engineering and Technology by

Srdjan Nesic

Professor of Chemical and Biomolecular Engineering

Maj Mirmirani

Interim Dean, Russ College of Engineering and Technology

Abstract [1]

MORADIGHADI, NEGAR, Ph.D., December 2022, Chemical Engineering

EIS Investigation of Corrosion Mechanisms of Iron in Acidic Solutions

Director of Dissertation: Srdjan Nesic

Corrosion of pipelines is one of the major problems in the oil and gas industry. The research discussed herein focuses on the mechanistic study of the electrochemical reactions associated with corrosion using electrochemical impedance spectroscopy (EIS) as an advanced technique along with direct current (DC) techniques such as steady state potentiodynamic sweeps. The outcome of this research is to increase the understanding of reaction mechanisms occurring at the steel surface which can improve the existing models for the prediction of the corrosion rate.

In acidic environments, which are studied in this work, the electrochemical reactions are the anodic dissolution of iron proceeding in parallel with the cathodic reduction of hydrogen ions and water. When using EIS to study an electrochemical reaction, it is important to know if at any given potential an impedance spectrum is collected that contains more information about one reaction or the other, or if it is a mixed response. Therefore, in the first part of this work, a model was developed to calculate the percent contribution of each electrochemical reaction to the measured impedance at different potentials. The model was developed based on calculated polarization resistances

---

[1] Portions of texts in this abstract appeared in publications of the author: *Electrochimica Acta* 400 (2021): p. 139460, AMPP proceeding paper no. 17900 (2022), AMPP proceeding paper no. 16753 (2021), NACE International proceeding paper no. 13004 (2019), and Corrosion 77 (2020): pp. 266–275 (reference numbers [1–5]).

of electrochemical reactions using steady state potentiodynamic sweep data. It was concluded that, at any chosen DC potential, the reaction having the lowest impedance has the highest contribution to the total measured impedance response of an electrochemical system. Consequently, the developed model can be used to determine the DC potential at which a specific reaction of interest has the highest contribution to the measured impedance data. The same approach was used as a part of this study related to determining the diffusion coefficient of hydrogen ions. The DC potential for EIS measurements was chosen to obtain the most information about the cathodic reduction of hydrogen ions.

In the following part of the work described in this dissertation, the mechanism of anodic dissolution of pure iron in acidic solutions was investigated. Among the proposed mechanisms in the literature, a broadly applicable multi-path mechanism was identified that could explain the behavior of anodic dissolution of iron; both in terms of steady state polarization sweeps and impedance data at various pH values and current densities in strong acidic sulfate solution. The mechanism of iron dissolution was then investigated in strong acid chloride solution and in weak acid chloride solution in the presence of CO_2. Results showed that the presence of chloride ion decreases the rate of the anodic iron dissolution and results in the formation of an additional adsorbed intermediate species which participate in the anodic reaction in parallel with the other intermediates in the multi-path mechanism. The presence of CO_2 increases the anodic current density mainly in transition and pre-passivation regions, however, EIS investigation of this mechanism showed that CO_2 does not react directly on the bare metal surface and does not form an additional adsorbed intermediate species that is involved in the anodic reaction. However,

it is implied that the presence of CO_2 might change the chemical composition of the adsorbed species, kinetic constants and extent of coverage of the iron surface by different adsorbed intermediated species and ions, leading to the change in the kinetics of the underlying reactions.

To extend developments of models related to the mechanism of cathodic reduction of hydrogen ion, a new module called "LABCORP-AC™" has been developed using the physicochemical model behind the MULTICORP™ corrosion predication package, to calculate the impedance response of cathodic reduction of hydrogen ion in strong acidic solutions and CO_2 aqueous environments. The developed module predicts both experimental steady state potentiodynamic sweeps and impedance data in terms of Nyquist plots and Bode plots in different acidic environments.

Originally, the plan was to study the behavior of CO_2 corrosion inhibitors using EIS. Even if this proved to be beyond the reach of the current project, given the time constraints and complexity of the subject matter, some work with corrosion inhibitors was initiated. Critical micelle concentration (CMC) is considered as one of the important features of the corrosion inhibitors which is considered by many researchers as an indication of their efficiency. This study investigated the accuracy of surface tension measurements along with fluorescence spectroscopy as the techniques for CMC measurements. Results showed that surface tension measurements only provide information regarding the air/solution surface saturation concentration which may not be related to micelle formation happening in bulk solution. Therefore, using this technique might result in an inaccurate CMC measurement. Moreover, the relationship between the

measured CMCs in this work and the metal surface saturation concentration reported by other studies was investigated. Results showed that CMC does not link to the maximum reduction in corrosion rate.

Dedication

I dedicate this dissertation to my loving family: To my husband, Ahmadreza, for his support, encouragement, and faith in me. To my parents, Mohammadreza, and Hayedeh for their endless sacrifices, love and support, and my sister, Bahar, for her support and love during my lifelong journey.

Acknowledgments

I would like to express my gratitude to my research advisor, Dr. Srdjan Nesic for his support, mentorship, encouragement, and critical input during my academic journey. I would like to give my sincere respect and appreciation for all I have learned from him both in my academic career and personal life.

I would like to express my appreciation to Dr. Bruce Brown, my project leader, for his professional suggestions, and endless support during these six years. I also thank Dr. David Young and Dr. Marc Singer for their immense support and valuable input in my Ph.D. study. I would like to thank Dr. Yoon-Seok Choi, Mr. Mohiedin Bagheri Hariri and Miss Starr Lewis for their support, scientific work, and patience during our collaboration in this research study.

My special gratitude to Dr. Bernard Tribollet, for the time he kindly spent reviewing my work and for provide valuable and fruitful input in my work. His guidance significantly contributed to the quality of this work.

I would like to express my appreciation to my committee members, Dr. Howard Dewald, Dr. David Young, Dr. Katherine Cimatu, Dr. Marc Singer, Dr. Sumit Sharma and Dr. Tadeusz Malinski, for their support and dedication to reviewing this work.

Special thanks to Mr. Alexis Barxias, Mr. Cody Shafer, Mr. Martin Colahan, Dr. Zineb Belarbi, and Dr. Fernando Farelas at the Institute for Corrosion and Multiphase Technology for their help and support. I am grateful to study for six years in a collaborative and friendly work environment at ICMT and I would like to thank all the lab mates, faculty members, and staff who enrich this environment.

And finally, my deepest appreciation and respect to my family for their sacrifices, encouragement, and inspiration which supported me to overcome the obstacles during my lifelong journey.

Table of Contents

Page

List of Tables

Page

List of Figures

Page

Chapter A: Introduction [2]

Integrity management of pipelines in the oil and gas industry, is a challenge in terms of safety, operational decisions, maintenance, inspection, and mitigation strategies. Therefore, corrosion is considered as one of the most destructive processes, necessitating the understanding of its mechanisms, as well as investigation of current and potentially new mitigation strategies.

Effective prediction of corrosion rate using electrochemical models is a strategy that is used to make decisions for the design of pipelines as well as management of operational conditions. Therefore, understanding the mechanism of electrochemical reactions underlying corrosion of iron and mild steel results in the development of better prediction models, which can determine corrosion rates in different environments; this is in contrast to empirical models that are limited to specific conditions and lack flexibility. Modeling is essential for optimization of materials selection and design decisions, as well as adoption of appropriate corrosion mitigation strategies.

Among different electrochemical analytical methods, EIS is considered a tool widely used in studies of complex phenomena such as an overall electrochemical reaction governed by more than one elementary step and intermediate species [6–8]. EIS can provide a wealth of information about the surface phenomena occurring, based on analysis of the impedance response of the system. The term *impedance* is defined as "the effective resistance of an electric circuit or component to alternating current, arising from the

---

[2] Portions of texts in this chapter appeared in publications of the author: *Electrochimica Acta* 400 (2021): p. 139460, AMPP proceeding paper no. 16753 (2021), NACE International proceeding paper no. 13004 (2019), and Corrosion 77 (2020): pp. 266–275 (reference numbers [1,3–5]).

combined effects of ohmic resistance and reactance"[9]. In other words, impedance measurements include the estimation of both the *ohmic resistance* to a flow of current and resistance to a change in current called *reactance* that arises from the effect of inductance and/or capacitance [8].

EIS technique enables the data acquisition about different phenomena proceeding on the metal surface based on their response to the alternating potential or current density. Once there is an imposed alternating potential, depending on the frequency and the phenomena proceeding on the metal surface, there will be a *delay* or *phase angle* between the imposed potential and responding current density. The physical meaning of the delay or phase angle can be further explained using a simple example of an electrical circuit consisting of a capacitor in series with a resistor as shown in Figure 1. In the electrical circuit shown in Figure 1, once the switch is closed, at the time equal to zero (t_0), the potential across the capacitor (V_c) is equal to zero and the potential difference between the capacitor and the source of power $|V_c - V_s|$ is at maximum. Therefore, at t_0 maximum current flows through the circuit and the capacitor starts to charge. This current is called the *charging current*. As the capacitor is being charged, the V_c keeps increasing over time. This behavior is shown in Figure 2. As the V_c increases, and the $|V_c - V_s|$ decreases, there is a decay in the current flow which eventually becomes zero once $|V_c - V_s|$ is equal to zero.

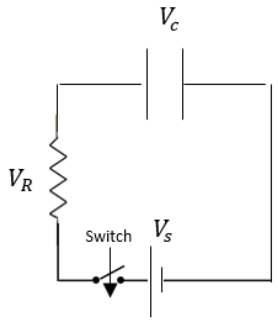

Figure 1

Example of an RC circuit.

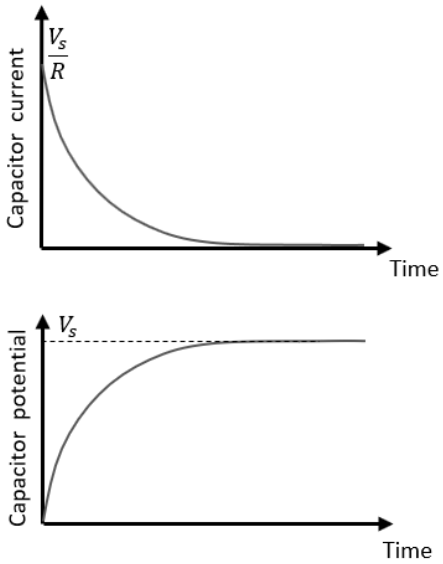

Figure 2

Charging of a capacitor in an RC circuit shown in Figure 1.

As shown in Figure 2, once the charging current is at maximum value, there is a delay for the potential across the capacitor to reach its maximum value. The time required for the potential across the capacitor to reach 63% of the maximum steady state value is called *time constant*. Generally, the time constant depends on the values of circuit elements, and it represents how fast the capacitor gets charged or discharged. When an alternating

potential is applied, the frequency related to the time constant, is called *characteristic frequency*. Characteristic frequency is commonly used in the analysis of the impedance response of an electrochemical system. Any process, involving charging and discharging of a double layer capacitance, happening in parallel with a charge transfer resistance, diffusion impedance, adsorption of species, etc., responds most strongly in the frequency range close to the characteristic frequency of that specific process. Therefore, the characteristic frequency can be seen as one of the physicochemical parameters that characterizes a given electrochemical process. As an example, diffusion of a species is a relatively slow process, and its impedance responses can be detected at a lower frequency when the species in the solution have enough time to respond to the alternating potential; charge transfer and electrical double layer charging are much faster and can be detected with EIS using higher frequencies [8].

As mentioned before, in EIS measurements, depending on the frequency of perturbated potential there is a delay in the responding current density, resulting in a phase angle shift between imposed alternating potential and responding current density. Using simple mathematical transformations as defined in standard analysis of AC circuits, the non-zero phase angle makes the impedance associated with a given process a complex value, with real and imaginary parts [8].

To study and analyze the impedance response of a system, generally the impedance data are illustrated using *Lissajous*, *Nyquist* and *Bode plots*. Lissajous plot shows the alternating potential versus the alternative current density at each frequency as shown by the examples in Figure 3. At 10 kHz, the phase angle is -88°, and the Lissajous plot is

similar to a circle (capacitive behavior). As the frequency and phase angle decreases, the Lissajous plot becomes similar to an oval and finally at very low frequency there is almost linear relationship between potential and current density (Ohmic behavior). Lissajous plot is commonly used for determining the value of the impedance and phase angle by which the real and imaginary parts of impedance are calculated [8] (this subject is further discussed in Section D.3.2.).

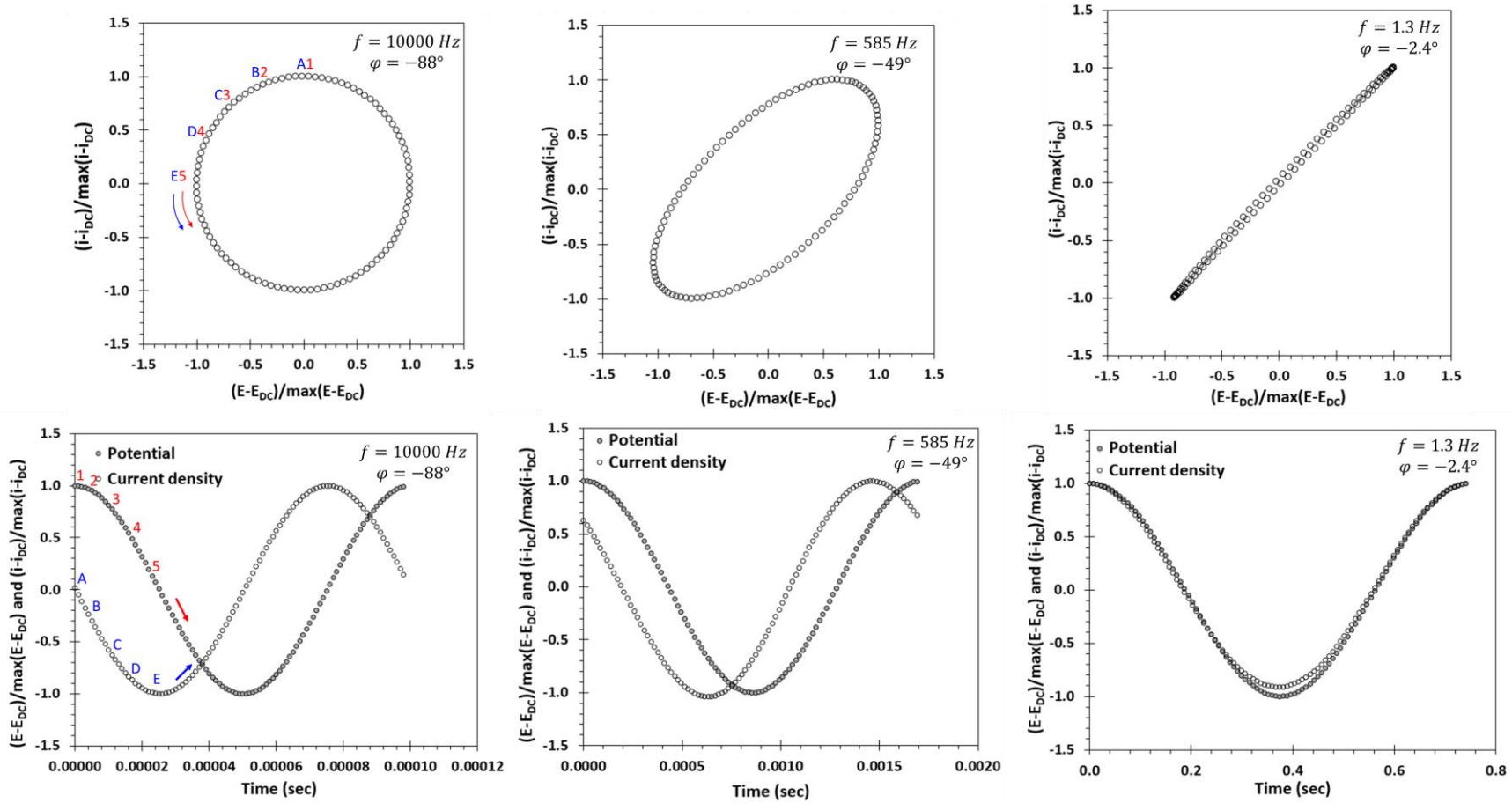

Figure 3

Example of Lissajous plots related to the alternating potentials, and current densities at different frequencies. Simulation parameters: $\bar{E}_{DC}$= -0.579 V vs. SHE, $C_{dl} = 2\ \mu F/cm^2$, *pN_2= 1 bar, pH 4.00, T=30°C, velocity=2.6 m/s, 0.1 M NaCl. The data obtained using LABCORP-AC™ in corrosion prediction package MULTICORP™.*

Generally, the real and imaginary parts of the impedance response of a system are shown in a Nyquist plot. The example of a Nyquist plot is shown in Figure 4 including the red data points related to the data shown in Figure 3. The "loops" or semicircles observed in the Nyquist plot are related to the response, seen as a phase angle (also called relaxation[3]) of different phenomena responding at different frequencies. In the example shown in Figure 4, the loop at high frequency is related to the response of the charge transfer resistance in parallel with electrical double layer capacitance, while the low frequency loop is related to the response of species diffusion to the change in potential of H^+ which is relatively slower process[2,8].

Nyquist plot can provide various information about a system. The basic information commonly obtained from the Nyquist plots includes the solution resistance (approximately equal to the real part of the impedance at the highest frequency[4]), charge transfer resistance (at the intersection of the high frequency loop with the x-axis) and polarization resistance (at the intersection of the lowest frequency loop with the x-axis. More information about the determination of the solution, charge transfer and polarization resistances are provided in Chapter D and Appendix II.2

---

[3] The term "*relaxation*" refers to the decay in the excited current density (due to the perturbated potential) until it reaches to its steady state value.

[4] In the example shown in Figure 3, the solution resistance is not considered.

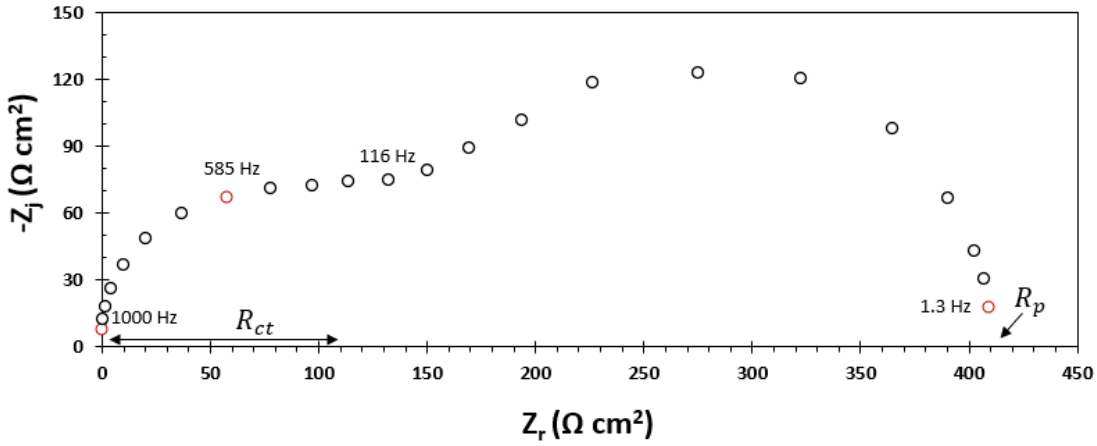

Figure 4

Example of a Nyquist plot. Red data points correspond to impedance data obtained by the Lissajous plots shown in Figure 3. Simulation parameters $\bar{E}_{DC}$= -0.579 V vs. SHE, $C_{dl} = 2\ \mu F/cm^2$, *pN₂= 1 bar, pH 4.00, T=30°C, velocity=2.6 m/s, 0.1 M NaCl. The data obtained using LABCORP-AC™ in corrosion prediction package MULTICORP™.*

The Nyquist plot does not explicitly show the information regarding the phase angle and the magnitudes of impedance at the corresponding frequencies. This information is directly shown in a Bode plot, examples are shown in Figure 5 related to the data shown in Figure 4. The date points in the frequency ranges of 10 kHz to 116 Hz and 116 Hz to 1.3 Hz are related to the high frequency loop and low frequency loop respectively. In the Bode magnitude plot, these two ranges are shown by different slopes while in the Bode phase angle plot there are two peaks attributed to the two loops related to different processes on the metal surface. Complimentary to the Nyquist plots, Bode plots clearly present additional information regarding the characteristics of a system, such as presence of non-ideal capacitors, information about the nature of the loops and the underlying phenomena, etc[8,10–13].

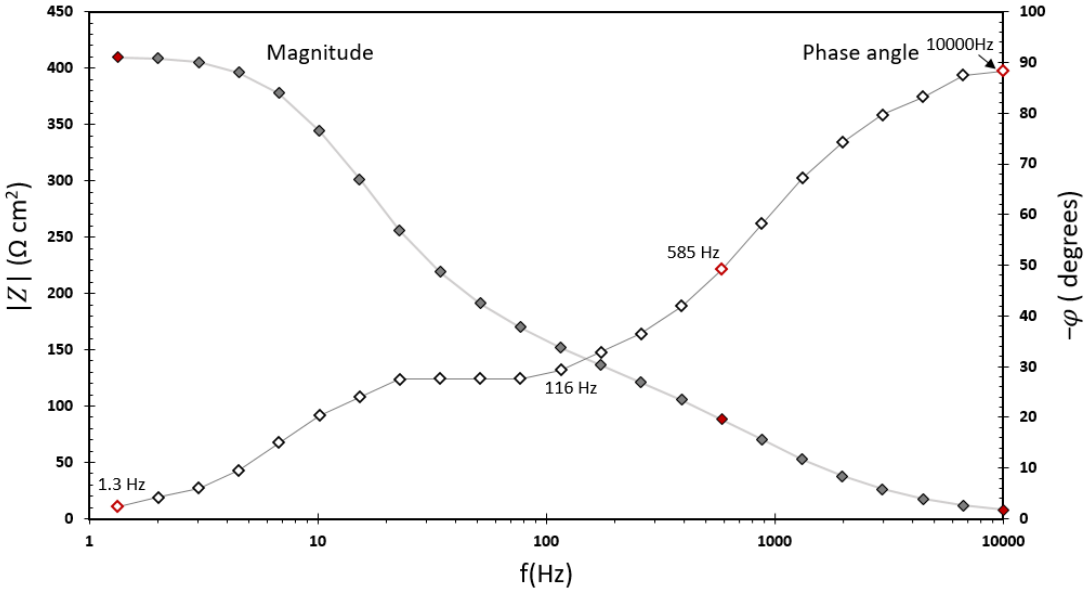

Figure 5

Example of a Bode plot. Red data points correspond to impedance data obtained by the Lissajous plots shown in Figure 3. $\bar{E}_{DC}$= -0.579 V vs. SHE, $C_{dl} = 2\ \mu F/cm^2$, pN_2= *1 bar, pH 4.00, T=30°C, velocity=2.6 m/s, 0.1 M NaCl. The data obtained using LABCORP-AC™ in corrosion prediction package MULTICORP™.*

Despite these very useful aspect of the EIS technique where we can distinguish the different reactions and processes occurring simultaneously, interpretation of the impedance data is complicated and often ambiguous, requiring much more additional information and analysis compared to a given DC technique such as steady state potentiodynamic sweeps, etc. In other words, any given impedance response of an electrochemical system can be interpreted in many different ways, depending on the assumptions made, what can make the analyzed results biased and inaccurate. Consequently, part of this study strives to develop systematic methodologies and models to better interpret the impedance response of a system acquired in various test conditions[1–3].

The current understanding of CO_2 corrosion, mainly related to the cathodic reaction mechanisms was used to build electrochemical models to predict the corrosion rate of mild steel[14–17]. However, the effect of CO_2 on the anodic reaction was less mechanistically studied, and remained as an open question for many years[18–22]. Therefore, one of the primary motivations of this research project was using the EIS technique to deepen, elucidate and complement our understanding about the role of CO_2 on the mechanism of iron dissolution.

Application of inhibitors is an established and cost-effective method to mitigate internal corrosion of mild steel pipelines in the oil and gas industry. The efficiency of surfactant-type organic inhibitors is often related to their critical micelle concentration (CMC) values and their adsorption evaluated based on laboratory tests that assume that a maximum reduction in corrosion rate is reached at CMC [23]. Critical micelle concentration (CMC) is an important feature of the corrosion inhibitors. It has been suggested that at a concentration equal to or above the CMC, the surface of the metal would be fully covered by corrosion inhibitor molecules [24,25]. Surface tension measurement is one of the most common methods for determining CMC. In this method, as the corrosion inhibitor is added to the solution, the change in the air/solution interfacial tension is measured. The concentration at which the interfacial tension reaches a plateau, is considered as CMC. This is based on an assumption the formation of micelles occurs when the bulk solution is saturated by the corrosion inhibitor. Below this concentration (CMC) any addition of the inhibitor results in an increase in free inhibitor concentration and corresponding increase in inhibitor accumulation at the air/solution interface. Above the CMC any further addition

of the corrosion inhibitor to the solution results in the formation of more micelles with no increase in the free inhibitor concentration and no change in their accumulation on the air/solution interface and therefore the interfacial tension becomes constant. However, there is always an alternative possibility that the saturation of the air/solution interface happens at the lower concentrations of the inhibitor than needed to achieve saturation of the solution and any formation of micelles, in which case surface tension measurements are not related to the CMC. There is another assumption associated with the use of CMC in inhibitor studies. The surface tension measurements used for CMC determination are conducted at the air/solution interface, whereas they are used to imply something about the adsorption of the inhibitor at the metal surface. Therefore it is assumed that the change of surface tension has a direct relationship to inhibitor coverage at the metal/solution interface via the CMC[4]. Therefore, the validity of this technique for detecting the extent of inhibitor adsorption at the metal surface as being related to micelle formation, happening in the bulk solution, based on the measurements of the corrosion inhibitor accumulation at the air/solution interface can be questioned. The work presented below attempts to unravel this issue by evaluating the techniques for CMC measurements and elucidate the relationship between the CMC and their adsorption at the metal surface resulting in the maximum corrosion rate reduction, as reported elsewhere[4,5,26,27]. Fluorescence spectroscopy technique is used in this study, as an alternative technique, for determining CMC directly form the bulk solution. In fluorescence spectroscopy, a fluorophore probe emits light in higher intensity in the non-polar environments inside the micelles compare to water as a polar environment. Therefore, the concentration at which the micelles start to

form can be determined directly from the bulk solution by evaluation of fluorophore probe light intensity.

Chapter B: Gaps and Objectives [5]

The studies related to the mechanism of the electrochemical reaction associated with corrosion of mild steel and pure iron were mainly based on DC techniques such as steady-state polarization curves and linear polarization resistance[18,20,28]. However, these techniques only show the total reaction rate which is controlled by the slowest step. Electrochemical impedance spectroscopy (EIS) is an advanced technique that can detect and distinguish different phenomena that occur on the surface using alternative signals and can provide information on the intermediate reactions. Consequently, using both steady state potentiodynamic sweeps and EIS measurements, the following gaps and questions are going to be investigated:

- As an initial step in a long journey one of the first questions asked was: at different potentials, which reaction contributes most to the recorded impedance spectra, cathodic or anodic? In other words, it was important to know if at any given potential an impedance spectrum that is collected that carries more information about one reaction or the other, or if it is a mixed response. Therefore, the first objective of this research is to develop a methodology to determine the DC potential at which the measured impedance data are dominated by a specific reaction, so that the information extracted from EIS is relevant.

---

[5] Portions of texts in this chapter appeared in publications of the author: *Electrochimica Acta* 400 (2021): p. 139460, AMPP proceeding paper no. 17900 (2022), AMPP proceeding paper no. 16753 (2021), NACE International proceeding paper no. 13004 (2019), and Corrosion 77 (2020): pp. 266–275 (reference numbers [1–5]).

- In CO_2 corrosion, the mechanisms of the cathodic reaction have been thoroughly investigated and explained. Comprehensive mechanistic models have been built and verified, with considerable success. However, the vast majority of experimental data used in developing the understanding and building the models were collected using DC electrochemical techniques. The challenge is to check if the new information that can be extracted by using EIS to study the mechanisms of the cathodic reaction in CO_2 corrosion is consistent with the current body of knowledge. Also, the question that needs answering is: can the existing mechanistic models for the cathodic reaction in CO_2 corrosion which seem to properly describe the DC behavior, be extended to cover the experimental EIS response. Therefore, the second objective of the present study is to model the EIS response for the cathodic reaction in CO_2 corrosion, considering the commonly accepted reaction mechanism, involving charge transfer, mass transfer and chemical buffering. Once this is done, the simulated EIS response of the cathodic reaction will be compared with the experimental EIS results to evaluate its validity and accuracy.
- The mechanism of the main anodic reaction in CO_2 corrosion of mild steel is much less understood. It has received much less attention in the past and the limited body of experimental work consists primarily of DC electrochemical studies. On the other hand, the understanding of the mechanism of iron dissolution in strong acidic[6] environments has been under investigation for many years. Even in that case, most

[6] Strong acid is defined as an acid which fully dissociates into ions while weak acid partially dissociates.

of the proposed mechanisms such as the Bockris' consecutive mechanism and Heusler's self-catalytic mechanism were based on steady state polarization measurements and Tafel slopes of the anodic reaction in the active dissolution region and near the open circuit potential[28,29]. The exception is the 1981 study of Keddam *et al.,* where the authors proposed a multi-path mechanism for iron dissolution in strong acid solutions based on polarization sweeps and EIS analysis[6,7]. However, their study was conducted in strong acid sulfate solutions and generally at lower pH than is of interest in CO_2 corrosion of mild steel. Therefore, the role of chlorides (almost always present in CO_2 corrosion of mild steel) and dissolved CO_2 and other carbonate species, on the kinetics of the anodic reaction remains unknown. Some previous studies claimed negligible differences between anodic sweeps in the active dissolution region, in the absence and presence of CO_2 close to the OCP, and therefore concluded that CO_2 does not affect the anodic reaction. However, the second group of researchers claimed that CO_2 affects the iron dissolution and increases the anodic reaction in transition and pre-passivation region[19,20,30]. Therefore, the question raised is this: what is the role of chlorides and dissolved CO_2 on the mechanism of iron dissolution in active, transition and pre-passivation region of the anodic reaction? Therefore, the third objective of this work is to use both DC (potentiodynamic sweeps) and EIS measurements to study the role of chlorides and CO_2 on the mechanism of the anodic reaction, and compare it to that in strong acidic solution.

- In the original plan for this project, it was ambitiously planned to extend the use of EIS to study of corrosion inhibitors in CO_2 corrosion of mild steel. However, this could not be done effectively before investigating the mechanisms of the cathodic and anodic reactions in the absence of corrosion inhibitors. Therefore, time only permitted the work on corrosion inhibitor to be initiated but not completed as originally planned. Therefore, the last and somewhat separate objective of this project described below is related to the characterization of the corrosion inhibitors and their role in corrosion mitigation. Critical micelle concentration (CMC) of corrosion inhibitors is considered an important measurable property. Moreover, it has been shown by many researchers that at the critical micelle concentration (CMC), the metal surface is fully covered and saturated by corrosion inhibitor molecules[24,25]. One of the well-known methods for determining CMC is surface tension measurements. However, this technique measured the change in surface tension of solution in the presence of inhibitors which may or may not be related to CMC which is a bulk property. Therefore, the fourth objective of the present work is evaluation of the techniques for determining CMC values relating to their accurate measurement. Finally, the relationship between CMC and inhibitor adsorption on the metal surface in terms of surface saturation concentration needs to be evaluated.

Chapter C: Identifying the Dominant Electrochemical Reaction in Electrochemical Impedance Spectroscopy [7]

Electrochemical Impedance Spectroscopy (EIS) is frequently used for the study of electrochemical reactions and associated mechanisms and phenomena. To study a specific reaction, it is important to choose the DC potential at which the measured impedance data carries information mostly related to that specific reaction. One of the first questions asked is typically, "at different potentials, which reaction contributes most to the recorded impedance spectra, cathodic or anodic?". For example, at the corrosion potential where the cathodic current density is equal to the anodic current density, does the impedance data carry information about the two reactions equally?

The first part of this chapter describes a methodology considered as an essential first step for the analysis of impedance data. This methodology consists of a new model that identifies the reaction dominated in a measured impedance at any specific potential. In the second part of the chapter, the same methodology was used to determine the DC potential at which the impedance response of cathodic reduction of hydrogen ions is dominant in order to determine the diffusion coefficient of hydrogen ion in a strong acid solution by using EIS data.

---

[7] The text, figures and tables in this chapter are taken from a publication of the author: N. Moradighadi, S. Nesic, and B. Tribollet, "Identifying the dominant electrochemical reaction in electrochemical impedance spectroscopy", *Electrochimica Acta* 400 (2021): p. 139460 (reference number [1]).

Part C.1. Approach for Determining the DC Potential for EIS Measurements and the Dominant Electrochemical Reaction

C.1.1. Introduction

EIS is an electrochemical technique that can be applied to study electrochemical mechanisms of reactions underlying corrosion, evaluate coating performance, characterize battery and fuel cell performance, etc.[6–8,13,21,31–37]. In EIS measurements, a small amplitude, alternating signal (current or potential) is applied at different frequencies to probe the impedance characteristics of a system being studied, in the research described herein corrosion.

In the field of corrosion, it has been common practice to use so-called direct current (DC) techniques to study the mechanisms of the electrochemical corrosion reactions; for some recent examples from aqueous CO_2 corrosion of mild steel, see Kahyarian, *et al.* [14]. Usually, DC techniques involve a rather slow change in potential and monitoring of the resulting steady state current response, such as done for example in potentiodynamic polarization methods. As an example, Figure 6.a shows the results of two separate potentiodynamic polarization sweeps (cathodic and anodic) conducted on mild steel in an aqueous CO_2 solution. Both potential sweeps were initiated at the open circuit potential (OCP), and then the potential was swept at the low rate of 0.125 mV/s in the cathodic and then anodic direction. At more positive potentials than the OCP, the measured steady state current density originates predominantly from the anodic reaction – in this case oxidation of iron– and therefore carries information mainly about the rate of this reaction. Similarly, at potentials more negative than the OCP, the measured steady state current density carries

information mostly about the rate of cathodic reactions in this case evolution of hydrogen *via* reduction of H^+ ions and water molecules.

But does that also mean that the analysis of the impedance obtained by EIS should follow the same logic: that is, at potentials more positive than OCP, the impedance of the anodic reaction is dominating, while at more negative potentials it is the impedance of the cathodic reaction that dominates. If so, at the OCP, where the rates of the anodic and cathodic reactions are equal, do the EIS measurements detect an even contribution of both reactions to the measured impedance (see the example in Figure 6.b)? The answer to this question is the main objective of the research described below. Restated more generally: before conducting EIS measurements, it is important to estimate what fraction of the impedance recorded at any given potential is contributed by one reaction or the other. In this work, a methodology is introduced to estimate the dominant electrochemical reaction contributing to the measured impedance at any given potential. The intention behind this research is that the described method will help corrosion scientists better select experimental conditions, so that the collected impedance spectra carry sufficient information about the electrochemical reactions of interest. In order to demonstrate the new methodology, an experimental study was first undertaken, where potentiodynamic sweep data were collected followed by EIS measurements conducted at different DC potentials.

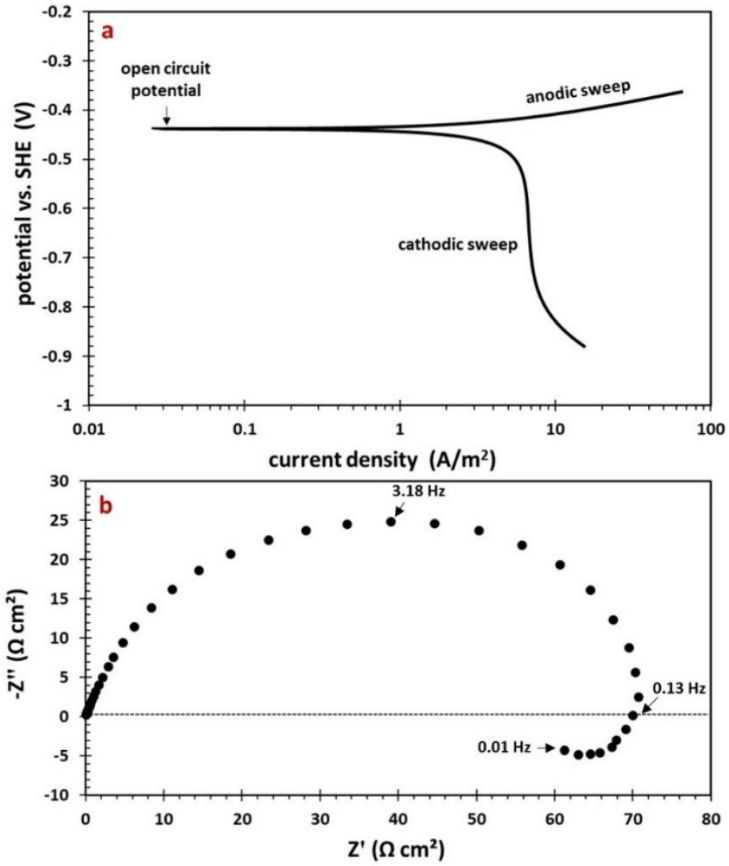

Figure 6

Corrosion of X65 mild steel RDE @ 2000 rpm, 0.1 M NaCl aqueous solution sparged with 1 bar CO_2, pH 4.0, 30°C: a) steady state potentiodynamic polarization sweeps; b) electrochemical impedance spectrum conducted at the open circuit potential (OCP) show as a Nyquist plot.

C.1.2. Methodology

Experiments were performed in a standard 1 L, three-electrode glass cell consisting of a rotating disk working electrode (RDE), a graphite rod counter electrode and an external saturated Ag/AgCl reference electrode, connected to the electrolyte *via* a salt bridge and a Luggin capillary. The experimental apparatus is shown in Figure 7.

The summary of the test conditions for the experiments is shown in Table 1. The test solution was continuously sparged with CO_2 gas during and two hours before the initiation of the experiments, to saturate the solution and purge any dissolved O_2 (concentration levels below 10 ppb are readily achieved). The pH of the test solution was adjusted to pH 4.0 using a dilute NaOH solution. The working electrode was made from API[8] 5 L X65 mild steel (composition provided in Table 2) in the shape of a 5 mm diameter disk. The pure iron disk electrode was press fitted to a Teflon sample holder to create a contact only between solution and base area of the sample. The surface of sample was polished using silicon carbide abrasive papers (up to 1000 grit) and finally mirror finished using diamond suspension liquids (down to 0.25 μm). Mirror finishing was performed to minimize formation of gas bubbles on the surface of the RDE during polarization and improve reproducibility of measurements. Following the surface preparation, the sample was cleaned with isopropyl alcohol in an ultrasonic bath and then dried with a N_2 gas stream.

Before each polarization sweep and EIS measurements, OCP was monitored for at least 10 minutes to achieve a stable value. After obtaining a stable OCP, the cathodic polarization sweep was conducted by polarizing the RDE from OCP to OCP – 350 mV using a scan rate of 0.125 mV/s. Following the cathodic polarization sweep, EIS measurements were performed in succession at different DC potentials, starting from OCP and stepping the DC potential by –50 mV, down to –300 mV more negative than OCP. For the measurements done at potentials more positive than OCP, an EIS measurement was

[8] American Petroleum Institute (API), 1220 L St. NW, Washington, DC, 20005.

performed only at OCP + 50 mV and, finally, a full anodic polarization sweep was conducted from OCP to OCP + 100 mV.

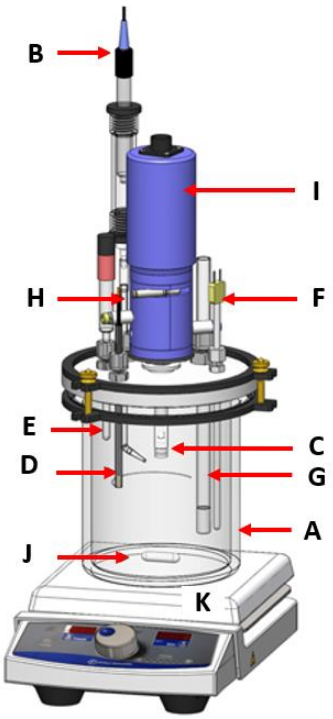

Figure 7

The experimental setup: A. glass cell; B. reference electrode; C. working electrode (X65 mild steel); D. counter electrode (graphite rod) ; E. pH probe; F. thermocouple; G. gas inlet; H. gas outlet; I. motor; J. stir bar; and K. hot plate.[9]

[9] Drawing courtesy of Cody Shafer, OU, ICMT.

Table 1

Experimental conditions.

Parameters	Values
Test apparatus	Rotating disk electrode Three-electrode glass cell
Sparge gas	pCO_2 = 1 bar
Temperature	30±0.5 ºC
pH	4.00±0.01
Supporting electrolyte	0.1 M NaCl
Rotation rate	2000 rpm
Electrode material	API 5L X65
Parameters of the EIS scans: Frequency AC potential DC potential	 from 10000 to 0.01 Hz 10 mV rms. OCP (– 435±1 mV vs SHE) OCP – 50 mV OCP – 100 mV OCP – 150 mV OCP – 200 mV OCP – 250 mV OCP – 300 mV OCP + 50 mV

Table 2

Chemical composition of API 5L X65.

Element	C	Nb	Cr	Ni	Mn	P	Ti	Al	Fe
Composition (wt.%)	0.05	0.03	0.15	0.38	1.51	0.004	0.01	0.033	Balance

C.1.3. Results and Discussion

C.1.3.1. Potentiodynamic Sweep and the Model. In corrosion of mild steel in acidic aqueous solutions, it is known that the main anodic reaction is the oxidation of iron

(Reaction (1)) and the main cathodic reaction is the reduction of hydrogen ions (Reaction (2)). At very negative potentials, reduction of water (Reaction (3)) occurs as well.

Dissolution of iron $$Fe \rightleftharpoons Fe^{2+} + 2e^{-} \quad (1)$$

Reduction of hydrogen ion $$H^{+} + e^{-} \rightleftharpoons \frac{1}{2}H_2 \quad (2)$$

Reduction of water $$H_2O + e^{-} \rightleftharpoons \frac{1}{2}H_2 + OH^{-} \quad (3)$$

Reaction (1) shows the general reaction for oxidative iron dissolution which involves 3 consecutive steps as shown in (Reactions (4)-(6))[28].

$$Fe + OH^{-} \rightleftharpoons (FeOH)_{ads} + e^{-} \quad (4)$$

$$(FeOH)_{ads} \xrightarrow{rds} (FeOH)^{+} + e^{-} \quad (5)$$

$$(FeOH)^{+} + H^{+} \rightleftharpoons Fe^{2+} + H_2O \quad (6)$$

The measured potentiodynamic sweep is shown in Figure 8 at which the potential is converted from Ag/AgCl reference electrode, used during experiment, to standard hydrogen electrode (SHE) considering 192 mV difference. In order to deconvolute the data shown and extract values pertaining to the individual electrochemical reactions, shown above, a simple mechanistic model was constructed using the kinetic equations of each electrochemical reactions (Equations (7)-(13)) with the calculated results shown in Figure 9 [28,38–41]. In the model, the iron dissolution is controlled purely by charge transfer and Equation (7) was used for modeling of this reaction, which is approximately valid at a limited potential range close to the OCP. Moreover, it was assumed that the water reduction is under pure charge transfer control (Equation (13)) while the reduction of hydrogen ion

is under charge transfer control at more positive potentials and under mass transfer and chemical reaction control at more negative potentials (Equations (8)-(12)).

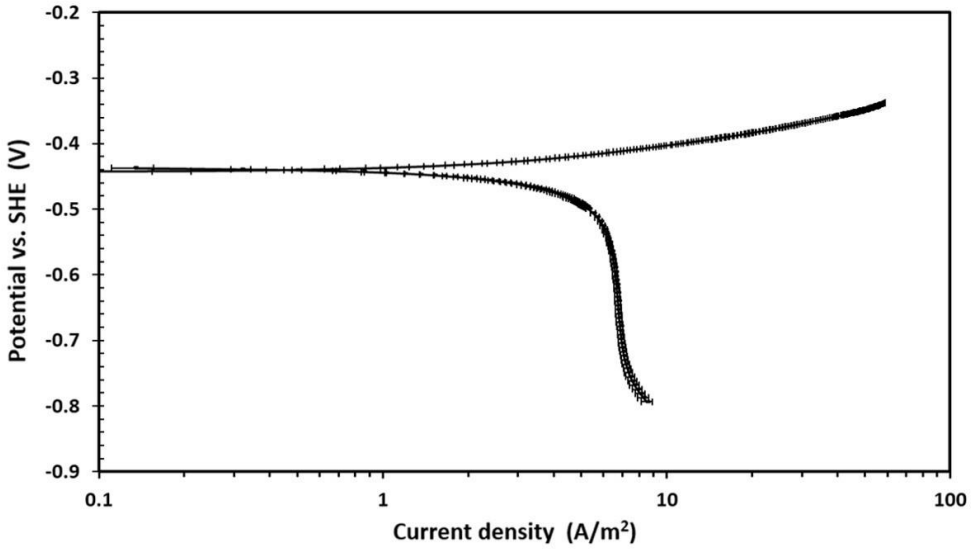

Figure 8

Steady state polarization sweep curve, measured using a sweep rate of 0.125 mV/s, on X65 mild steel RDE at 2000 rpm, corroding in an aqueous solution at pH 4.0, 30°C, saturated at 1 bar CO_2, with 0.1 M NaCl supporting electrolyte. Error bars represent minimum and maximum current densities calculated in duplicated experiments.[10]

Iron dissolution - charge transfer current density:

$$i_{ct,Fe} = i_{0,Fe} e^{\left(\frac{1.5F\eta}{RT}\right)} \quad (7) \quad [28]$$

Hydrogen ion reduction - charge transfer controlled current density:

[10] In analysis of the anodic potentiodynamic sweeps it was seen that sometimes the OCP measured before the sweep was done was somewhat different (about 20 mV) compared to that obtained prior to the cathodic sweep (due to the presence of adsorbed hydrogen ion on the metal surface as a result of preceding cathodic potentiodynamic and EIS measurements in cathodic region). This was corrected by adjusting the measured OCP of the anodic sweep until the two matched.

$$i_{ct,H^+} = i_{0,H^+} e^{\left(\frac{-0.5F\eta}{RT}\right)} \quad (8)$$ [38]

Hydrogen ion reduction - mass transfer and chemical reaction limiting current density:

$$i_{lim,H^+} = 0.62F{D_{H^+}}^{2/3}\omega^{1/2}\nu^{-1/6}C_{H^+} + \frac{FD_{H^+}(C_{CO_2} + C_{H^+})}{\delta_d + \frac{\delta_r}{K_{hy,CO_2}}} \quad (9)$$ [40,41]

Diffusion layer thickness:

$$\delta_d = 1.61{D_{H^+}}^{1/3}\omega^{-1/2}\nu^{1/6} \quad (10)$$ [40]

Reaction layer thickness:

$$\delta_r = \left(\frac{D_{H^+}}{\left(k_{f,hy,CO_2} + k_{b,hy,CO_2}\right)}\right)^{1/2} \quad (11)$$ [40]

Hydrogen ion reduction - total current density:

$$\frac{1}{i_{H^+}} = \frac{1}{i_{ch,H^+}} + \frac{1}{i_{lim,H^+}} \quad (12)$$ [40]

Water reduction-charge transfer controlled current density:

$$i_{ct,H_2O} = i_{0,H_2O} e^{\left(\frac{-0.5F\eta}{RT}\right)} \quad (13)$$ [38]

Summing the current densities for the three reactions yields the overall potentiodynamic sweep, shown in Figure 9. The good fit between the experimental results and the modeled potentiodynamic sweep is shown in Figure 9. The outcome of this exercise showed that at OCP the cathodic reaction rate is dominated by hydrogen ion reduction, which is under mixed charge transfer, mass transfer and chemical reaction control, as shown in Figure 9, given that the corrosion current density (5.1 A m^{-2}), is close in magnitude to the limiting current density (6.7 A m^{-2}).

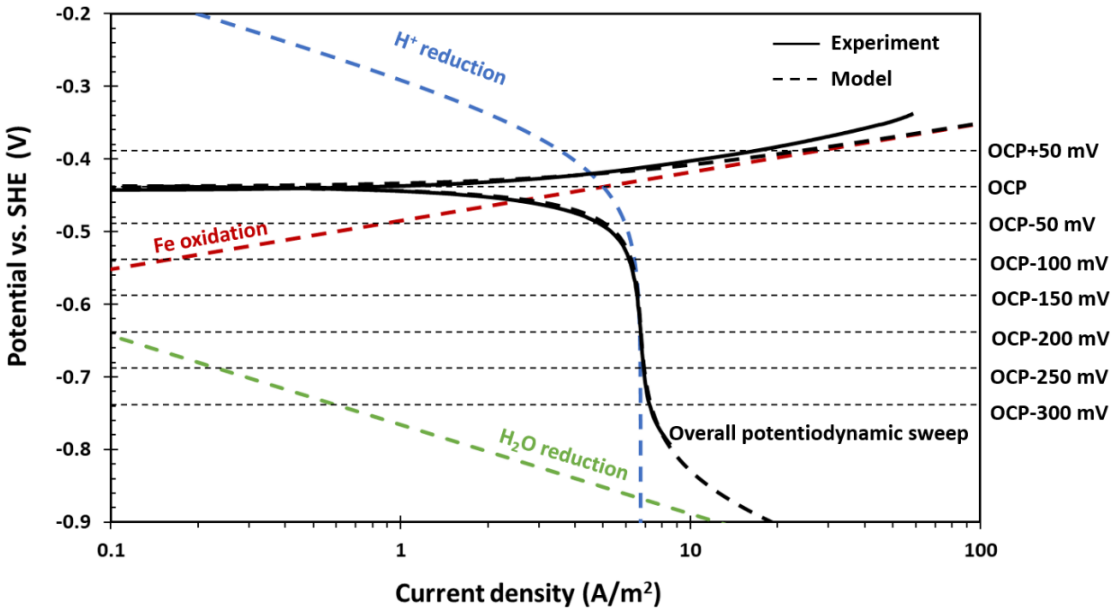

Figure 9

Experimental and modeled steady state potentiodynamic sweep of individual reactions underlying the overall potentiodynamic sweep shown in Figure 8. Modeling parameters: mild steel RDE at 2000 rpm, pH 4.0, 30°C, aqueous solution saturated at 1 bar CO_2, with 0.1 M NaCl supporting electrolyte.

C.1.3.2. Identifying the Dominant Electrochemical Reaction. As shown above, Figure 9 identifies the individual electrochemical reactions in a potentiodynamic sweep measurement during CO_2 corrosion of a mild steel. Using Equation (14), the percent contributions of individual electrochemical reaction to the total current density obtained at different potentials can be calculated, shown as a bar graph in Figure 10.

$$\text{Contribution of current density of reaction j} = \frac{i_j}{(i_{ct,Fe} + i_{H^+} + i_{ct,H_2O})} \times 100 \qquad (14)$$

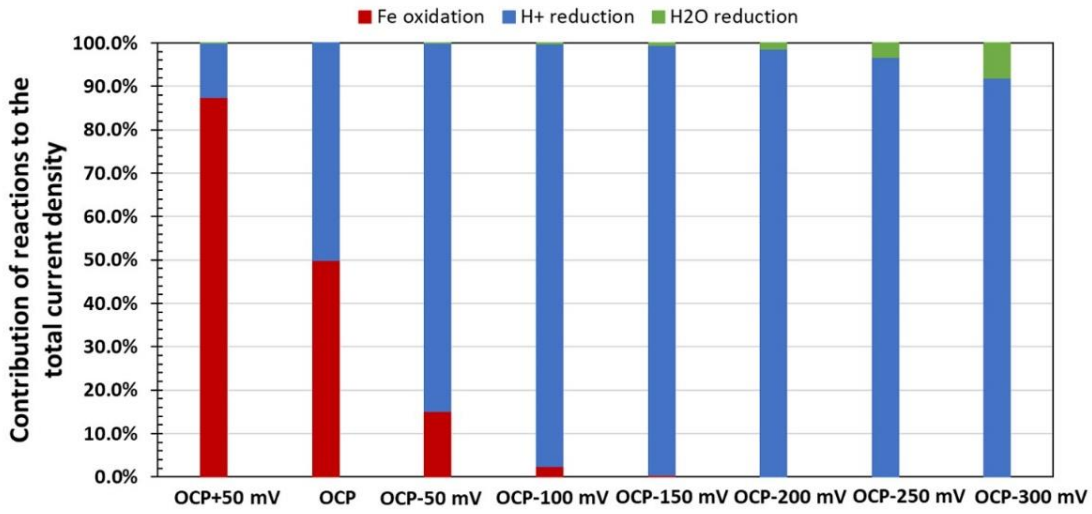

Figure 10

Contribution of each reaction (H^+ reduction, Fe oxidation and H_2O reduction) to the total current density, based on Figure 4. Modeling parameters: X65 mild steel RDE, 2000 rpm, pH 4.0, 30°C, aqueous solution saturated at 1 bar CO_2, and with 0.1 M NaCl supporting electrolyte.

At OCP + 50 mV, 88.8%. of the measured current density was related to the oxidation of iron. Conversely, at OCP – 50 mV, 86.8% of the measured current density was associated with the H^+ reduction. As the potential becomes more negative than OCP, the contribution of the current density originating from H^+ reduction to the total current density increases, and at the same time the water reduction contribution grows. As indicated in Figure 9, at very negative potentials the cathodic reaction is dominated by the water reduction reaction (not shown in Figure 10).

The deconvoluted data shown in Figure 9 can also be used to estimate the contribution of the individual reactions to the overall impedance that would be measured at different DC potentials. Given that the value of impedance includes both the resistance and the reactance, only the resistance (real part of the impedance) can be calculated from

the steady state data shown in Figure 9. As the mass transfer and chemical reactions (that give rise to the reactance – the imaginary part of the overall impedance) and the charge transfer reactions (manifested as the real part of the overall impedance) are linked in an electrochemical process such as corrosion, it can be argued that estimating the real part of the impedance gives a reasonable estimate of the relative magnitude of the overall impedance [42].

Potentiodynamic sweep data can be further treated in order to estimate the real part of the impedance at any potential (which is called here the *polarization resistance*, R_p), by calculating the first derivative of the current density-potential curve using Equation (15), for each individual electrochemical reaction, shown in Figure 9. The results are plotted in Figure 11.

$$R_p = \frac{\Delta V}{\Delta I} \qquad (15)$$

The line representing the anodic reaction in Figure 11 shows an increase in $R_{p,Fe}$ as potential becomes more negative, while for the cathodic reactions the polarization resistance decreases. However, as the limiting current density range for the H^+ reduction reaction is approached, the R_{p,H^+} for this reaction reverses course and starts to increase, as shown in Figure 11. This is because it becomes harder to change the rate of this reaction by polarization as it gets closer to the limiting current density, which is controlled by slow mass transfer and homogenous chemical reaction rates. The R_{p,H_2O} keeps getting smaller at more negative potential across the whole range of potentials.

Using an electrical circuit analog model of this electrochemical process, where resistances arranged in parallel represent individual electrochemical reactions, the overall

polarization resistance $R_{p,overall}$ can be calculated using Equation (16). It shows that the overall polarization resistance is dominated by the smallest of the individual polarization resistances. In other words, the reaction/process with the smallest polarization resistance will be dominant. The overall polarization resistance for the 3 reactions is shown as the thick black line in Figure 11.

$$\frac{1}{R_{p,overall}} = \frac{1}{R_{p,Fe}} + \frac{1}{R_{p,H^+}} + \frac{1}{R_{p,H_2O}} \qquad (16)$$

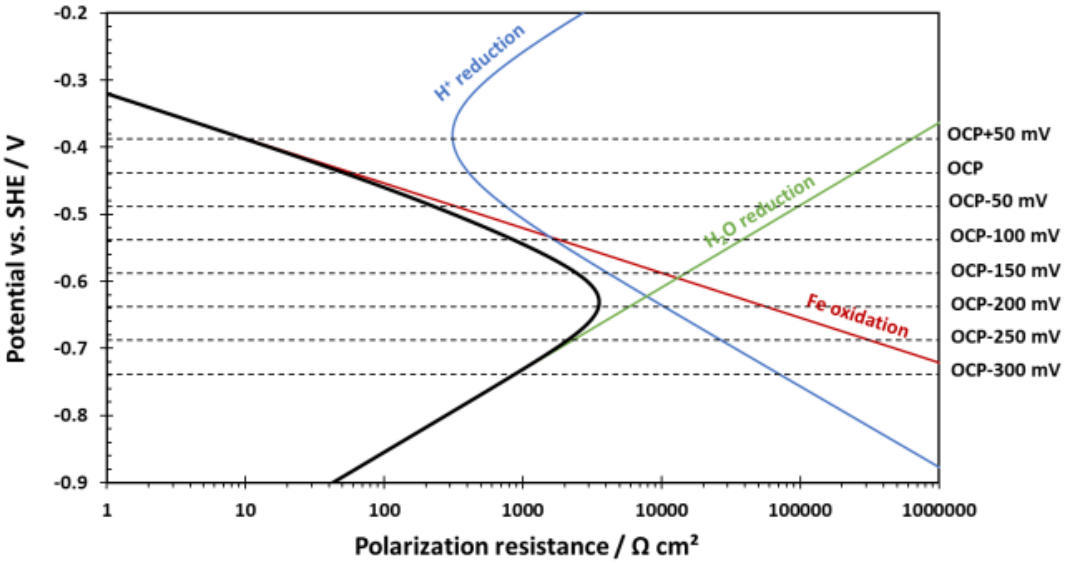

Figure 11

Modeled polarization resistance of H^+ reduction, Fe oxidation, H_2O reduction and overall polarization resistance, derived from the modeled potentiodynamic sweeps shown in Figure 9. Modeling parameters: X65 mild steel RDE, 2000 rpm, pH 4.0, 30°C, aqueous solution saturated at 1 bar CO_2, and with 0.1 M NaCl supporting electrolyte.

It is shown in Figure 11 that at more positive potentials the overall polarization resistance is dominated by the anodic reaction, given that the Fe oxidation reaction has the smallest polarization resistance in this range. In the mid-range of potentials, the

contribution of H^+ reduction (which is under mass transfer control) has the largest influence on the $R_{p,overall}$. Finally, at the more negative range of potentials, the R_{p,H_2O} dominates (being the smallest of the three). Even if this behavior is qualitatively similar to the changes seen in the current density, shown in Figure 9, the two do not align entirely.

The same information is represented in Figure 12 where using Equation (17) the contributions of the three reactions to the polarization admittance ($1/R_p$) are calculated and explicitly shown at different potentials. Now, the contributions of individual reactions to the measured current density (shown in Figure 10) can be directly compared the contributions to the overall polarization admittance (shown in Figure 12).

$$\text{Contribution of admittance of reaction "}j\text{"} = \frac{R_{p,overall}}{R_j} \times 100 \tag{17}$$

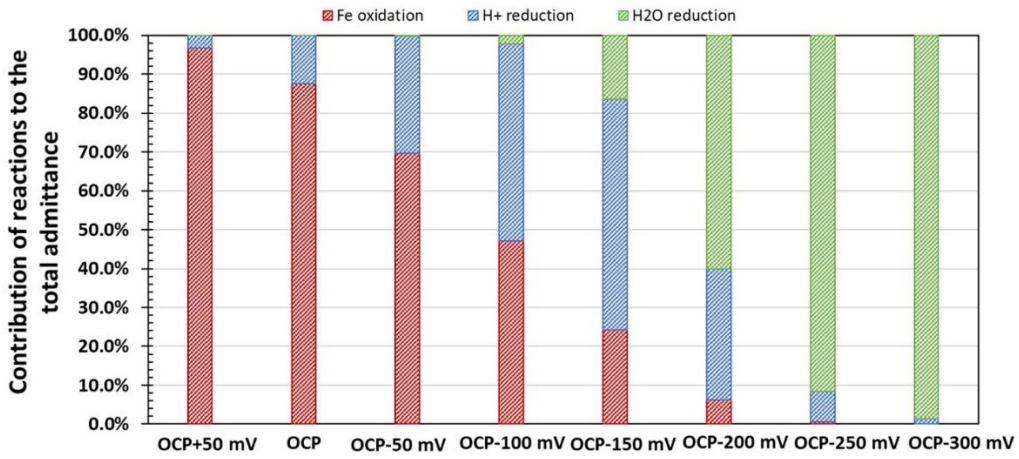

Figure 12

Contribution of individual reaction (H^+ reduction, Fe oxidation and H_2O reduction) to the total admittance, based on Figure 11. Modeling parameters: X65 mild steel RDE, 2000 rpm, pH 4.0, 30°C, aqueous solution saturated at 1 bar CO_2, and with 0.1 M NaCl supporting electrolyte.

At OCP + 50 mV, where 88.8% of the measured current density comes from the anodic reaction, the overall polarization resistance is also dominated by the same reaction. At this potential, the $R_{p,Fe}$ is much smaller than it is for the other reactions and represents 96.8% of the overall polarization admittance ($1/R_{p,overall}$). Thus, both the measured current density and the measured polarization resistance carry the information about the same reaction: Fe oxidation.

At the OCP, the anodic and cathodic current densities are balanced (equal) and no current is flowing in the external circuit and the rates of the individual reactions cannot be assessed directly. However, at the OCP, the measured polarization resistance is still dominated by the $R_{p,Fe}$: polarization resistance for this reaction is about 4 times smaller than that for R_{p,H^+} and orders of magnitude smaller than R_{p,H_2O}. Thus, at OCP, the polarization resistance carries information mostly about Fe oxidation: polarization admittance of this reaction is 87.6% of the overall polarization admittance.

At OCP – 50 mV, the contribution of the $R_{p,Fe}$ to the overall polarization resistance is still dominant. The polarization admittance of this reaction is 69.7% of the overall polarization admittance, while at the same time the current density is dominated by the H^+ reduction reaction (which contributes 86.8% to the measured current density). Therefore, while at this potential, the current density mostly carries information about the H^+ reduction, the polarization resistance gives us information mostly about Fe oxidation.

At OCP – 100 mV, the $R_{p,Fe} \approx R_{p,H^+}$, while the R_{p,H_2O} is still orders of magnitude higher. At the same time 97.6 % of the measured current density comes from the cathodic reactions (mostly H^+ reduction). Again, the measured current density mostly carries

information about the H^+ reduction reaction, while the measured polarization resistance gives mixed information, contributed approximately equally by both Fe oxidation and H^+ reduction.

At OCP – 150 mV, the R_{p,H^+} is approximately half of the $R_{p,Fe}$, which is again about half of R_{p,H_2O}. At the same time, 99.6% of the measured current density comes from the cathodic reactions (with 99.1% of that contributed by H^+ reduction). Therefore, the current density carries information about the H^+ reduction, while the polarization resistance gives mixed information dominated by the cathodic reactions: mostly H^+ reduction (polarization admittance of H^+ reduction is 59.5% of the overall polarization admittance).

At OCP – 200 mV, 99.9% of the current density comes from the cathodic reaction (98.6% of that from H^+ reduction). At the same time, the $R_{p,Fe}$ is about 15 times higher than the ones for the R_{p,H^+} and R_{p,H_2O}. So, the current density carries information about the H^+ reduction, while the overall polarization resistance gives us mixed information mostly about the cathodic reactions contributed more by H_2O reduction and less by H^+ reduction; polarization admittance of H_2O reduction is 60.2% of the overall polarization admittance.

At OCP – 250 mV, 99.99% of the current density comes from the cathodic reactions (with 96.6% of that from H^+ reduction) while the overall polarization resistance is dominated by R_{p,H_2O} which is an order of magnitude lower than R_{p,H^+} and two orders of magnitude lower than $R_{p,Fe}$. In this case the current density carries information about H^+ reduction, while the measured polarization resistance gives us information predominantly

about H_2O reduction: polarization admittance of H_2O reduction is 91.6% of the overall polarization admittance.

At OCP – 300 mV, almost 100% of the current density comes from the cathodic reactions (mostly H^+ reduction) while the overall polarization resistance is dominated by R_{p,H_2O} , which is two orders of magnitude smaller than R_{p,H^+} and three orders of magnitude smaller than $R_{p,Fe}$. Therefore, the current density carries information predominantly about H^+ reduction, while the overall polarization resistance carries information predominantly about H_2O reduction: polarization admittance of H_2O reduction is 98.7% of the overall polarization admittance.

C.1.3.3. Comparisons with the Experimental EIS Data. The conclusions drawn above about the dominant reactions at different potentials, based on estimated polarization resistance, were examined next to determine if they are consistent with EIS measurements conducted at those same potentials.

In Figure 13 collected at the potential OCP + 50 mV and at the OCP is examined to establish whether the diameter of the high frequency loop increases, meaning that the charge transfer resistance value increases, *i.e.*, the rate of that reaction decreases at more negative potentials. This confirms that, in this potential range, the impedance of the anodic reaction is dominant and is the one being detected by the model in Figure 11 and Figure 12.

Moving on to even more negative potentials such as OCP – 50 mV, the same trend continues, *i.e.*, the diameter of the high frequency loop and the charge transfer resistance keeps on increasing. This confirms that in, this range of potentials, the impedance of the

anodic reaction remains dominant, even at OCP – 50 mV where 69.7% of the measured impedance is estimated to come from the anodic reaction, while most of the measured current density (84.8%) is related to the cathodic reaction (Figure 10).

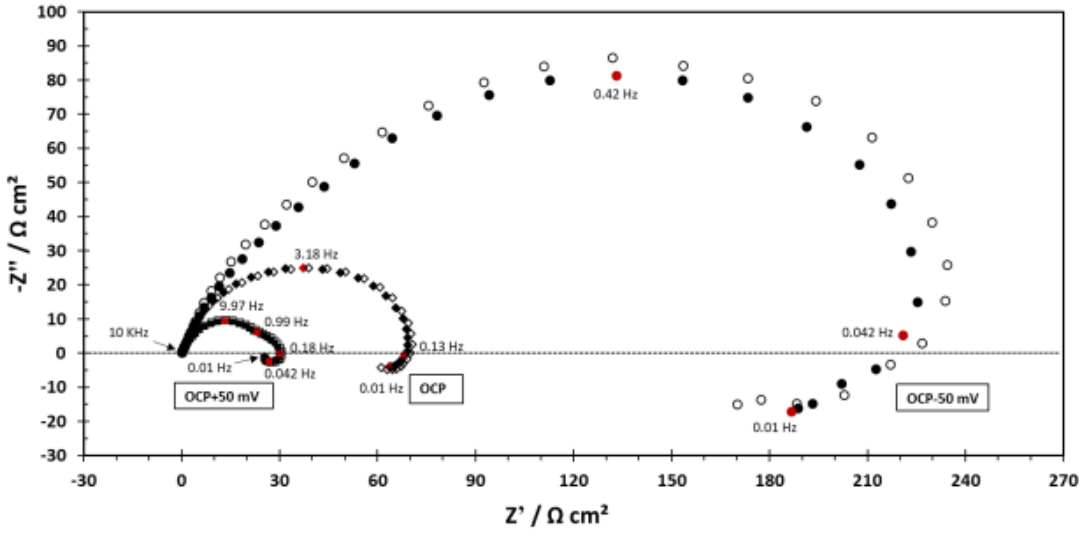

Figure 13

Nyquist plot at OCP + 50 mV, OCP, and OCP – 50 mV. Experimental parameters: X65 mild steel RDE, 2000 rpm, pH 4.0, 30°C, aqueous solution saturated at 1 bar CO_2, 0.1 M NaCl supporting electrolyte and frequency range from 10,000 - 0.01 Hz. Nyquist plots having the same shaped markers represents duplicated experiments.

In Figure 13 it can also be observed that the EIS curves collected at the OCP + 50 mV, at the OCP and at the OCP – 50 mV look quite similar: a depressed semi-circle with an inductive loop at low frequencies that carry information mostly about the anodic reaction – oxidation of iron, which dominates the measured impedance in this potential range, as shown above. It has been argued in some previous studies that the high frequency capacitive loop is related to the double layer capacitance followed by a low frequency

inductive loop representing the relaxation of $Fe(I)_{ads} \equiv FeOH_{ads}$ as an intermediate species in the iron dissolution reaction [6,7,43]

In Figure 14, the spectrum collected at OCP – 100 mV is added, which indicates the same trend: an increase in the overall impedance with the decreasing potential. This is consistent with the analysis above, where it was concluded that about half of the measured impedance at this potential comes from the anodic reaction, even if it is 100 mV more negative than the OCP. However, the key difference is the absence of the inductive loop, which was associated with the anodic reaction. This is related to the fact that the measured impedance at OCP – 100 mV is influenced by the cathodic reactions as much as the anodic reaction, making it difficult to observe the inductive loop at low frequencies.

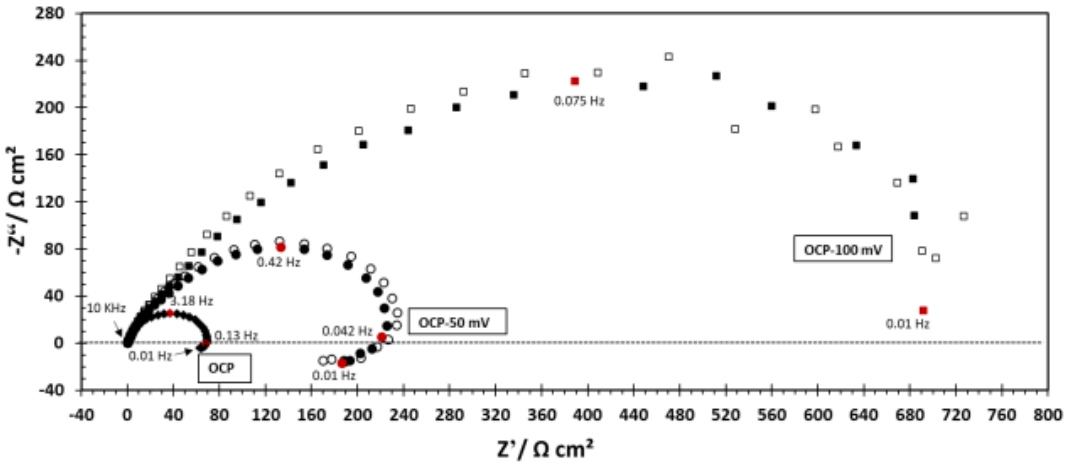

Figure 14

Nyquist plot at different OCP, OCP – 50 mV and OCP – 100 mV. Experimental parameters: X65 mild steel RDE, 2000 rpm, pH 4.0, 30°C, aqueous solution saturated at 1 bar CO_2, 0.1 M NaCl supporting electrolyte and frequency range from 10,000 - 0.01 Hz. Nyquist plots having the same shaped markers represents duplicated experiments.

In Figure 15, the spectrum collected at OCP – 150 mV is compared to the one obtained at OCP – 100 mV, where a profound change in the shape of the spectrum is apparent. According to the analysis above, at OCP – 150 mV the measured impedance is dominated by the cathodic reaction – H^+ reduction; being almost entirely under limiting current density control. This is reflected in Figure 15 where this behavior which is consistent with an existence of a so-called Warburg impedance at this potential indicates the influence of the limiting current density in the low frequency range.

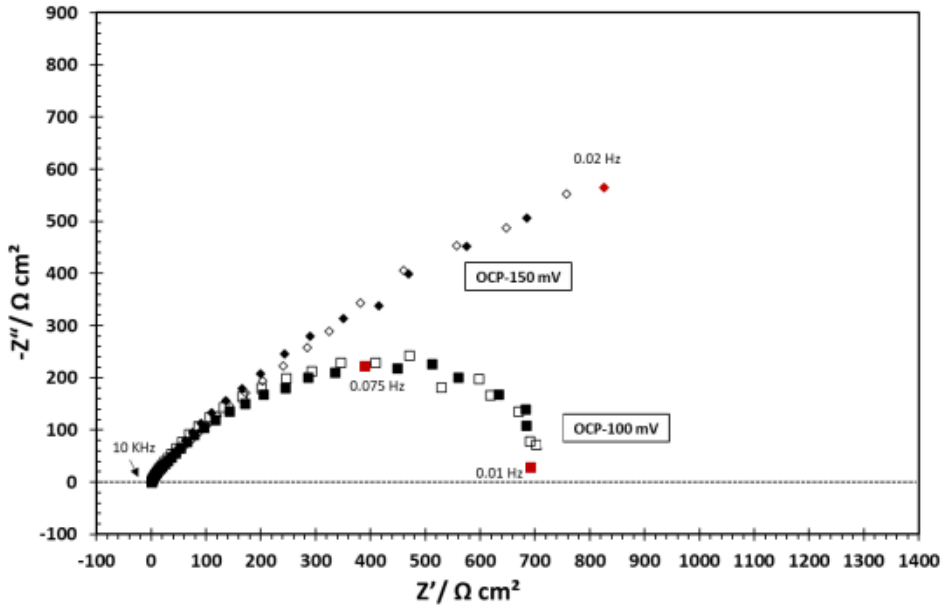

Figure 15

Nyquist plot at different OCP – 100 mV and OCP – 150 mV. Experimental parameters: X65 mild steel RDE, 2000 rpm, pH 4.0, 30°C, aqueous solution saturated at 1 bar CO_2, 0.1 M NaCl supporting electrolyte and frequency range from 10,000 - 0.01 Hz. Nyquist plots having the same shaped markers represents duplicated experiments.

Almost the same behavior is seen at OCP – 200 mV and OCP – 250 mV (Figure 16 where the overall impedance is predominantly influenced by the same cathodic

reactions – reduction of H^+ and H_2O, with the former being under limiting current density control and the latter being under charge transfer control. According to Figure 12, potential becomes more negative the impedance associated with the reduction and H_2O becomes dominant; and being under charge transfer control it could be expected that the shape of the spectrum undergoes a change. While this is difficult to discern from spectra collected at OCP – 200 mV and OCP – 250 mV, it becomes clear when comparing with a spectrum collected at OCP – 300 mV. There, the measured impedance is significantly smaller, the shape of the curve is quite different with at least two time constants, all suggesting a new reaction dominating the impedance in this potential range. This is consistent with the analysis presented in Figure 11. It is noteworthy that the H_2O reduction reaction is not clearly discernable in this potential range by just looking at the potentiodynamic sweeps presented in Figure 9. To identify it clearly, it would take approximately another 100 mV of polarization in the more negative direction, yet it dominates the impedance spectrum at this potential.

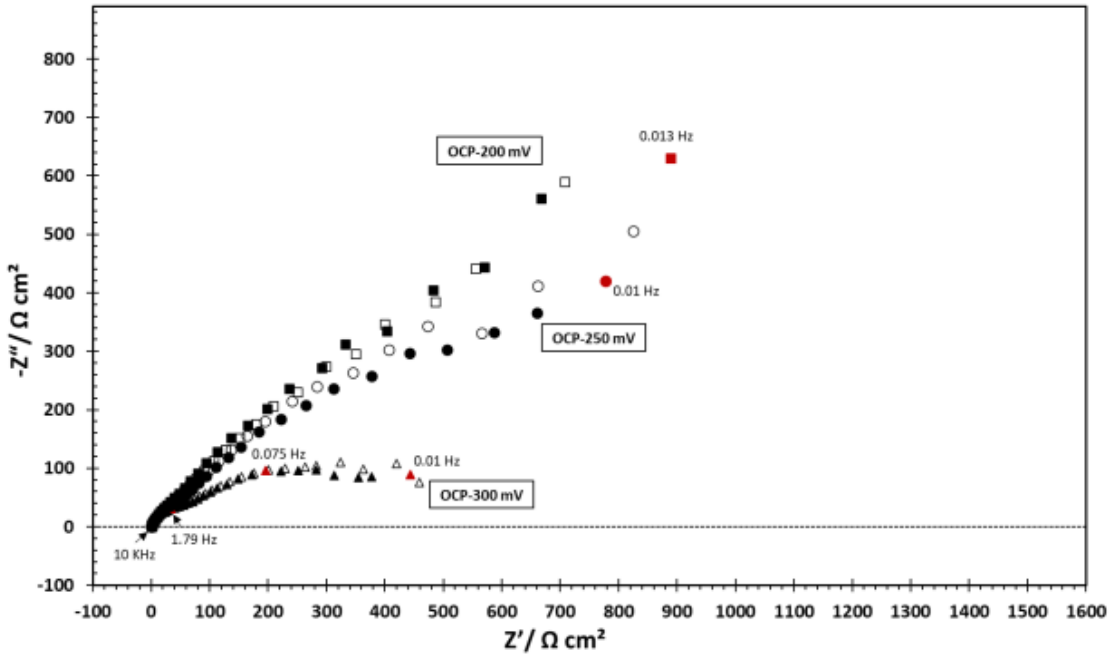

Figure 16

Nyquist plot at different OCP – 200 mV, OCP – 250 mV and OCP – 300 mV. Experimental parameters: X65 mild steel RDE, 2000 rpm, pH 4.0, 30°C, aqueous solution saturated at 1 bar CO_2, 0.1 M NaCl supporting electrolyte and frequency range from 10,000 - 0.01 Hz. Nyquist plots having the same shaped markers represents duplicated experiments.

The values of the charge transfer resistance and polarization resistance are estimated from the impedance spectra (Figure 13-Figure 16) then compared to polarization resistance calculated from the model fitted to the potentiodynamic sweep curves (Figure 11), and are presented in Table 3. The charge transfer resistance and the polarization resistance were determined by a simple visual inspection of the provided Nyquist plots (shown in Appendix II.2), without resorting to equivalent circuit analysis and fitting algorithms. Charge transfer resistance is the resistance related to pure charge transfer

current density. In other words, when the change in current density is only related to the change in potential, as shown in Equation (18).

$$R_{ct} = \left(\frac{\Delta V}{\Delta i}\right)_{C_i(0),\theta_i} \qquad (18)$$

For H^+ reduction, the polarization resistance is the combination of charge transfer and mass transfer resistances. For iron oxidation, the polarization resistance is related to the charge transfer resistance and the adsorption kinetics of FeOH on the metal surface. In the vicinity of the corrosion potential, the overall polarization resistance can be represented mostly by the anodic and cathodic polarization resistances in parallel to each other. Reliable estimation of the polarization resistance was possible only for spectra collected at the most positive potentials and the most negative potentials. The spectra collected in the mid-range of potentials, which are strongly influenced by the H^+ reduction reaction, which is under limiting current density control, were not able to provide an accurate estimation of the polarization resistance. Overall, a reasonable agreement is observed which reinforces the validity of the methodology and the interpretations presented above.

Table 3

Comparison of charge transfer resistance estimated from EIS measurements (Figure 13-Figure 16) with the polarization resistance calculated from the model fitted to the potentiodynamic sweeps (Figure 11). Modeling and experimental parameters: mild steel RDE at 2000 rpm, pH 4.0, 30°C, aqueous solution saturated at 1 bar CO_2, with 0.1 M NaCl supporting electrolyte.

	OCP +50 mV	OCP	OCP –50 mV	OCP –100 mV	OCP –150 mV	OCP –200 mV	OCP –250 mV	OCP –300 mV
R_{ct} from EIS experiments (Ω cm^2)	25±1	69.5±0.5	224±3	740±5	125±5	123±4	98±3	64.5±0.5
R_p from EIS experiments (Ω cm^2)	25±1	58.5±0.5	148±5	740±5	cannot be reliably determined	cannot be reliably determined	cannot be reliably determined	456±6
R_p from model potentiodynamic sweep (Ω cm^2)	10	51	225	851	2447	3518	2772	883

C.1.4. Summary

A new methodology based on modeling potentiodynamic sweeps has been developed to estimate the dominant electrochemical reaction(s) contributing to the impedance measured by EIS at any potential. This model can help to design experiments by selecting DC potentials in EIS measurements which can best elucidate the behavior of reactions of interest.

At various potentials, the relative contributions of different reactions to the measured impedance in EIS measurements are not always analogous to their contributions to the measured current density. For example, in the case presented above related to corrosion of mild steel in a CO_2 solution, at a potential 50 mV more negative than the open circuit potential, the dominant reaction contributing to the measured current density is due to the cathodic reaction (H^+ reduction) while the dominant reaction contributing to the measured impedance is the anodic reaction (Fe oxidation).

Part C.2. Determining the DC Potential to Study the Cathodic Reduction of Hydrogen Ion- Example of Determining the Diffusion Coefficient of Hydrogen Ion in Strong Acidic Solutions [11]

C.2.1. Introduction

In the study of corrosion of mild steel in a strong acid solution, the electrochemical reactions are anodic dissolution of iron and the cathodic reduction of hydrogen ions and water. For an EIS study of the mentioned electrochemical reactions, choosing the appropriate DC potential is of great importance. For example, to study the hydrogen reduction reaction, which is influenced by the mass transfer and diffusion of hydrogen ions, a DC potential must be chosen at which the EIS response provides mostly information about the hydrogen reduction reaction and the influence of impedance of other reactions should be minimized.

In this work, a DC potential range at which the impedance of the hydrogen evolution reaction is dominant will be determined using the method describe in Section C.1., assuming that the resistance of the electrochemical reactions is due to iron oxidation, hydrogen reduction and water reduction. Next, the EIS data, obtained at the determined DC potential, will be analyzed using a method developed by Tribollet, *et al.*,[8,44] to determine the diffusion coefficient of the hydrogen ion in a strong acid solution.

---

[11] Portion of the text, figures and tables in this part are taken from a publication of the author: N. Moradighadi, B. Brown, and S. Nesic, "Note on Selecting DC Potentials for EIS Measurements: An Example of Determining the Diffusion Coefficient of Hydrogen Ion in Aqueous Solutions," in CORROSION 2021, paper no. 16753 (Virtual: AMPP, 2021) (reference number [3]).

C.2.2. Background-Theory Behind Calculation of Diffusion Coefficients [12]

For an electrochemical reaction that depends both on potential and metal surface concentration of electroactive species, the faradic impedance related to it is a faradic resistance in series with a diffusion impedance as shown in Figure 17. As an example, the diffusion impedance of a cathodic reduction of hydrogen ions, in a simple system such as a strong acid solution, is related to mass transfer phenomena such as diffusion of hydrogen ions.

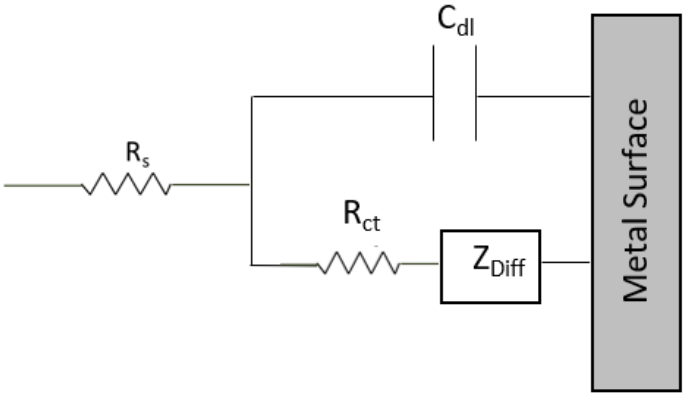

Figure 17

The schematic of the Randles circuit representing the surface phenomena and faradic reactions depending on potential and concentration of species at the metal surface[3].

As shown in Figure 17 the faradic impedance (Z_F) is a summation of faradic resistance (R_{ct}) and diffusion impedance (Z_{Diff}) as shown in Equation (19) where Z_{Diff} is defined in Equation (20) [8].

---

[12] The mathematical descriptions provided in this section is from reference[8,44]. The variables are defined in Appendix I.

$$Z_F = R_{ct} + Z_{Diff} \tag{19}$$

$$Z_{Diff} = R_{Diff}\left(-\frac{1}{\acute{\theta}_i(0)}\right) \tag{20}$$

R_{Diff} is diffusion resistance, $\theta_i(0)$ is defined as dimensionless concentration (Equations (21)) , $\acute{\theta}_i(0)$ is its first derivative with respect to dimensionless distance from the surface (Equations (22)) and $\widetilde{c_i}$ is transient concentration of species i [8,44]. δ_i can be obtained using Equation (23) [44]. Other variables are defined in Appendix I.

$$\theta_i(0) = \frac{\widetilde{c_i}(y)}{\widetilde{c_i}(0)} \tag{21}$$

$$\acute{\theta}_i(0) = \frac{d(\frac{\widetilde{c_i}}{\widetilde{c_i}(0)})}{d(\frac{y}{\delta_i})} \tag{22}$$

$$\delta_i = \left(\frac{3D_i}{a\nu}\right)^{1/3}\sqrt{\frac{\nu}{\Omega}} \tag{23}$$

The discussion below is based on an approach described by Tribollet, *et. al.*[44]. The second term in the diffusion impedance $(-\frac{1}{\acute{\theta}_i(0)})$ can be expressed with the Taylor series in jK and considering low frequency close to zero as shown in Equation (24) [44]. K is a dimensionless frequency parameter shown by Equation (25) and parameters defined in Equation (26) and Equation (27) [44]. Variables are defined in Appendix I.

$$-\frac{1}{\acute{\theta}_i(0)} = \left(-\frac{1}{\acute{\theta}_i(0)}\right)_{K=0} + jK\left.\frac{d\left(-\frac{1}{\acute{\theta}_i(0)}\right)}{d(jK)}\right|_{K=0} + \frac{(jK)^2}{2}\left.\frac{d^2\left(-\frac{1}{\acute{\theta}_i(0)}\right)}{d(jK)^2}\right|_{K=0} + \cdots \tag{24}$$

$$K = 3.2576pSc^{1/3} \tag{25}$$

$$Sc = \frac{\nu}{D} \tag{26}$$

$$p = \frac{\omega}{\Omega} \tag{27}$$

To analyze the derivative of dimensionless concentration with respect to time and position ($\acute{\theta}_i(0)$), a convective-diffusion equation will be used as given by Equation (28). Moreover, any complex (time varying) value such as concentration can be defined by Equation (29) having a steady state and transient part. By substituting Equation (29) into Equation (28), the convective-diffusion Equation (30) is obtained. In addition, considering the dimensionless concentration (Equations (21)) and the axial velocity profile near the surface of a rotating disk electrode (Equation (31)), the dimensionless form of the convective-diffusion equation can be obtained as shown in Equation (32)[44]. The dimensionless parameters in Equation (32) are defined in Equations (21), (25), (26) and (33) [44]. Variables are defined in Appendix I.

$$\frac{\partial c_i}{\partial t} + v_y \frac{\partial c_i}{\partial y} - D_i \frac{\partial^2 c_i}{\partial y^2} = 0 \tag{28}$$

$$c_i(\mathrm{y}) = \overline{c}_i(y) + Re\{\tilde{c}_i e^{j\omega t}\} \tag{29}$$

$$j\omega\tilde{c}_i + v_y \frac{\partial \tilde{c}_i}{\partial y} - D_i \frac{\partial^2 \tilde{c}_i}{\partial y^2} = 0 \tag{30}$$

$$v_y = -\sqrt{\nu\Omega}\left(\frac{-a\Omega}{\nu} y^2 + \frac{1}{3}\left(\frac{\Omega}{\nu}\right)^{3/2} y^3 + \frac{b}{6}\left(\frac{\Omega}{\nu}\right)^{2} y^4 + \cdots\right) \tag{31}$$

$$\frac{d^2\theta_i}{d\xi^2} + \left(3\xi^2 - \left(\frac{3}{a^4}\right)^{1/3} \frac{\xi^3}{{Sc_i}^{1/3}} - \frac{b}{6}\left(\frac{3}{a}\right)^{5/3} \frac{\xi^4}{{Sc_i}^{2/3}} + \cdots\right)\frac{\partial\theta_i}{\partial\xi} - jK_i\theta_i = 0 \tag{32}$$

$$\xi = \frac{y}{\delta_i} \tag{33}$$

θ_i obtained from Equation (32) should follow the boundary conditions shown below [44]:

$$\theta_i \to 0 \ \ as\, \xi \to \infty$$

$$\theta_i \to 1\ at\, \xi = 0$$

Equation (32) can be solved by Levart and Schuhmann[45] and Newman's approaches [44,46,47]. The series expansion of θ_i in $Sc^{1/3}$ is shown in Equation (34) developed by Levart and Schuhmann[45]. The $\theta_{i,0}$, $\theta_{i,1}$ and $\theta_{i,2}$ in Equation (34) can be obtained considering the boundary conditions shown below and Newman's approach for solving the differential Equations numerically (35)-(37) [44,46,47]:

$$\theta_{i,0} \to 0;\ \theta_{i,1} \to 0;\ \theta_{i,1} \to 0 \ \ as\, \xi \to \infty$$

$$\theta_{i,0} \to 1;\ \theta_{i,1} \to 0;\ \theta_{i,1} \to 0\ at\, \xi = 0$$

$$\theta_i(\xi, Sc_i, K) = \theta_{i,0}(\xi, K) + \frac{\theta_{i,1}(\xi, K)}{Sc_i^{1/3}} + \frac{\theta_{i,2}(\xi, K)}{Sc_i^{2/3}} + \cdots \tag{34}$$

$$\frac{d^2\theta_{i,0}}{d\xi^2} + 3\xi^2 \frac{\partial \theta_{i,0}}{\partial \xi} - jK_i\theta_{i,0} = 0 \tag{35}$$

$$\frac{d^2\theta_{i,1}}{d\xi^2} + 3\xi^2 \frac{\partial \theta_{i,1}}{\partial \xi} - jK_i\theta_{i,1} = \left(\frac{3}{a^4}\right)^{1/3} \xi^3 \frac{\partial \theta_{i,0}}{\partial \xi} \tag{36}$$

$$\frac{d^2\theta_{i,2}}{d\xi^2} + 3\xi^2 \frac{\partial \theta_{i,2}}{\partial \xi} - jK_i\theta_{i,2} = \frac{b}{6}\left(\frac{3}{a}\right)\xi^4 \frac{\partial \theta_{i,0}}{\partial \xi} + \left(\frac{3}{a^4}\right)^{1/3} \xi^3 \frac{\partial \theta_{i,1}}{\partial \xi} \tag{37}$$

Based on the above discussion, and the Taylor expansion of $\acute{\theta}_i(0)$, Equation (38) represents the second term in the diffusion impedance where α and β can be obtained using Equation (39) and Equation (40) [44].

$$-\frac{1}{\acute{\theta}_i(0)} = \boldsymbol{\Gamma}\left(\frac{4}{3}\right)[1 + 0.298Sc^{-1/3} + 0.145Sc^{-2/3} + \left(pSc^{1/3}\right)^2 \alpha + j\left(pSc^{1/3}\right)\beta] \quad (38)$$

$$\alpha = -1.19125 - 1.96\, Sc^{-1/3} - 2.36Sc^{-2/3} \quad (39)$$

$$\beta = -0.96154 - 0.9323\, Sc^{-1/3} - 0.790Sc^{-2/3} \quad (40)$$

According to Tribollet, *et al.*, the slope of the plot shown in Figure 18 is a function of the Schmidt number as shown in Equations (41) and (42) [8,44]. Once the Schmidt number is obtained the diffusion coefficient can be calculated using Equation (26) [8,44].

$$\lim_{p\to 0}\left(\frac{dRe\left\{-\frac{1}{\acute{\theta}_i(0)}\right\}}{dpIm\left\{-\frac{1}{\acute{\theta}_i(0)}\right\}}\right) = \frac{\alpha}{\beta} = \lambda Sc^{1/3} \quad (41)$$

$$\lambda = 1.2261 + 0.84Sc^{-1/3} + 0.63Sc^{-2/3} \quad (42)$$

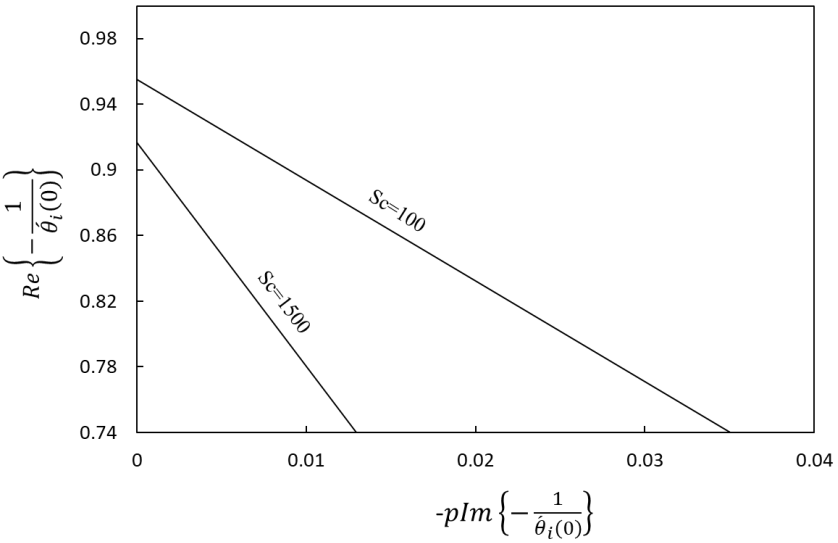

Figure 18

Determining the Schmidt number from the complex value of $\left(-\frac{1}{\acute{\theta}_i(0)}\right)$.[44] *Figure reconstructed from paper of Tribollet, et al.* [3,44]

C.2.3. Methodology

The test conditions for determining the DC potential at which the impedance is dominated by the hydrogen reduction reaction are shown in Table 4. The procedures for the preparation of the test solution and the surface preparation are described in Section C.1.2. The pH of the solution is adjusted using dilute HCl solution. The analysis method of the potentiodynamic sweeps for determination the DC potential for EIS measurement is described in the Section C.1.

Table 4

Experimental conditions.

Parameters	**Values**	
Test apparatus	Rotating disk electrode Three-electrode glass cell	
Sparge gas	$pN_2 \approx 1$ bar	
Temperature	30 ± 0.5 °C	
pH	3.00 ± 0.01	
Supporting electrolyte	0.1 M NaCl	
Rotation rate	1000, 2000, 3000 rpm	
Electrode material	API 5L X65	
Potentiodynamic sweep rate	0.5 mV/s	
Parameters of the EIS scans		
Frequency	10000 to 0.001 Hz	
AC potential	10 mV rms.	
DC potential	Rotation speed	DC potential
	1000 rpm	-250 mV vs. OCP
	2000 rpm	-290 mV vs. OCP
	3000 rpm	-280 mV vs. OCP

C.2.4. Results and Discussion

C.2.4.1. Determining of the DC potential for EIS measurement. The measured potentiodynamic sweeps at three different rotation speeds are shown in Figure 19. In the next step, the measured sweeps were fitted to a mechanistically modeled potentiodynamic sweep. An example of a measured sweep fitted to the model potentiodynamic sweep for rotation speed of 2000 rpm is shown in Figure 20.

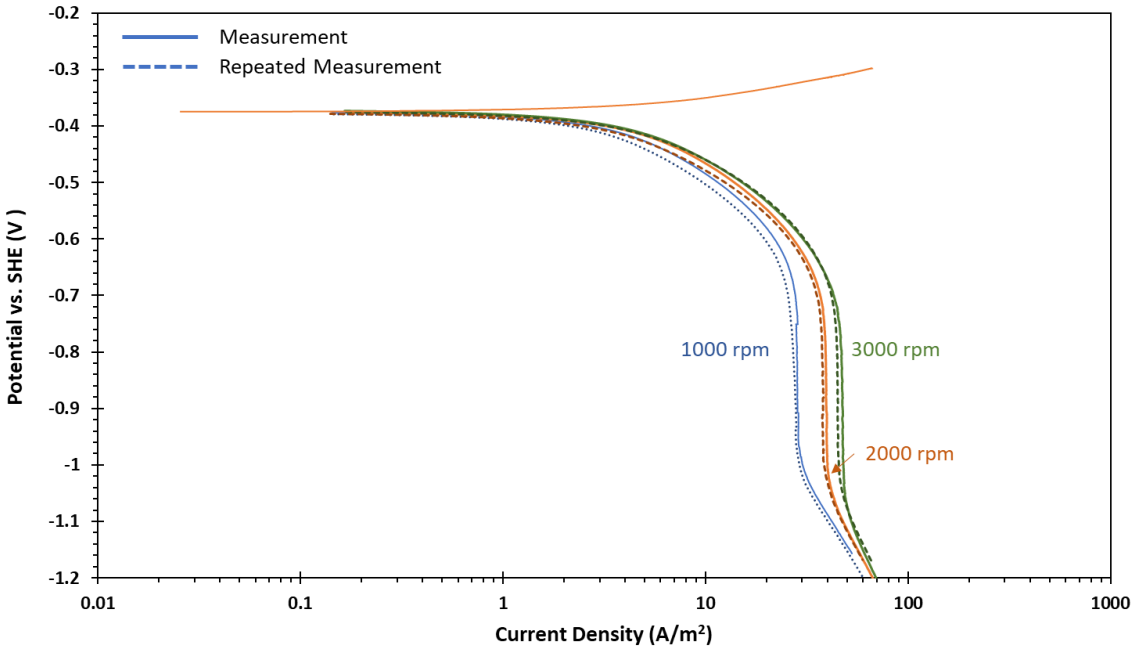

Figure 19

Steady-state polarization sweep curves, 30°C, pH 3.0, 0.1 M NaCl, sparged with nitrogen. The dotted line represents the repeated experiment [3].

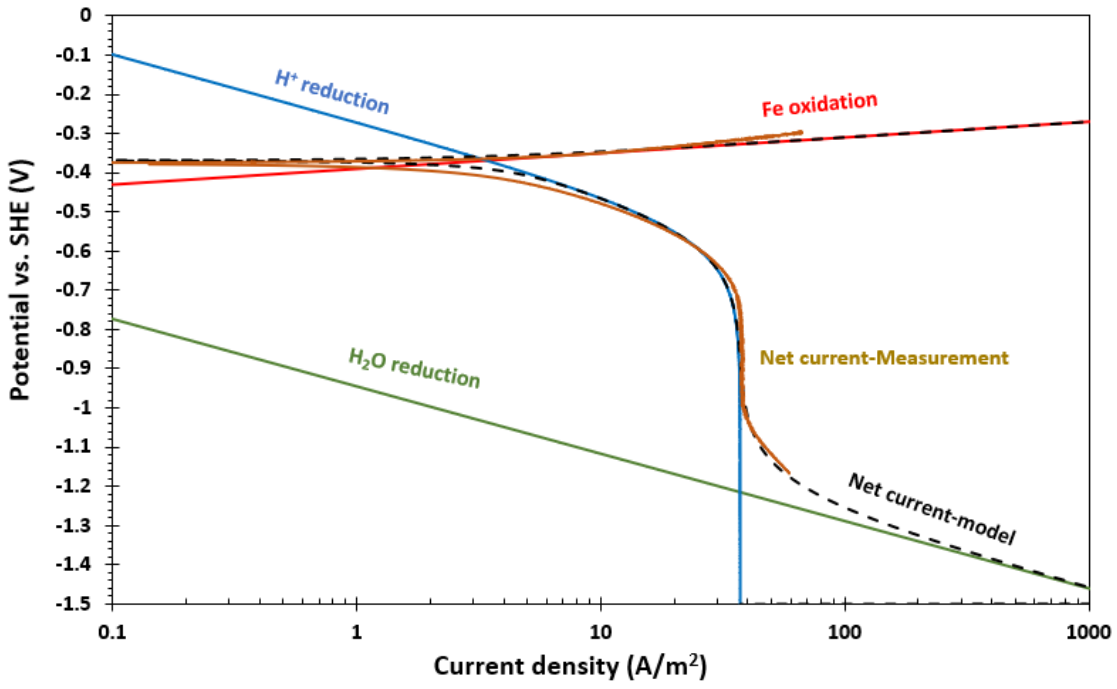

Figure 20

The fit of the experimental data to the modeled potentiodynamic data at 1 bar N_2, pH 3, T= 30°C, 0.1 M NaCl, and 2000 rpm.

The model data was then used to estimate the polarization resistances of each electrochemical reaction for the process at various potentials. For each reaction (cathodic and anodic), the resistance was calculated using Equation (15) at different potentials. Using the parallel resistance assumption for the electrochemical reactions, the overall resistance is calculated using Equation (16) which shows that the overall resistance is dominated by the smallest of the three resistances.

Therefore, the range of potential at which the net resistance is dominated by the resistance of H^+ reduction reaction is approximately in the range of -25 mV vs. OCP to -505 mV vs OCP as shown by the blue box in Figure 21. In other words, in the determined

range of potential, the contribution of the impedance of the iron oxidation and water reduction to the overall impedance is small and therefore the measured impedance can be considered as the response of the hydrogen reduction reaction as shown in Figure 22. The same range is shown on potentiodynamic data in Figure 23.

This analysis indicates that only part of the potential range for the cathodic reaction is suitable for EIS measurement and carries useful information about the hydrogen evolution reaction. In the potential range from OCP to -25 mV below the OCP the current is dominated by the H^+ reduction being under charge transfer control; however, the impedance is dominated by the anodic reaction having the smallest resistance value of the resistance of all three electrochemical reactions. Moreover, at potential -505 mV below OCP the impedance is dominated by the water reduction although the current is still dominated by the H^+ reduction being controlled by mass transfer of H^+ ion.

The same analysis was performed for the experimental data at rotation speeds of 1000 and 3000 rpm. For the EIS measurement, the potentials of -250 mV vs. OCP, -290 mV vs, OCP and -280 mV vs. OCP were chosen for 1000 rpm, 2000 rpm and 3000 rpm, respectively.

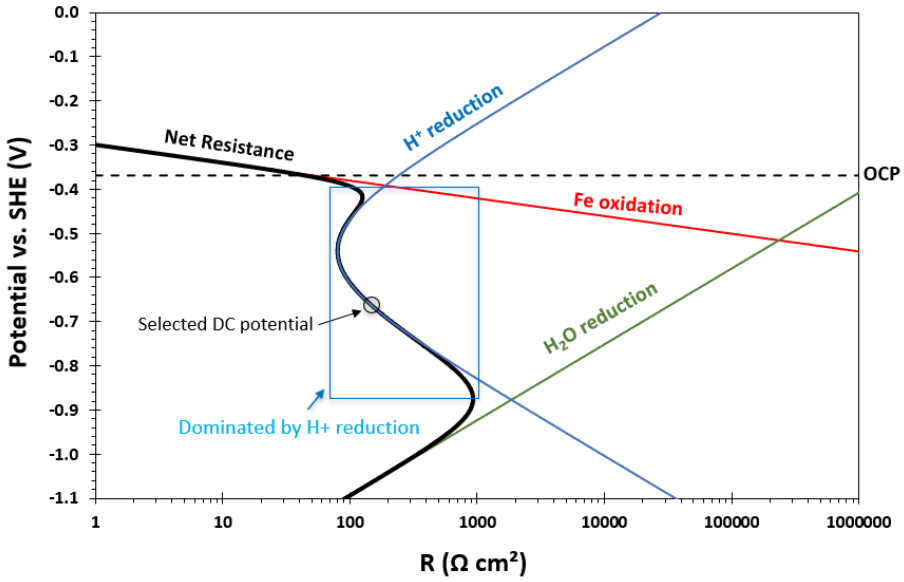

Figure 21

The calculated polarization resistance as a function of potential for experimental data at 1 bar N_2, pH 3, T= 30°C, 0.1 M NaCl, and 2000 rpm.

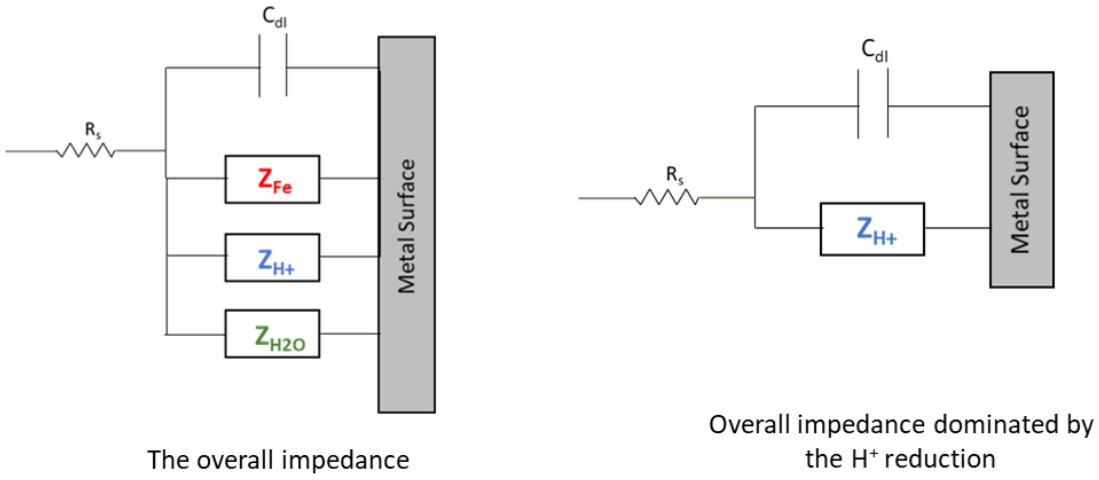

Figure 22

The schematic of the Randles circuit. The figure on the left side is the overall impedance. The figure on the right side is the overall impedance at the potential range dominated by the H^+ reduction [3].

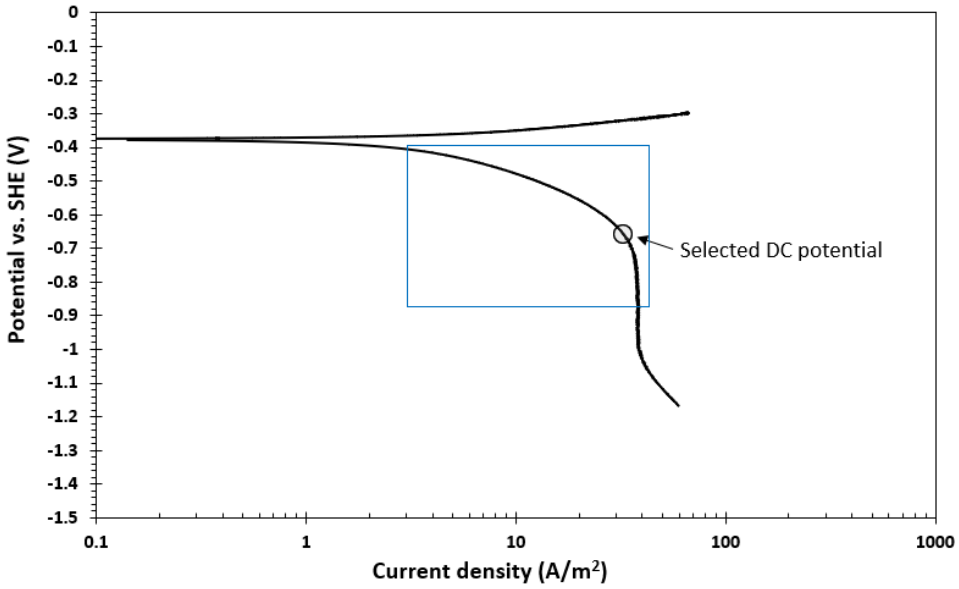

Figure 23

Potentiodynamic sweep for the experiments at 1 bar N_2, pH 3, T= 30°C, 0.1 M NaCl, and 2000 rpm. The blue box represents the potential range at which the impedance of the cathodic reaction, H^+ reduction, is dominant for EIS measurements.

C.2.4.2. Determining the Schmidt Number from the Data in the Low Frequency Range. Figure 24 shows the impedance data for experimental data at rotation speeds of 1000, 2000, and 3000 rpm. Each Nyquist plot presents two loops. The high-frequency loop (near the origin) corresponds to the double layer capacitance in parallel with a charge transfer resistance while the low-frequency loop is associated with the diffusion impedance. The data shown in Figure 24, were normalized with respect to the corrected real part of the impedance data (Figure 25) according to the Tribollet, *et al*., method [8,44] explained in Section C.2.2.

According to Tribollet, *et al*., the *p* value can be calculated using Equation (43) [8,44]. Based on the analysis discussed in Section C.2.2., the slope of the low frequency data

shown in Figure 26 yields information about the Schmidt number using Equations (41) and (42). The linear portion of the plot on the left-hand side of Figure 26 yields a slope of -6.6±0.4, which corresponds to a Schmidt number of 97±19. Finally, by using Equation (26) [8,44], the diffusion coefficient of hydrogen ions in water is $8.6 \times 10^{-5} \pm 1.6 \times 10^{-5}$ cm^2/s.

$$p = \frac{\omega}{\Omega} = \frac{60 \times f}{(rpm)} \qquad (43)$$

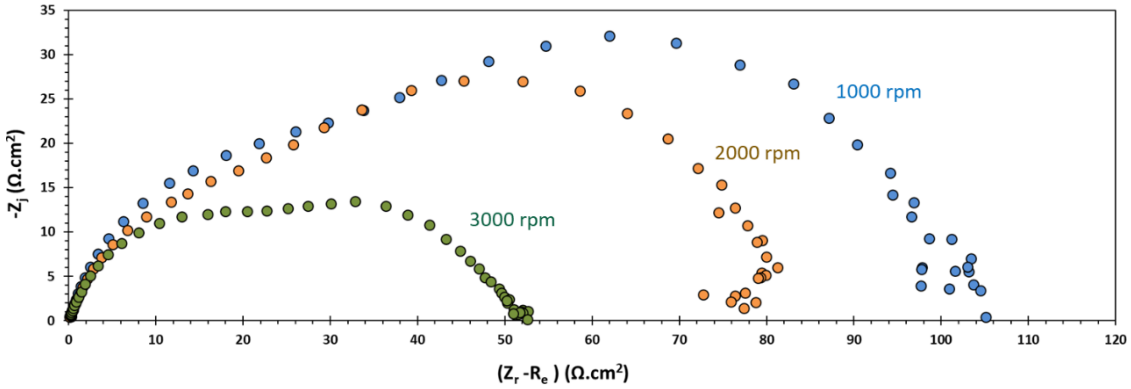

Figure 24

Impedance data at different rotation speeds from the experiments at 1 bar N_2, pH 3, T= 30°C, 0.1 M NaCl. [3]

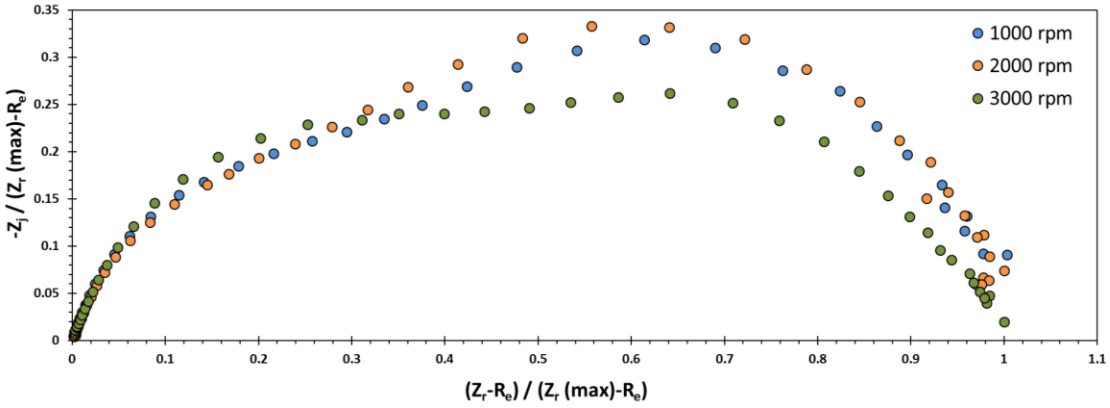

Figure 25

Normalized impedance data from Figure 24.[3]

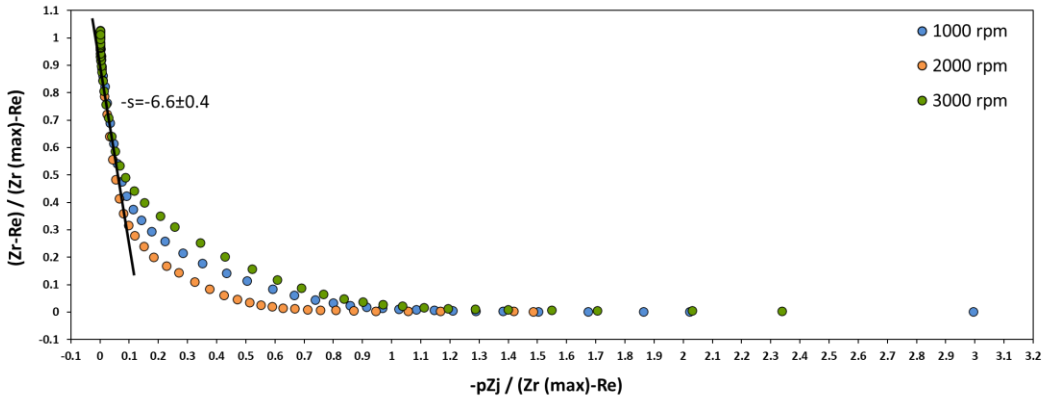

Figure 26

Illustration of the method developed by Tribollet, et al., to determine the Schmidt number [8,44] *from the normalized data in Figure 24.*

C.2.4.3. Determining the Diffusion Coefficient Using Potentiodynamic Sweeps (DC Technique). The diffusion coefficient of the hydrogen ion in water was also determined using steady state potentiodynamic sweeps in order to verify the value obtained by the EIS technique. The pure mass transfer controlled limiting current on a rotating disk

electrode can be calculated using the Levich equation, shown as Equation (44)[41]. Therefore, the rate of change in limiting current with respect to square root of rotation speed carries information about the diffusion coefficient of the electroactive species, being H^+ ion in this study.

$$i_{lim} = 0.62nFD^{2/3}\nu^{-\frac{1}{6}}C_b\omega^{1/2} \qquad (44)$$

The value of limiting current obtained in the potentiodynamic experiments shown in Figure 19 is plotted *versus* the square root of the rotation speed, which, according to Equation (44), must pass through the origin; meaning that at zero rotation speed (quiescent condition), the limiting current must be equal to zero [41]. However, at a quiescent condition there is still mass transfer due to molecular diffusion of the hydrogen ion and, therefore, the limiting current must actually be a small positive value close to zero. Based on Equation (44), the slope of the line shown in Figure 27 $(\tan(\alpha))$, is equivalent to the term $0.62nFD^{2/3}\nu^{-\frac{1}{6}}C_b$. Solving for the diffusion coefficient, *D*, provides Equation (45). According to Equation (45) [41], the diffusion coefficient of hydrogen ion in water is $8.7\times 10^{-5}\pm 6.7\times 10^{-6}$ cm^2/s.

$$D = \left[\frac{\tan(\alpha)\nu^{\frac{1}{6}}}{0.62nFC_b}\right]^{\frac{3}{2}} \qquad (45)$$

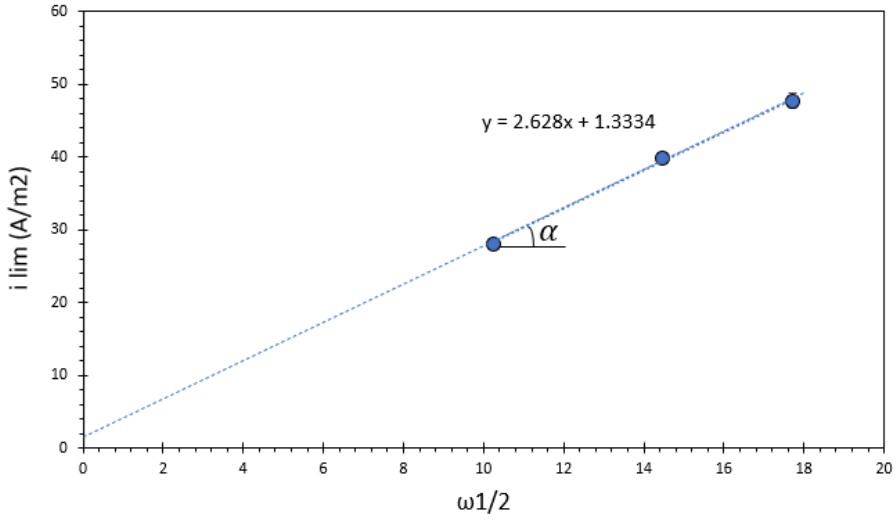

Figure 27

Using the limiting current density values, shown in Figure 19, to determine the diffusion coefficient of hydrogen ion using Equation (44).

C.2.4.4. Comparison of the Diffusion Coefficients Obtained by EIS and Potentiodynamic Sweeps. The diffusion coefficients of the hydrogen ion in water obtained by EIS and potentiodynamic sweeps are $8.6 \times 10^{-5} \pm 1.6 \times 10^{-5}$ cm^2/s and $8.7\times 10^{-5} \pm 6.7 \times 10^{-6}$ cm^2/s respectively. The calculated error and difference between the two values is 2%. This discrepancy can be postulated to correspond to the impact of impedance related to other electrochemical reactions happening simultaneously on the metal surface. As discussed in Section C.2.4.1, at the chosen potential, the measured impedances are dominated by the H^+ ion reduction; however, there are still small contributions from the iron dissolution reaction and water reduction reaction to the measured impedance which might be responsible for the calculated error. The two values obtained for diffusion coefficient of hydrogen ion can also be compared to 8.0×10^{-5}

cm^2/s, which is the diffusion coefficient of hydrogen ion in 0.1 M NaCl aqueous solution at 25 ºC reported in the literature [48]. The differences and errors between the measured values and the one reported in the literature are shown in Table 5. The errors might be due to the slight difference in the temperature at which the diffusion coefficient was calculated (30 ºC) and reported in the literature (25 ºC). Moreover, the errors might be related to the difference in the techniques used in this study compared to the ones implemented and reported in the literature [48].

Table 5

Comparison of the Measured Diffusion Coefficients with the Literature Value [3].

Measurement technique	**Measured D_{H^+} (cm^2/s)**	**Error between the measured D_{H^+} and the value reported in the literature: 8.0×10^{-5} (cm^2/s)** [48]
EIS	$8.6 \times 10^{-5} \pm 1.6 \times 10^{-5}$	7%
Potentiodynamic sweep	$8.7\times 10^{-5} \pm 6.7\times 10^{-6}$	9%

C.2.5. Summary

DC potential range at which the impedance of hydrogen evolution reaction is dominant was determined using potentiodynamic polarization sweep data. At the selected DC potential, the EIS experiments were performed to calculate the diffusion coefficient of the hydrogen ions.

The diffusion coefficient value obtained from the EIS method was similar to the value obtained by the DC technique with 2% of error and close to the reported literature value with 7% of error.

Chapter D: Mechanistic Modeling of the Impedance Response of Cathodic Reduction of Hydrogen Ion in Aqueous Acidic Solutions [13]

Studying the mechanism of electrochemical reactions often benefits from implementing an advanced technique such as electrochemical impedance spectroscopy (EIS). To develop an understanding of EIS results with respect to corrosion mechanisms requires their comparison with a mechanistic model. In this study, a physicochemical model was used to simulate both steady state potentiodynamic sweeps and the impedance response of cathodic reduction of H^+ in acidic environments. The modeled steady state potentiodynamic sweep, Nyquist, and Bode plots were studied in several test conditions, then validated by comparison with experimental data.

D.1. Introduction

EIS is one of the techniques which is frequently used for studying mechanisms of electrochemical reactions on a metal surface in an aqueous environment. However, one of the main challenges in using EIS is the interpretation of results. Several possible interpretations and their associated uncertainties have the potential to lead to biased and even incorrect analysis of investigated phenomena in an electrochemical system. One of the methods frequently used is the so-called "equivalent electrical circuit", which models the response of an electrochemical system at or near the metal surface by comparing it to a similar system comprised of standard electrical components in a circuit[8,49]. However, the

[13] Portion of the text, figures and tables in this chapter are taken from a publication of the author: N. Moradighadi, Y.S. Choi, and S. Nesic, "Mechanistic Modeling of the Impedance Response of Cathodic Reduction of Hydrogen Ion in Strong Acidic Environments," in AMPP 2022, Paper No. 17900 (San Antonio, TX: AMPP, 2022) (reference number [2]).

problem is ambiguity – it is known that in most real cases, many different equivalent electrical circuits can mimic the impedance response of an electrochemical system and, therefore, the analysis of the results using this approach is ambiguous and can lead to erroneous results[8]. Furthermore, it is not always straightforward to assign proper physical meaning to the various electrical components obtained in an equivalent electrical circuit. While using the equivalent electrical circuits is a useful stepping stone in analysis of the behavior of electrochemical systems, the real goal is to translate this kind of information into knowledge about the mechanisms of the elementary reactions underlying the overall electrochemical process. In other words, the observed resistive-like, capacitive-like, inductive-like, etc., behaviors, need to be transformed into useful information about the mechanisms of the equivalent physicochemical processes, such as charge transfer, double layer capacitance, diffusion, adsorption, etc. Without this additional step, any analysis that finishes with the electrical circuit analysis, falls short of utilizing the true potential of EIS.

Therefore, the main motivation of the present work is to directly analyze the measured impedance response of an electrochemical system by representing its behavior by a physicochemical model system that includes the description of all the key electrochemical reactions, their mechanisms and rates[15,50–52]. Consequently, the simulated impedance response of such a model system can be directly compared to the experimental results to evaluate if the assumed mechanisms of electrochemical reactions are correct. The usual stepping stone – the electrical circuit analysis, is entirely unnecessary in this method, even if the findings can always be recast in the forms of electrical circuit analogs such resistors, capacitors, inductors, etc.

In this work, the transient physicochemical model behind LABCORP-AC™ has been created as a base for modeling the current response of a real electrochemical system to an imposed alternating potential perturbation[50]. The physical, mathematical, and numerical aspects of the model are explained in detail in other publications[15]. The model covers main features of an electrochemical system such as electrochemical and chemical reactions at the steel surface, transport of species between the steel surface and the bulk solution, and formation/growth of corrosion product layers. All these features make the model a suitable tool for simulating the impedance response of electrochemical reactions associated with the corrosion of mild steel.

D.2. Background

D.2.1. Water Chemistry

Understanding the mechanism of corrosion of mild steel in aqueous CO_2 environment was the objectives of many research studies in the past. CO_2 is not a corrosive species, but when it reacts with water it produces carbonic acid. In research studies from as early as 1975, it has been reported that the corrosion rate in the presence of CO_2 is higher than in an environment containing a strong acid at the same pH[14,38,53,54]. Therefore, understanding the mechanism of this phenomenon has been a challenge for decades. The first step in study of CO_2 corrosion is to understand the water chemistry based on calculations using the equilibrium constants of the chemical Reactions (46), (48), (50), (52) and (54) that occur in the bulk solution. The chemical reactions are listed in Table 6 with their associated equilibrium constant expressions (Equations (47),(49),(51),(53) and (55)).

Table 6

Chemical reactions in an aqueous CO_2 environment and the equilibrium constant expressions.[52]

Name	Chemical reaction		Equilibrium constant	
Carbon dioxide dissolution	$CO_{2(g)} \rightleftharpoons CO_{2(aq)}$	(46)	$K_{sol} = \frac{[CO_{2(aq)}]}{pCO_{2(g)}}$	(47)
Carbon dioxide hydration	$H_2O_{(l)} + CO_{2(aq)} \rightleftharpoons H_2CO_{3(aq)}$	(48)	$K_{hyd} = \frac{[H_2CO_{3(aq)}]}{[CO_{2(aq)}]}$	(49)
Carbonic acid dissociation	$H_2CO_{3(aq)} \rightleftharpoons HCO_3^-{}_{(aq)} + H^+{}_{(aq)}$	(50)	$K_{ca} = \frac{[HCO_3^-{}_{(aq)}][H^+{}_{(aq)}]}{[H_2CO_{3(aq)}]}$	(51)
Bicarbonate ion dissociation	$HCO_3^-{}_{(aq)} \rightleftharpoons CO_3^{2-}{}_{(aq)} + H^+{}_{(aq)}$	(52)	$K_{bi} = \frac{[CO_3^{2-}{}_{(aq)}][H^+{}_{(aq)}]}{[HCO_3^-{}_{(aq)}]}$	(53)
Water dissociation	$H_2O_{(l)} \rightleftharpoons OH^-{}_{(aq)} + H^+{}_{(aq)}$	(54)	$K_w = [OH^-{}_{(aq)}][H^+{}_{(aq)}]$	(55)

To calculate the concentration of the ions and pH of the solution, there are five equations, shown in Table 6 for the equilibrium reactions and six unknown species concentrations. To solve this system the electroneutrality Equation (56), is required as shown below[39]:

$$c_{H^+} = c_{HCO_3^-} + 2c_{CO_3^{2-}} + c_{OH^-} \qquad (56)$$

The addition of any other species such as Fe^{2+}, Na^+, Cl^- (by adding NaOH and HCl), etc., to the solution can be added to the electroneutrality equation and may change the pH of the solution.

D.2.2. Aqueous CO_2 Corrosion and the Cathodic Reaction

D.2.2.1. Direct Reduction of Carbonic Acid. The first model for the cathodic reaction accountable for CO_2 corrosion was postulated by de Waard and Milliams [53]. Their model considered the reduction of carbonic acid (Reactions (57) and (58)) and H^+ ion (Reaction (59)), with the former as the primary cathodic reaction. This mechanism is called the "direct reduction of carbonic acid".

$$H_2CO_{3(aq)} + e^- \rightarrow HCO_3^-{}_{(aq)} + \tfrac{1}{2}H_{2\,(g)} \qquad (57)$$

$$HCO_3^-{}_{(aq)} + e^- \rightarrow CO_3^{2-}{}_{(aq)} + \tfrac{1}{2}H_{2\,(g)} \qquad (58)$$

$$H^+{}_{(aq)} + e^- \rightarrow \tfrac{1}{2}H_{2(g)} \qquad (59)$$

Schmitt and Rothmann studied the cathodic limiting current in different flow velocities and pCO_2 values [55]. Their findings showed that the limiting current density is function of hydration of CO_2 (slow step), and mass transfer of carbonic acid and H^+ ion. therefore, increasing the mass transfer rate, by an increase in flow velocity, can increase the limiting current to less extent compared to other weak acids[16,55].

In 1989 Gray, *et al.*, investigated the mechanism for cathodic reactions at different pCO_2 values [16,56]. In their experiments, as a first step they considered the reduction of H^+ ion in a solution without CO_2, and by plotting the limiting current *vs.* rotation speed, they observed that the linear data crossed the origin, characteristic of a purely diffusion-controlled reaction based on the Levich equation [41]. Again, they repeated the same analysis for the solution containing CO_2, and this time the linear data did not cross the origin. By subtracting the effect of H^+ ion from their data, the limiting current *vs.* rotation speed became approximately a horizontal line, which suggested almost no diffusion effect, which implied that a chemical reaction controls the reaction rate. Therefore, since the direct reduction of carbonic acid is under chemical reaction control, while the reduction of H^+ is under diffusion control, they concluded that the direct reduction of carbonic acid is the primary cathodic reaction. Considering hydration of CO_2, being the slow step, followed by the direct reduction of carbonic acid, H^+ ion, and water, Gray, *et al.*, provided a mathematical and mechanistic model which was the most popularly adopted, and applied, CO_2 corrosion mechanism for decades [16,56].

D.2.2.2. Buffering Effect of Carbonic Acid. Many mechanistic models for prediction of CO_2 corrosion rate were based on the direct reduction of H_2CO_3 as the dominant cathodic reaction [38,52,53,56]. However, other studies described the dissolved CO_2 and carbonic acid as a reservoir for H^+ ions. In other words, since carbonic acid is a weak acid, therefore, it partially dissociates in aqueous solution [30,57–59]. However, near the metal surface since the pH, due to the reduction of H^+ ions, increases then carbonic acid dissociation reaction goes forward and provides more H^+ ions. This mechanism is called

the “buffering effect” which was further investigated and confirmed by other researchers [14,16,17,57,58,60].

Remita, *et al.,* studied the cathodic reaction in a CO_2 environment [58]. They used the Levich equation, to calculate the cathodic current in solution without CO_2. In the next level, using the same analysis, they could model the cathodic current in the presence of CO_2, considering only the reduction of H^+ ion. Moreover, they calculated the interfacial pH for both strong acid solution and weak acid solution (CO_2 environment). Their model showed that in CO_2 environment, by increasing the mass transfer rate, the pH of the surface decreases more due to the buffering effect. In fact, if there was a direct reduction of carbonic acid, then by increasing the mass transfer, the pH must have increased due to the presence of bicarbonate ions[16,58].

In many research studies, it was shown that the cathodic current can be predicted by both mechanisms, direct reduction of carbonic acid and the buffering effect [14,38,52,53,56,58,61,62]. Therefore, studying the limiting current could not explain a convincing mechanism. Tran, *et al.*, investigated the mechanism for the cathodic reaction by monitoring the charge transfer region of the cathodic potentiodynamic sweeps[16,60]. They hypothesized that if the carbonic acid is an electroactive species, then by increasing the pCO_2, as the concentration of carbonic acid increases, the charge transfer reaction rate must increase as well. The author used stainless steel instead of carbon steel to significantly retard the anodic reaction and to visibly observe the charge transfer region of the cathodic reaction. Their results showed that in pH 4 and pH 5 electrolytes, as pCO_2 increased from 1 bar to 5 bars, it did not affect the charge transfer cathodic current. Therefore, the

experimental results supported the buffering effect mechanism. This conclusion seemed to be based on accurate reasoning and analysis, but since the electrochemical behavior of a system can depend on the nature of the surface, testing this hypothesis using carbon steel instead of a stainless steel surface would be needed for confirmation[14,17].

In more recent years, Kahyarian, *et al.*, performed a comprehensive mechanistic study for the cathodic reaction [14,17,61,62] using the hypotheses of Tran, *et al.*, [60] on X65 carbon steel. The experimental challenge was that the charge transfer cathodic current was not visible in the test condition and was masked by anodic charge transfer current[16]. To solve this problem, thin channel flow cell was used in order to perform experiments at, high velocities and pCO_2., Moreover, the temperature was adjusted to 30°C and 10°C to separate the charge transfer and mass transfer regions of the potentiodynamic sweeps for better analysis[17].

Using a thin channel flow cell (TCFC) to perform the experiments at higher pressures, they concluded that the pCO_2, even at 5 bar, did not influence the pure charge transfer cathodic current[17]. This conclusion confirmed the buffering effect which indicates that carbonic acid is not electroactive. The mechanistic model was able to accurately predict the corrosion rate for different values of pH and pCO_2[17]. Moreover, Kahyarian, *et al.*, showed that depending on the controlling mechanism, an increase in the pCO_2 may or may not increase the corrosion rate [14,17,61]. For example, in the pH 4 solution, the mechanism of corrosion is under charge transfer control, hence by increasing the pCO_2 the corrosion rate does not change significantly. On the other hand, in acidic solutions at pH 5, because the corrosion mechanism is under mass transfer control, increasing the pCO_2

significantly increases the corrosion rate[14,17,61]. This is more supporting evidence for the buffering mechanism for the cathodic reaction in aqueous CO_2 environments.

D.3. Methodology for Modeling of the Potentiodynamic Sweep and Impedance Spectra

D.3.1. Modeling Steady-State Potentiodynamic Sweep

This section described the methodology for modeling of the potentiodynamic sweep of the electrochemical reactions by showing an example in an aqueous CO_2 environment. The same methodology is used for modeling of the potentiodynamic sweep of the electrochemical reaction in strong acidic solutions.

In the first step, the modeling of the steady state potentiodynamic sweep is required in order to evaluate whether the model can properly generate the steady state sweeps and to choose the desired DC potential at which the impedance response will be simulated. In an experiment, generating a potentiodynamic sweep initially requires waiting for the concentrations of the ions to get established near the metal surface in order to obtain a constant open circuit potential (OCP). Similarly, because the model used in this work is based on the physicochemical model, when the simulation is started it takes a certain amount of simulation time to obtain a constant OCP.

Table 7 shows the simulation parameters for generating a steady state potentiodynamic sweep. The velocity used in the simulation is the superficial velocity in a pipe with 0.1 m internal diameter, 0.02 m thickness, 20 μm roughness and conductivity of 60 (W/m.K). The model was modified to output the open circuit potential at a specified

time step (0.01 sec). Consequently, as shown in Figure 28, it only required about 0.2 sec to establish a stable OCP.

Table 7

Simulation parameters for generating steady state potentiodynamic sweep.

Parameter	Value
pCO_2	1 bar
Temperature	30ºC
pH	4.00
Electrolyte	0.1 M NaCl
Velocity	2.6 m/s

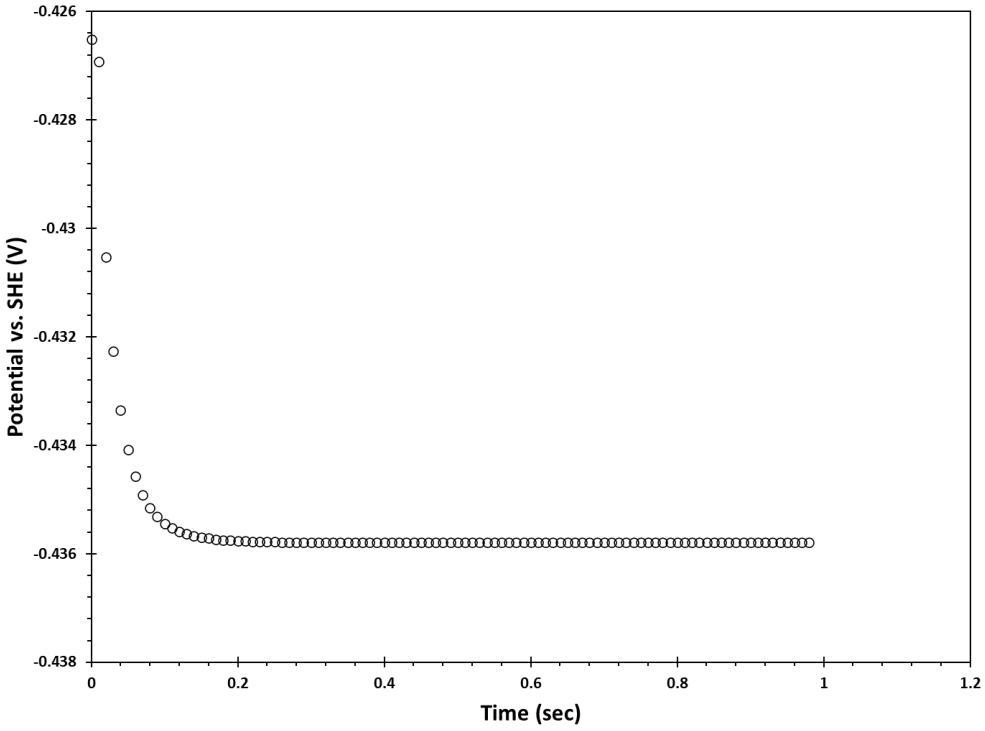

Figure 28

Calculated open circuit potential using 0.01 s time step. Simulation parameters: pCO_2= 1 bar, pH 4.00, T=30ºC, velocity=2.6 m/s, 0.1 M NaCl.

After obtaining a stable OCP, the potential in the simulation was changed toward the cathodic direction from OCP using a -1 mV/s sweep rate using (Figure 29a) and the corresponding current densities were calculated at a specified time step (0.01 s). as shown in Figure 29b. However, it is important to note that the chosen sweep rate should be small enough to obtain a steady state current density at each potential step before changing the potential. Figure 29b shows that the current density reached steady state in less than 1 s. Therefore, this analysis confirms that the potential sweep rate of -1 mV/s is acceptable for generating the steady state potentiodynamic sweep.

After obtaining the stable OCP and determining the adequate potential sweep rate, then the potential was swept stepwise, and the response analyzed. To generate the potentiodynamic sweep the last data point for the current density obtained at each potential step was used. The corresponding current densities were calculated for generating the potentiodynamic sweeps of both the anodic reaction (dissolution of iron) and the cathodic reaction (reduction of H^+). By summation of the anodic current density and cathodic current density, the steady state potentiodynamic sweep was obtained as shown in Figure 30.

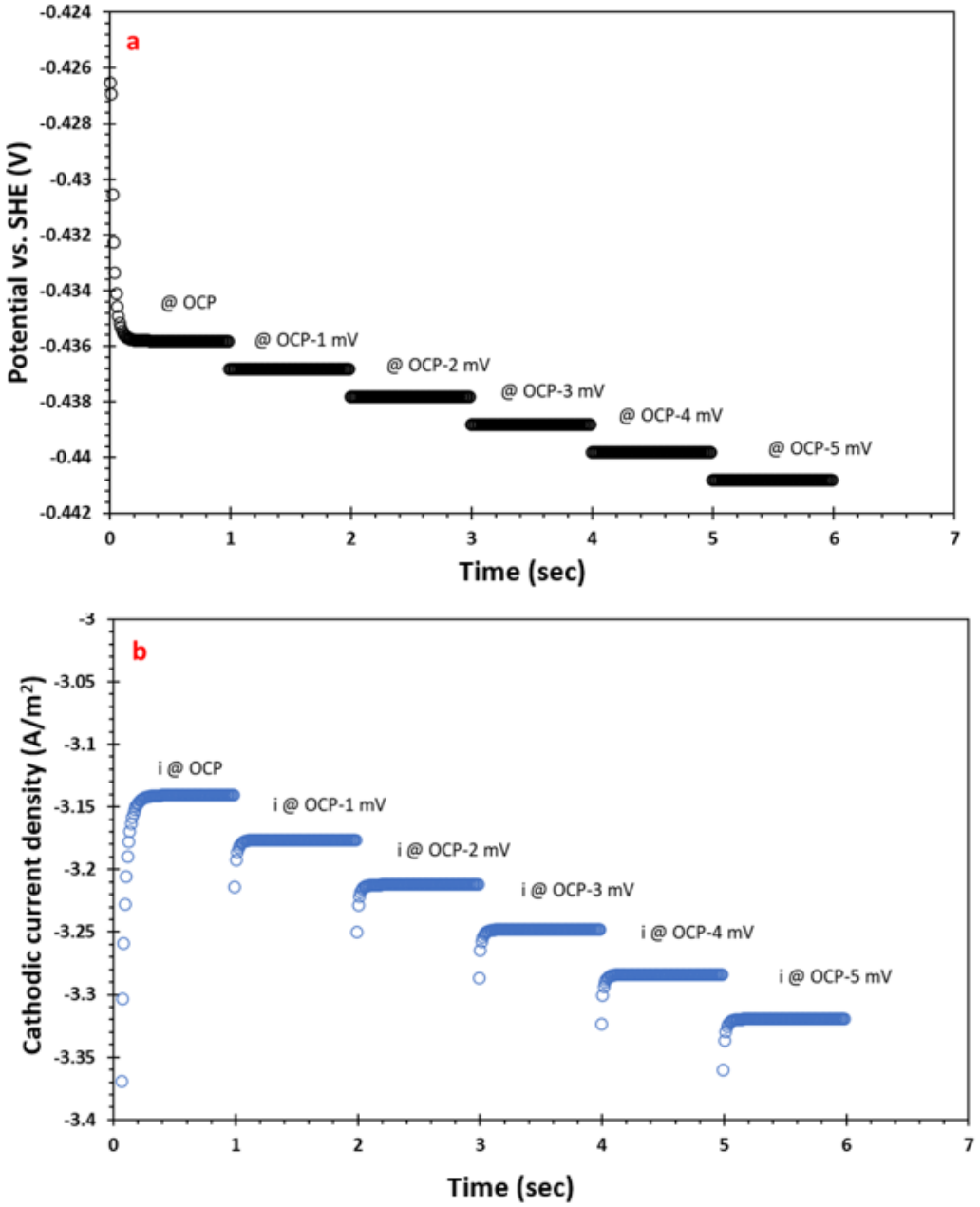

Figure 29

(a) Response when changing the potential from OCP using -1 mV/s sweep rate. (b) Current density response to each potential step. Simulation parameters: pCO_2= 1 bar, pH 4.00, T=30°C, velocity=2.6 m/s, 0.1 M NaCl.

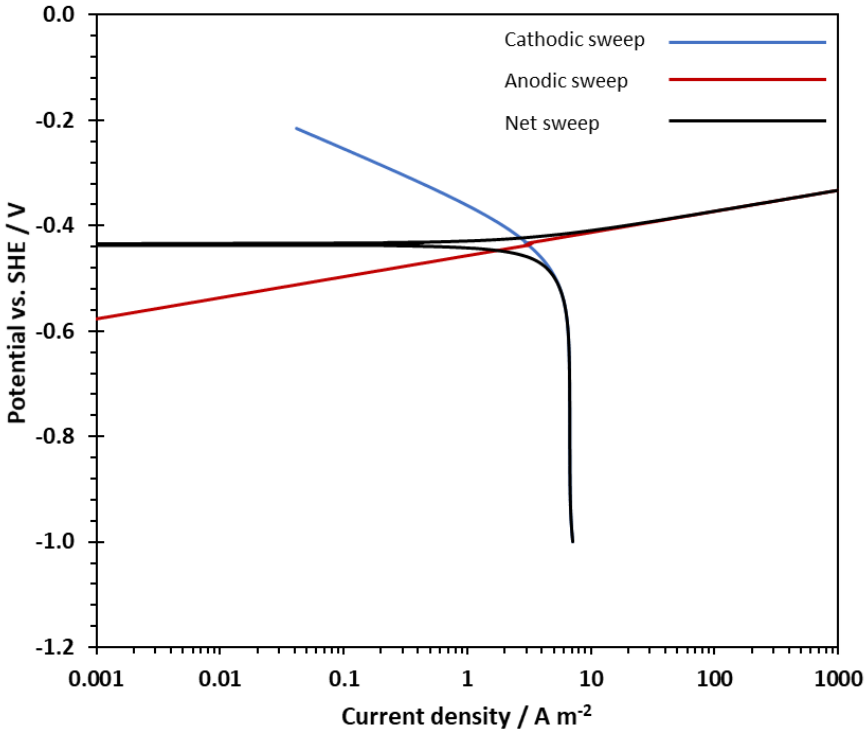

Figure 30

Calculated steady state potentiodynamic sweep. The black line represents the net current density. Simulation parameters: pCO_2= 1 bar, pH 4.00, T=30°C, velocity=2.6 m/s, 0.1 M NaCl, sweep rate =-1 mV/s.

D.3.2. Alternative Current (AC) Response to the Imposed Alternating Potential

In section D.3.1., it is described how the steady state potentiodynamic sweep for both anodic and cathodic electrochemical reactions was modeled. However, since the main objective of this part of the work is an analysis of the impedance response of the cathodic reaction, only the potentiodynamic sweep data of the cathodic reaction is considered without considering any influence of the anodic reaction. To study the impedance response of only the cathodic reaction, as an example, the DC potential was considered at OCP-214 mV corresponding to the limiting current density region of the potentiodynamic sweep.

In order to model the impedance response of the cathodic reaction, it is required to calculate the OCP as described in Section D.3.1. Once the OCP is established, then the surface potential is changed to the desired DC potential as illustrated in Figure 31a. In the next step, the potential is kept constant in order to obtain a steady current density at the chosen DC potential, which is illustrated in Figure 31b. Once the steady current density is established then the potential is cycled in a sinusoidal fashion (Equation (60)) at 11 Hz frequency by using 100 steps per cycle[8]. The sinusoidal perturbation of potential at the chosen DC potential is shown in Figure 32a.

$$E = \bar{E}_{DC} + |\Delta E|\cos(\omega t) \tag{60}$$

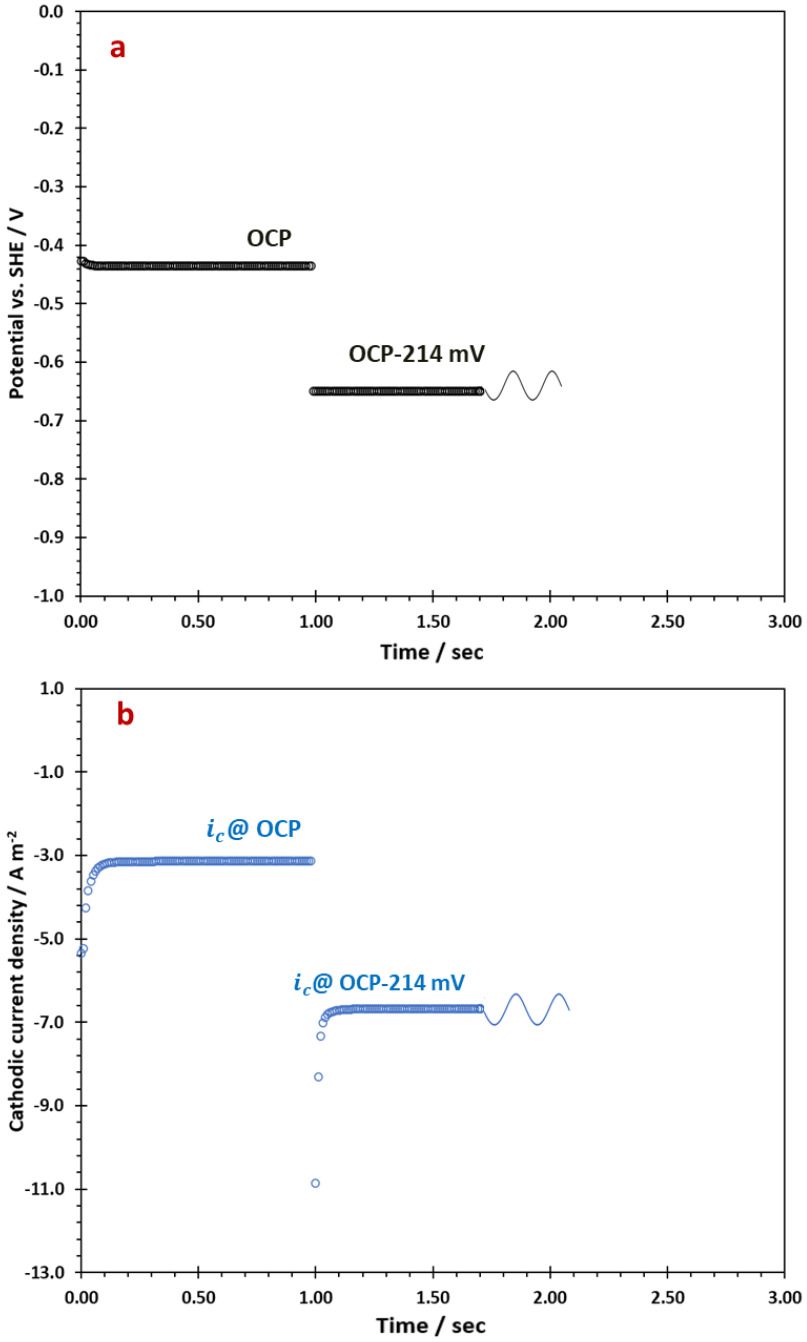

Figure 31

(a) Steps in changing the potential from OCP to DC potential and the imposed alternating potential; (b) Corresponding current density. Simulation parameters: $\bar{E}_{DC}$ *= OCP-214 mV,* $|\Delta E|$*=±10 mV, f=11 Hz,* pCO_2*= 1 bar, pH 4.00, T=30°C, velocity=2.6 m/s, 0.1 M NaCl.*

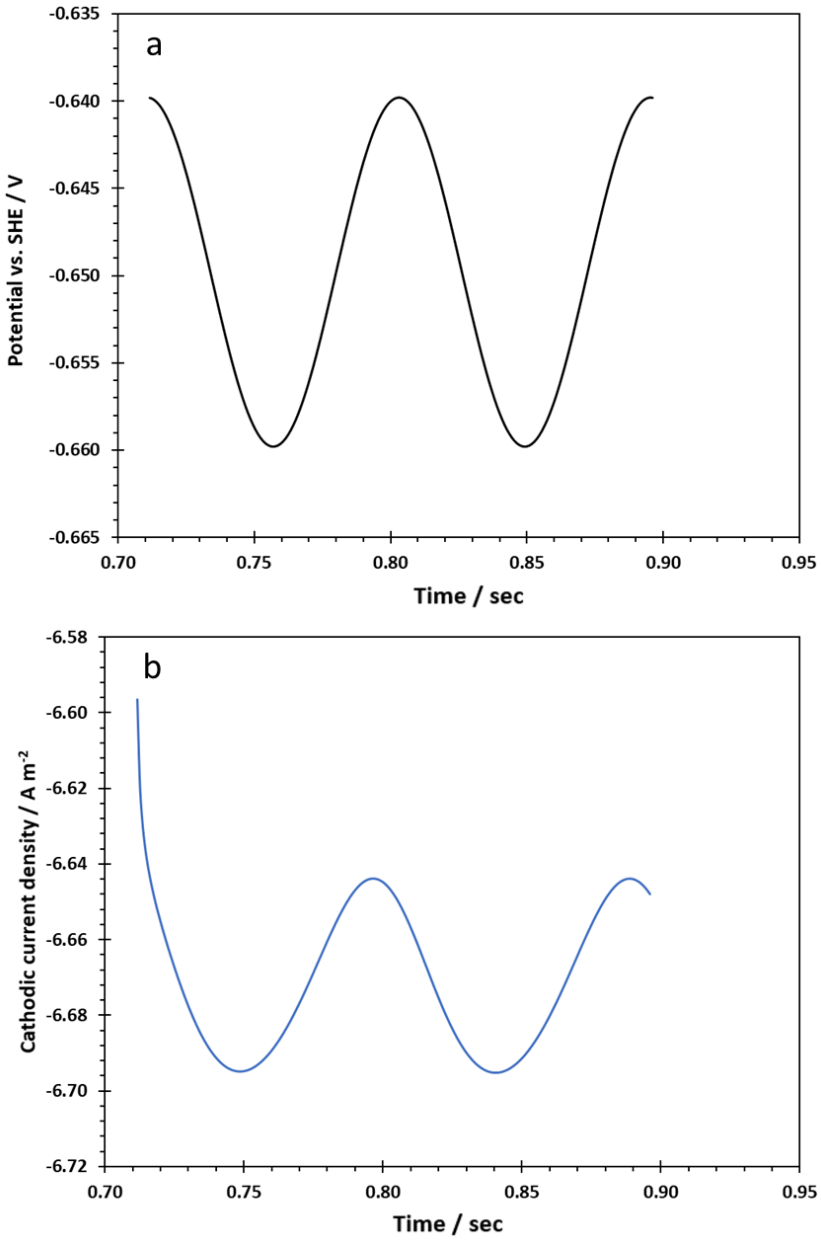

Figure 32

(a) Imposed alternating potential; (b) Corresponding cathodic current density. Simulation parameters: $\bar{E}_{DC}$= OCP-214mV, $|\Delta E|$=±10 mV, f=11 Hz, pCO_2= 1 bar, pH 4.00, T=30 °C, velocity=2.6 m/s, 0.1 M NaCl.

When there is a sinusoidal perturbation in potential, the responding current density originating from the electrochemical reactions (Faradaic current) as well as the double layer (charging current) at the metal surface are obtained. The current originating from the double layer can generally be modeled to mimic that of an RC circuit. The Faradic current density and double layer charging current density can be summed according to Equation (61)[8] to obtain the total current density.

$$i_T = \overline{i_F} + \Delta i_F \cos(\omega t) - C_{dl}|\Delta E|\omega \sin(\omega t) \qquad (61)$$

Since in the present example the impedance response of the Faradaic cathodic reaction is the focus, the value of the double layer capacitance is considered to be zero. As the potential was stepped (Figure 32a), the current density was calculated 100 times at each potential step and the last point of the calculation was used for generating Figure 32b.

As shown in Figure 32b, the first period for the current perturbation is not harmonic. This behavior is observed due to a sudden change of potential from the DC potential to 10 mV above it (Equation (60)). Once the potential is changed suddenly, it takes time for the concentration of the ions near the metal surface to get established. Therefore, the current density at the beginning of the potential perturbation is not equal to the current density at the end of the first period. However, in the second period of the potential perturbation, the corresponding sinusoidal current density is stable and shows a harmonic behavior. Consequently, the data points of the second period were used for impedance calculation.

Once the current response to the alternating potential was obtained, the impedance was calculated using the maximum current density and the maximum perturbed potential from Equation (62)[8], resulting in a Lissajous plot, which is shown in Figure 33.

Impedance is a complex value as the total current density lags the imposed potential. The analysis of the impedance response is based on the real (Z_r) and imaginary (Z_J) parts which are obtained using Equations (63) and (64)[8] . As shown in Equations (63) and (64), the real and imaginary part of the impedance depends on phase angle (φ) between the current density and the potential. Therefore, phase angle was calculated using Equation (65) or Equation (66) [8], where the time difference is considered between the two minimum peaks in the imposed alternating potential and the obtained current shown in Figure 33.

$$\mathrm{Z} = \frac{|OA|}{|\mathrm{OB}|} \tag{62}$$

$$Z_r = Z\cos(\varphi) \tag{63}$$

$$Z_J = Z\sin(\varphi) \tag{64}$$

$$\varphi = sin^{-1}(-\frac{OD}{OA}) \tag{65}$$

$$\varphi = (t_{\varphi_V} - t_{\varphi_I})2\pi f \tag{66}$$

Using the same procedure for calculation of the impedance at different frequencies, the Nyquist plot related to the impedance response of the cathodic reaction was generated and shown in Figure 34.

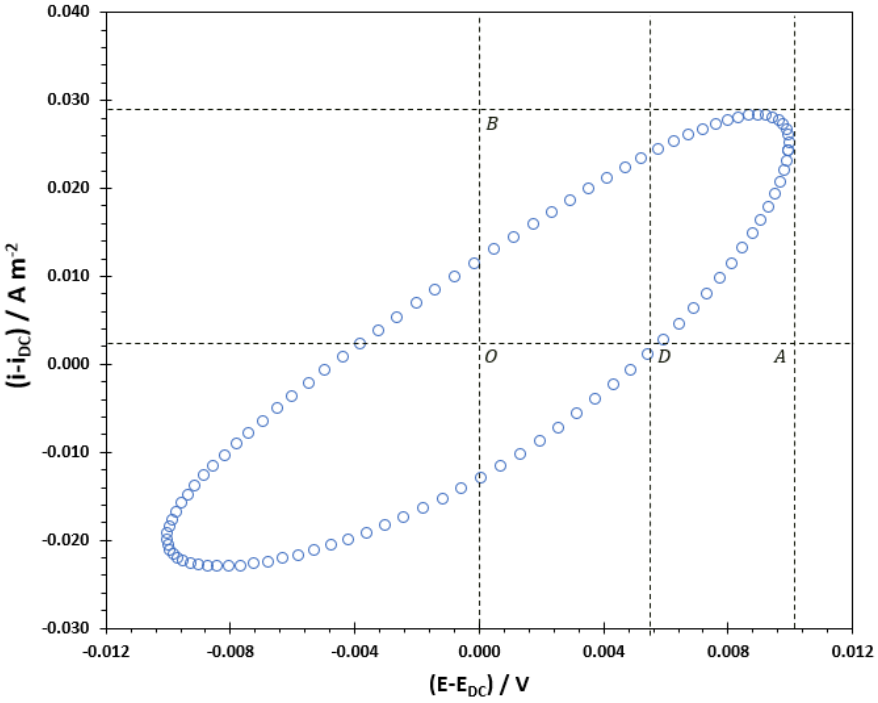

Figure 33

Modeled Lissajous plot using the data shown in Figure 32 at 11 Hz frequency [14].

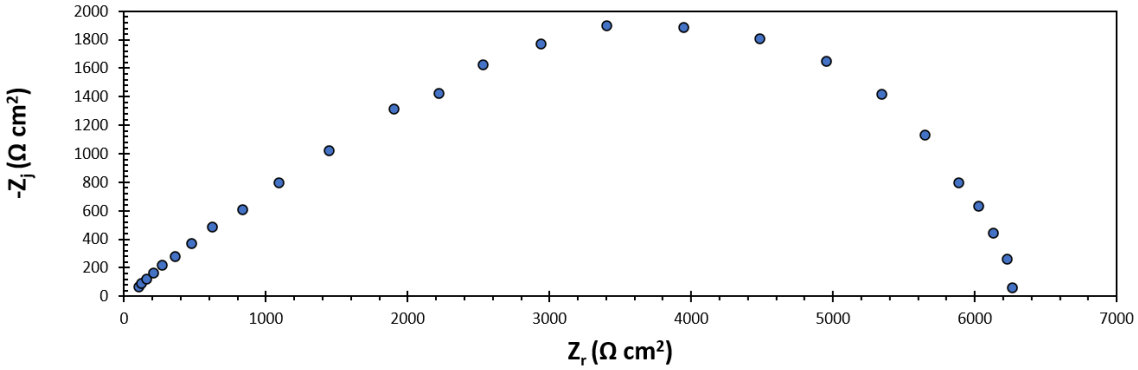

Figure 34

Nyquist plot of the cathodic reduction of H+. Simulation parameters: $\bar{E}_{DC}$ *= OCP-214 mV,* $|\Delta E|$*=±10 mV,* pCO_2*= 1 bar, pH 4.00, T=30 °C, velocity=2.6 m/s, 0.1 M NaCl.*

[14] Lines OD and OA cross the y-axis at the average current density between maximum and minimum current density. Similarly, line OB crosses the x-axis at the average potential between maximum and minimum perturbated potential.

D.4. Results and Discussion

D. 4.1. Case of Strong Acid Solution

D.4.1.1. Steady State Potentiodynamic Sweep. The potentiodynamic sweep of the electrochemical reactions for a strong acid solution were modeled as described in section D.3.1. Table 8 shows the simulation parameters. Figure 35 shows the simulated potentiodynamic sweeps of the cathodic reaction (H^+ reduction) and anodic reaction (iron dissolution).

Table 8

Simulation parameters for generating steady state potentiodynamic sweeps [2].

Parameter	Value
pN_2	1 bar (de-aerated environment)
Temperature	30°C
pH	4.00
Electrolyte	0.1 M NaCl
velocity	2.6 m/s

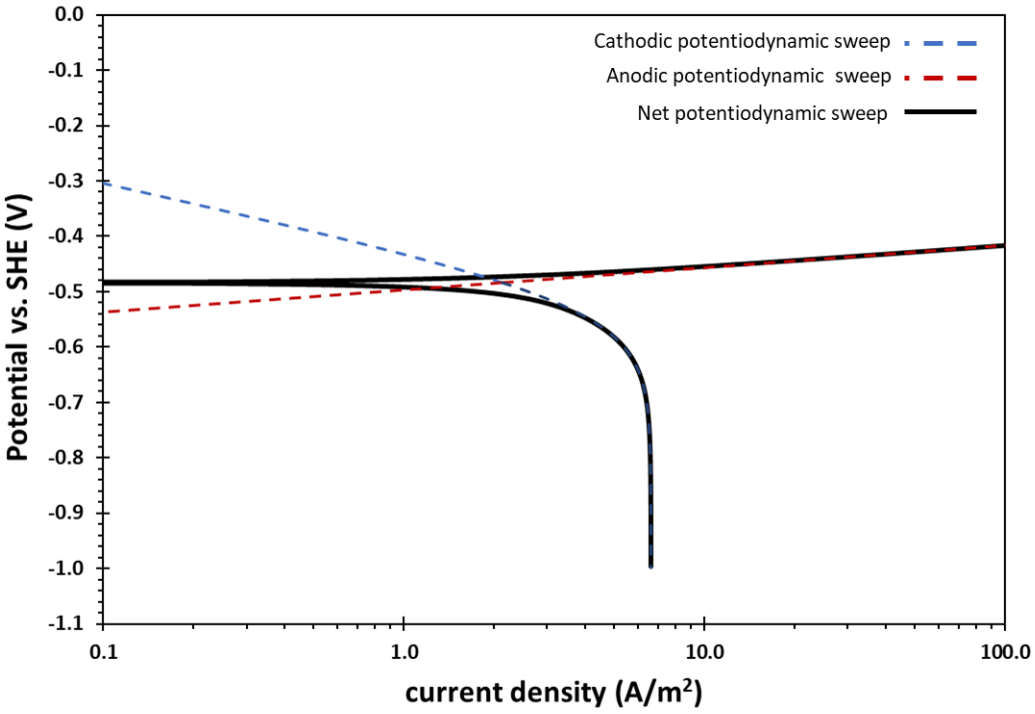

Figure 35

Calculated steady state potentiodynamic sweep. The black line represents the net current density. Simulation parameters: pN_2= 1 bar, pH 4.00, T=30°C, velocity=2.6 m/s, 0.1 M NaCl, sweep rate =1 mV/s. [2]

D.4.1.2. Effect of Double Layer Capacitance on the Simulated Impedance Behavior of Cathodic Reaction. To study and model the cathodic reduction of H^+, the DC potential was chosen to be 95 mV below the OCP (at $\frac{3}{4}\, i_{lim}$), where the current density is under mixed charge transfer and mass transfer control. At this potential, the electrochemical system can be modeled with a very simple Randles electrical circuit as shown in Figure 36, in which the charge transfer resistance (R_{ct}) is in series with the diffusion impedance (Z_D) and all in parallel to the double layer capacitance (C_{dl}). Since a

solution resistance (R_s) would be unnecessary in a computer simulation, this value was not used for the Randles circuit.

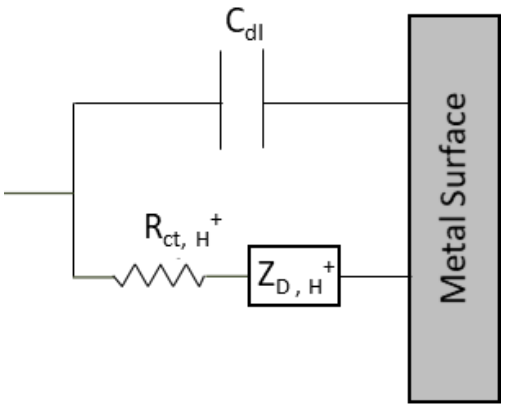

Figure 36

Equivalent electrical circuit corresponding to the electrochemical system used in this study. [2]

Figure 37 and Figure 38 show the Nyquist plot and Bode plot of only the cathodic reaction (without the effect of double layer capacitance) as blue solid-color markers. The impedance responses of the cathodic reaction were calculated in the frequency range of 10 kHz to about 1 Hz.

In the Nyquist plot, the impedance response at the highest frequency corresponds to the charge transfer resistance (R_{ct}) of the cathodic reaction while the diameter of the Nyquist plot is related to the diffusion resistance (R_D). The polarization resistance (R_p) in this study case is the summation of the charge transfer resistance and the diffusion resistance.

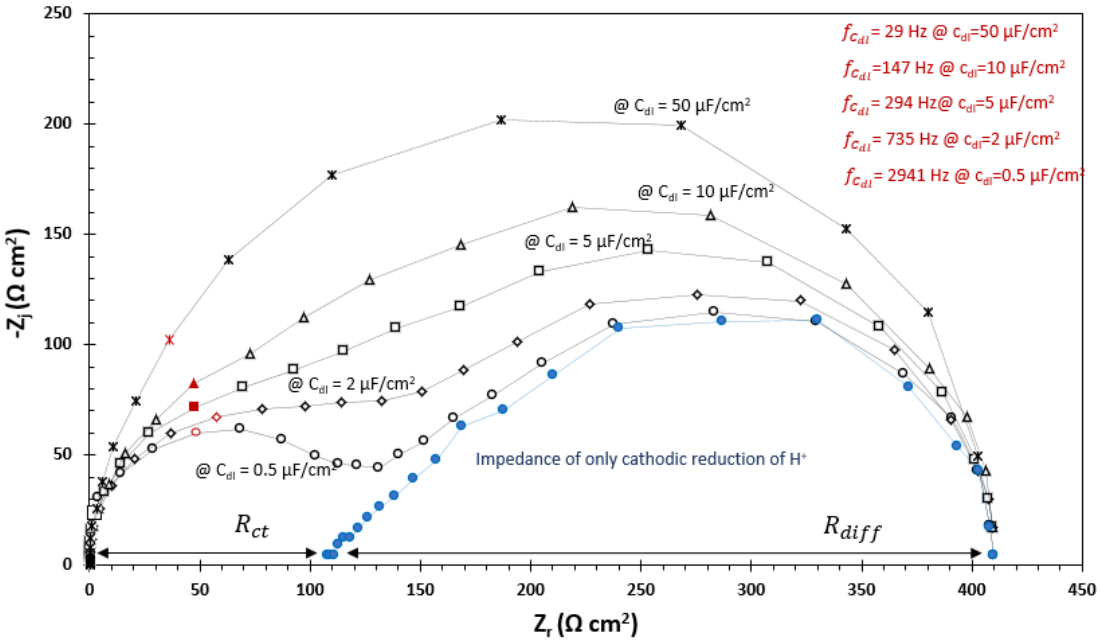

Figure 37

Diffusion impedance of the cathodic reaction and the effect of different values of the double layer capacitance on the Nyquist plot. Simulation parameters: $\bar{E}_{DC}$ *= OCP-95 mV,* $|\Delta E|$*=±10 mV,* pN_2*= 1 bar, pH 4.00, T=30°C, velocity=2.6 m/s, 0.1 M NaCl.* [2]

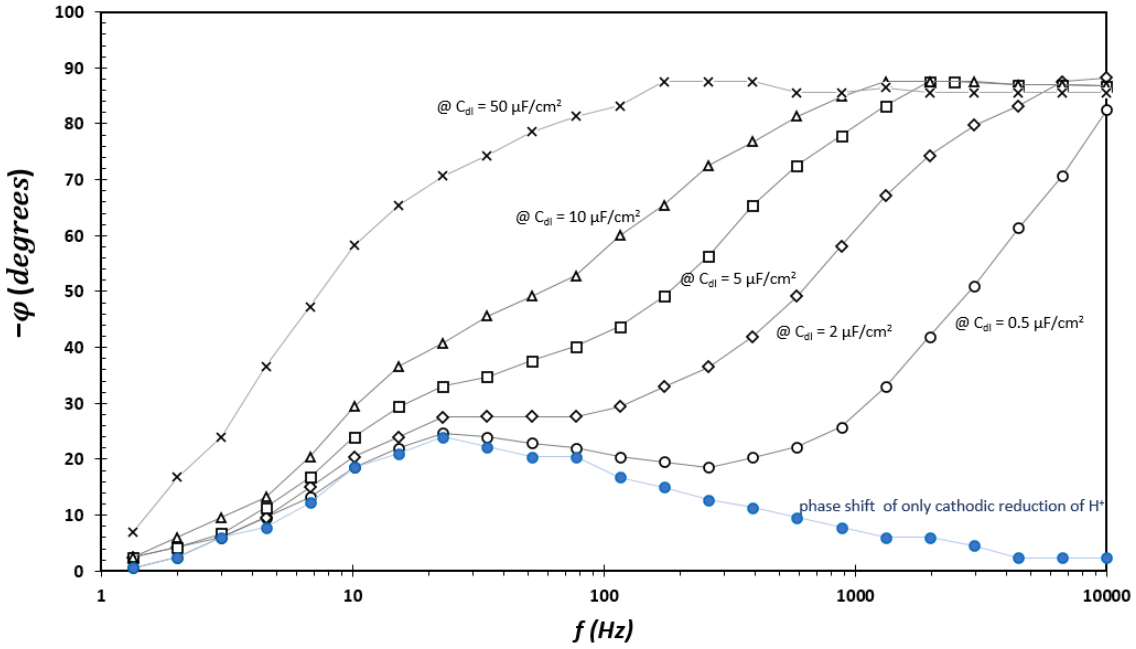

Figure 38

Bode plot of the of the cathodic reaction and the effect of different values of the double layer capacitance on the Bode plot. Simulation parameters: $\bar{E}_{DC}$ *= OCP-95 mV,* $|\Delta E|$ *=±10 mV,* pN_2 *= 1 bar, pH 4.00, T=30°C, velocity=2.6 m/s, 0.1 M NaCl.* [2]

Figure 37 also shows the effect of the double layer capacitance values on the impedance response of the cathodic reaction when the charging current density of the double layer is added to the Faradaic current density. The value of double layer capacitance varied from 0.5 to 50 µF/cm^2. Generally, the double layer capacitances of 10-50 µF/cm^2 are reported for bare metals [8]. However, in order to elaborate on the effect of the double layer capacitance value on the impedance response of the cathodic reaction, the additional values of 0.5, 2 and 5 µF/cm^2 were considered as well.

When the C_{dl} decreases from 50 to 0.5 µF/cm^2, the two loops decouple from each other. The two loops are clearly observed in the Nyquist plot and the Bode plot when the

C_{dl} is equal to 0.5 μF/cm^2. The high frequency loop is related to the double layer capacitance in parallel with a charge transfer resistance and the low frequency loop is related to the diffusion impedance. The red data points indicate the impedance data at the approximate characteristic frequency of the double layer capacitance in parallel with the charge transfer resistance. Based on Equation (67), as the value of double layer capacitance decreases, the relative characteristic frequency increases meaning that the relaxation of the double layer capacitance in parallel with a charge transfer resistance happens at higher frequency range making the corresponding capacitive loop decouple from the low frequency capacitive loop related to the diffusion impedance.

$$f_{C_{dl}} = \frac{1}{2\pi R_{ct} C_{\mathrm{dl}}} \qquad (67)$$

In addition, the impedance of the double layer capacitance and the diffusion impedance are in parallel, the impedance with the lowest value has the largest contribution to the overall impedance[1]. As shown in Equation (68), the impedance response of the double layer has an inverse relationship with its capacitance value. As the value of the capacitance increases, its impedance decreases. Consequently, the contribution of the double layer capacitance to the overall impedance increases compared to the diffusion impedance. Therefore, as the value of the double layer capacitance increases, it is harder to distinguish the two described loops.

$$Z_C = \frac{1}{\mathrm{j}\omega \mathrm{C}_{dl}} \qquad (68)$$

The outcome of this analysis shows the importance of using a model in order to extract the correct information from the experimental EIS data including the double layer

capacitance ($f_{C_{dl}}$) and charge transfer resistance (R_{ct}). As shown in Figure 37, if the value of the double layer capacitance is small (for example 0.5 μF/cm^2), the two loops clearly decouple from each other. In this case, the high frequency loop is related to the double layer capacitance in parallel with a charge transfer resistance (Figure 39) and the impedance response is a semicircle with a diameter equal to the charge transfer resistance. In addition, the impedance data point with maximum imaginary part is related to the $f_{C_{dl}}$. Using the $f_{C_{dl}}$, the value of the double layer capacitance can be calculated considering Equation (67).

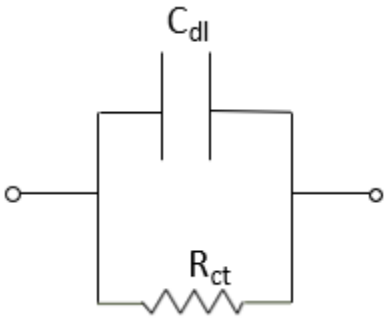

Figure 39

The equivalent electrical circuit related to a system with a charge transfer resistance in parallel with a double layer capacitance.

At higher value of the double layer capacitance (2, 5 and 10 μF/cm^2), the high frequency and low frequency loops partially merged due a decrease in the $f_{C_{dl}}$. Therefore, the relatively high frequency data is no longer relater to only double layer capacitance and charge transfer resistance, but they are affected partially by the diffusion impedance.

Therefore, for such a system, the equivalent electrical circuit for relatively high frequency data is not similar to Figure 39, and a model is required to reliably estimate R_{ct} and $f_{C_{dl}}$. This consideration is more critical in case of the Nyquist plots obtained at 50 μF/cm^2, where the two loops are fully merged. As the behavior of this system is not similar to an RC circuit shown in Figure 39, the data with maximum imaginary part is not related to the $f_{C_{dl}}$ and should not be considered for determining the double layer capacitance. In addition, the intersection of the loop with the x-axis is only related to R_p and a mechanistic model can be used to determine R_{ct}.

D.4.1.3. Effect of Velocity on the Simulated Impedance Behavior of Cathodic Reaction. Figure 40 shows the effect of velocity on the impedance response of only cathodic reaction (without the influence of the double layer capacitance). The chosen DC potential for the simulation is set at -239 mV vs. OCP, which is in the limiting current region.

As the velocity was increased from 1 m/s to 10 m/s, the diameter of the diffusion impedance decreases as expected. This behavior can be explained by considering the effect of mass transfer. In the limiting current region, the current density is controlled by mass transfer of H^+ from the bulk solution to the metal surface, so increasing the velocity increases the mass transfer which reduces the diffusion impedance.

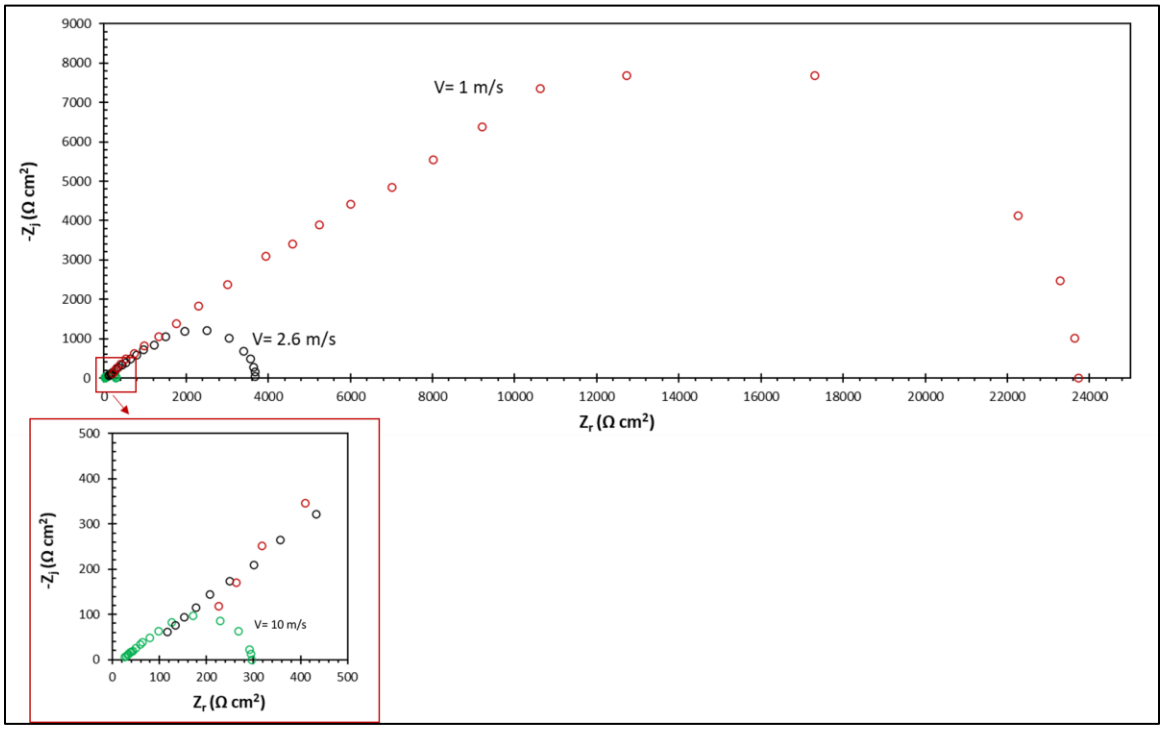

Figure 40

Effect of velocity of the diffusion impedance of the cathodic reaction. Modeling parameters: Simulation parameters: $\bar{E}_{DC}$ *= OCP-239 mV,* $C_{dl} = 0$*,* $|\Delta E|$*=±10 mV,* pN_2*= 1 bar, pH 4.00, T=30 °C, 0.1 M NaCl.* [2]

D. 4.1.4. Effect of Direct Current (DC) Potential on the Simulated Impedance Behavior of Cathodic Reaction. In the next step, the impedance response of the only cathodic reaction (without the influence of the double layer capacitance) was examined at different DC potentials. Four different potential values were selected as shown in Figure 41: +18 mV vs. OCP (at $\frac{1}{4}\,\boldsymbol{i_{lim}}$), -39 mV vs. OCP (at $\frac{2}{4}\,\boldsymbol{i_{lim}}$), -95 mV vs. OCP (at $\frac{3}{4}\,\boldsymbol{i_{lim}}$), and -239 mV vs. OCP (at $\boldsymbol{i_{lim}}$). Impedance responses of the cathodic reaction at these different potentials are shown in Figure 42. As potential becomes more negative, toward the limiting current density, the diameter of the diffusion impedance increases.

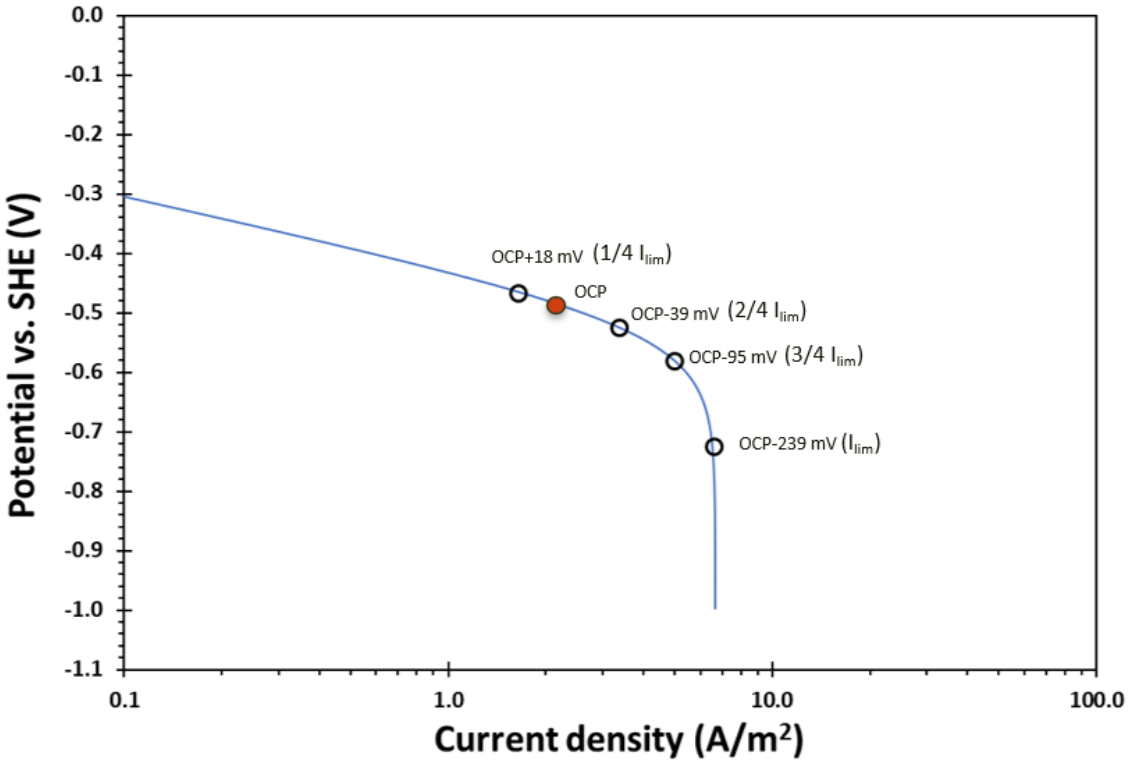

Figure 41

Steady state potentiodynamic sweep of cathodic reduction of H^+. The points on the sweep show the DC potential for calculation of impedances shown in Figure 42. [2] *Simulation parameters: pN_2= 1 bar, pH 4.00, T=30°C, velocity=2.6 m/s, 0.1 M NaCl, sweep rate =1 mV/s.* [2]

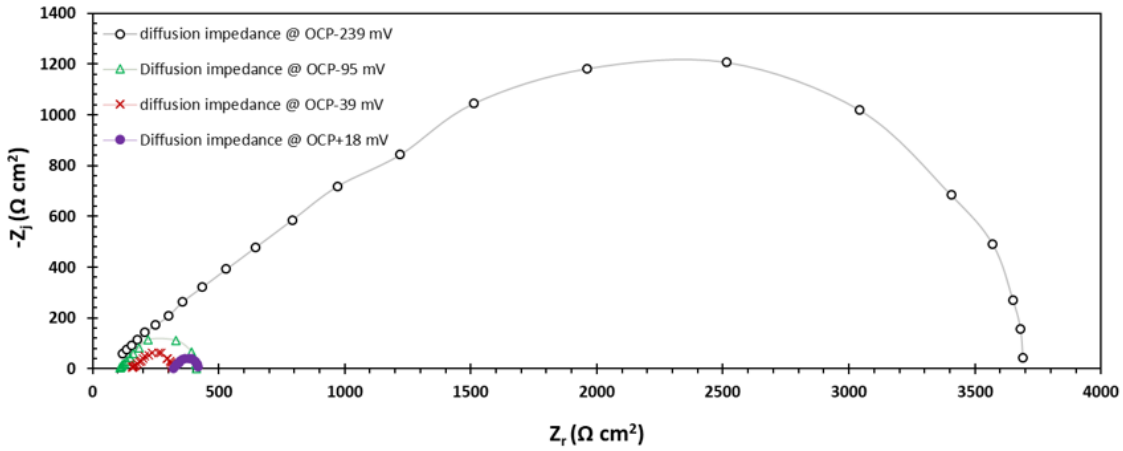

Figure 42

Nyquist plots showing the large change in diffusion impedance for the cathodic reduction of H^+ at OCP+18mV, OCP-39mV, OCP-95mV, & OCP-239 mV. [2] *Simulation parameters:* $|\Delta E|$*=±10 mV,* pN_2*= 1 bar,* $C_{dl} = 0$*, velocity=2.6 m/s, pH 4.00, T=30 °C, 0.1 M NaCl.*

Figure 43 shows the change in the charge transfer resistance, diffusion resistance and polarization resistance predicted by the impedance response of the cathodic reaction shown in Figure 42.

Notice that charge transfer resistance (R_{ct}) decreases from OCP+18 mV to OCP-95 mV, but then remains approximately constant. In fact, the cathodic reduction of H^+ depends on both potential and surface concentration of H^+.

Therefore, at limiting current density, in which the concentration of the hydrogen ion is approximately constant, the charge transfer resistance also has a constant value. In contrast, as the potential reaches the limiting current density region, the diffusion resistance and polarization resistance keep increasing. This behavior is consistent with the experimental results and analysis reported in the literature[63].

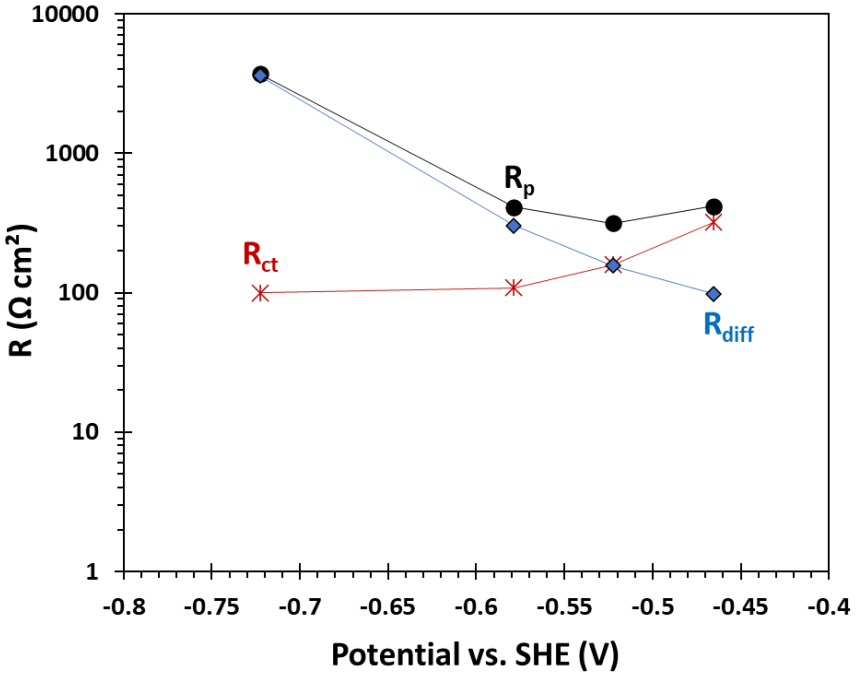

Figure 43

Values of charge transfer resistance (R_{ct}), diffusion resistance (R_{diff}) and polarization resistance (R_p) for the cathodic reduction of H^+ at OCP+18mV, OCP-39mV, OCP-95mV, & OCP-239 mV. [2]

D.4.1.5. Model Validation with Experimental Data. Experiments were performed to validate the simulated impedance response of the reduction of H^+. Table 9 shows the simulation parameters and the experimental test conditions. The details of the experimental procedure are described is Section C.2.3. Using the experimental data at high frequency (Figure 44**)**, the value of the double layer capacitances at different rotation speeds and potentials were determined and implemented in the model.

Table 9

Modeling and experimental parameters for steady state potentiodynamic sweeps and EIS [2].

Parameters	Values	
Test apparatus	Rotating disk electrode (RDE), three-electrode glass cell	
Sparged gas	pN_2 = 1 bar	
Temperature	30 ± 0.5 ºC	
pH	3.00 ± 0.01	
Potentiodynamic sweep rate	0.5 mV/s	
E_{DC}-experiment	OCP-250 mV at 1000 rpm	
	OCP-290 mV at 2000 rpm	
	OCP-280 mV at 3000 rpm	
E_{DC}-Model [15]	OCP-232 mV at 1000 rpm	
	OCP-273 mV at 2000 rpm	
	OCP-264 mV at 3000 rpm	
Supporting electrolyte	0.1 M NaCl	
Electrode material	API 5L X65	
Rotation rate/Velocity	For experiment using RDE	For simulation in a pipe[39,64]
	1,000 rpm	1.75 m/s
	2,000 rpm	2.61 m/s
	3,000 rpm	3.28 m/s
C_{dl} used in the simulation	80 μF/cm^2 at 1,000 rpm	
	70 μF/cm^2 at 2,000 rpm	
	70 μF/cm^2 at 3,000 rpm	

Figure 44 shows the comparison between the experimental and simulated potentiodynamic sweeps at different velocities. Figure 45 shows the comparison of the simulated and experimental Nyquist plots. Comparisons of the two experimental Nyquist plots obtained at 2000 rpm and 3000 rpm show the sensitivity of the impedance response of cathodic reaction during the experiment. In other words, a slight difference in test

[15] The DC potentials for experiment and model were at approximately 85% of the limiting current density.

conditions such as temperature, pH, surface preparation, etc., might result in large difference between the impedance response of cathodic reduction of hydrogen ion Moreover, in the experiments conducted close to the limiting current density, the reduction of H^+ is suspected to make small bubbles which might increase the polarization resistance. The model prediction is between the two experimental data obtained in 2000 rpm and 3000 rpm. Experiment#1 shows approximately similar polarization resistance compared to the model while the frequency of the experimental data is relatively smaller compared to the model. In contrast, the polarization resistance of the Experiment #2 is smaller compared to the model while the frequency of the experimental data is approximately similar to the model. Both models and experiments at different velocities show two loops. The high frequency capacitive loop in both model and experiments is related to the double layer capacitance in parallel with the charge transfer resistance while the low frequency loop is related to the diffusion impedance. The low frequency loops in experiment #1 at 2000 rpm and 3000 rpm were hardly observed. This behavior might be justified by a larger value of the double layer capacitance due to the slight difference in experimental conditions or possible generated bubbles as discussed above. As explained in Section D.4.1.2., a large value of double layer capacitance makes it harder to distinguish the loops related to the double layer capacitance in parallel with a charge transfer resistance from the ones related to the diffusion impedance. In addition, as the velocity increases, the diameter of the low frequency loop decreases due to the increase in the mass transfer.

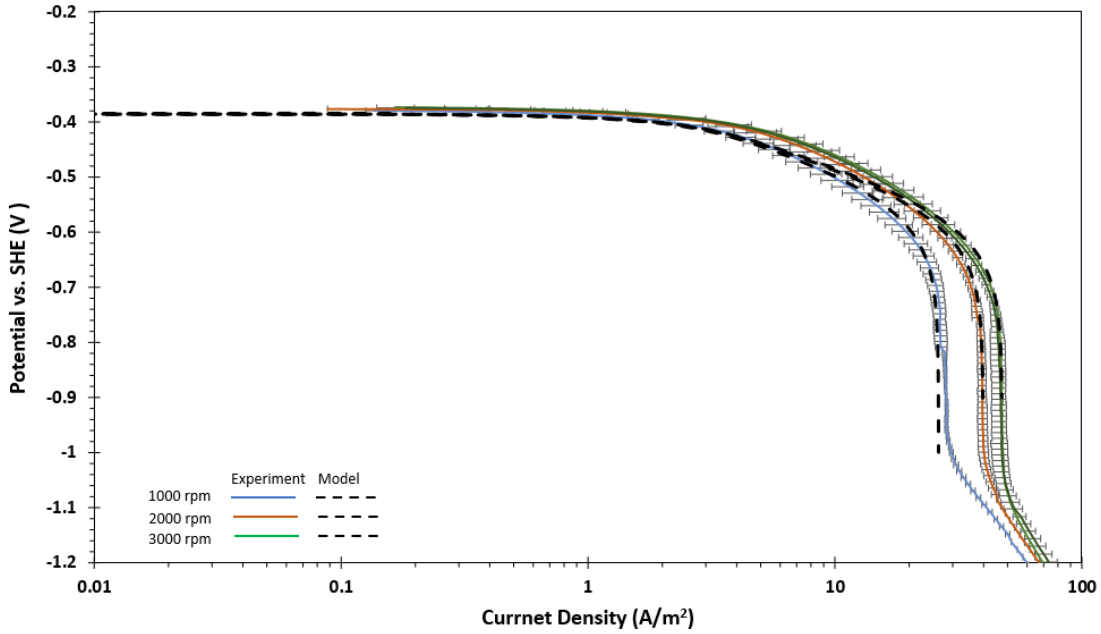

Figure 44

Comparison between the experimental and simulated steady state potentiodynamic sweep at different rotation speeds. Experimental and simulation parameters shown in Table 9.

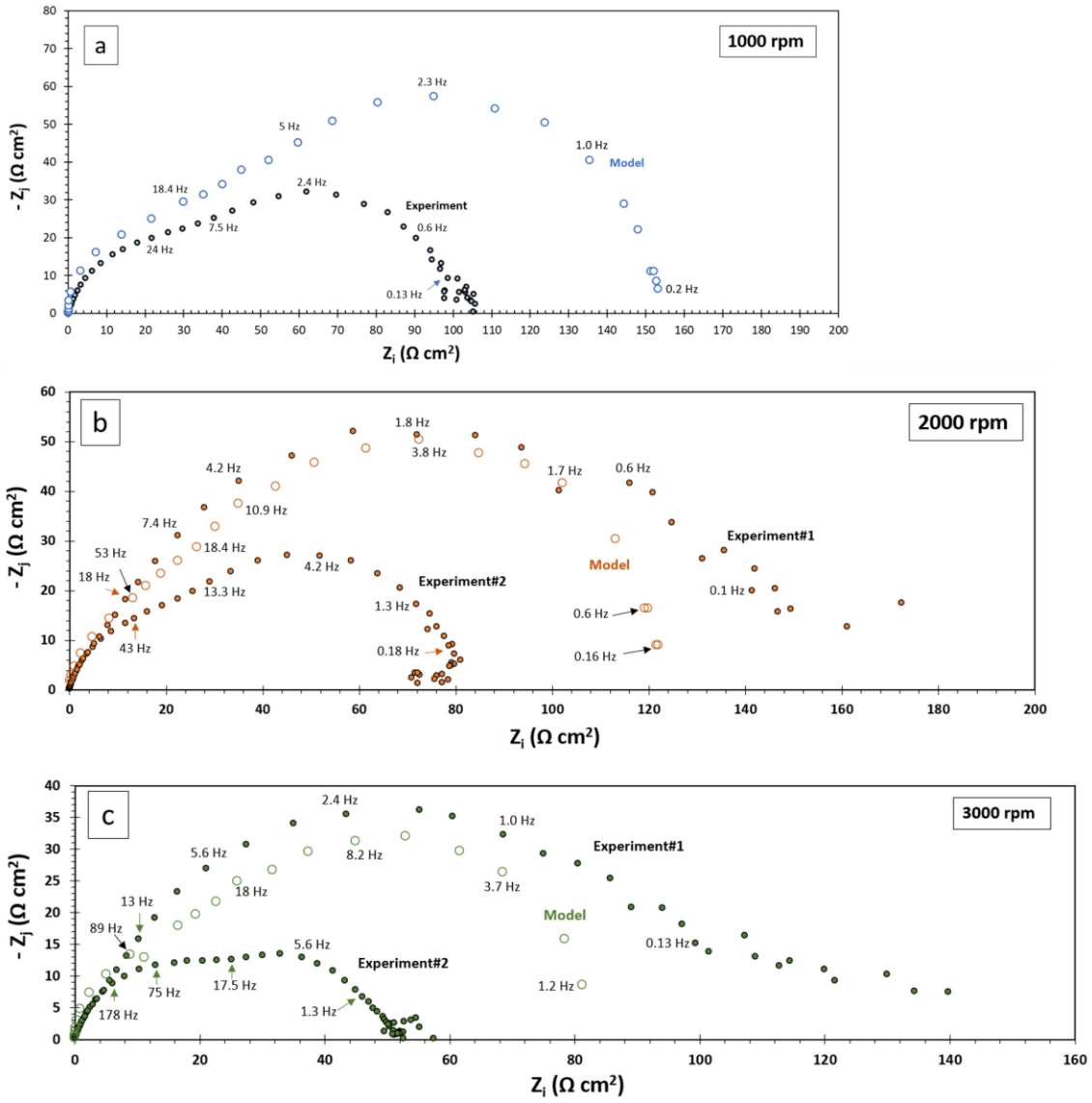

Figure 45

Comparison between the experimental and modeled Nyquist plots at different rotational rates. Experimental and simulation parameters shown in Table 9.

D.4.2. Case of CO_2 Aqueous Solutions.

In Section D.4.1., the impedance response of the cathodic reduction of H^+ was modeled and discussed in a strong acid environment under various conditions. This section describes the modeled impedance response of the same reaction in aqueous CO_2 solutions.

D.4.2.1. Effect of Temperature on the Simulated Impedance Behavior of Cathodic Reaction in CO_2 Aqueous Solutions. The effect of temperature on the potentiodynamic sweep related to the hydrogen reduction reaction is shown in Figure 46. The temperature was increased from 20°C to 30°C and 40°C, while all other parameters were kept constant (Table 7).

As shown in Figure 46, as the temperature increases, the current density for charge transfer control increases. The reaction rate constant of the cathodic reaction has an Arrhenius dependency with temperature as shown in Equation (69) and therefore as the temperature increases, the rate of the cathodic reaction increases.

Moreover, as temperature increases, the limiting current density increases. Generally, in an aqueous CO_2 saturated solution, the current density is controlled by the rate of a chemical reaction related to the hydration of CO_2 [55]. Meanwhile, the mass transfer has a key effect on the limiting current density as well. Mass transfer of hydrogen ion in the diffusion layer is expressed by the Nernst-Planck Equation which depends on both diffusion coefficient and the velocity. Based on Equation (70), the diffusion coefficient of hydrogen ion increases as temperature increases, which leads to an increase in mass transfer. Besides that, the convective mass transfer depends on the physical properties of water such as density and viscosity shown in Equations (71) and (72). Moreover, it has

been shown that the temperature has no significant effect on the dissociation of carbonic acid in a CO_2 saturated aqueous environment[17].

$$k_{0,\mathrm{j}} = k_{0,\mathrm{j,ref}} e^{\left(-\frac{E_a}{R}\left(\frac{1}{T}-\frac{1}{T_{ref}}\right)\right)} \quad (69)$$

$$D_{H^+} = D_{H^+,ref}\,\frac{T}{T_{ref}}\,\frac{\mu_{ref}}{\mu} \quad (70)$$

$$\rho_w = 753.596 + 1.87748T - 0.003562T^2 \quad (71)$$ [65]

$$\mu = \mu_{,ref}\, 10^{\left(\frac{1.1709(T_{ref}-T)-0.001827(T_{ref}-T)^2}{(T-273.15)+89.93}\right)} \quad (72)$$ [66]

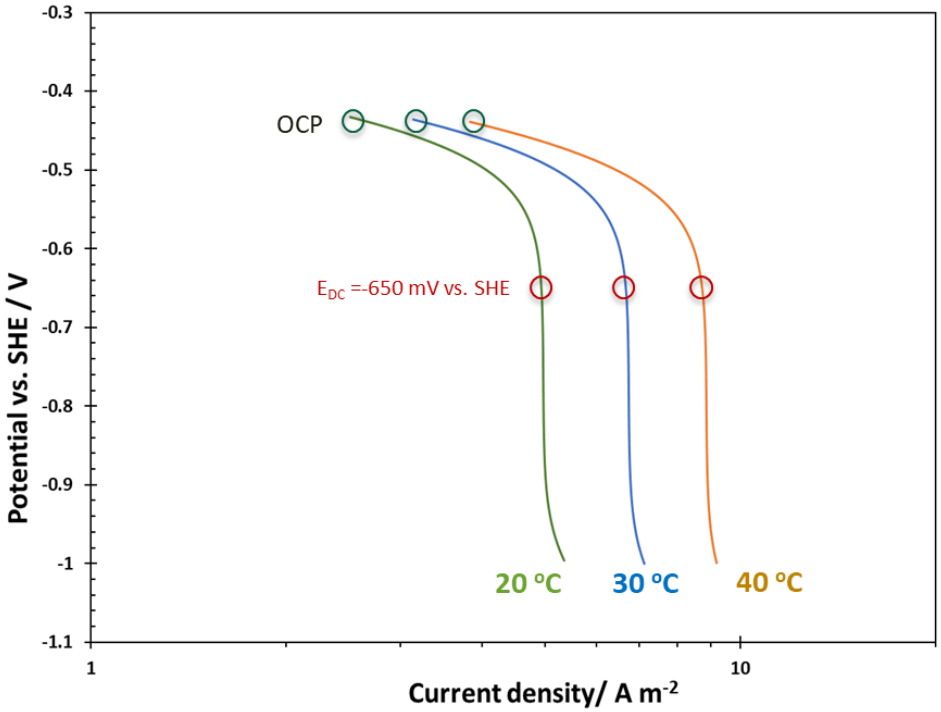

Figure 46

Calculated potentiodynamic sweep of the cathodic reaction at different values of temperature. Simulation parameters: pCO_2= 1 bar, pH 4.00, velocity=2.6 m/s, 0.1 M NaCl, sweep rate =-1 mV/s.

To observe and study the effect of temperature on the diffusion impedance of the cathodic reaction, the DC potential has been chosen at the limiting current density (-650 mV vs. SHE). In order to analyze only the cathodic reaction, the effect of the double layer is not considered in the calculations.

Following the methodology explained in Section D.3.2, Figure 47 shows the impedance response of the cathodic reaction at different temperatures. As explained above, when temperature decreases, the diffusion impedance and the polarization resistance increase. For the cathode reduction of H^+, the polarization resistance is the combination of charge transfer and mass transfer resistances.

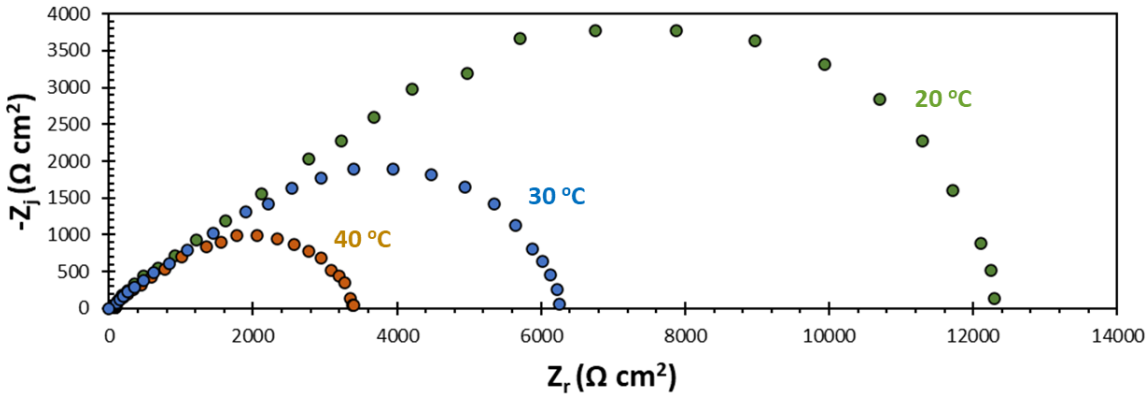

Figure 47

Effect of temperature on the diffusion impedance of the cathodic reaction. Modeling parameters: Simulation parameters: $\bar{E}_{DC}$ = -650 mV vs. SHE, $C_{dl} = 0$, pCO_2= 1 bar, pH 4.00, velocity= 2.6 m/s, 0.1 M NaCl.

D.4.2.2. Effect of Velocity on the Simulated Impedance Behavior of Cathodic Reaction in CO_2 Aqueous Solutions. Figure 48 shows the effect of velocity on the potentiodynamic sweep of the cathodic reaction. An increase in velocity increases the mass

transfer. Consequently, the limiting current density increases. The chosen DC potential for the impedance calculation is -650 mV vs. SHE, which is in the limiting current region of the potentiodynamic sweep.

Figure 49 shows the calculated Nyquist plot at different velocities. As the velocity was increased from 2.6 m/s to 10 m/s, the diameter of the diffusion impedance decreased as expected. This behavior can be explained by considering the increase in the mass transfer which reduces the diffusion impedance.

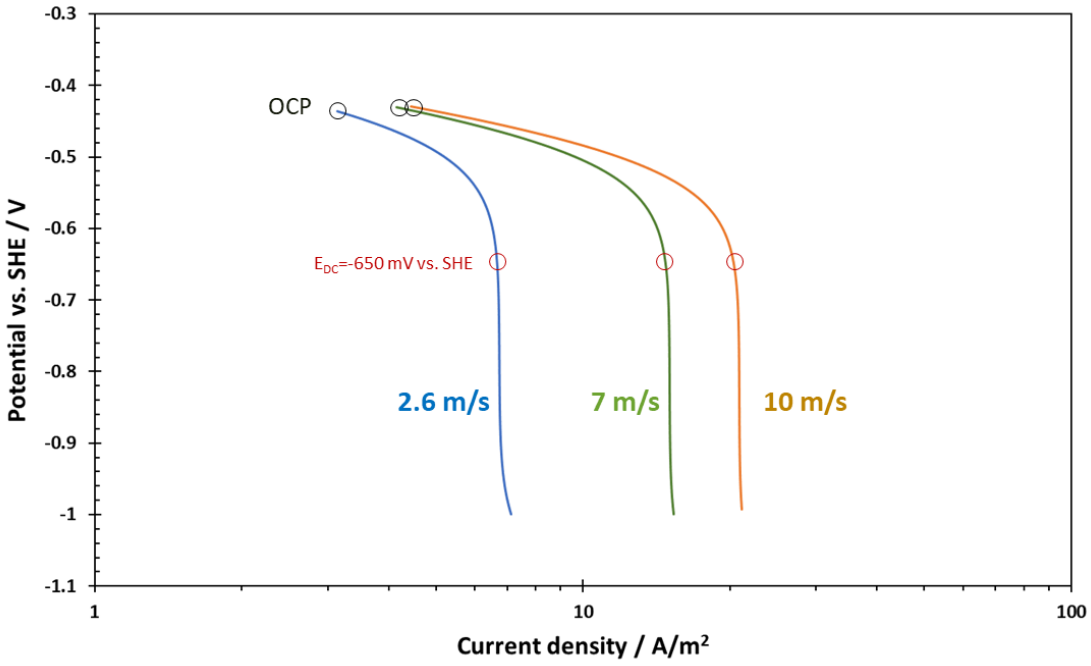

Figure 48

Calculated potentiodynamic sweep of the cathodic reaction at different velocities. Simulation parameters: pCO_2= 1 bar, pH 4.00, 30°C, 0.1 M NaCl, sweep rate =-1 mV/s.

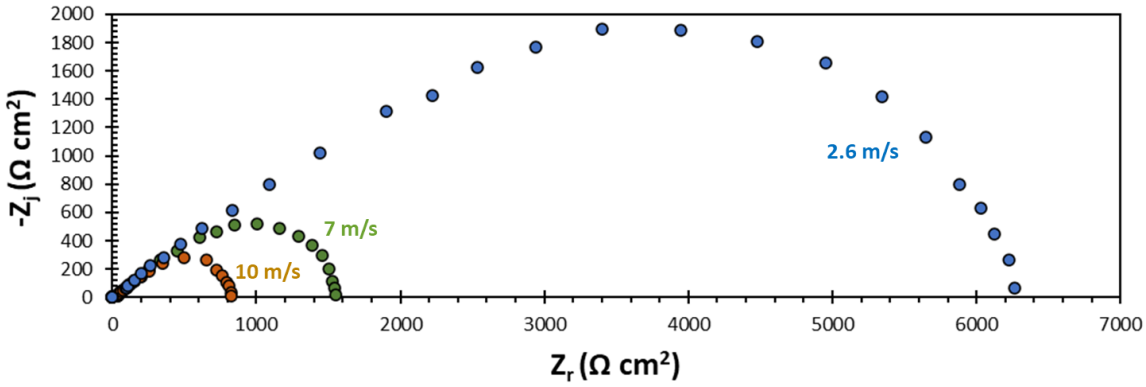

Figure 49

Effect of velocity on the diffusion impedance of the cathodic reaction. Modeling parameters: Simulation parameters: $\bar{E}_{DC}$ *= -650 mV vs. SHE,* $C_{dl} = 0$*,* pCO_2*= 1 bar, pH 4.00, T=30 °C, 0.1 M NaCl.*

D.4.2.2. Effect of pCO_2 on the Simulated Impedance Behavior of Cathodic Reaction in CO_2 Aqueous Solutions. In the next step, the impedance response of the cathodic reaction was examined for environments having different partial pressures of CO_2. Figure 50 shows the effect of pCO_2 on the potentiodynamic scans for the cathodic reaction. As the pCO_2 increases the limiting current density increases. The chosen DC potential for the simulation is set at -750 mV vs. SHE, which is in the limiting current region of the potentiodynamic sweep.

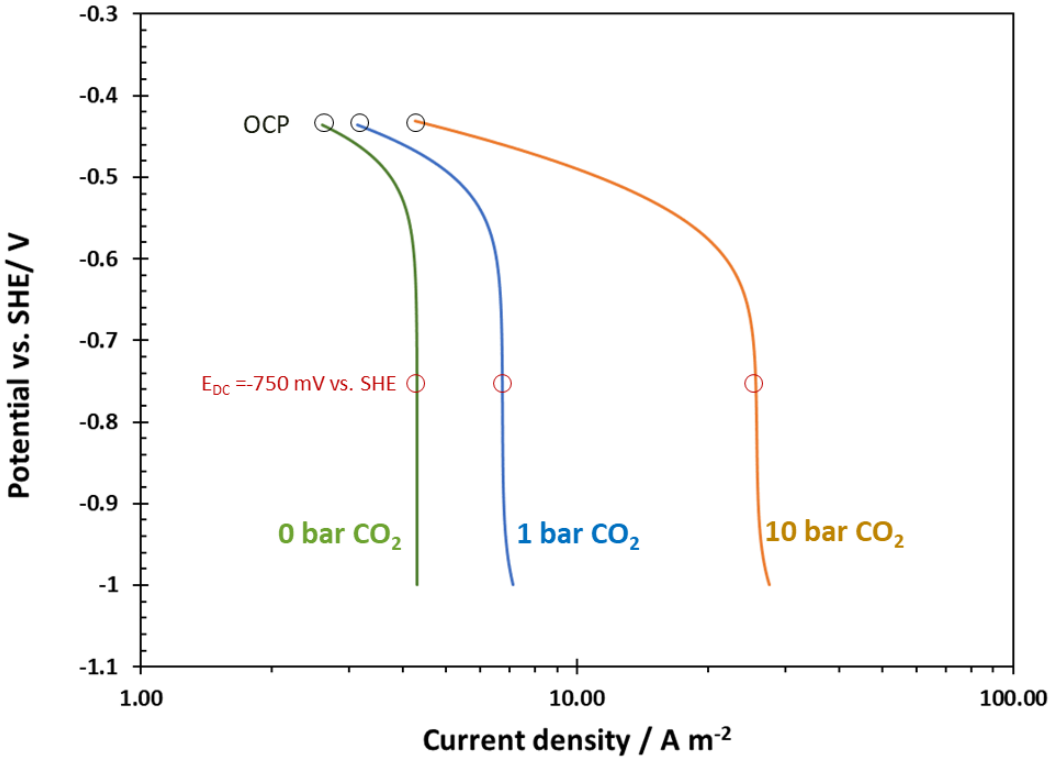

Figure 50

Calculated potentiodynamic sweep of the cathodic reaction at different pCO_2. Simulation parameters: pH 4.00, 30°C, 0.1 M NaCl, velocity=2.6 m/s, sweep rate =-1 mV/s.

Impedance responses of the cathodic reaction at three different pCO_2 are shown in Figure 51. As pCO_2 increases, the solubility of CO_2 in water increases which leads to a higher concentration of H_2CO_3. As the concentration of H_2CO_3 increases, its buffering effect increases which leads to higher limiting current density. Consequently, an increase in pCO_2 makes the diffusion impedance decrease.

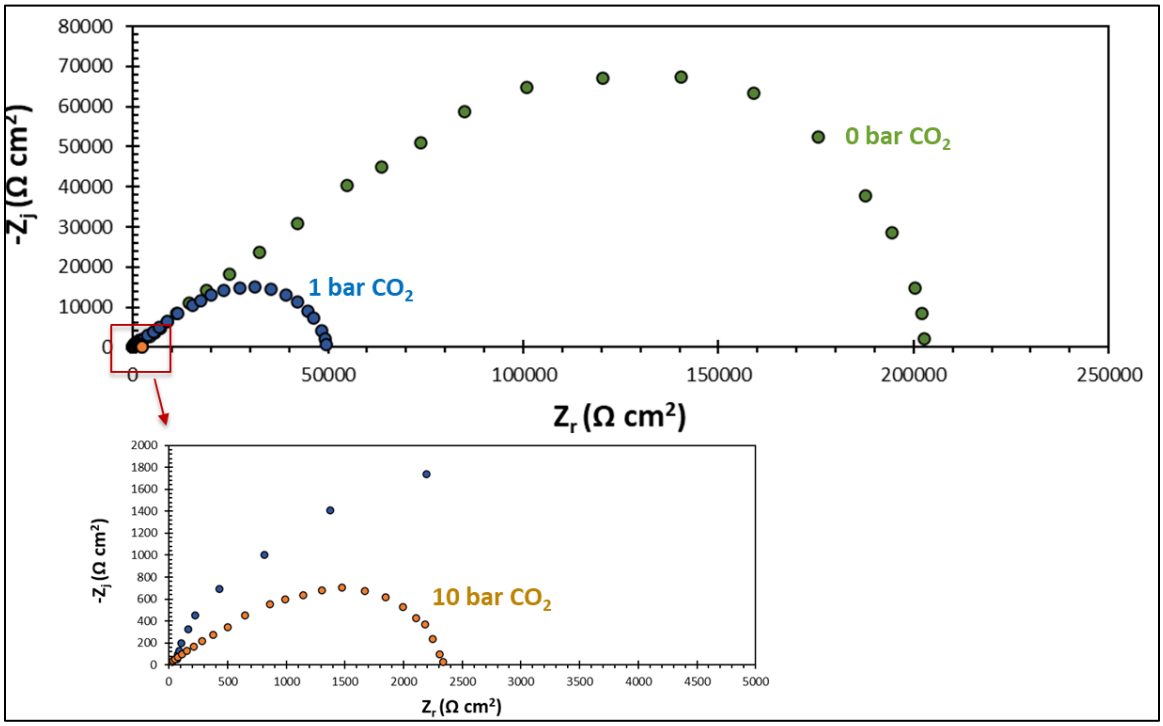

Figure 51

Effect of pCO_2 on the diffusion impedance of the cathodic reaction. Modeling parameters: Simulation parameters: $\bar{E}_{DC}$ = -650 mV vs. SHE, $C_{dl} = 0$, velocity= 2.6 m/s, pH 4.00, T=30 °C, 0.1 M NaCl.

D.4.2.3. Model Validation with Experimental Data at Different pH Values. Experiments were performed in order to validate the simulated impedance response of the reduction of H^+. Table 10 shows the simulation parameters and the experimental test conditions. The experiments were performed at pH 2.6, pH 4.0 and pH 5.0. The DC potentials for EIS measurements were considered in the charge transfer controlled region of the potentiodynamic sweeps at pH 2.6, while at pH 4.0 and 5.0, the DC potential was chosen at the limiting current density shown in Figure 52.

Table 10

Modeling and experimental parameters for steady state potentiodynamic sweeps and EIS.

Parameter	Value	
Test apparatus	Rotating disk electrode, three-electrode glass cell	
Sparged gas	pCO_2 = 1 bar	
Temperature	25 ± 0.5 ºC	
pH	2.6, 4.0, 5.0	
Potentiodynamic sweep rate	0.5 mV/s	
E_{DC}-experiment	OCP-221mV at pH 2.6	
	OCP-165 mV at pH 4 (≈ 94% i_{lim})	
	OCP-86 mV at pH 5 (≈ 80% i_{lim})	
E_{DC}-model	OCP-221 mV at pH 2.6	
	OCP-197 mV at pH 4 (≈ 96% i_{lim})	
	OCP-78 mV at pH 5 (≈ 82% i_{lim})	
Supporting electrolyte	0.5 M NaCl	
Electrode material	99.99 wt% pure iron	
Rotation rate/Velocity	Rotation rate/Velocity	For experiment using RDE
	2.4 m/s	1600 rpm
C_{dl} used in the simulation	13 μF/cm^2 at pH 2.6	
	1 μF/cm^2 at pH 4.0	
	5 μF/cm^2 at pH 5.0	

Figure 52 shows the comparison between the experimental and calculated potentiodynamic sweeps. Overall, there was a good agreement between the experiment and the calculated potentiodynamic sweeps in both charge transfer controlled and limiting current density regions. The experimental potentiodynamic sweep at the very negative potential is related to water reduction and was not considered in the calculations.

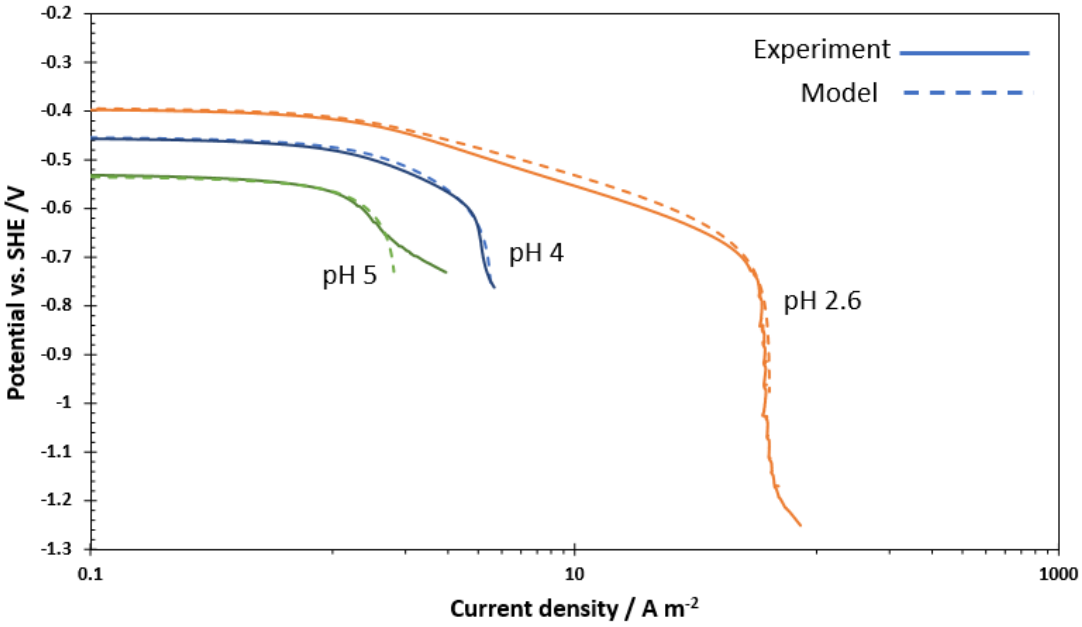

Figure 52

Comparison between the experimental and simulated steady state potentiodynamic sweeps at different pH values.

Figure 53 shows the comparison of the simulated and experimental Nyquist plots at different pH values. At pH 5.0, in the first glance, the Nyquist plot shows only one capacitive loop. However, at the chosen DC potential, there are two phenomena proceeding on the metal surface being double layer relaxation (response at high frequency) and the diffusion of the hydrogen ion (response at low frequency). As explained in Section D.4.1.2., distinguishing between the loops related to the double layer capacitance in parallel with the charge transfer resistance from the diffusion impedance becomes hard when the value of the double layer capacitance is relatively high. Since determining the value of the double layer capacitance was not possible without additional measurements, therefore,

using trial and error, the value of 5 $\mu F/cm^2$ was used at pH 5.0 to make a good fit between the experimental data and the modeled Nyquist plot.

At pH 2.6 and 4.0, the experimental Nyquist data shows two capacitive loops representing the double layer capacitance in parallel with the charge transfer resistance (high frequency loop) and diffusion impedance (low frequency loop). Using the experimental data at high frequency, the double layer capacitances at pH 2.6 and 4.0 were calculated to be 59 $\mu F/cm^2$ and 137 $\mu F/cm^2$, respectively. However, in order to fit the model to the experimental data at high frequency, the optimum values for double layer capacitance used were 13 $\mu F/cm^2$ and 1 $\mu F/cm^2$, respectively. This behavior can be explained by comparison between the frequencies of the data shown on the Nyquist plot. Comparing the frequencies of the modeled and experimental data points, it is shown that the frequencies of the modeled data is relatively higher than for the experimental data. Meanwhile, decreasing the time steps or eliminating the effect of turbulent flow did not change the frequencies of the modeled data. The difference between the frequencies of the modeled and experimental data might also be related to the experimental error as was explained in the comparison between the experimental and modeled data obtained in case of strong acid solution (Section D.4.1.5).

Comparison of the experimental and calculated data at pH 4.0 shows that the polarization resistance was higher compared to the modeled data. However, the charge transfer resistance was reasonably similar to the experimental results. The same comparison at pH 2.6 shows that the charge transfer resistance was lower than the experimental data while the polarization resistance was very close to the experimental data.

It is important to mention that, as explained in Section D.4.1.5, the experimental impedance response is sensitive to slight variation of experimental parameters such as temperature, surface pH, etc. Therefore, the difference between resistances obtained by the experimental and modeled data, might also be related to the experimental error as well. Despite some errors, the model data mechanistically show the same response as the experimental impedance data with two time constants related to the diffusion impedance and double layer capacitance in parallel with a charge transfer resistance.

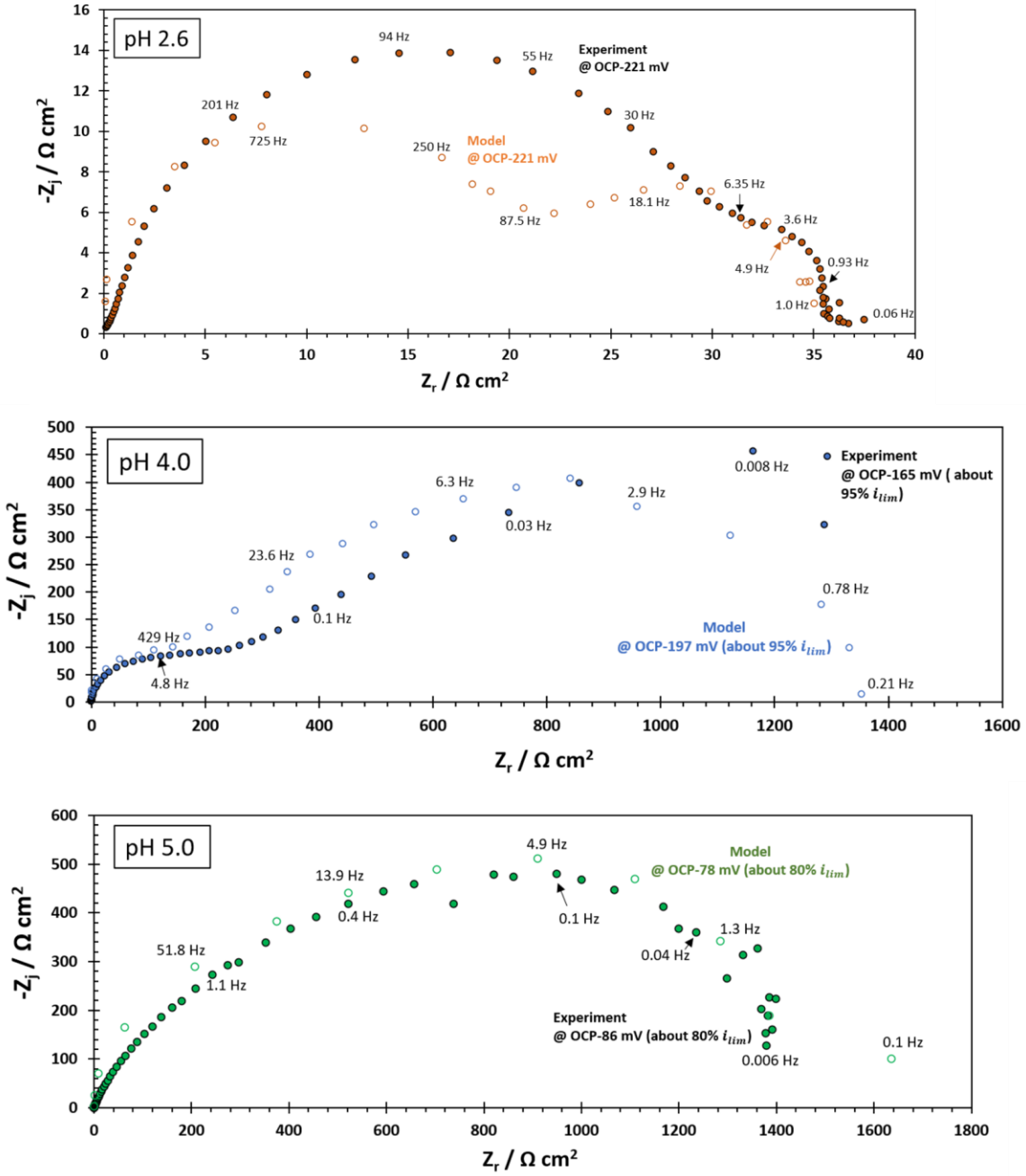

Figure 53

Comparison between the experimental and modeled Nyquist plots at different pH values. Experimental and simulation parameters shown in Table 10.

D.5. Summary

- The impedance response, Nyquist plot and Bode plot for the cathodic reduction of hydrogen ions, in both strong acid and CO_2 aqueous environments, were successfully modeled.
- The model predictions associated with the effect of several parameters such as temperature, pCO_2, velocity, etc., were investigated.
- The model was validated by comparing the experimental and modeled data. Both potentiodynamic sweep and EIS experimental results were predicted reasonably by the model in both strong acid and CO_2 aqueous environments.
- The model described in this study can be used to analyze the experimental EIS results to study the cathodic reduction of the hydrogen ion related to the corrosion of mild steel in acidic environments.

Chapter E: Mechanistic Study of Anodic Dissolution of Pure Iron in Acidic Solutions

E.1. Introduction

Understanding the mechanism of the iron dissolution along with the cathodic reaction in acidic environments has been was the subject of many research studies, with different mechanisms proposed for the anodic reaction [6,7,18–22,28–30,43,67–70]. One of the objectives of these studies was the development of mechanistic models to calculate and control the corrosion rate in different acidic environments, which contrasts with empirical models that are only capable of corrosion rate prediction in limited conditions.

Among different mechanisms proposed for the anodic reaction, the "consecutive mechanism" proposed by Bockris [28] and the "self-catalytic mechanism" proposed by Heusler [29,71] are most accepted among corrosion researchers. In 1958, Heusler introduced the "self-catalytic mechanism" considering a Tafel slope of 30 mV/decade [29,71], while in 1961, experiments conducted by Bockris, *et al.*, showed a Tafel slope of 40 mV/decade [28]. Both mechanisms were used in order to justify the steady state polarization data including the Tafel slope.

Most of the mechanistic studies related to the dissolution of iron were based on direct current (DC) techniques such as steady-state polarization sweeps. However, these techniques measure the total reaction rate which is controlled by the slowest reaction step and consequently, it can provide little information about a multi-step reaction [6,7]. Moreover, it has been shown that defining a mechanism solely based on steady state data, specifically Tafel slope, might result in an inaccurate conclusion [6,22,43]. Explaining this further, it has

been proven that two different Tafel slopes might be related to the same mechanism, considering the experimental error margins[22] or, in another scenario, Tafel slopes with similar values might be related to two different mechanisms[22,68].

Complementing the DC techniques, electrochemical impedance spectroscopy (EIS) is a more advanced methodology that can be used to study complex multi-step reaction. In 1981, Keddam, *et al.*, introduced a multi-path mechanism for anodic iron dissolution including three parallel dissolution paths using both steady state polarization and EIS techniques[6,7]. The proposed mechanism was justified by both steady state polarization and EIS data in a sulfate strong acidic environment (details about this mechanism are provided in Section E.2).

As mentioned before, many research studies focused on the iron anodic mechanism in acidic environments. However, corrosion of mild steel in the oil and gas industry always happens in the presence of CO_2 and carbonic acid. Experiments performed by Kahyarian et al.[20] showed that increasing the pCO_2 affects the rate of mild steel dissolution in acidic environments. Therefore, elucidating and understanding the role of CO_2 on the mechanism of the anodic dissolution of iron is one of the primary objectives of the current study. The accomplishment of this objective will help to improve the existing electrochemical models for corrosion rate prediction.

E.2. Background

El Miligy, *et al.,* categorized the anodic dissolution of iron into four regions based on steady-state polarization curves; namely active dissolution, transition, pre-passivation, and passivation regions similar to Figure 54 [67].

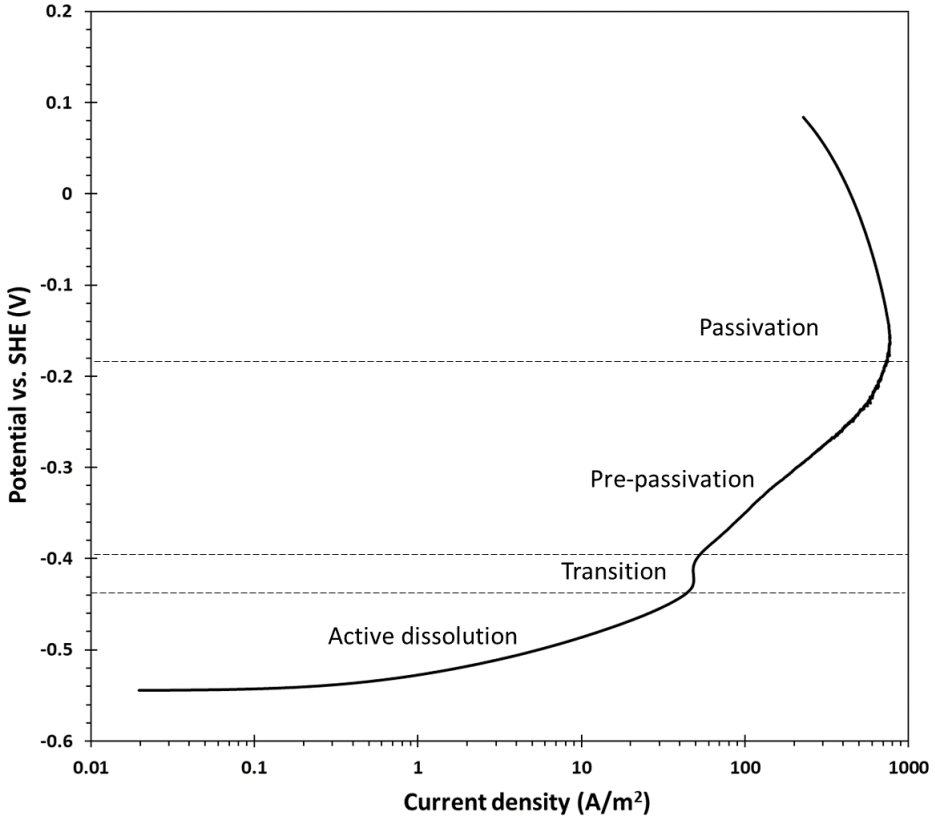

Figure 54

Anodic dissolution of iron in 0.5 M NaCl, pH 6.0, 25°C, 1 bar CO_2, using rotating disk pure iron electrode at 16000 rpm and a scan rate of 0.5 mV/s.

In 1958, Heusler proposed the "self-catalytic mechanism" considering Tafel slope of 30 mV/decade [29,71]. This consists of two sets of parallel reactions. In the first pH-dependent reaction step (Reaction (73)), there is formation of a catalytic surface species ($FeOH_{(ads)}$).

$$Fe_{(s)} + OH^-_{(aq)} \rightleftarrows FeOH_{(ads)} + e^- \quad (73)$$

In 1965, Kelly suggested that this reaction actually occurs in 3 steps adding up to the overall Reaction (73) as shown by (Reaction (74)-Reaction (76))[69].

$$Fe_{(s)} + H_2O_{(l)} \rightleftarrows Fe(H_2O)_{(ads)} \quad (74)$$

$$Fe(H_2O)_{(ads)} \rightleftarrows Fe(OH^-)_{(ads)} + H^+_{(aq)} \quad (75)$$

$$Fe(OH^-)_{(ads)} \rightleftarrows FeOH_{(ads)} + e^- \quad (76)$$

Either way, the Huesler mechanisms suggests that once it is formed, $FeOH_{(ads)}$ acts as a catalyst for iron dissolution in the second sequence of reactions, as shown in Reaction (77)-Reaction (79)[29,71] below, which is the main iron dissolution sequence as it produces most of the current. It is important to mention that in this sequence, Reaction (78) is not a true elementary reaction step as it presents two electrons transferred simultaneously, which is very unlikely and is not consistent with the electrochemical theory behind an elementary reaction.

$$Fe_{(s)} + FeOH_{(ads)} \rightleftarrows Fe(FeOH)_{(ads)} \quad (77)$$

$$Fe(FeOH)_{ads} + OH^-_{(aq)} \xrightarrow{rds} (FeOH)^+_{(aq)} + FeOH_{(ads)} + 2e^- \quad (78)$$

$$(FeOH)^+_{(aq)} \rightleftarrows Fe^{2+}_{(aq)} + OH^-_{(aq)} \quad (79)$$

In 1961, experiments conducted by Bockris, *et al.*, showed a Tafel slope of 40 mV/decade[28]. They proposed a mechanism known as the "consecutive mechanism" which is shown by Reaction (80)-Reaction (82).

$$Fe_{(s)} + OH^-{}_{(aq)} \rightleftarrows FeOH_{(ads)} + e^- \quad (80)$$

$$FeOH_{(ads)} \xrightarrow{rds} (FeOH)^+_{(aq)} + e^- \quad (81)$$

$$(FeOH)^+_{(aq)} \rightleftarrows Fe^{2+}_{(aq)} + OH^-_{(aq)} \quad (82)$$

The first step is the same as in the Heusler mechanisms, which can be shown as a sequence of three reactions as suggested by Kelly, (Reaction (74)-Reaction (76))[69]

Both of these iron dissolution mechanisms, self-catalytic (Heusler) and consecutive (Bockris), were obtained based on steady-state polarization curves and near the open circuit potential (OCP); assuming that each elementary step follows the Tafel law with a charge transfer coefficient of 0.5. Both catalytic and consecutive mechanisms were subsequently adopted in many different research studies, sometimes with minor modifications.

Years later, the mechanism for the anodic dissolution of iron was reevaluated by Epelboin and Keddam using the EIS technique[43]. The experimental impedance data of the anodic dissolution of iron in the active dissolution region and near the open circuit potential showed a high frequency capacitive loop related to the double layer capacitance in parallel with a charge transfer resistance and a low frequency inductive loop related to the adsorbed $FeOH$. However, considering the consecutive mechanism and its assumptions, Keddam, *et al.,* showed that the modeled impedance data near the open circuit potential shows only one capacitive loop which was not consistent with the experimental data near the open circuit potential [43,68]. Therefore, a reevaluation of assumptions behind the consecutive mechanism was required.

The assumption behind the consecutive mechanism includes the first step being in pseudo-equilibrium and a charge transfer coefficient value of 0.5 for all elementary steps[28].

However, based on electrochemical theory, it has been argued that the charge transfer coefficient can be any value between zero and one [40]. Moreover, as Keddam, *et al.,* explained, once the potential is highly positive (with respect to equilibrium potential), it can be assumed that the first step in the consecutive mechanism (Reaction (80)) is practically irreversible[6,7,43]. Consequently, following the revised assumptions for the consecutive mechanism, Keddam, *et al.*, successfully modeled the impedance response of the anodic dissolution of iron at the active dissolution region and near the open circuit potential [6,7,43,68].

Considering the revised version of the Bockris mechanism, Keddam, *et al.*, reported a calculated Tafel slope of 60 mV/s, which is significantly higher compared to the experimental value reported by other researchers (40 mV/s)[6,7,28]. The higher value of Tafel slope was justified based on the effect of adsorbed hydrogen on the iron surface [6,7].

In 1981, Keddam, *et al.*, studied the mechanism of the anodic dissolution of iron at different pH values and over a much broader range of potentials: in the active dissolution, transition, pre-passivation and passivation regions, using steady state polarization sweeps and electrochemical impedance spectroscopy (EIS) measurements [6,7]. In the mechanism proposed in that study, there are three parallel iron dissolution paths. Reaction (83) is the first pH dependent elementary reaction step in which $Fe(I)_{ads}$ or ($FeOH_{(ads)}$) is formed as the first intermediate/adsorbed species. In the next step the $Fe(I)_{ads}$ participates in 3 parallel sets of reactions. Path 1 which includes Reactions (83) and Reaction (84) is valid in the active dissolution region. Considering $Fe(II)_{sol}$ being $FeOH^{+}$, path 1 is similar to the modified consecutive mechanism in which step 1 is considered to be irreversible.

$$Fe \xrightarrow{k1,pH^{16}} Fe(I)_{ads} + e^- \quad (83)$$

$$Fe(I)_{ads} \xrightarrow{k2} Fe(II)_{sol} + e^- \quad (84)$$

Path 2 of the multi-step mechanism, similar to the self-catalytic mechanism, includes two reactions. In the first reaction, there is the formation of a catalytic surface species $Fe(I)_{ads}^{*}$[17] (that might have a chemical composition of $Fe(FeOH)_{(ads)}$) through Reaction (83) and Reaction (85). In the next step, the iron dissolution proceeds in a self-catalytic reaction as shown by Reaction (86). The difference between the Heusler self-catalytic mechanism and path 2 is the formation of a catalytic species through a chemical reaction (Reaction (85)) which depends on potential[6,7]. Although the general chemical rate theory suggests that a non-redox chemical rection cannot depend on potential, still Keddam, *et al.* considered this assumption in order to fit the modeled data to the experimental polarization sweep and EIS measurements.

$$Fe(I)_{ads} \underset{\xleftarrow[k_{-3}]{}}{\xrightarrow{k_3, pH}} Fe(I)_{ads}^{*} \quad (85)$$

$$Fe + Fe(I)_{ads}^{*} \xrightarrow{k_4,pH} Fe(II)_{sol} + Fe(I)_{ads}^{*} + 2e^- \quad (86)$$

Similar to path 2, path 3 includes the formation of another catalytic species $Fe(II)_{ads}^{*}$ (which might have a chemical composition of $Fe(OH)_{2\,(ads)}$) through electrochemical Reactions (83) and (87) [6,7]. In the next step, the iron dissolution proceeds

[16] pH on arrows indicates that the rection is pH dependent.
[17] Star sign indicates that the chemical component acts as a catalyst in the reaction.

through Reaction (88). Moreover, at very positive potentials, the passivation of iron begins with the formation of $Fe(II)_{ads}$ through Reaction (89).

$$Fe(I)_{ads} \underset{k_{-5}}{\overset{k_5,\, pH}{\rightleftarrows}} Fe(II)^{*}_{ads} + e^{-} \tag{87}$$

$$Fe + Fe(II)^{*}_{ads} \overset{k_6}{\rightarrow} Fe(II)_{sol} + Fe(II)^{*}_{ads} + 2e^{-} \tag{88}$$

$$Fe(II)^{*}_{ads} \underset{k_{-7}}{\overset{k_{7,pH}}{\rightleftarrows}} Fe(II)_{ads} \tag{89}$$

The overall scheme of Keddam, *et al.*'s multipath mechanism is shown in Figure 55 [6,7]. Figure 56 shows an example of modeled anodic polarization sweep at pH 5 [6,7] following Kedam *et al.* model and using their kinetic parameters.

Keddam, *et al.*'s study [6,7] was conducted in strong acid sulfate solutions, and the question that needed answered is, was there an influence of the sulfate anion on the reaction mechanism and rate, and would the results be different in a different solution, say one that contains chlorides? For the purposes of the present study, another question is also important: is there an effect of aqueous CO_2. Those will be discussed next.

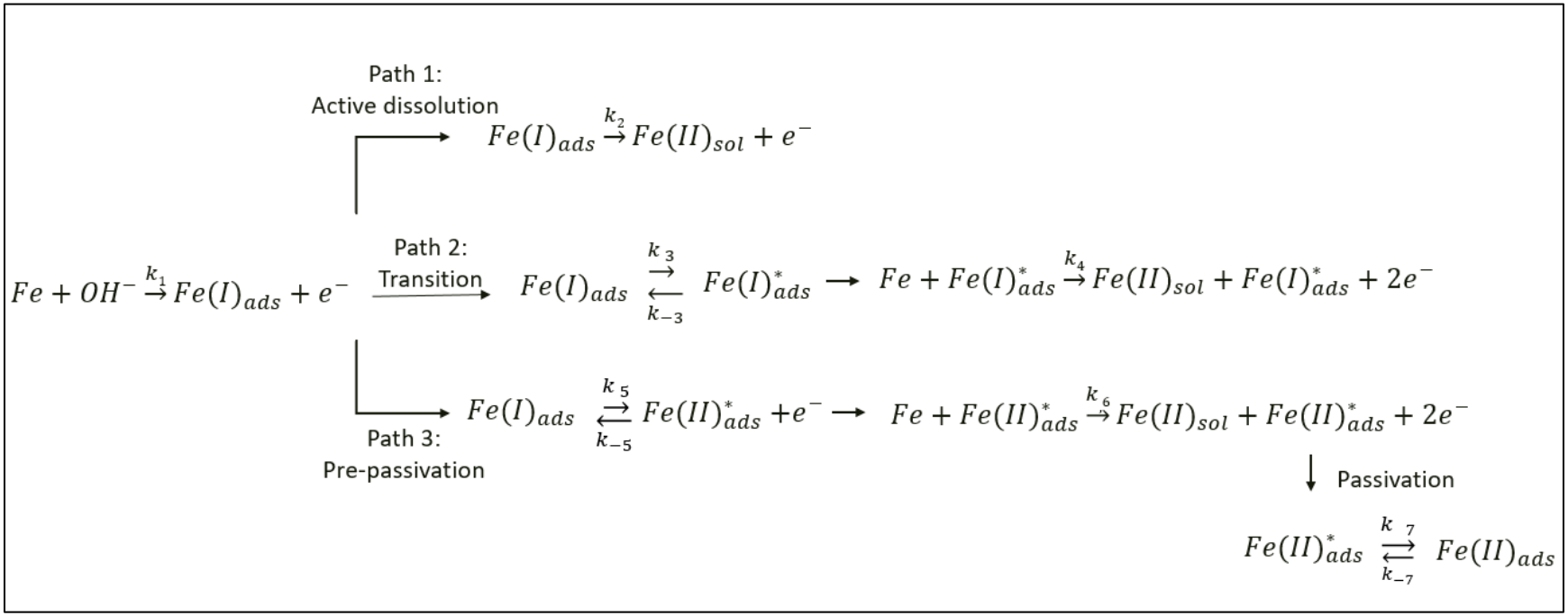

Figure 55

Scheme of multi-path mechanism [6,7.]

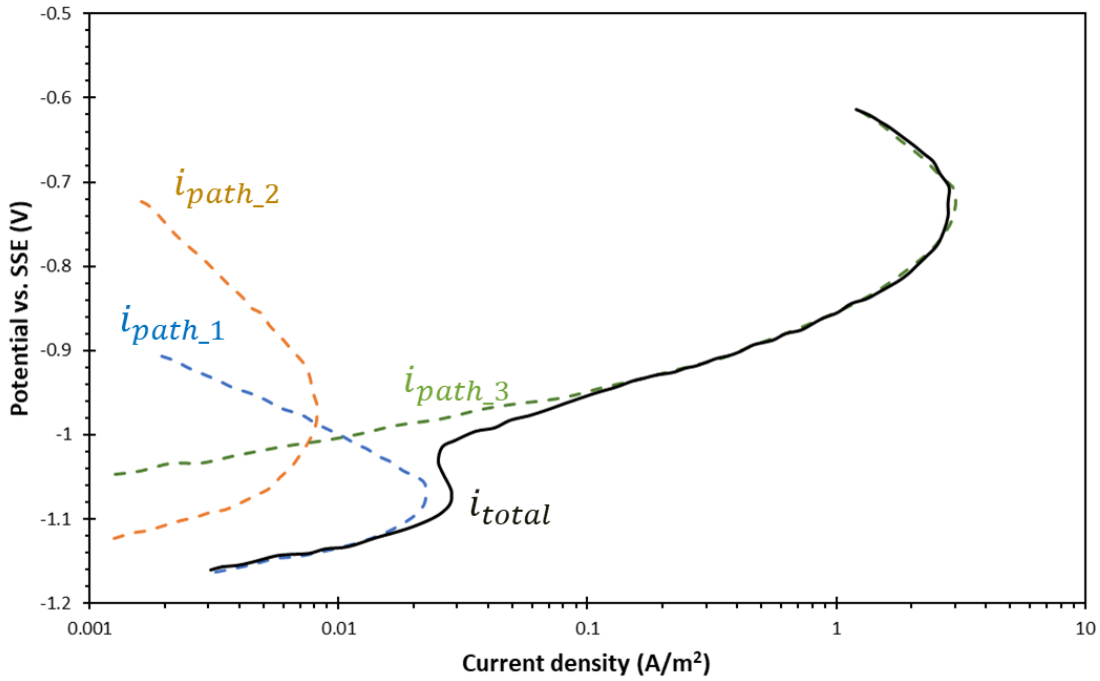

Figure 56

Modeled anodic polarization sweep using multi-path mechanism [6,7]*. Modeling parameters: pH 5, 1 bar Ar, 25 °C, 1 M Na_2SO_4, 1600 rpm, RDE, pure iron. Data taken and reconstructed from paper of Keddam, et al.* [6]

E.2.1. Effect of Anions on the Mechanism of Iron Dissolution

There are several major findings reported in the literature regarding role of anions in the mechanism of anodic dissolution of metals[70,72–78]. Amongst them, there are contradictory conclusions regarding the role of sulfate ions on the mechanism of the iron dissolution. In fact, there are papers indicating that sulfate ions can participate in the iron dissolution, while others indicate that it does not have an effect on the iron dissolution[70,73]. On the other hand, it seems to be a consensus that halide ions such as Cl^-, Br^- and I^- might replace OH^- from the iron surface through competitive adsorption[70,72,74,77,78]. Some studies

indicate that halides such as Cl^- can decelerate the anodic rection while there are other studies reporting the acceleration effect of Cl^- on the anodic dissolution of iron [70,77–80].

The effects of I^- on iron dissolution were discussed earlier by Heusler and Cartledge[74]. The authors observed S-shaped anodic polarization curves indicating two Tafel slopes of 60 mV/decade at lower potential and 30 mV/decade at higher anodic potential[70,74]. Therefore, the anodic dissolution of iron proceeds through two parallel reactions according to Equation (90) where i_2 is the current density dependent on the surface coverage by halide ion and is dominating at lower potential where the Tafel slope is equal to 60 mV/decade[70,74]. $i_1$is the current density from the free iron surface, where Tafel slope is 30 mV/decade. As halides adsorb on the iron surface and surface coverage by the hydroxide ion decreases, consequently, the current density decrease[70,74].

$$i_{total} = i_1 + i_2 \tag{90}$$

Considering simultaneous adsorption of $FeOH$ and FeX^- where X^- is a halide ion, the first species participates in a reaction following the self-catalytic or non-catalytic mechanism while the second reaction proceeds in the presence of halides through several different proposed mechanisms. One of the mechanisms proposed is the so-called "*halide inhibited*" mechanism shown by Reactions (91)-(95)[70,77,80].

$$Fe + H_2O \leftrightarrow Fe(H_2O)_{ads} \tag{91}$$

$$Fe(H_2O)_{ads} \leftrightarrow Fe(OH^-)_{ads} + H^+ \tag{92}$$

$$Fe + X^- \leftrightarrow Fe(X^-)_{ads} \tag{93}$$

$$Fe(OH^-)_{ads} + Fe(X^-)_{ads} \rightarrow Fe + FeOH^+ + X^- + 2e^- \tag{94}$$

$$FeOH^+ + H^+ \leftrightarrow Fe^{2+} + H_2O \tag{95}$$

McCafferty and Hackerman proposed another mechanism for iron dissolution incorporating the effect of adsorbed OH^- and Cl^-. Reactions (96)-(100) show the proposed mechanism in solutions with pH value above zero, while for lower pH values Reactions (101)-(105) were proposed [70,81].

$$Fe + H_2O \leftrightarrow Fe(H_2O)_{ads} \quad (96)$$

$$Fe(H_2O)_{ads} + X^- \leftrightarrow Fe(X^-)_{ads} + H_2O \quad (97)$$

$$Fe(H_2O)_{ads} + X^- \leftrightarrow Fe(OH^-)_{ads} + H^+ + X^- \quad (98)$$

$$Fe(OH^-)_{ads} + Fe(X^-)_{ads} \rightarrow Fe + FeOH^+ + X^- + 2e^- \quad (99)$$

$$FeOH^+ + H^+ \leftrightarrow Fe^{2+} + H_2O \quad (100)$$

$$Fe + H_2O \leftrightarrow Fe(H_2O)_{ads} \quad (101)$$

$$Fe(H_2O)_{ads} + X^- \leftrightarrow Fe(X^-)_{ads} + H_2O \quad (102)$$

$$Fe(X^-)_{ads} + H^+ \leftrightarrow Fe(X^-).H^+ \quad (103)$$

$$Fe(X^-).H^+ + H^+ \rightarrow FeX^+ + 2H^+ + 2e^- \quad (104)$$

$$FeX^+ \leftrightarrow Fe^{2+} + X^- \quad (105)$$

In recent years, impedance measurements were performed in strong acid solution and weak acidic CO_2 aqueous solutions[21]. Experiments were performed without the presence of any supporting electrolyte and only at open circuit potential, using two electrode experimental setup in which the electrodes were large and the distance between them were small enough to avoid the effect of large solution resistances. The Nyquist plots were similar to each other and to the Nyquist plots obtained in strong acid solution with

3.2 M NaCl. Therefore, this finding might indicate that the presence of CO_2 and NaCl did not have an effect on the anodic dissolution of mild steel at open circuit potential[21].

MacFarlane and Smedley studied the mechanism of iron dissolution in 4.5 M chloride solution and over a pH range of 0-4, considering the Keddam, *et al.*, multi-path mechanism in sulfate solution[6,7] and Kuo, *et al.*, mechanism[79] in chloride solution[76]. The proposed mechanism was based on two distinct Tafel slopes at low and high current density. Reaction (106) and (107) are similar to the mechanism proposed by Kuo, et al., dominating at lower current density in which $Fe(I)_{ads}^{1}$ is $[FeClOH]^{-}$[76,79]. Moreover, Reaction (108)-(111) represents path 1 and path 2 in the Keddam, *et al.*, multi-path mechanism dominating at higher potential and current density[6,7,76].

$$Fe \leftrightarrow Fe(I)_{ads}^{1} + e^{-} \quad (106)$$

$$Fe(I)_{ads}^{1} \rightarrow Fe(II)_{sol} + e^{-} \quad (107)$$

$$Fe \leftrightarrow Fe(I)_{ads} + e^{-} \quad (108)$$

$$Fe(I)_{ads} \rightarrow Fe(II)_{sol} + e^{-} \quad (109)$$

$$Fe(I)_{ads} \leftrightarrow Fe\ (I)_{ads}^{*} \quad (110)$$

$$Fe\ (I)_{ads}^{*} + Fe \rightarrow Fe\ (I)_{ads}^{*} + Fe(II)_{sol} + 2e^{-} \quad (111)$$

Keddam, *et al.,* postulated a mechanism composed of three parallel paths validated by both EIS and steady state polarization measurements in sulfate solution, as shown by Reactions (83)-(89) [6,7]. Further investigations on this mechanism in sulfate and chloride solutions were performed by Barcia, *et al.*[75]. Experimental results showed validation of the same mechanism considering the presence of chloride in the chemical structure of some of the intermediate species, while changing the contribution of some reactions in the

mechanism at pH <3. The experimental results did not show any indication of the effect of chloride on the iron dissolution at pH≥3.

E.2.2. Effect of CO_2 on the Mechanism of Iron Dissolution

The anodic dissolution of iron in strong acidic environments has been the subject of many research studies, however, few considered the effect of CO_2 on the anodic dissolution of iron [14,18–21,30,57].

In 1996, Nesic, *et al.*, studied the effect of CO_2 on the anodic dissolution of iron[18]. The authors suggested that the effect of aqueous CO_2 is considerable for $0.2<pCO_2<1$, which affects the surface coverage of steel by aqueous CO_2 species. The author also indicated that below 0.2 bar CO_2, the coverage of the metal surface by aqueous CO_2 species is small and the effect is negligible. However, above 1 bar CO_2, as the surface coverage fraction of the metal by aqueous CO_2 species becomes saturated, the effect fades away, the authors speculated. The mechanism proposed by Nesic, *et al.*, is shown in Reaction (112)-Reaction (117).

$$Fe + CO_2 \leftrightarrow FeCO_{2_{ads}} \quad (112)$$

$$FeCO_{2_{ads}} + H_2O \leftrightarrow FeHCO_{3_{ads}} + H^+ + e^- \quad (113)$$

$$FeHCO_{3_{ads}} \rightarrow FeHCO_{3_{ads}}^+ + e^- \quad (114)$$

$$FeHCO_{3_{ads}}^+ + H_2O \leftrightarrow FeOH_2CO_{3_{ads}} + H^+ \quad (115)$$

$$FeOH_2CO_{3_{ads}} \leftrightarrow FeOH_2CO_{3_{sol}} \quad (116)$$

$$FeOH_2CO_{3_{sol}} + 2H^+ \leftrightarrow Fe^{2+} + CO_2 + 2H_2O \quad (117)$$

Davies and Burstein as well as Linter and Burstein studied the effect of CO_2 on the anodic dissolution of mild steel [19,30]. They showed that the presence of CO_2 did not affect

the active dissolution region. However, it was reported that the presence of CO_2 increases the first current "maximum", and its effect is more visible in the transition and pre-passivation region where there is a semi-passive film by $Fe(OH)_2$ [19,30]. They mentioned that the effect of CO_2 is due to its interaction with the film resulting in the formation of a complex which is soluble in water. As the coverage by the film increases on the surface, the anodic current starts to decrease as shown in the transition region. At higher potentials, CO_2, H_2CO_3 or HCO_3^- directly interact with the film and result in the formation of $FeCO_3$, which further reacts with HCO_3^- and results in the formation of $Fe(CO_3)_2^{2-}$ Reactions (118)-(121), and as this ion dissolves in water, anodic current increases.

$$Fe(OH)_2 + CO_2 \rightarrow FeCO_3 + H_2O \quad (118)$$

$$Fe(OH)_2 + H_2CO_3 \rightarrow FeCO_3 + 2H_2O \quad (119)$$

$$Fe(OH)_2 + HCO_3^- + H^+ \rightarrow FeCO_3 + 2H_2O \quad (120)$$

$$FeCO_3 + HCO_3^- \rightarrow Fe(CO_3)_2^{2-} + H^+ \quad (121)$$

Kahyarian, *et al.*, studied the anodic dissolution of mild steel in CO_2 aqueous environment [20]. They showed that the presence of CO_2 affects the mild steel dissolution in the active, transition, and pre-passivation regions. In the active region, the presence of CO_2 decreased the Tafel slope from 28 mV/decade, in a solution without CO_2, to 22 mV/decade. Although this is a small difference, Kahyarian. *Et al.*, concluded that the mechanism of iron dissolution is different in the presence of CO_2. Almeida, *et al.*[22], challenged this finding by discussing different Tafel slopes as a parameter which cannot solely be an indication of different mechanisms.

In 2017, Almeida, *et al.,*[21] studied the role of CO_2 on the anodic reaction mechanism using EIS at different pCO_2 values and at the open circuit potential. In their special setup, experiments were performed in aqueous solution sparged with high CO_2 pressure and without the presence of any additional anions as supporting electrolyte. The result shows that CO_2 does not have an effect on the mechanism of iron dissolution at open circuit potential, under the conditions used in their experimentation.

E.2.3. The Origin of the S-shaped Transition Region in the Anodic Polarization Sweep for Iron Dissolution

There is a hypothesis in several research studies that the S-shaped transition region in the anodic polarization sweep might be related to the adsorption of species which acts similarly to a soluble film or behaves like a porous layer which inhibits the mass transfer across the metal surface, [30,67]. Consequently, formation of such species leads to the presence of the first current maximum and a decrease in current density in the transition region. However, analysis based on the Keddam, *et al.*, multi-path mechanism provides another more plausible explanation of the role of adsorbed species on the S-shaped behavior of the anodic reaction in the transition region, which is discussed in detail below.

Figure 57.a and Figure 57.b show the anodic polarization sweeps of each path related to the Keddam, *et al.*, multi-path mechanism and the associated surface coverage fraction by intermediate species on the iron surface at pH 5.0 in strong acid solution. The data shown in Figure 57 is reproduced using the Keddam, *et al.*, multi-path mechanism, and the reported kinetic constants[6,7].

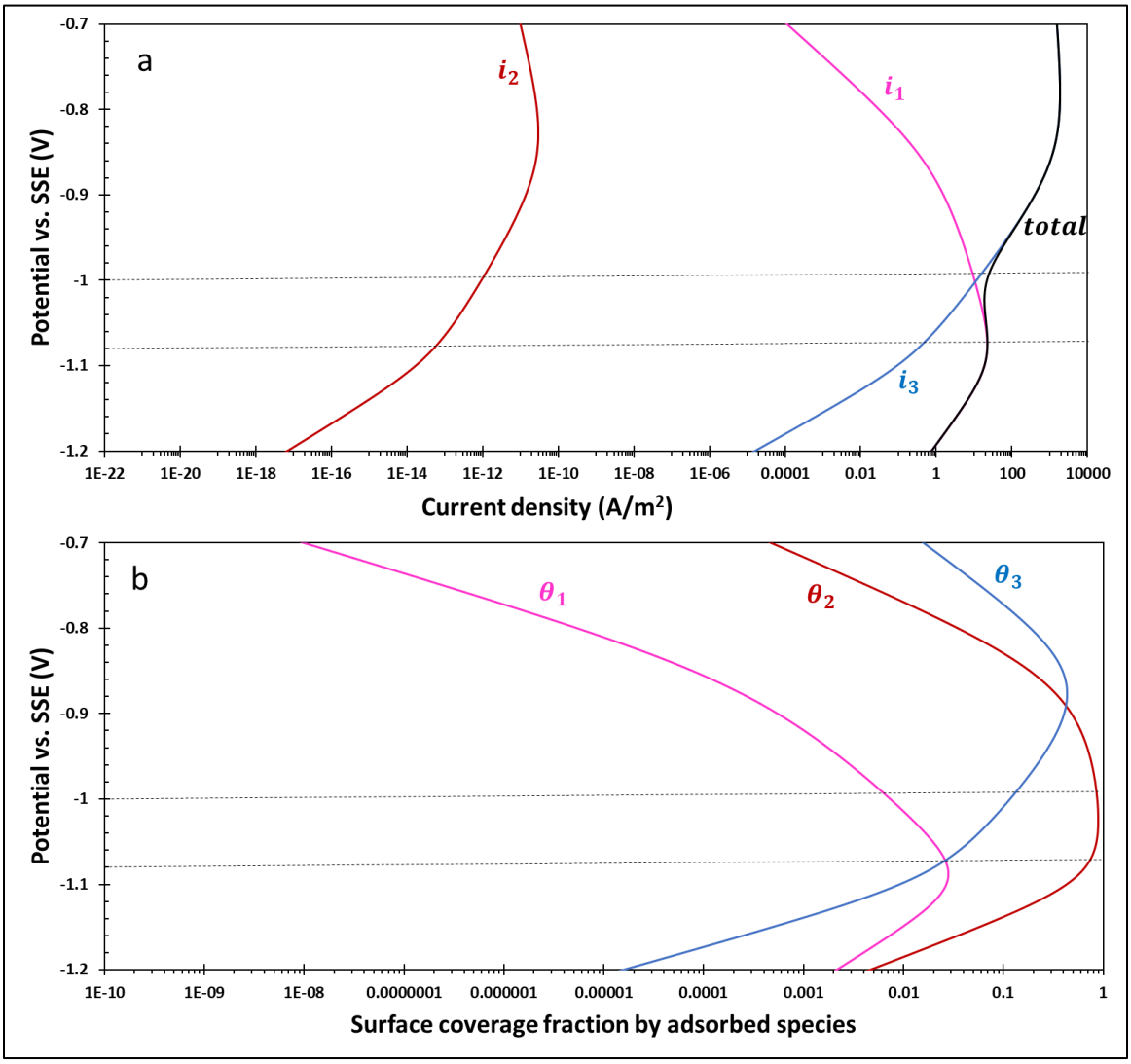

Figure 57

Reproduced data using Keddam, et al., multi-path mechanism and their reported kinetic constants at pH 5, 1 M Na_2SO_4, 1 bar Ar, 25 °C, 1600 rpm, iron RDE [6,7]*.a: Current density of each dissolutions path with respect to potential; b: surface coverage of the adsorbed intermediate species with respect to potential.*

This shows that the total current density in the active dissolution and transition regions is dominated by i_1, while there is a small contribution from i_2. The maximum current density in the transition region coincides with the maximum in θ_1 and θ_2 which are

covered by $Fe(I)_{ads}$ and $Fe(I)^{*}_{ads}$ respectively. The current density related to path 1 (i_1) is a direct function of coverage θ_1. Therefore, once at more positive potential, when θ_1 starts to decrease, then i_1 decreases as well. However, the question is why θ_1 starts to decrease?

Figure 55 shows the general scheme of the Keddam, *et al.,* multi-path mechanism. If only path 1 and path 2 exists, then θ_1 participates in both Reaction (84) and Reaction (85). Reaction (85) is at equilibrium in all potentials with the kinetic Equation (122) where kinetic constants are defined based on Equation (123) and Equation (124) [6].

$$\theta_1 k_3 = \theta_2 k_{-3} \tag{122}$$

$$k_3 = k_{0,3} \tag{123}$$

$$k_{-3} = k_{0,-3}\exp\left(-b_{-3}V\right) \tag{124}$$

Consequently, Figure 58 shows the change in k_3 and k_{-3} with respect to potential using the kinetic data reported by Keddam, *et al.*, [6,7]. Based on Figure 58 and Equation (122), k_3 is constant and independent of potential while it has a higher value compared to k_{-3}, which is decreasing with respect to potential. Meanwhile, as Reaction (83) proceeds rapidly, θ_1 keeps increasing with respect to potential. Therefore, since Reaction (85) must remain at equilibrium (Equation (122)), θ_2 starts to increase rapidly until it reaches in maximum close to unity. At this point Equation (122) is simplified to Equation (125). Because k_3 is constant and k_{-3} keeps decreasing as potential becomes more positive, consequently, to make Reaction (85) and Equation (125) remain in equilibrium, θ_1 starts to decrease rapidly.

$$\theta_1 k_3 \cong k_{-3} \tag{125}$$

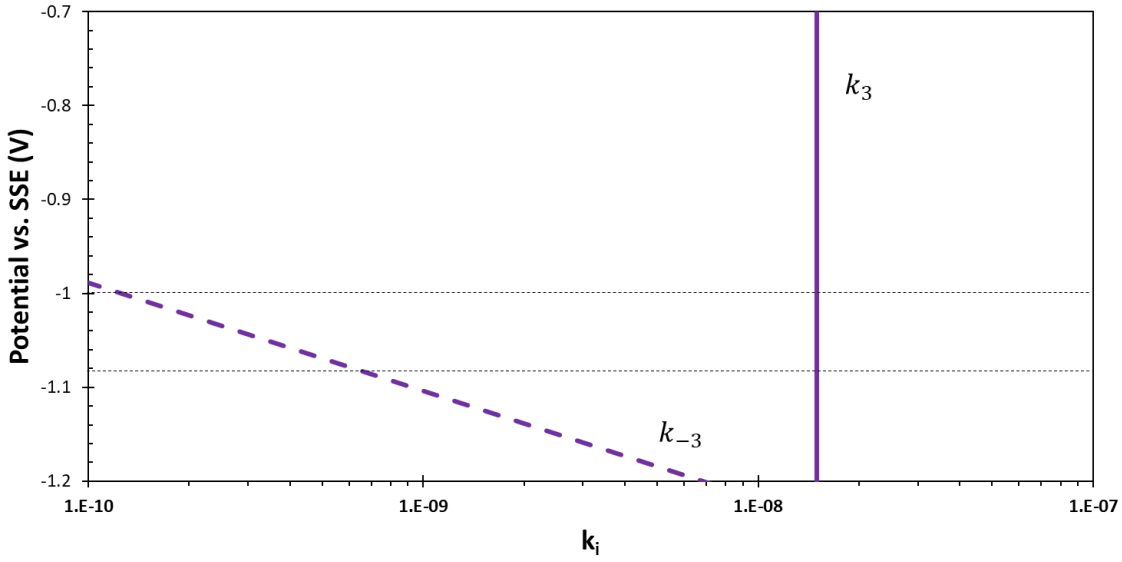

Figure 58

The change in kinetic parameters of Reaction (85) with respect to potential at pH 5.0, 1 M Na_2SO_4, 1 bar Ar, 25 °C, 1600 rpm, iron RDE [6,7]*. The black horizontal dotted lines represent the potential of the first maximum and minimum current densities of the anodic polarization sweep shown in Figure 57a.*

Summarizing the above argument, the S-shaped transition region discussed in the example above is related to significantly higher coverage of the iron surface by $Fe(I)^*_{ads}$ (θ_2) at more positive potential (transition region) compared to other adsorbed species especially $Fe(I)_{ads}$ (θ_1). This change in the surface coverage of the adsorbed species in this region is mainly related to the chemical Reaction (85) which remains in equilibrium as discussed in detail above. Moreover, the rate of electrochemical reaction dependent on the surface coverage of adsorbed $Fe(I)^*_{ads}$ (path 2) is lower compared to the rate of electrochemical reaction dependent on surface coverage of adsorbed $Fe(I)_{ads}$ (path 1) and $Fe(II)^*_{ads}$ (path 3). Consequently, as the surface coverage by $Fe(I)^*_{ads}$ reaches close to unity, the total current density starts to decrease due to the relatively smaller contribution

of the $i_1$and i_3 which are dependent on the surface coverage by $Fe(I)_{ads}$ and $Fe(II)^{*}_{ads}$ respectively. Consequently, the inhibitory effect of the adsorbed species related to θ_2 might not be related to its porous structure preventing the mass transfer across the metal surface as proposed in other studies[30,67]. This important question was revisited in the present study, and is described below.

E.3. Methodology[18]

Experiments were performed in a standard 1 L, three-electrode glass cell consisting of a rotating disk working electrode (RDE), an external saturated Ag/AgCl reference electrode connected to the electrolyte *via* a salt bridge and a Luggin capillary. The counter electrode was a graphite rod which was isolated in a separate glass chamber to avoid contaminating the main solution. The test solution was continuously sparged with CO_2 or N_2 gas one hour before initiation and during the experiments, to saturate the solution and purge any dissolved O_2. The pH of the test solution was adjusted to the desired pH using the reagents described in Table 11. The working electrode (WE) was made from pure iron in the shape of a disk with surface area of 0.198 cm^2. The pure iron disk electrode was press fitted to a Teflon sample holder to create a contact only between solution and base area of the sample. The working electrode was polished using silicon carbide abrasive papers 1200 grit. Following the surface preparation, the WE was cleaned with isopropyl alcohol in an ultrasonic bath and then dried with a N_2 gas stream[1].

---

[18] Some text in this section are taken from a publication of the author: Moradighadi, N., S. Nesic, and B. Tribollet, "Identifying the dominant electrochemical reaction in electrochemical impedance spectroscopy", *Electrochimica Acta* 400 (2021): p. 139460 (reference number [1]).

Before an experiment, OCP was monitored for at least 10 minutes to achieve a stable value and once the change in the OCP was about or less than 1 mV/s the experiment started. The solution resistance was measured using EIS once the WE was immersed into the solution or when the OCP reached to its stable value. If at the beginning of the experiments, bubbles were generated on the RDE sample (due to the sparged gas or the reduction of H^+), the WE was taken out and repolished and OCP was measured again before the experiments. The summary of the test conditions for the experiments is shown in Table 11.

To obtain the corrosion current density at open circuit potential, linear polarization resistance was performed by sweeping the working electrode 5 mV below and above the OCP, using a sweep rate of 0.125 mV/s. For EIS experiments depending on the required resolution at high frequency, the experiments were performed from 20 kHz or 10 kHz down to 2 ± 1 mHz. The AC potential was 8 mV (rms), and the data was acquired with an average of 10 ± 2 points per decade. In some cases, multiple anodic sweeps were performed in the same test solution considering that the anodic reaction depends on the electrode surface and pH of the solution, which did not change. An example showing the comparison between the tests performed in the same solution is shown in Appendix II.5 which indicate that the experiments were repeatable. However, per further discussion, it is understood that generally it is more favorable to perform each experiment in new test solution.

Table 11

Experimental condition.

Parameters	Value
Test apparatus	Rotating disk electrode
Electrode material	99.99 wt% pure iron
Temperature	25±0.5 ºC
Rotation rate	1600 rpm
Sweep rate	0.5 mV/s
Sulfate solution	
Sparge gas	1 bar N_2
pH	2.60±0.01, 4.00±0.01, and 5.00±0.01
Salt	0.3 M Na_2SO_4
Reagent for pH adjustment	H_2SO_4, NaOH
Chloride solution	
Sparge gas	1 bar N_2 or 1 bar CO_2
pH	4.00±0.01 and 5.00±0.01
Salt	0.5 M NaCl
Agent for pH adjustment	HCl, NaOH

E.4. Results and Discussion

E.4.1. Effect of Chloride Ion on the Anodic Dissolution of Iron in Strong Acid Solutions

Figure 59 shows the steady state polarization sweeps in strong acid sulfate solution at different pH values in comparison with data reported by Keddam, *et al.*[6]. At pH 2.6, the current density increases as potential becomes more positive, while the transition region (S-shaped region) is not observed. However, at pH 4.0 and 5.0, the transition region is clearly observed. Comparing the result with Keddam, *et al.*, [6] the polarization sweeps were relatively similar. The difference between the two sweeps might be due to slight differences between the WE materials, surface preparation, temperature and pH control, etc. In

addition, at pH 5.0, Keddam, *et al,.* used sodium acetate as a buffer for controlling the rapid change in pH during the polarization sweep, while in this work sodium acetate was not used.

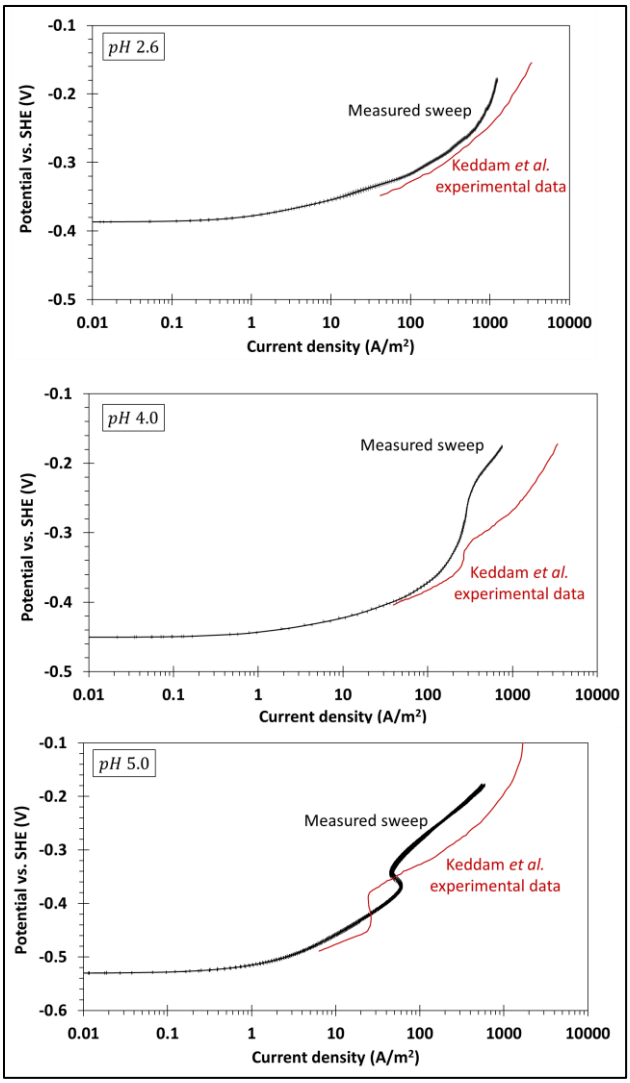

Figure 59

Comparison between experimental steady state polarization sweep obtained in this study and data reported by Keddam et al.[6] *Red colored sweeps were reconstructed from paper of Keddam et al.* [6] *Experimental parameters: sulfate strong acid solution, pure iron RDE, 1600 rpm, 25 °C, pH 2.6, 4.0 and 5.0.*

Years of study on the mechanism of iron dissolution in acidic environments showed that the role of anions such as halides, etc., is not only limited to being a supporting electrolyte, as they can participate in the reaction and change the electrochemical mechanism[70,72,74–77]. Figure 60 show the anodic potentiodynamic sweeps in strong acid chloride and sulfate solutions at pH 4.0. The current density decelerated in chloride solution compared to sulfate solution, especially in the transition and pre-passivation regions. Considering that the only variable in both solutions is the nature of the anions, originating from the added supporting electrolyte and the acid, consequently, the presence of different anions can be postulated to be the reason behind the acceleration or deceleration of the current density**.**

Based on studies reported in the literature, halide can participate in the anodic reaction by replacing OH^- on the iron surface through competitive adsorption[70,72,74,76–78,81]. Some studies illustrate that the adsorbed halide forms complexes with iron and participates along with anodic reactions governed by adsorbed hydroxide ion[70,74,76–78,81]. Therefore, the change in the current density in the presence of such complexes can be interpreted by the two scenarios explained below:

- The total current density depends on the contributions of the reactions that proceed in the presence of the intermediate species formed in the presence of adsorbed OH^- and the halide respectively. Moreover, studies suggest that the OH^- catalyzed reaction is faster, producing more current[70,74]. Consequently, once the OH^- intermediates are partially replaced by the halides intermediates, the current density decreases.

- A more general scenario is that the presence of anions such as sulfate and chloride change the nature of some complex adsorbates, except for $FeOH$ formed in the first step of the anodic reaction mechanism[43,75]. Therefore, the kinetic constants of the reaction might be different due to the change in the nature of the adsorbate leading to an acceleration or deceleration of anodic current density.

Elucidating the role of chloride on the mechanism of iron dissolution, experiments were performed at different DC potentials corresponding to the active dissolution, transition and pre-passivation regions of the anodic potentiodynamic sweeps in strong acid chloride and sulfate solutions marked by the alphabetic orders on the potentiodynamic sweeps shown in Figure 60.

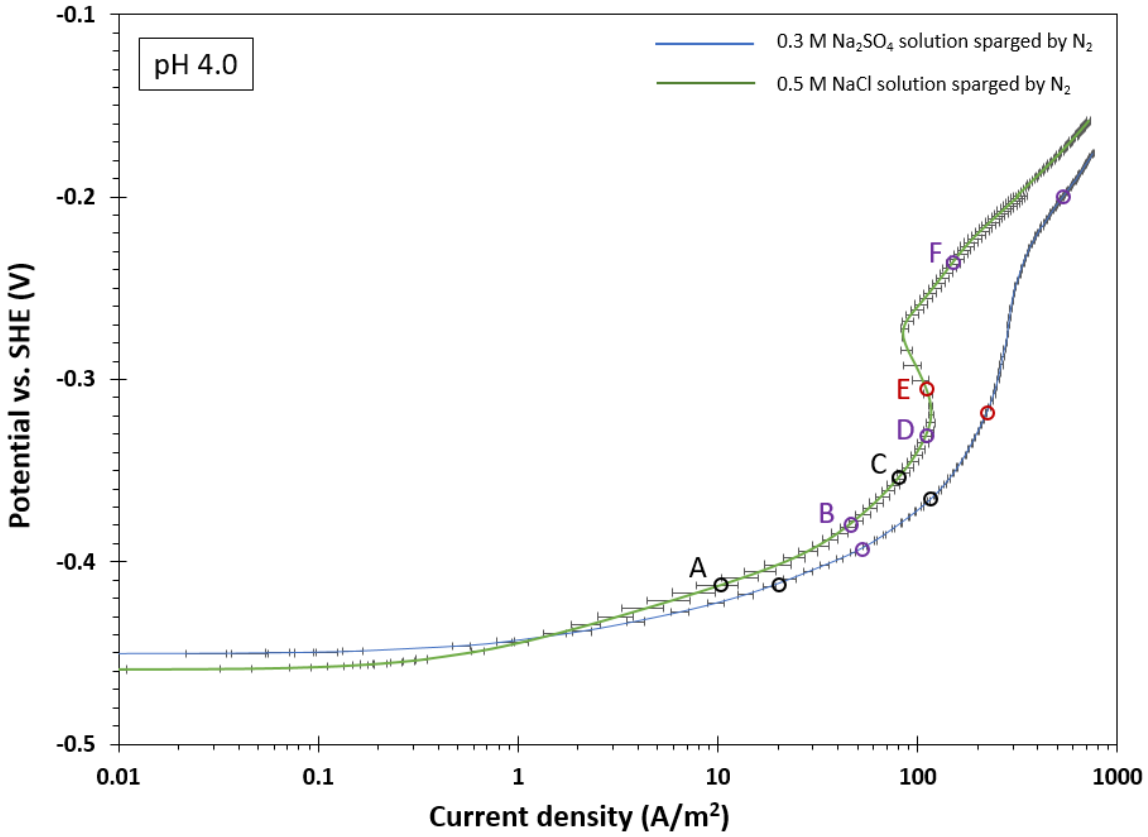

Figure 60

Comparison between the anodic steady state potentiodynamic sweep curves in strong acid chloride and sulfate solutions measured using a sweep rate of 0.5 mV/s, on pure iron RDE at 1600 rpm, corroding in an aqueous solution at pH 4.0 and 25°C. The alphabetic letters show the DC potential at which EIS measurements were conducted.[19]

Figure 61 shows the Nyquist plots obtained at the DC potentials (A) in the active dissolution of the potentiodynamic sweep at pH 4.0 (marked in Figure 60). In all the Nyquist plots shown in this study, the high frequency capacitive loop is assumed to be related to the double layer capacitance in parallel with charge transfer resistance. In the

[19] There are some uncertainties regarding the measured solution resistance in these experiments which were not fully resolved, due to raw data which could not be recovered.

active dissolution region, the two Nyquist plots in sulfate and chloride solutions show three loops at low frequency marked by letters *a*, *b* and *c*, which indicate the relaxation of three different adsorbed intermediate species involved in the anodic dissolution of iron. The first inductive loop (*a*) is always related to the adsorbed species $Fe(I)$ being $FeOH$ in the multi-path mechanism (refer to Figure 55)[6,7,43]. In addition, according to Keddam, *et al.,* the loop at the very low frequency is due to adsorbed hydrogen and will become negligible at higher current density (above 200 A/m^2). [6] However, in this study, conclusions regarding the exact nature of the loops *b* and *c*, and presence of adsorbed hydrogen at such high current density remains uncertain and requires further analysis.

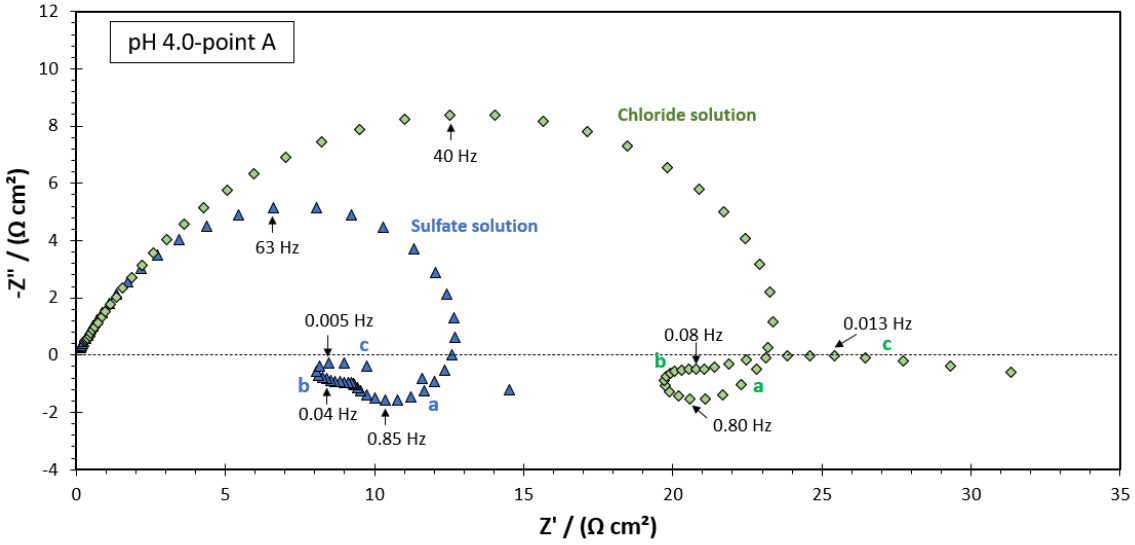

Figure 61

Nyquist plots at the DC potentials marked by letter A in the active dissolution region shown in Figure 60. Experimental parameters: 1 bar N_2, 0.3 M Na_2SO_4 and 0.5 M NaCl, pH 4.0, 25°C, pure iron RDE, 1600 rpm.

Figure 62 shows the Nyquist plot at point B of the potentiodynamic sweep marked in Figure 60. The Nyquist plots show similar behavior explained for the impedance data at point A, except that loop *b* in sulfate solution changed from an inductive loop at DC potential A (Figure 61) to a capacitive loop at DC potential B (Figure 62). Generally, both the inductive and capacitive loops *b* are related to the relaxation of the same species (as judged by the similar magnitude of the characteristic frequency related to the time constant of each loop[20]). However, due to the change in potential and kinetics of the reaction steps, the impedance response in terms of the Nyquist plot, can be either inductive or capacitive (for further information refer to the examples in Appendix II.4 or the literature [8]).

[20] Note that the characteristic frequency discussed in here is related to the time constant of an RC or RL circuit representing the loops generated from the relaxation of the adsorbed species. Therefore, this characteristic frequency is related to the approximate time constant of the relaxation of the adsorbed species.

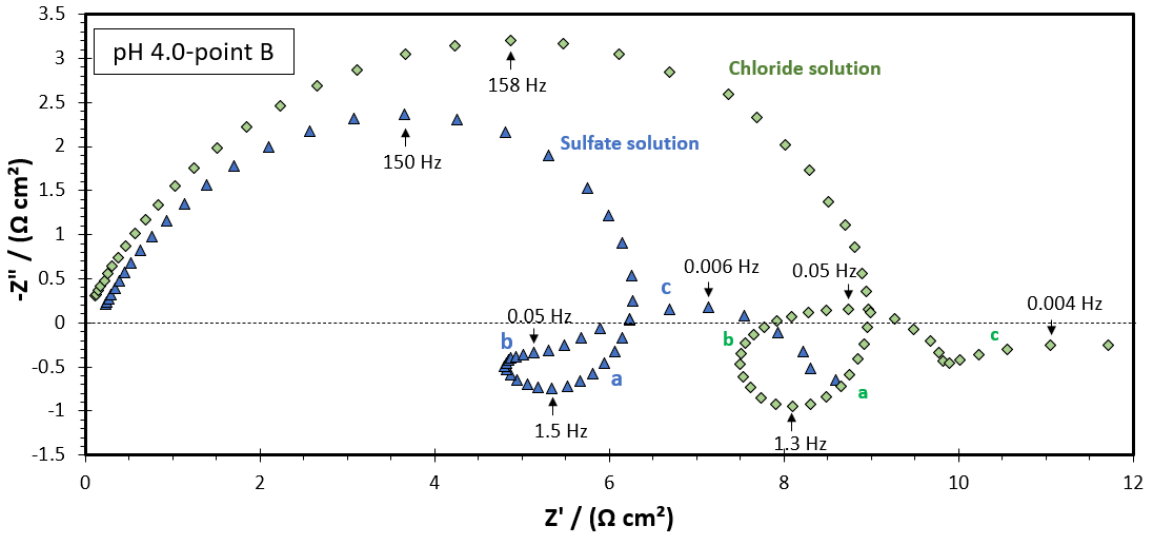

Figure 62

Nyquist plots at the DC potentials marked by letter B in the active dissolution region shown in Figure 60. Experimental parameters: 1 bar N_2, 0.3 M Na_2SO_4 and 0.5 M NaCl, pH 4.0, 25°C, pure iron RDE, 1600 rpm.

At more positive potential (point C), the Nyquist plot obtained in sulfate solution shows two loops *a* and *b* while loop *c* disappeared (Figure 63). As mentioned before, according to Keddam, *et al.,* the loop *c* at the very low frequency observed at DC potentials A and B might be attributed to the presence of adsorbed hydrogen which disappears at higher current density[6,7]. Moreover, in chloride solution three loops *a*, *b* and *c* were observed. Presence of the additional loop *c* in chloride solution might be due to two different possibilities:

1) The presence of hydrogen on the iron surface at DC potential C in chloride solution.

2) The presence of an additional adsorbate in chloride solution compared to the sulfate solution.

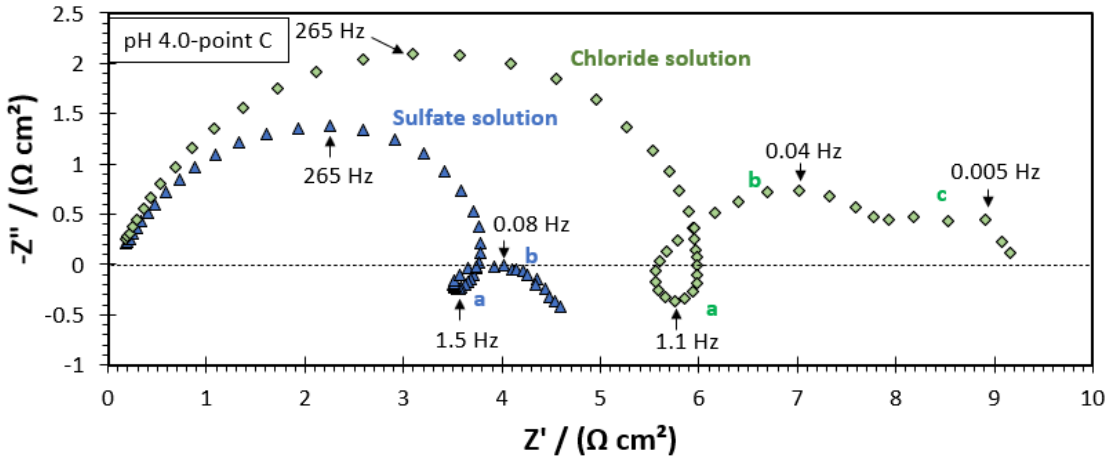

Figure 63

Nyquist plots at the DC potentials marked by letter C in the active dissolution region shown in Figure 60. Experimental parameters: 1 bar N_2, 0.3 M Na_2SO_4 and 0.5 M NaCl, pH 4.0, 25°C, pure iron RDE, 1600 rpm.

As observed in Figure 60, at more positive potentials, the transition region in the anodic dissolution sweeps is similar to an S-shaped curve. In chloride solution, the sweep in the transition region shows a negative slope. In other words, in this region, the polarization resistance must have a negative value. Figure 64 shows the Nyquist plot at the DC potential D (in the active dissolution region and near the first shoulder of the transition region), where at the very low frequency, the capacitive loop shows impedance data with negative real part. However, obtaining similar behavior on the Nyquist plot at the transition region cannot be always achieved, which will be discussed here.

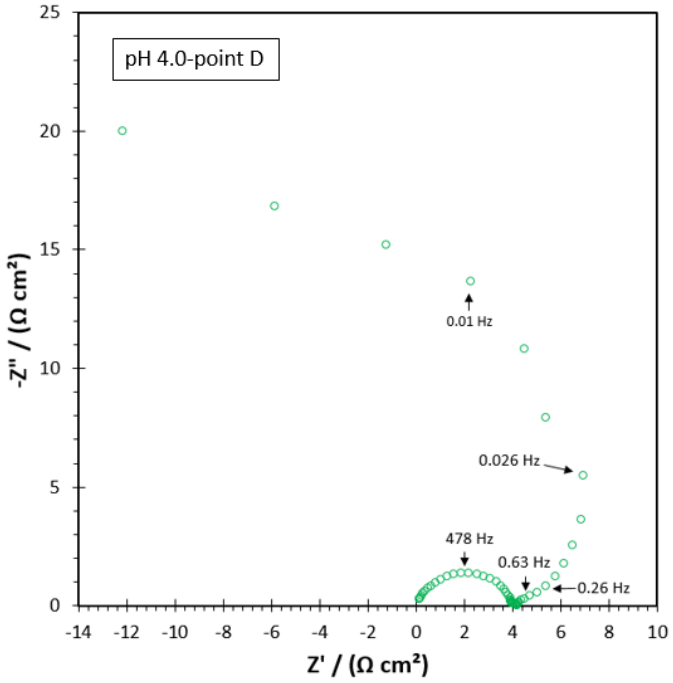

Figure 64

Nyquist plots at the DC potentials marked by letter D and E of the transition region shown in Figure 60. Experimental parameters: 1 bar N_2, 0.5 M NaCl, pH 4.0, 25°C, pure iron RDE, 1600 rpm.

EIS measurements were performed in strong acid chloride solution (pH 4.0), and at more positive potential in the transition region, marked by letter E in Figure 60. Figure 65 shows the obtain Nyquist plot. Despite a negative polarization resistance at this point (indicated by the negative slope of the potentiodynamic sweep at point E), the Nyquist plot at the same DC potential shows impedance data with positive real part at the very low frequency. A reason for not observing impedance data with a negative real part might be due to the difficulty in reproducing the exact potential where the DC current density is reversed (has a local maximum) and the small range where this reaction has a negative polarization resistance.

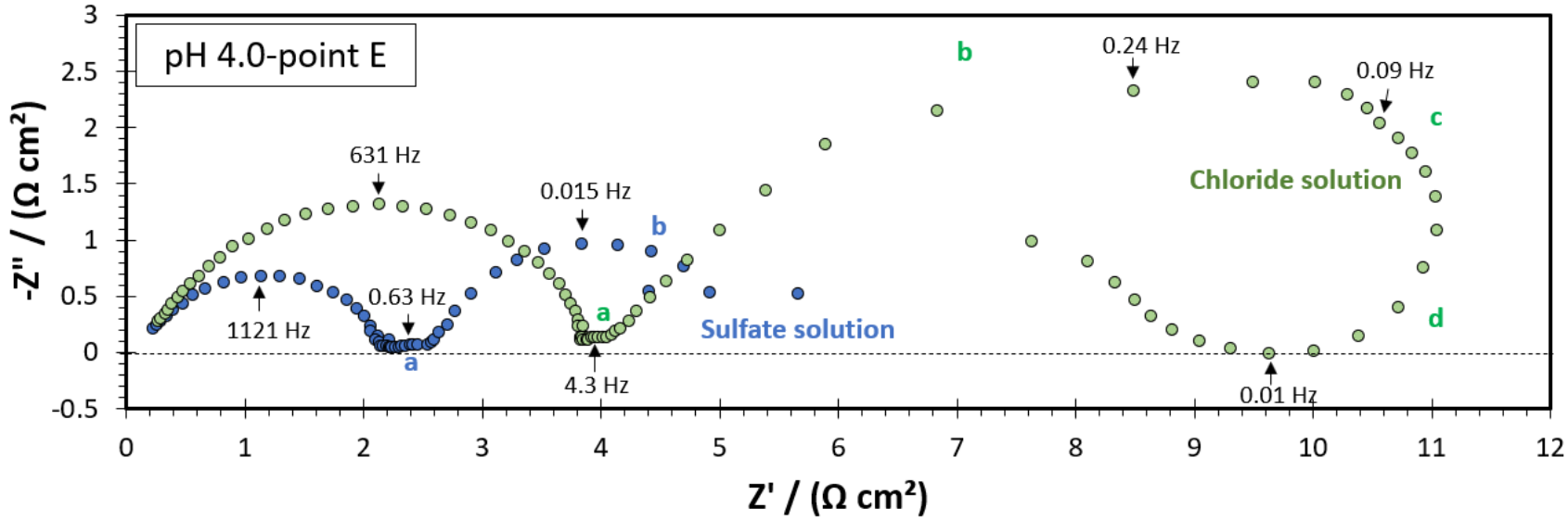

Figure 65

Nyquist plots at the DC potentials marked by letter E in the transition region shown in Figure 60. Experimental parameters: 1 bar N_2, 0.3 M Na_2SO_4 and 0.5 M NaCl, pH 4.0, 25°C, pure iron RDE, 1600 rpm.

Figure 66 shows the variation of the DC current density at different frequencies during the EIS measurements in potentiostatic mode. Generally, at the beginning of the experiment, when the potential is stepped from OCP to a specific DC potential, the steady state current is relatively higher and then decreases gradually. Because experiments were performed for a long time, at high potential and current density, there are variations in steady-state current density during the EIS measurements. This behavior was observed during EIS measurements in the active dissolution (point C and D), transition (point E), and pre-passivation (point F) regions shown in Figure 66. However, the extent of variation in steady state current density at point E in chloride solution (where the polarization resistance must be a negative value) is relatively more compared to other DC potentials in which the polarization resistance has a positive value. In fact, at this potential in the transition region there is an unusual negative polarization resistance, and the instability of the electrochemical process increases. Consequently, it becomes more difficult to measure a negative polarization resistance at a very low frequency during EIS measurements. In contrast, at DC potential E in sulfate solution where the slope of the steady state potentiodynamic sweep is positive, the DC current density is relatively more stable. This higher stability in DC current density was also observed in the experimental EIS data obtained in the active dissolution and pre-passivation region in the chloride solution where the polarization resistance has a positive value. One of the recommendations provided by Dr. Bernard Tribollet meant to remedy this problem, is to keep the sample in the desired DC potential to obtain a stable current density and only then run the EIS experiments. This

procedure might result in more consistent impedance data with negative polarization resistance in the transition region.

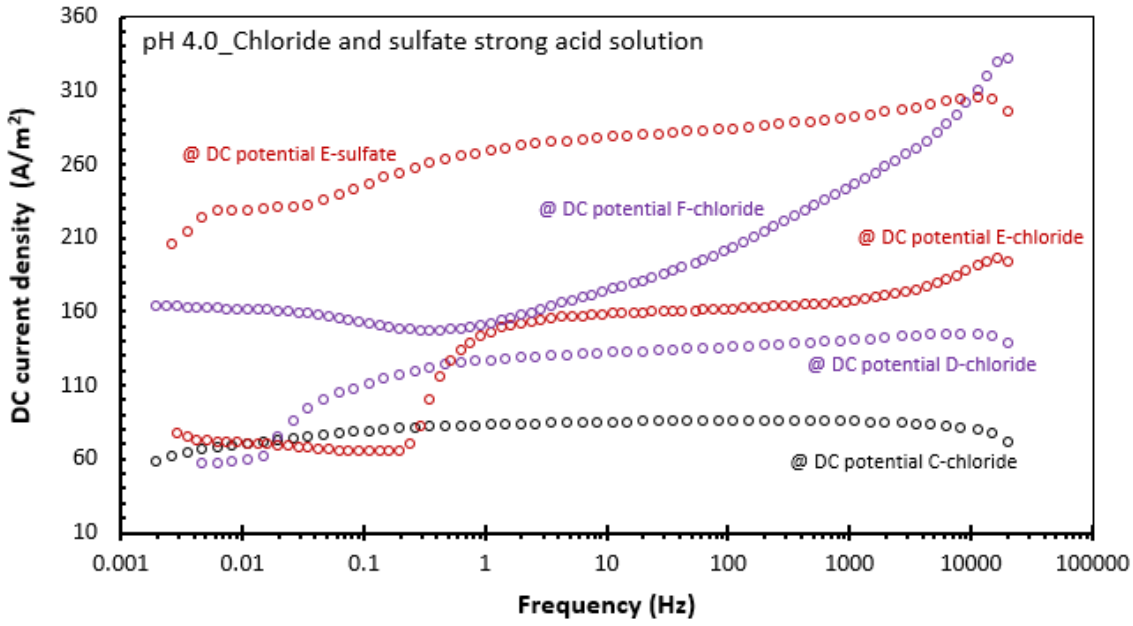

Figure 66

Variation of the steady state current density in strong acid chloride and sulfate solution and at the DC potential in the active dissolution (points C and D), transition (point E) and pre-passivation region (point F). Experimental parameters: 1 bar N_2, 0.3 M Na_2SO_4 and 0.5 M NaCl, pH 4.0, 25°C, pure iron RDE, 1600 rpm.

Figure 65 shows the Nyquist plot in the transition region of the potentiodynamic sweep marked by the letter E in Figure 60. The Nyquist plot related to sulfate solution shows two loops *a* and *b* at low frequency which according to Keddam, *et al.,* might be related to the adsorbed species $Fe(I)$ and $Fe(I)^*$ participating in path 1 and 2 of the multi-path mechanism (refer to Figure 55)[6,7]. However, the Nyquist plot in chloride solution

shows four loops (*a*, *b*, *c* and *d*). The low frequency inductive loops *d* observed in chloride solutions corresponds to the adsorbed $Fe(II)^*$ which is related to the pre-passivation region or path 3 of the multi-path mechanism. However, the inductive loop related to $Fe(II)^*$ was not observed in the Nyquist plot related to the sulfate solution. In fact, the steady state potentiodynamic sweep shown in Figure 60 shows a larger transition region in sulfate solution compared to chloride solution. Therefore, in sulfate solution, the pre-passivation region begins at a relatively more positive potential than the DC potential E. Consequently, the recorded impedance response does not provide information about the relaxation of $Fe(II)^*$.

Following the above discussion, excluding the low frequency inductive loop related to $Fe(II)^*$, the Nyquist plot in the transition region shows one additional loop in chloride solution, indicating that there is one additional adsorbed intermediate species participating in the anodic reaction in strong acid chloride solution compared to the sulfate solution.

Figure 67 shows the Nyquist plots at point F in the pre-passivation region of the potentiodynamic sweep in strong acid chloride and sulfate solution at pH 4.0. In both chloride and sulfate solutions, loop "*a*" (related to adsorbate $Fe(I)$) disappeared. Moreover, although in the transition region loops *b* and *c* in chloride solution were barely distinguished from each other (Figure 65), the two loops got decoupled clearly at more positive potential in the pre-passivation region. Comparing the two Nyquist plots, there is one additional loop in chloride solution compared to the sulfate solution, indicating that there is one additional adsorbed intermediate species in the presence of chloride.

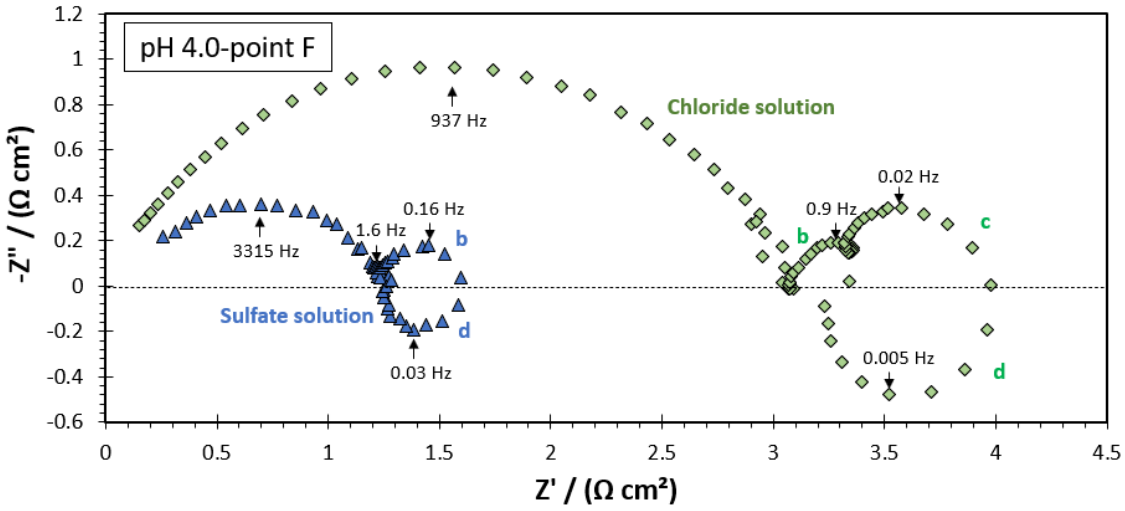

Figure 67

Nyquist plots at the DC potentials marked by letter F in the pre-passivation region shown in Figure 60. Experimental parameters: 1 bar N_2, 0.3 M Na_2SO_4 and 0.5 M NaCl, pH 4.0, 25°C, pure iron RDE, 1600 rpm.

The mechanism proposed by Keddam, *et al.*,[6,7] consisting of three paths, each involving a distinct adsorbed intermediate species playing a key role in the different potential regions was confirmed in this study, as similar behavior was observed in sulfate solution, while in chloride solution, the impedance data showed the presence of an additional adsorbed species involved in the mechanism of the anodic reaction. This conclusion was further investigated by analyzing the impedance response of anodic reaction at pH 5.0 which is discussed below.

Figure 68 show the anodic potentiodynamic sweeps in strong acid sulfate and chloride solution at pH 5.0. Similarly to the sweeps at pH 4.0, the anodic current density decelerated mainly in the transition and pre-passivation regions. Figure 69 shows the Nyquist plot obtained in the active dissolution of the anodic potentiodynamic sweep at DC

potential A. The Nyquist plot is very similar to the graph obtained at pH 4.0 at point C (Figure 63) where there is an additional loop observed in chloride solution compared to sulfate solution.

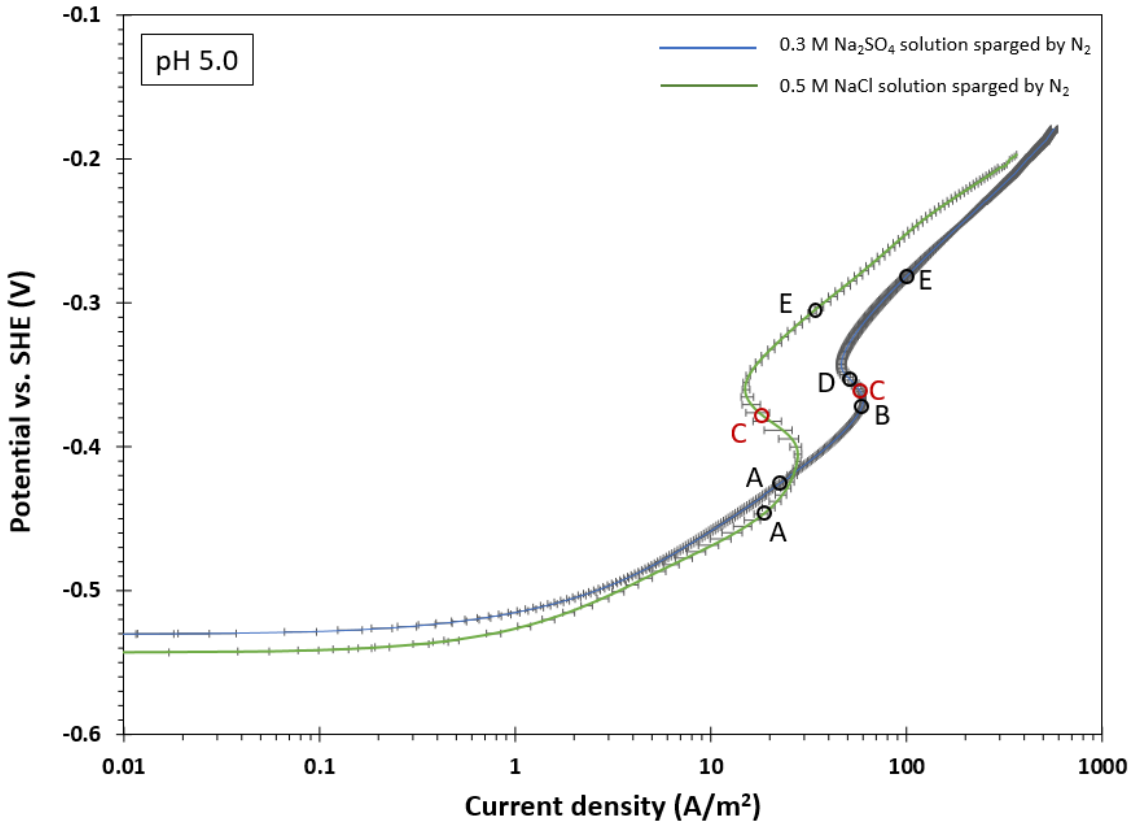

Figure 68

Comparison between the anodic steady state potentiodynamic sweep curves in strong acid chloride and sulfate solutions measured using a sweep rate of 0.5 mV/s, on pure iron RDE at 1600 rpm, corroding in an aqueous solution at pH 5.0 and 25°C. The alphabetic letters show the DC potential at which EIS measurements were conducted.[21]

[21] There are some uncertainties regarding the measured solution resistance in these experiments which were not fully resolved, due to raw data which could not be recovered.

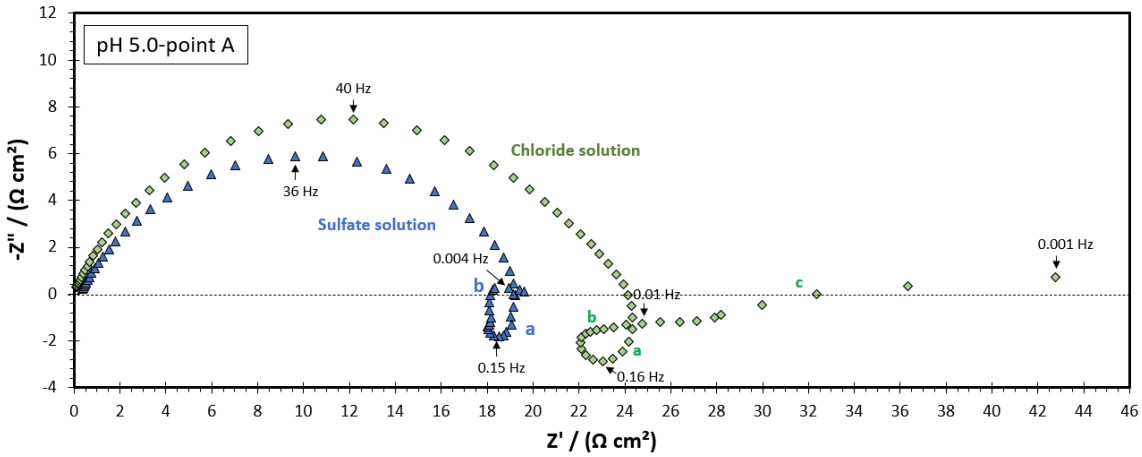

Figure 69

Nyquist plots at the DC potentials marked by letter A in the active dissolution region shown in Figure 68. Experimental parameters: 1 bar N_2, 0.3 M Na_2SO_4 and 0.5 M NaCl, pH 5.0, 25°C, pure iron RDE, 1600 rpm.

Figure 70 shows the Nyquist plots at DC potentials B, C and D marked in the transition region of iron anodic potentiodynamic sweep in strong acid sulfate solutions at pH 5.0 shown in Figure 68. Based on the steady state potentiodynamic sweep shown in Figure 68, there is a negative polarization resistance in the transition region. The Nyquist plot at point B, which is very close to the current maximum of the transition region, clearly shows a capacitive loop with the data point having a negative real part at the very low frequency. However, at more positive DC potential (point C and D), the impedance data at very low frequencies have a positive real part. The Nyquist plot at point C shows an inductive loop, and the measured polarization resistance has a positive value (indicated by the cross-section of the inductive loop with the real axis at the very low frequencies). Meanwhile, at DC potential D, the Nyquist plot shows two capacitive loops at low frequency. These results are very similar to the Nyquist plots obtained in chloride solution at pH 4.0 and at the transition region (see Figure 60, Figure 64 and Figure 65). As explained

in pages 150 and 151 of this document, the measurements of the impedance data in a potential range where the polarization resistance has a negative value is very difficult and sensitive to the instability of the DC current density, which is shown in Figure 71. Therefore, measuring the impedance data with negative polarization resistance cannot always be achieved.

Moreover, the impedance response related to the relaxation of an adsorbate can be an inductive or capacitive response, depending on the potential and kinetics of the reaction steps. Regardless of the shape of the low frequency loops obtained at point B, C and D (Figure 70) all the Nyquist plots clearly show two loops at low frequency (loop *b* and *c*). The Inductive loop *a* (related to adsorption of $Fe(I)$) observed in the active dissolution region at DC potential A (Figure 69), has disappeared in the Nyquist plot in the transition region while loops *b* and *d* are related to the adsorbed species $Fe(I)^*$ and $Fe(II)^*$ involved in path 2 and 3 of the multi-path mechanism.

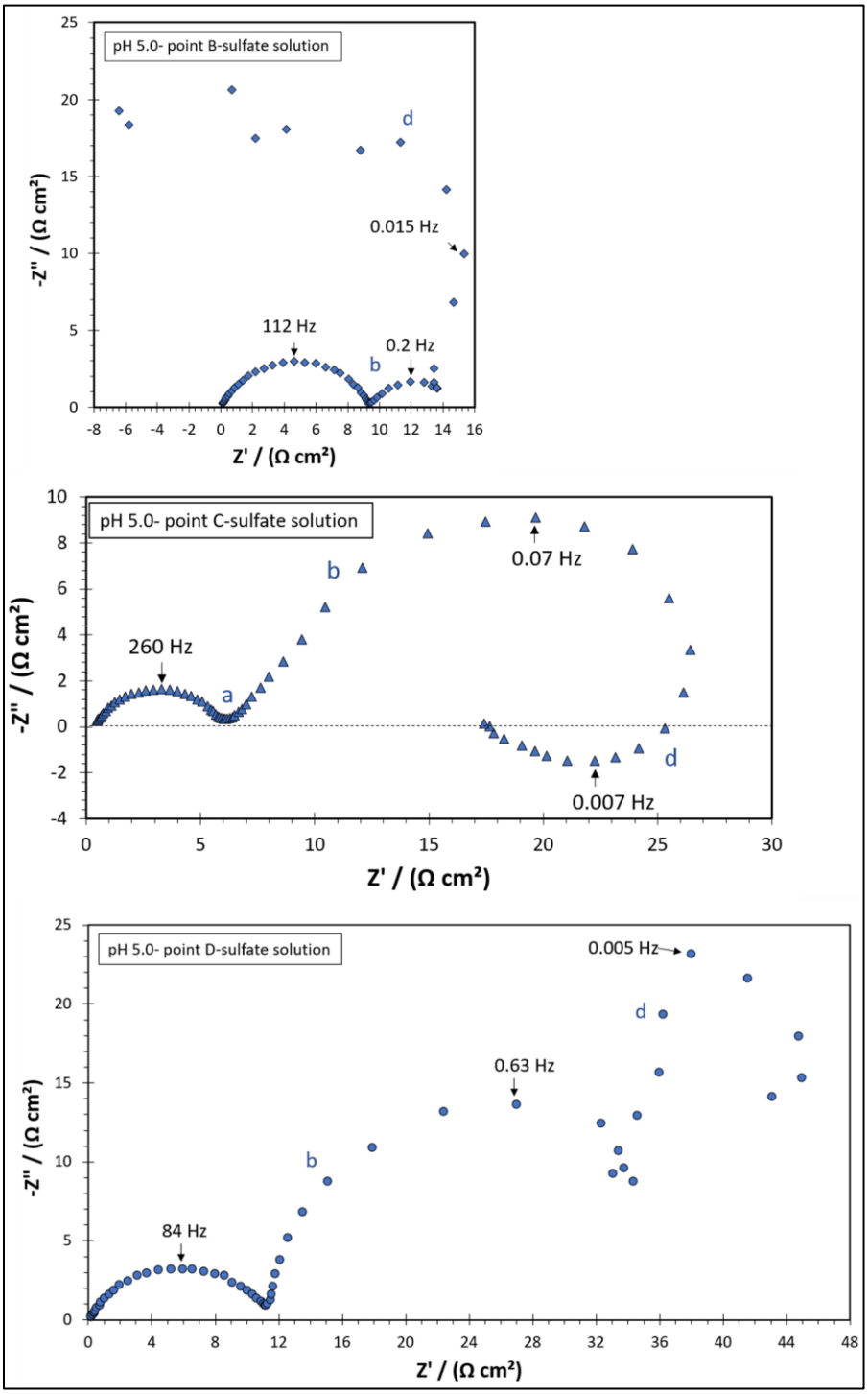

Figure 70

Nyquist plots at the DC potentials marked by letter B, C and D at the region close to the current maximum and the transition region shown in Figure 68. Experimental parameters: 1 bar N_2, 0.3 M Na_2SO_4, pH 5.0, 25°C, pure iron RDE, 1600 rpm.

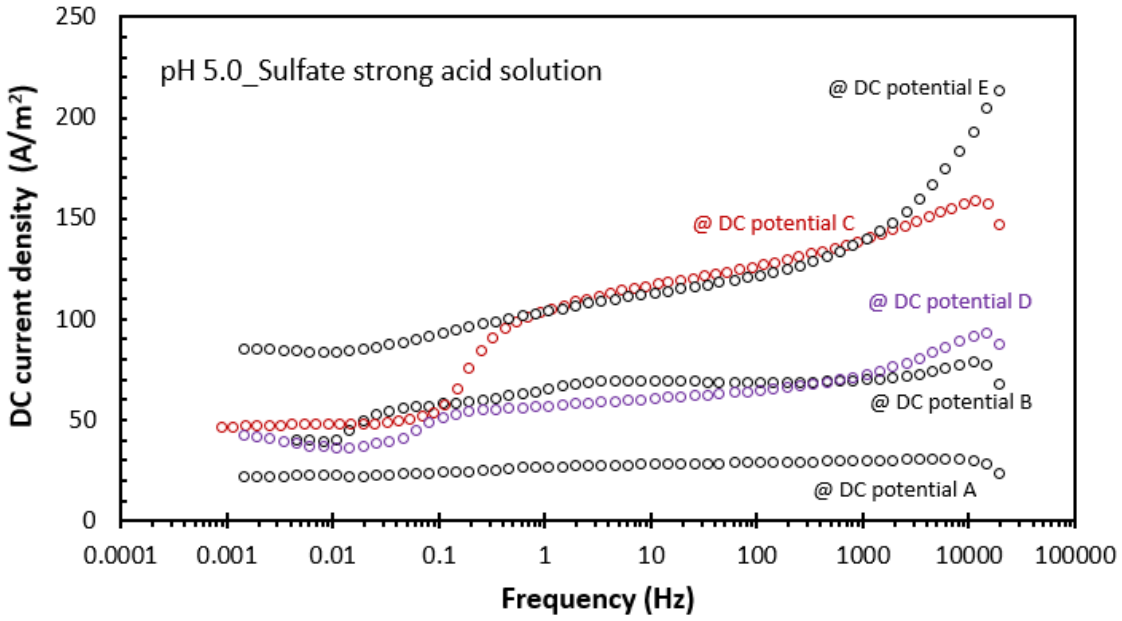

Figure 71

Variation of the steady state current density in sulfate strong acid solution and at the DC potential in the active dissolution (points A and B), transition (points C and D) and pre-passivation region (point E). Experimental parameters: 1 bar N_2, 0.3 M Na_2SO_4, pH 5.0, 25°C, pure iron RDE, 1600 rpm.

Figure 72 shows the impedance response of iron dissolution in strong acid chloride solution at pH 5.0. The impedance response related to $Fe(I)$ is observed at the region *a* which is dissimilar to a capacitive loop. In fact, in this frequency range, there is a transition from an inductive loop observed in the active dissolution region (loop *a* in Figure 69) to a capacitive loop in the transition region (Figure 72)[22]. Once there is such a transformation, there are some frequency ranges in which the corresponding loop almost collapses or

[22] Due to the change in potential and kinetics of the reaction steps, the impedance response in terms of the Nyquist plot, can be either inductive or capacitive (for further information refer to the examples in Appendix II.4 or the literature [8]).

disappears. Therefore, the shape of the impedance response in the region marked by letter *a* in Figure 72 is not very clear.

In addition, the Nyquist plot obtained in chloride solution (Figure 72) shows two loops *b* and *d* at lower frequency. Although the Nyquist plots obtained at pH 5.0 in sulfate and chloride solutions show similar number of loops (except for loop *a* which is hard to observe in both cases), but this similarity might not be related to the same number of adsorbed species. In fact, loop *b* in the chloride solution, might be related to two adsorbate species for which their relaxation happens in the similar frequency range. This point is further discussed, below using experimental data at more positive potential.

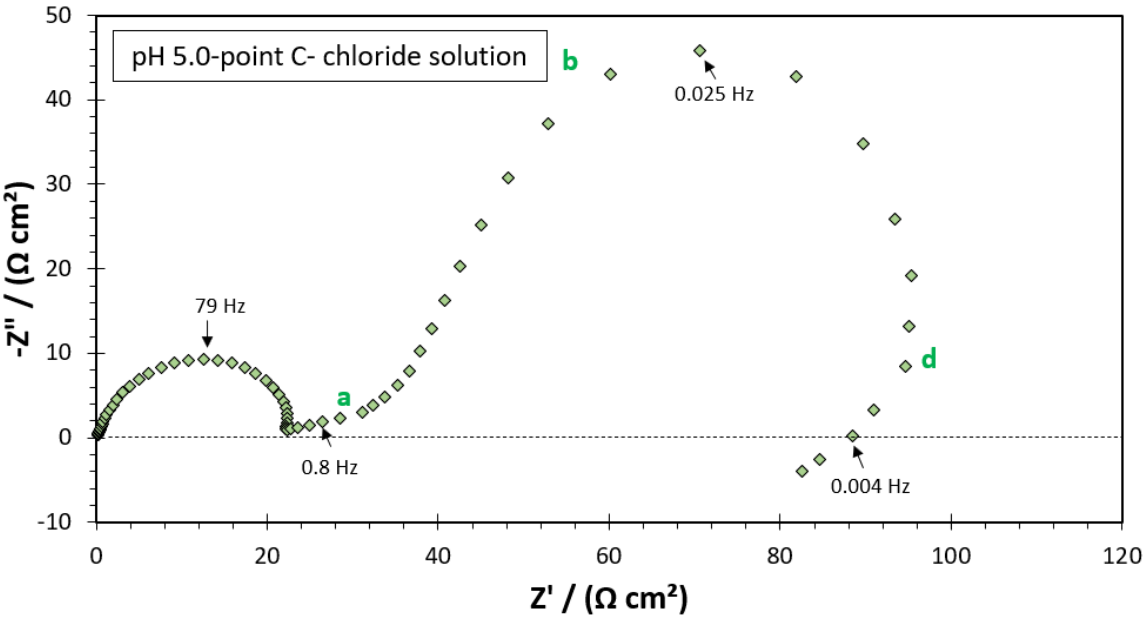

Figure 72

Nyquist plots at the DC potentials marked by letter C in the transition region shown in Figure 68. Experimental parameters: 1 bar N_2, 0.5 M NaCl, pH 5.0, 25°C, pure iron RDE, 1600 rpm.

Figure 73 shows the impedance response of iron dissolution in the pre-passivation region at pH 5.0 and in strong acid sulfate solution (refer to Figure 68). The Nyquist plot shows three loops at low frequency. In order to understand the role of each loop, comparisons between the experimental data at different DC potentials and pHs are required, which is discussed below.

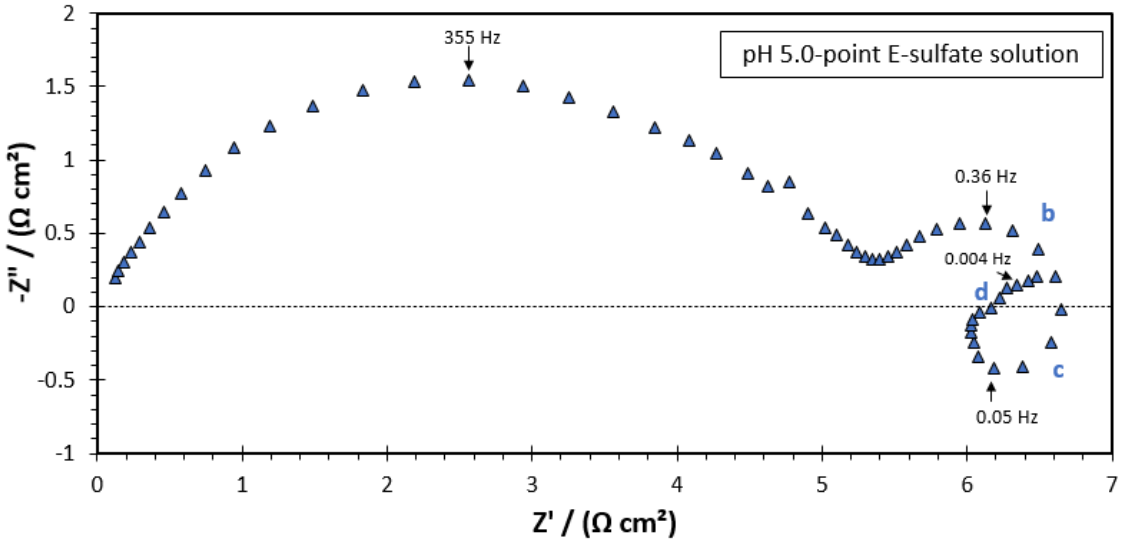

Figure 73

Nyquist plots at the DC potentials marked by letter E in the pre-passivation region shown in Figure 68. Experimental parameters: 1 bar N_2, 0.3 M Na_2SO_4, pH 5.0, 25°C, pure iron RDE, 1600 rpm.

Comparison of the Nyquist plots in the pre-passivation region and transition regions at pH 5.0 and in strong acid sulfate solution is shown in Figure 74. Loops *b* and *c*, related to $Fe(I)^*$ and $Fe(II)^*$, respectively, shrank as potential changed from the transition region to pre-passivation region. The same behavior was observed for loop *b* in sulfate solution at pH 4.0 (compare loop *b* in Figure 65 and Figure 67).

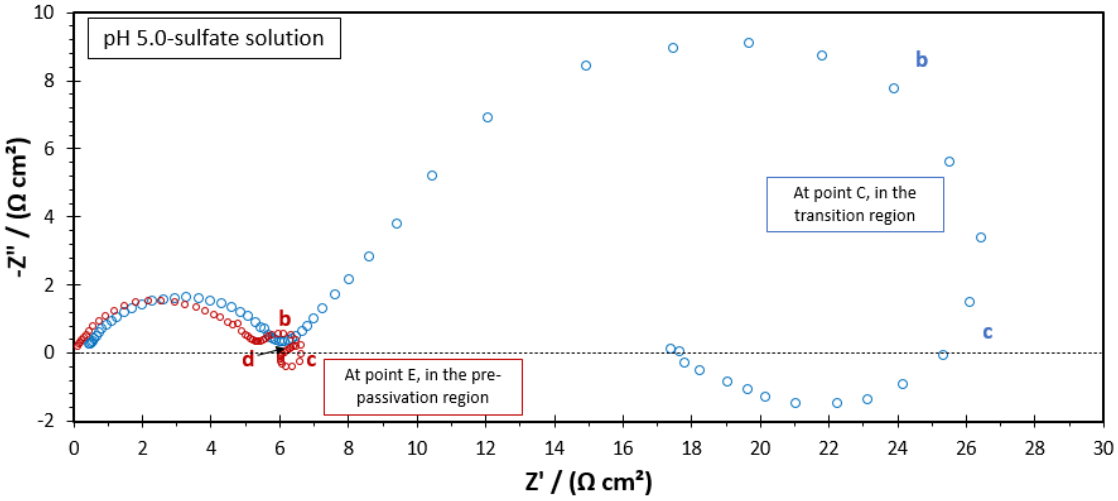

Figure 74

Comparison between Nyquist plots obtained in the transition and pre-passivation regions at the DC potentials marked by letter C and E in Figure 68. Experimental parameters: 1 bar N_2, 0.3 M Na_2SO_4, pH 5.0, 25°C, pure iron RDE, 1600 rpm.

Moreover, as shown in Figure 75, at pH 5.0 and in strong acid sulfate solution, in the pre-passivation region an additional loop is observed at very low frequencies (loop *d*) compared to the Nyquist plot obtained at pH 4.0 in the pre-passivation region. Loop *d* at pH 5.0 might be related to $Fe(II)$ which is the species responsible for the passivation of the iron. This loop was not observed at pH 4.0, as the passivation regions might begin at relatively more positive potential compared to pH 5.0.

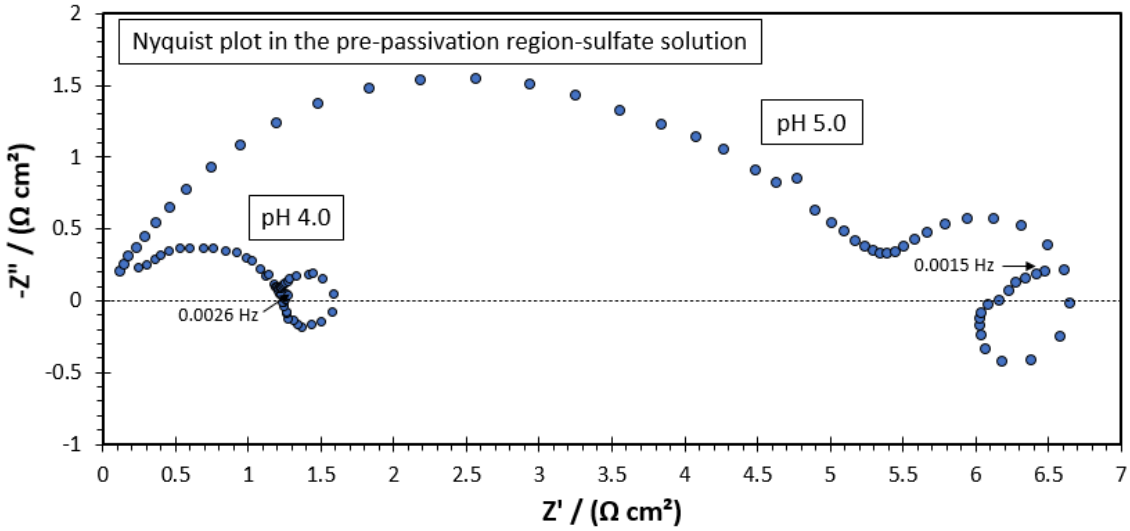

Figure 75

Comparison between Nyquist plots obtained in the pre-passivation regions at pH 4.0 and 5.0. Experimental parameters: 1 bar N_2, 0.3 M Na_2SO_4, 25°C, pure iron RDE, 1600 rpm.

Figure 76 shows the Nyquist plot in pre-passivation regions at pH 5.0 in strong acid sulfate and chloride solutions. A similar number of loops were observed in both solutions, but this similarity might not be related to the same adsorbed species which is described below.

As mentioned above, in the Nyquist plot obtained in the transition region and in chloride solution (shown in Figure 72), loop *b* might be related to relaxation of two adsorbed species when their relaxation happens in the similar frequency range. However, at more positive potential and higher current density, due to the change in the characteristic frequency of the relaxation of the two adsorbed species, the two loops separate as shown by loops *b* and *c* in the pre-passivation (shown in Figure 76). In conclusion, in chloride solution, the Nyquist plot in the pre-passivation regions shows three loops. Loop *b* and *c*

are related to $Fe(I)^*$, and an additional species formed in the presence of chloride. Loop *d* is related to $Fe(II)^*$. In sulfate solution the same number of loops are observed. Loops *b*, *c*, and d are related to $Fe(I)^*$, $Fe(II)^*$ and $Fe(II)$, respectively, as discussed in detail above. Therefore, although in both sulfate and chloride solutions the Nyquist plots showed similar number of loops, further analysis showed that there is one additional adsorbed species in chloride solution compared to sulfate solution.

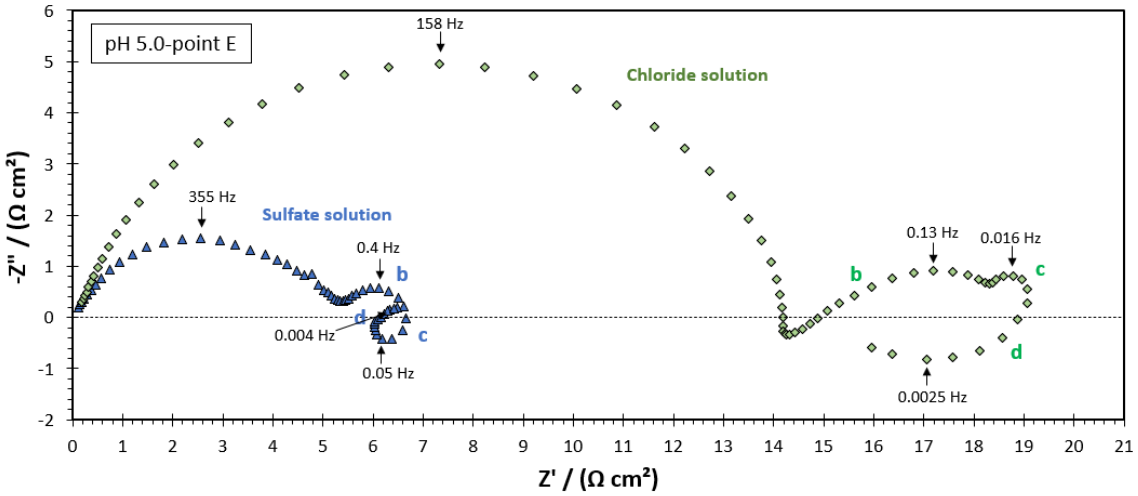

Figure 76

Nyquist plots at the DC potentials marked by letter E in pre-passivation region shown in Figure 68. Experimental parameters: 1 bar N_2, 0.3 M Na_2SO_4 and 0.5 M NaCl, pH 5.0, 25°C, pure iron RDE, 1600 rpm.

The experimental EIS data obtained at different potentials in the sulfate and chloride strong acidic solutions showed that there is one additional adsorbed species in chloride solution involved in the anodic reaction. In the study performed by Keddam, *et al.*[6,7], experimental EIS data in strong acid sulfate solution showed that there are mainly

three adsorbed intermediate species (excluding the species formed at very positive potential related to passivation of iron). Therefore, they have proposed the multi-path mechanism in which there are three parallel dissolution paths.

The current study showed that in strong acid chloride solution there is one additional loop corresponding to one additional adsorbed intermediate species. Consequently, it is required to add an additional path to the multi-path mechanism in order to justify the behavior of the anodic dissolution of iron in chloride strong acid solution.

Reactions (126)-(128) shows a proposed mechanism for iron dissolution at low potential in the presence of acidic chloride solution [79]. MacFarlane and Smedley simplified this mechanism to Reaction (129) and Reaction (130) in which $Fe(I)^{1}_{ads}$ is $[FeClOH]^{-}{}_{ads}$. The author considered path 1 and path 2 of the multi-path mechanism along with Reactions (129) and (130) to justify the impedance response of iron dissolution in strong acid chloride solution. In the first step (129), $[FeClOH]^{-}{}_{ads}$ is formed, however, Keddam et al. showed that always in first step there is formation of $FeOH$ to justify the impedance response of iron dissolution[43]. Therefore, in this study, the Reactions (126)-(130) is modified into two different mechanism and the possibility of each mechanism is discussed below.

$$Fe + OH^- + Cl^- \rightleftarrows [FeClOH]^{-}{}_{ads} + e^- \quad [23] \qquad (126)$$

$$[FeClOH]^{-}{}_{ads} \rightarrow FeClOH + e^- \qquad (127)$$

$$FeClOH + H^+ \rightleftarrows Fe^{2+} + Cl^- + H_2O \qquad (128)$$

---

[23] The Reaction (126) is a different representation of the reaction shown below as reported in the literature[79].
$Fe.H_2O + Cl^- \rightleftarrows [FeClOH]^{-}{}_{ads} + H^+ + e^-$

$$Fe \rightleftarrows Fe(I)^{1}_{ads} + e^{-} \qquad (129)$$

$$Fe(I)^{1}_{ads} \rightarrow Fe(II)_{sol} + e^{-} \qquad (130)$$

Mechanism (I), which includes Reactions (131)-(134), shows that in the first step there is formation of $FeOH$ which in the second step reacts with Cl^{-}, and forms the adsorbed intermediate $[FeClOH]^{-}{}_{ads}$. Therefore, presence of the intermediate $[FeClOH]^{-}{}_{ads}$ always depends on the presence of $FeOH$. However, the EIS experimental data in the pre-passivation region ,shown in Figure 67 and Figure 76, indicate that loop *a* related to the adsorbed intermediate $FeOH$ disappeared, but still adsorbed intermediate $[FeClOH]^{-}{}_{ads}$ exist on the iron surface (indicated by loop *b* or *c*). Therefore, mechanism (I) might not justify the EIS experimental data.

Mechanism (I):

$$Fe + OH^{-} \rightarrow FeOH + e^{-} \qquad (131)$$

$$FeOH + Cl^{-} \rightleftarrows [FeClOH]^{-}{}_{ads} \qquad (132)$$

$$[FeClOH]^{-}{}_{ads} \rightarrow FeClOH + e^{-} \qquad (133)$$

$$FeClOH + H^{+} \rightleftarrows Fe^{2+} + Cl^{-} + H_2O \qquad (134)$$

In mechanism (II), which includes Reactions (135)-(137), the $[FeClOH]^{-}{}_{ads}$ is a catalyst formed by the reaction between $FeOH$ and Cl^{-}. Once the catalyst is formed, it will be both consumed and produced by Reaction (137). Therefore, its presence does not always depend on the presence of $FeOH$. This possible behavior can justify the impedance data related to the pre-passivation region (Figure 67 and Figure 76), in which the intermediate species $[FeClOH]^{-}{}_{ads}$ exists on the iron surface (indicated by loops *b* or *c*) while loop *a* related to the adsorbed intermediate $FeOH$ disappeared.

Mechanism II:

$$Fe + OH^- \rightarrow FeOH + e^- \quad (135)$$

$$FeOH + Cl^- \rightleftarrows [FeClOH]^-_{ads} \quad (136)$$

$$Fe + FeClOH^- + OH^- \rightarrow FeOH^+ + FeClOH^- + 2e^- \quad (137)$$

Considering mechanism II, the revised version of the multi-path mechanism for acidic chloride solutions is shown in Figure 77. Paths 1-3 are similar to the original multi-path mechanism including the OH^- intermediates species . Path 4 is related to mechanism II described above in which the additional adsorbed intermediate species ($Fe(I)^{**}_{ads}$ or $[FeClOH]^-_{ads}$) participating in the anodic dissolution of iron. Moreover, detecting the exact chemical structure of the adsorbates in the revised version of the multi-path mechanism is outside the scope of this work. in the chloride strong acid solution once the OH^- intermediates are partially replaced by $Fe(I)^{**}_{ads}$ (due to the competitive adsorption between Cl^- and OH^-), consequently the current density decreases. One should allow for the possibility that the presence of anions such as chloride might change the nature of some of the complex adsorbates, except for $FeOH$ which is formed in the first step of the anodic reaction mechanism[6,7,43]. Consequently, the kinetic constants of the reaction steps might be different in the presence of Cl^- leading to a deceleration of anodic current density in chloride solutions compared to sulfate solutions.

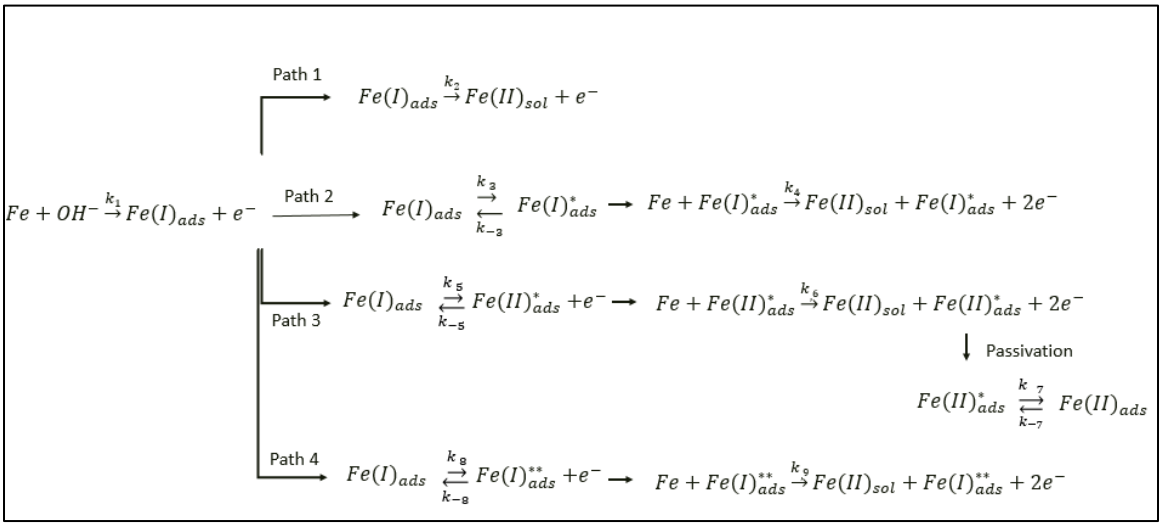

Figure 77

Revised version of multi-path mechanism for acidic chloride solution.

E.4.2. Mechanism of Anodic Dissolution of Iron in Aqueous CO_2 Environment

In section E.4.1, the effect of Cl^- on the mechanism of iron dissolution was investigated. It was shown that in strong acid chloride solution, there is an additional intermediate adsorbed species adsorbed compared to strong acid sulfate solution. It can also be postulated that the presence of chloride to change the chemical composition of the remaining intermediate species and, consequently, its presence can change the kinetic constants of the reaction steps. This study was extended to investigate the mechanism of the iron dissolution in an aqueous CO_2 environment. Once CO_2 dissolves in aqueous solution, it produces carbonic acid which dissociates into HCO_3^- and CO_3^{2-} which might influence the mechanism and kinetics of anodic dissolution of iron.

Figure 78 shows two steady state anodic potentiodynamic sweeps in chloride solutions at pH 4.0 which were sparged with 1 bar N_2 (strong acid solution) and 1 bar CO_2

(weak acid solution) respectively. The rate of anodic dissolution of iron was increased in aqueous CO_2 environments compared to the strong acid solution, in the active dissolution, transition and pre-passivation regions. EIS measurements were performed to study the anodic dissolution of iron in aqueous CO_2 environments.

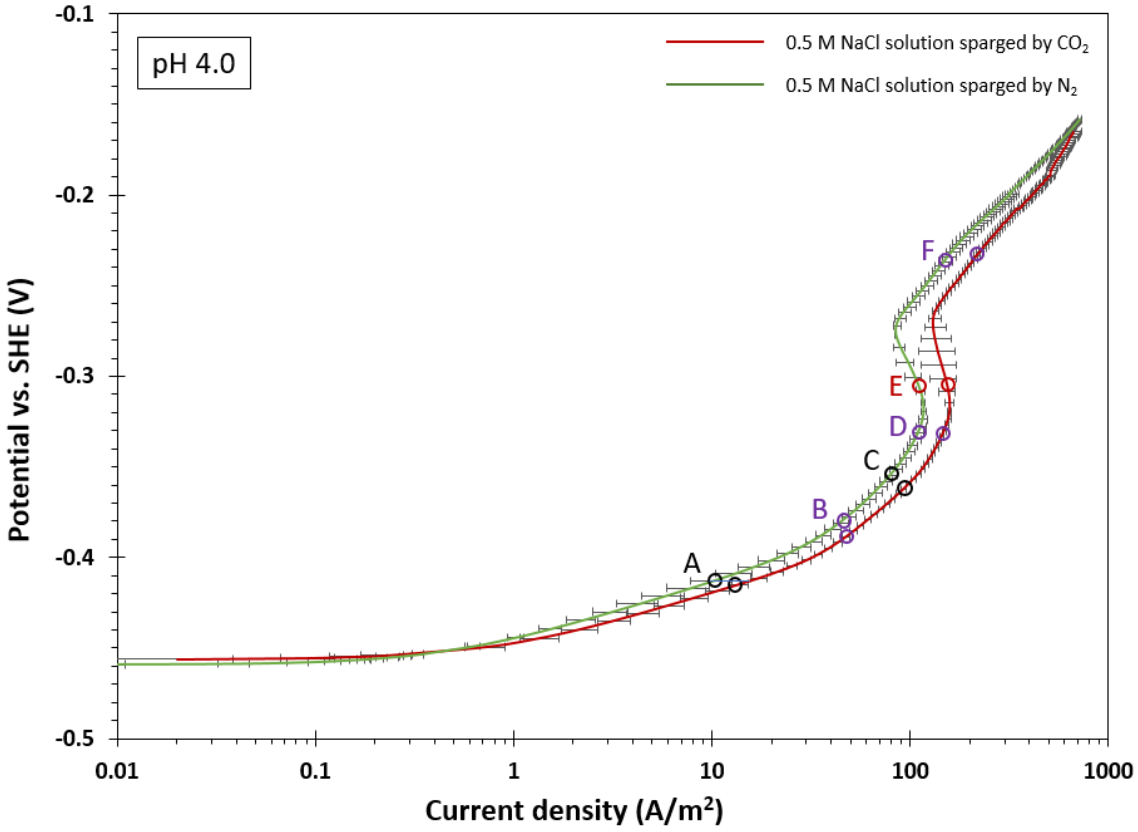

Figure 78

Comparison between the anodic steady state potentiodynamic sweep curves in chloride solution sparged with 1 bar CO_2 or N_2, measured using a sweep rate of 0.5 mV/s, on pure iron RDE at 1600 rpm, corroding in an aqueous solution at pH 4.0 and 25°C.[24]

[24] There are some uncertainties regarding the measured solution resistance in these experiments which were not fully resolved, due to raw data which could not be recovered.

Figure 79-Figure 81 illustrates the impedance response of anodic dissolution of iron in strong acid and aqueous CO_2 solutions, at DC potentials A, B and C in the active dissolution region marked in Figure 78. Considering the first high frequency loop as the relaxation of the double layer capacitance in parallel with the charge transfer resistance, in all the Nyquist plots there are three loops marked by letters *a*, *b* and *c*. These loops decoupled (separated) as DC potential increased from point A to B and C. In fact, as the kinetics of the underlying reaction steps increased, it affected the frequency range where relaxation of the adsorbed species happened. These observations indicated there are three adsorbed species involved in the mechanism of iron dissolution in both strong acid chloride solution and weak acid chloride CO_2 solution in the active dissolution region.

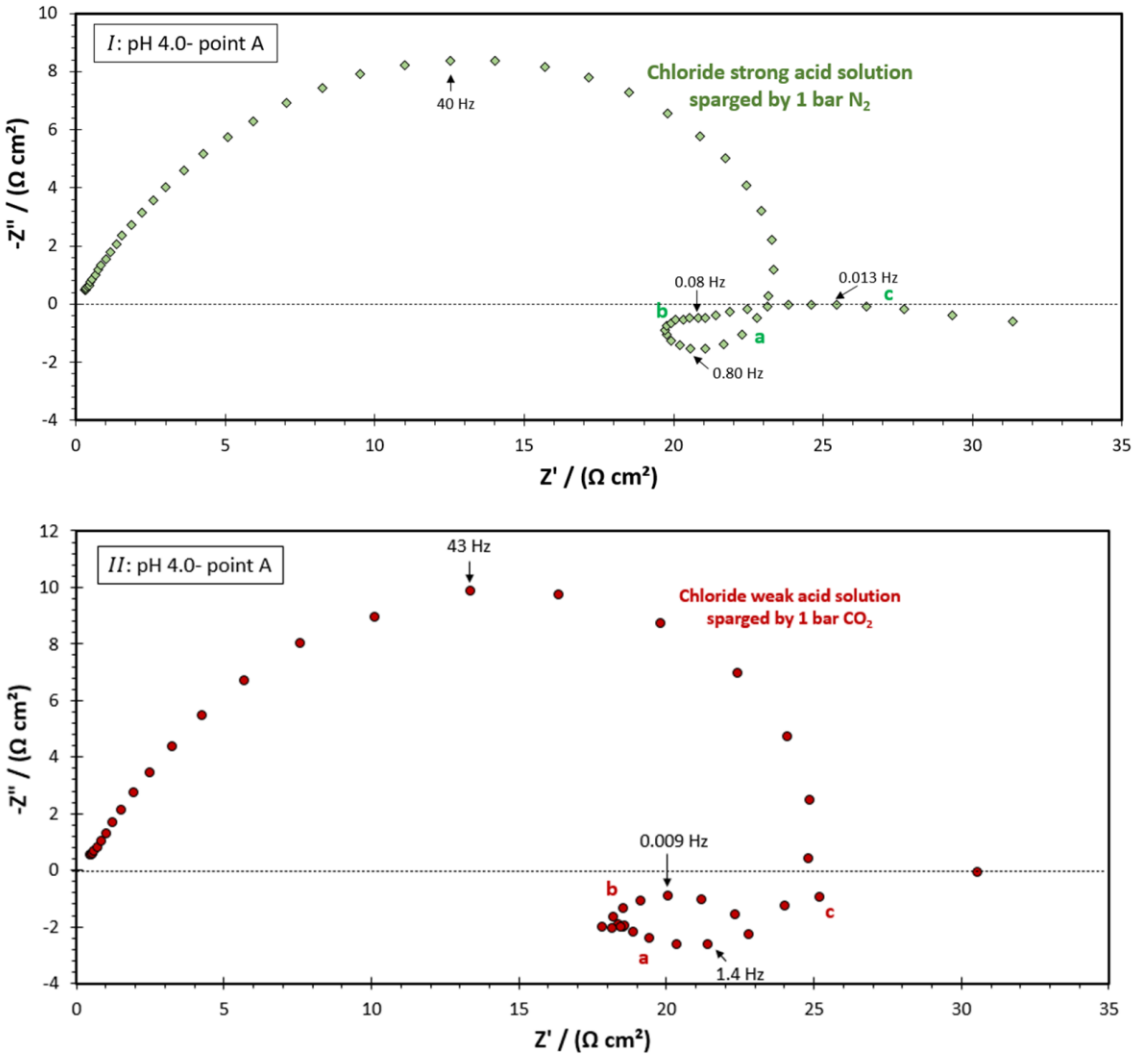

Figure 79

Nyquist plots at the DC potentials marked by letter A in the active dissolution region shown in Figure 78. I: Chloride strong acid solution; II: Chloride weak acid solution. Experimental parameters: 0.5 M NaCl, pH 4.0, 25°C, pure iron RDE, 1600 rpm.

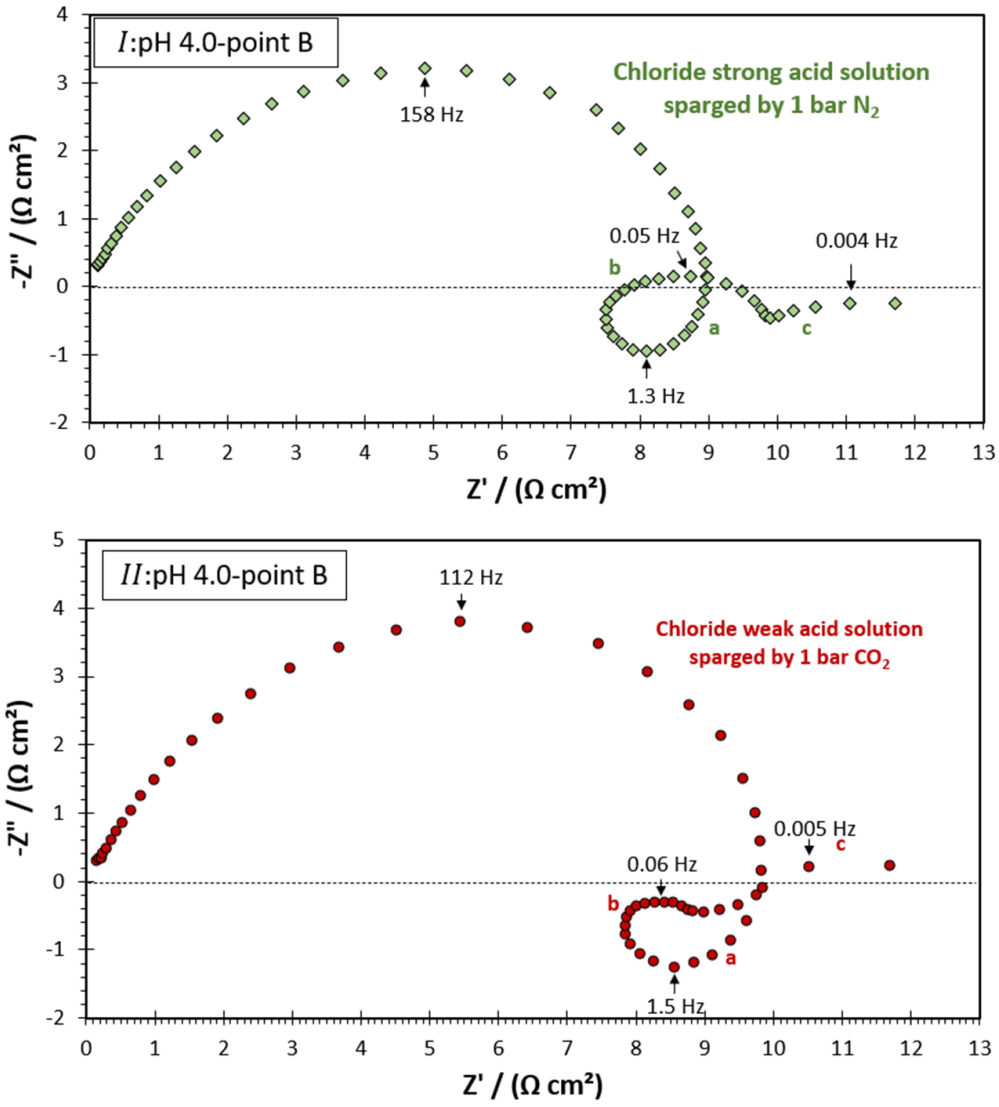

Figure 80

Nyquist plots at the DC potentials marked by letter B in the active dissolution region shown in Figure 78. I: Chloride strong acid solution; II: Chloride weak acid solution. Experimental parameters: 0.5 M NaCl, pH 4.0, 25°C, pure iron RDE, 1600 rpm.

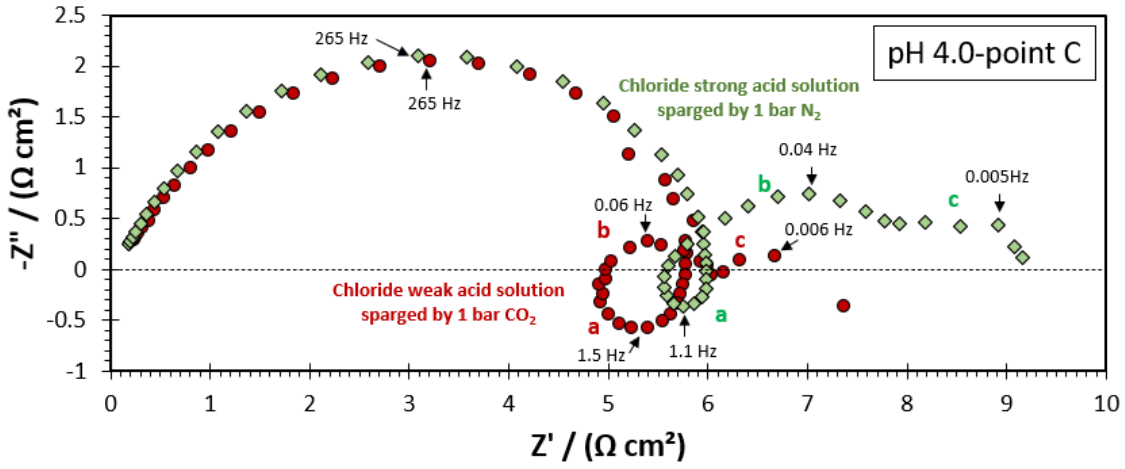

Figure 81

Nyquist plots at the DC potentials marked by letter C in the active dissolution region shown in Figure 78. Experimental parameters: 0.5 M NaCl, pH 4.0, 25°C, pure iron RDE, 1600 rpm.

Figure 82 shows the Nyquist plots at pH 4.0 and DC potential D marked in Figure 78. The Nyquist plot at the beginning of the transition region shows a negative polarization resistance. At more positive potential in the transition region (point E), despite a negative slope in the potentiodynamic sweep (negative polarization resistance), the Nyquist plots show impedance data with a positive real part (Figure 83). As discussed in section E.4.1. this behavior is due to instability of the DC current density during impedance measurement (shown in Figure 66 and Figure 84) which makes it hard to consistently obtain a Nyquist plot with a negative polarization resistance.

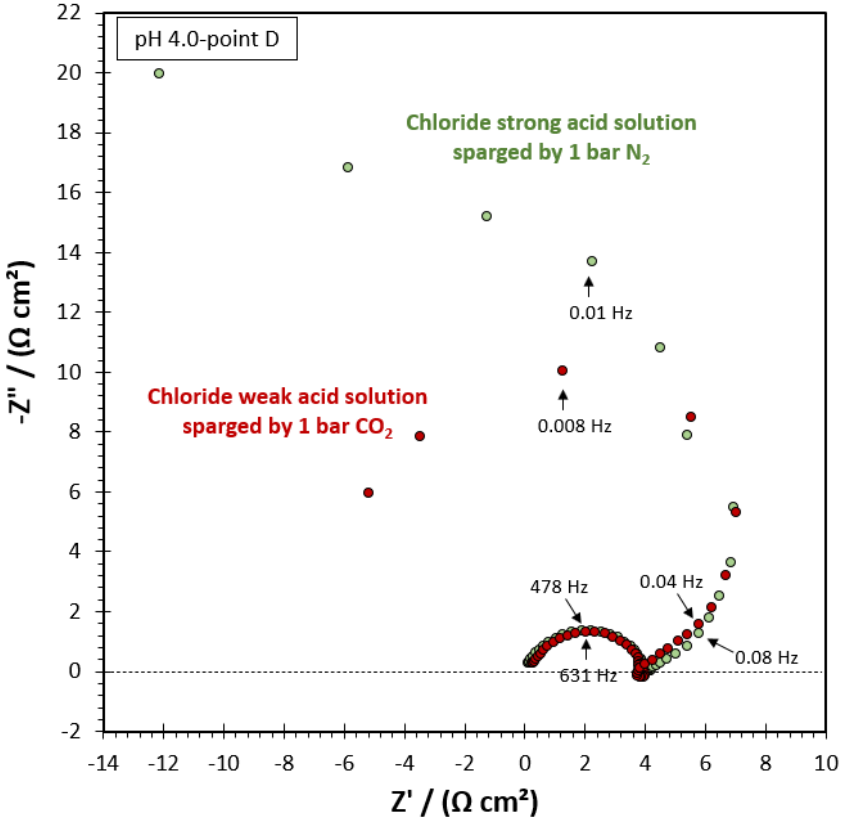

Figure 82

Nyquist plots at the DC potentials marked by letter D in the transition region shown in Figure 78. Experimental parameters: 0.5 M NaCl, pH 4.0, 25°C, pure iron RDE, 1600 rpm.

Both Nyquist plots in the transition region illustrated in Figure 83 show four loops in addition to the high frequency capacitive loop. This observation indicates that there are a similar number of adsorbed intermediate species involved in the mechanism of iron dissolution in acidic solution, both in the presence and absence of dissolved CO_2. As marked in Figure 83, the capacitive loop *a* related to $Fe(I)$ in multi-path mechanism can hardly be observed. As explained in section E.4.1., based on the kinetics of the underlying reaction steps, at this frequency range the inductive loop *a* observed at DC potential C (in

the active dissolution region shown in Figure 81) transformed into a capacitive loop at DC potential E (in the transition region shown in Figure 83) [25]. Therefore, at this condition, the capacitive loop might collapse or disappear, making it hard to distinguish. Moreover, although the two loops *b* and *c* are not quite decoupled in the transition region, experiments in pre-passivation regions show that, at higher current density, the two loops are clearly distinguished due to the change in their characteristic frequencies (Figure 85).

As illustrated in Figure 83 and Figure 85 there are similar number of adsorbed intermediates in both solutions. Considering that experiments were performed at approximately the same anodic potential in the transition and pre-passivation regions (point E and F), the charge transfer resistance and polarization resistance of the anodic reaction in aqueous CO_2 environment is lower compared to strong acid solution. Therefore, it can be concluded that the presence of CO_2, and the associated anions, changed the kinetics of the underlying reaction steps. This conclusion is further discussed by analyzing the experimental data at pH 5.0 as discussed below.

[25] For further information regarding the effect of kinetics of the reaction steps on the transformation of an inductive loop to a capacitive loop refer to the examples in the Appendix II.4 or the literature [8].

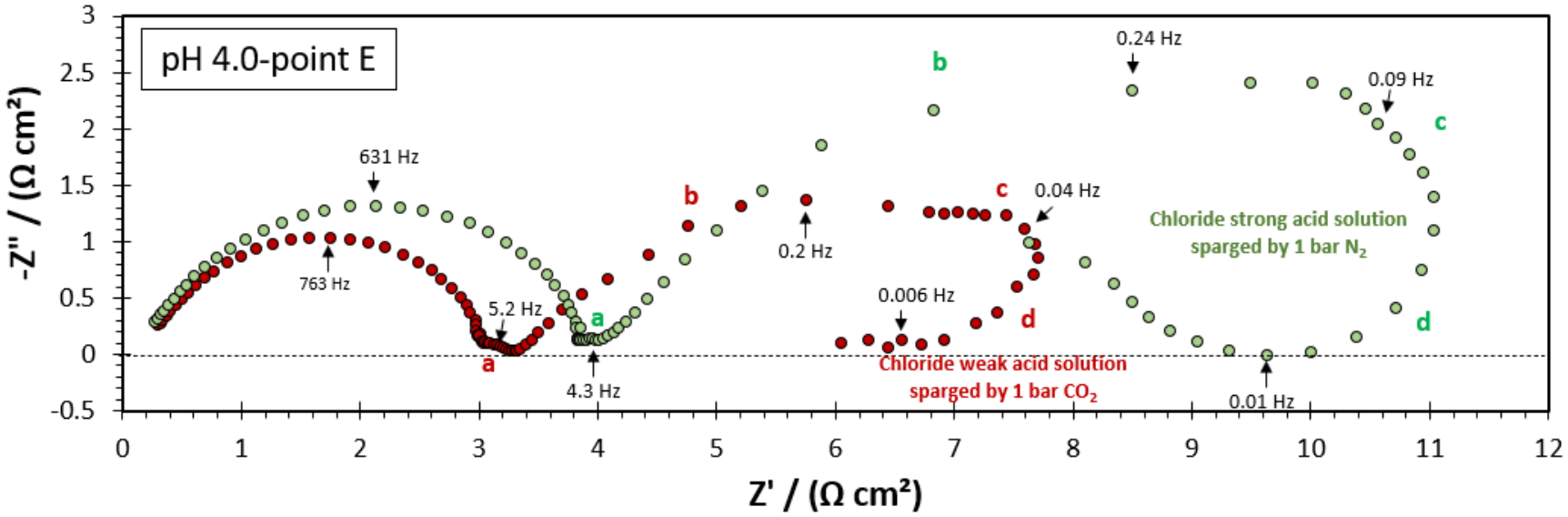

Figure 83

Nyquist plots at the DC potentials marked by letter E in the transition region shown in Figure 78. Experimental parameters: 0.5 M NaCl, pH 4.0, 25°C, pure iron RDE, 1600 rpm.

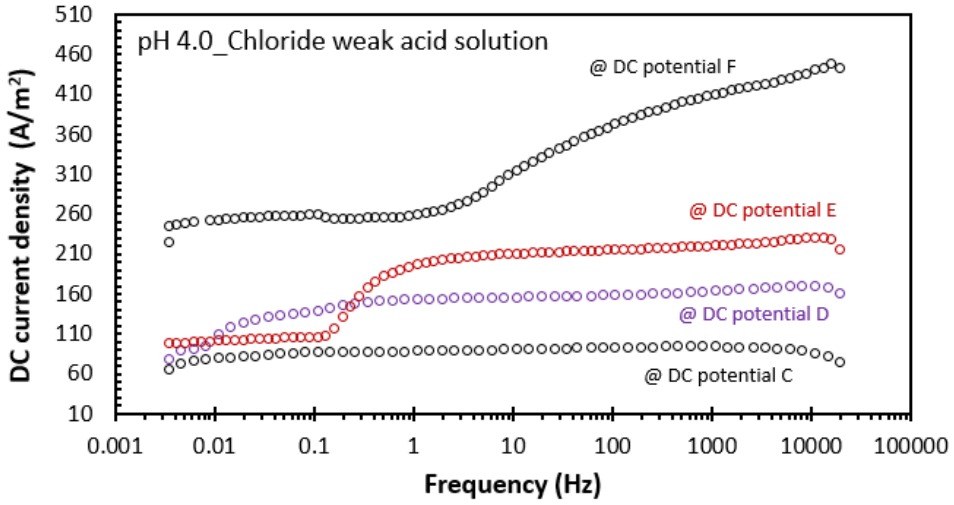

Figure 84

Variation of the steady state current density in chloride weak acid solution and at the DC potential in the active dissolution (points C and D), transition (point E) and pre-passivation region (point F). Experimental parameters: 0.5 M NaCl, pH 4.0, 1 bar CO_2, 25°C, pure iron RDE, 1600 rpm.

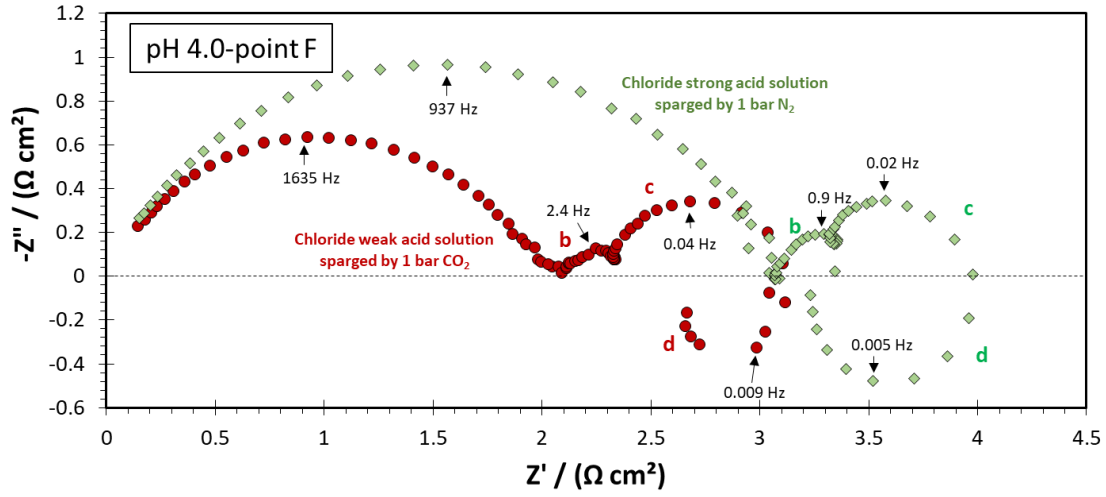

Figure 85

Nyquist plots at the DC potentials marked by letter F in the pre-passivation region shown in Figure 78. Experimental parameters: 0.5 M NaCl, pH 4.0, 25°C, pure iron RDE, 1600 rpm.

Figure 86 shows the anodic steady state potentiodynamic sweeps in strong acid chloride solution (sparged with 1 bar N_2) and weak acid chloride solution (sparged with 1 bar CO_2) at pH 5.0. Similarly, to pH 4.0, the rate of anodic reaction was increased in the presence of CO_2 mainly in the transition and pre-passivation regions. In order to elucidate the role of CO_2 on the mechanism of anodic reaction, EIS experiments were performed at the DC potential shown by alphabetic letters on the sweeps.

Figure 87 shows the Nyquist plots obtained at pH 5.0 in strong acid and weak acid CO_2 solution in the active dissolution region marked by letter A and B in Figure 86. Similarly, to the results at pH 4.0, the Nyquist plots shows similar number of loops and adsorbed intermediates in both solutions.

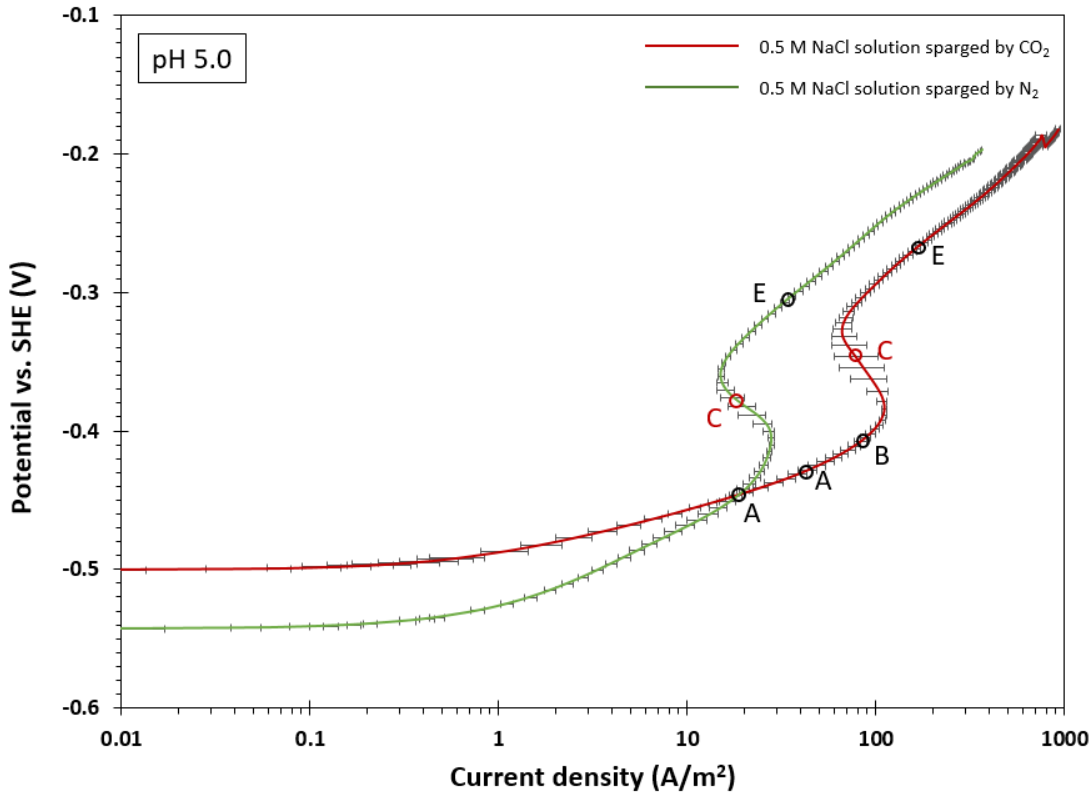

Figure 86

Comparison between the anodic steady state potentiodynamic sweep curves in chloride solution sparged with 1 bar CO_2 or N_2, measured using a sweep rate of 0.5 mV/s, on pure iron RDE at 1600 rpm, corroding in an aqueous solution at pH 5.0 and 25°C.[26]

[26] There are some uncertainties regarding the measured solution resistance in these experiments which were not fully resolved, due to raw data which could not be recovered.

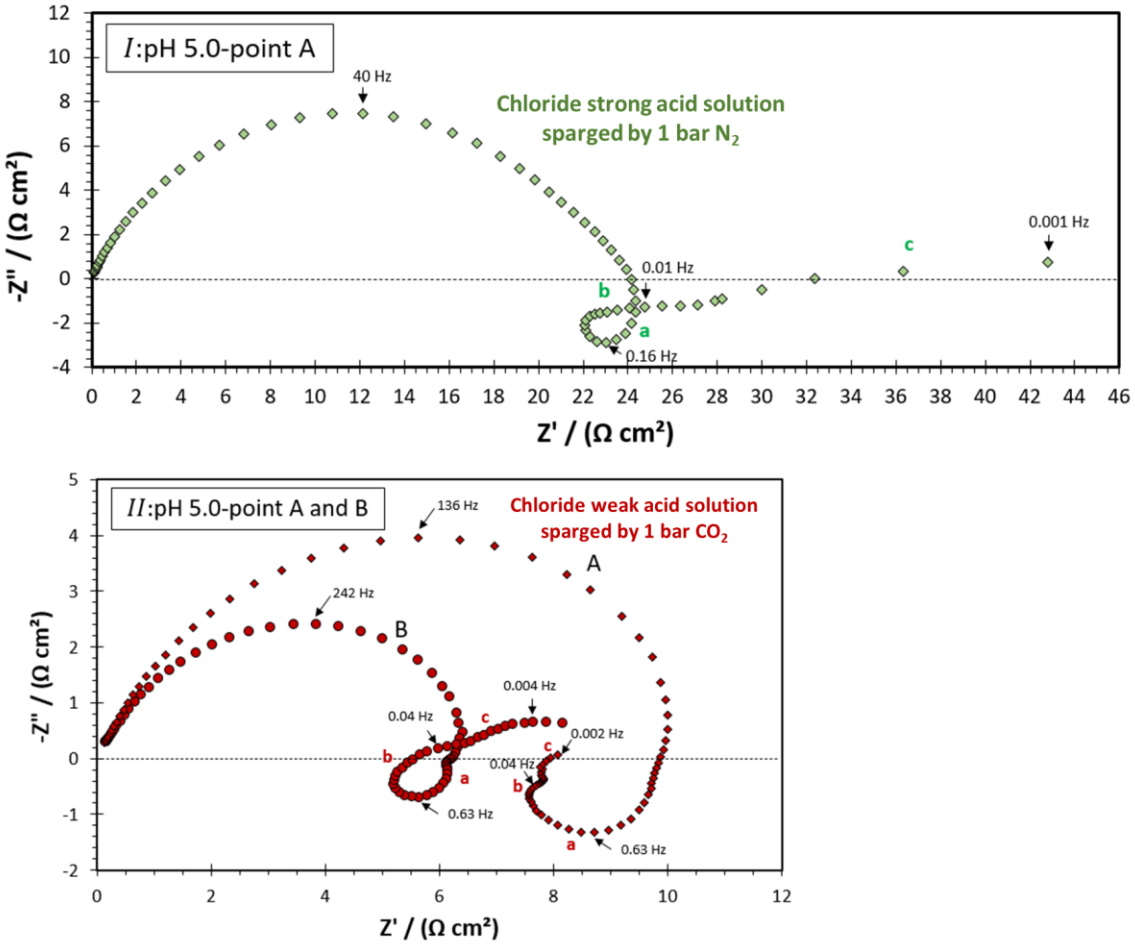

Figure 87

Nyquist plots at the DC potentials marked by letter A and B in the active dissolution region shown in Figure 86. I: Chloride strong acid solution; II: Chloride weak acid solution. Experimental parameters: 0.5 M NaCl, pH 5.0, 25°C, pure iron RDE, 1600 rpm.

Figure 88 shows the impedance response of anodic dissolution of iron in the transition region marked by letter C in Figure 86. As discussed in detail in a previous section, although the Nyquist plot shows three loops at low frequency, they might indicate the presence of four adsorbates on the metal surface. Region *a* is related to the impedance response of $F(I)$ at which the capacitive loop was collapsed. Meanwhile loop *b* is related

to the relaxation of two species ($Fe(I)^{*}\ and\ Fe(I)^{**}$) responding at the same frequency range. In addition, loop *d* is related to the adsorbed $Fe(II)^{*}$, which is the dominant species in the pre-passivation region[6,7].

The same behavior is observed in the impedance response of iron dissolution in a CO_2 environment. Based on the steady state potentiodynamic sweep, in the transition region, the current density is higher in CO_2 environment compared to the strong acid solution. The relatively higher current density helped loops b and c related to the adsorbates $Fe(I)^{*}$ and $Fe(I)^{**}$ decouple clearly while in strong acid chloride solution that they responded in the same frequency range represented by loop *b*. Therefore, in both solutions there is a similar number of intermediate adsorbates participating in the mechanism of iron dissolution. Moreover, the EIS data in the pre-passivation region (in Figure 89) supports the above conclusion.

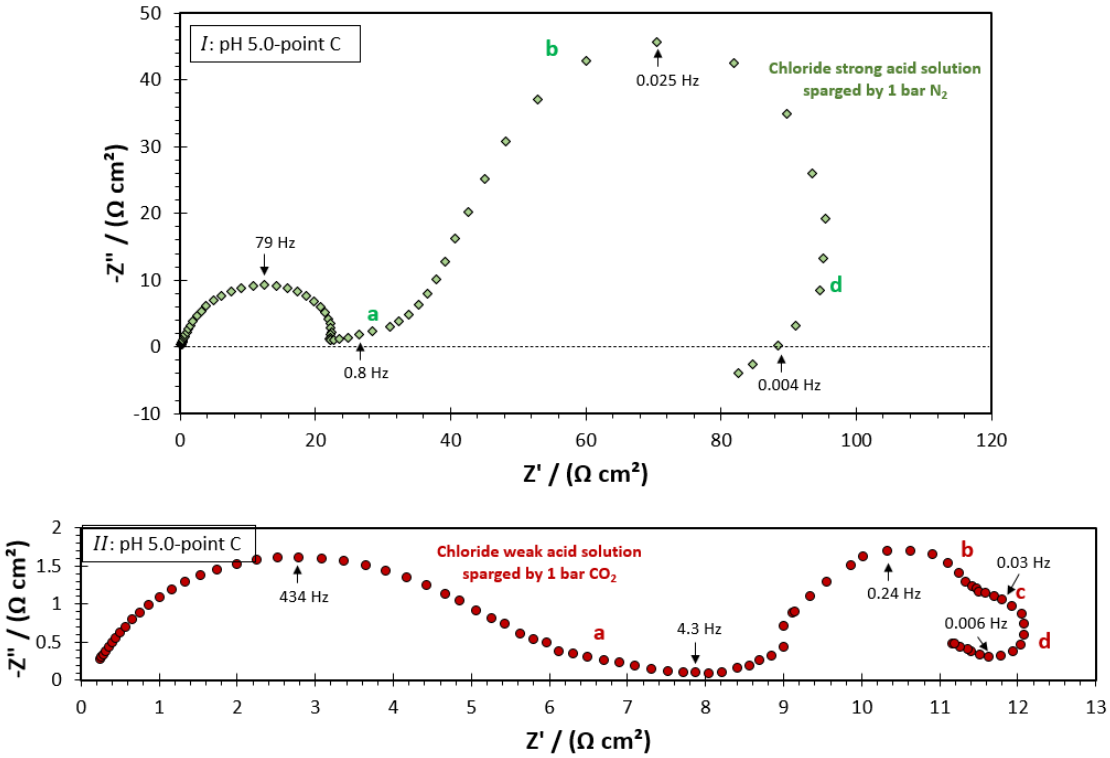

Figure 88

Nyquist plots at the DC potentials marked by letter C in the transition region shown in Figure 86. I: Chloride strong acid solution; II: Chloride weak acid solution. Experimental parameters: 0.5 M NaCl, pH 5.0, 25°C, pure iron RDE, 1600 rpm.

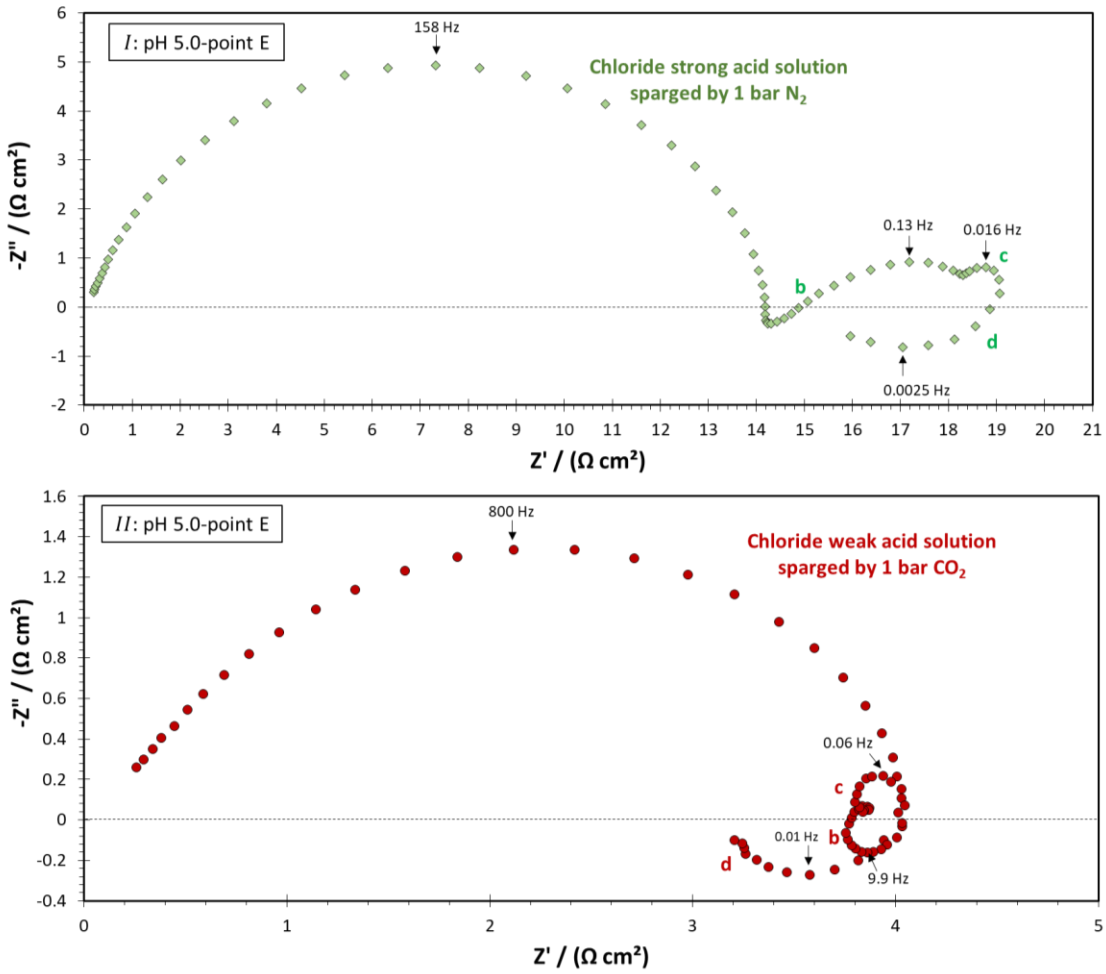

Figure 89

Nyquist plots at the DC potentials marked by letter E in the pre-passivation region shown in Figure 86. I: Chloride strong acid solution; II: Chloride weak acid solution. Experimental parameters: 0.5 M NaCl, pH 5.0, 25°C, pure iron RDE, 1600 rpm.

In Section E.4.1. it was shown that Cl^- can displace some hydroxide ions from the metal surface, to form an additional adsorbed intermediate complex which participates in the anodic reaction by forming the 4th path occurring in parallel to the already existing 3 paths already identified in solutions without chlorides. Meanwhile, based on the impedance response of the anodic dissolution of iron in strong acid chloride solutions and weak acid

chloride solutions (sparged by CO_2), there is the same number of intermediate adsorbates participating in the anodic reaction. Consequently, this experimental evidence indicates that unlike chloride ion, dissolved CO_2, H_2CO_3, and the associated anions (HCO_3^- and CO_3^{2-}) do not form additional intermediate adsorbed complexes. Therefore, in CO_2 solutions, the anodic mechanism follows the same revised version of the four-path mechanism which was proposed for the anodic dissolution of iron in chloride-containing strong acid solutions, as described in Section E.4.1.

- Despite a similar number of intermediate, reaction steps and dissolution pathways in both solutions, the kinetics of the anodic reaction is higher in CO_2 aqueous environments compared to the strong acid solution. This is illustrated by the steady state potentiodynamic sweeps obtained at different pH values and shown in Figure 78 and Figure 86. If fact, the kinetics of the underlying reaction is likely to be different in CO_2 environments compared to strong acid solutions due a change in the solution composition close to the metal surface including a more acidic pH, and the presence of CO_2, H_2CO_3, HCO_3^- and CO_3^{2-} These may change the nature and chemical composition of the adsorbed species which affects kinetic constants of the underlying reactions. It is also possible that there is change in the extent of coverage of the iron surface by different adsorbed intermediated species and ions, for example a decreased coverage by chloride containing intermediates that retard the iron dissolution rate.

Overall, the analysis discussed in Sections E.4.1. and E.4.2. demonstrated that the presence of anions can influence the mechanism of iron dissolution. Chloride ion can

replace the hydroxide ion through competitive adsorption and form an additional adsorbate which is directly involved in the iron dissolution mechanism via a distinct pathway. It is particularly noteworthy that, in the chloride-containing CO_2 environment, impedance data showed that there were no additional adsorbed species compared to chloride-containing strong acid solution, indicating that CO_2 and the associated carbonate species in solution did not directly participate in the anodic reaction through forming distinct intermediate adsorbates, but rather changed the chemical composition of the solution at the metal surface leading to an accelerating kinetics.

E.4.3. Calculation of Kinetic Parameters of Multi-path Mechanism for Anodic Dissolution of Iron [27]

Considering the Keddam, *et al.,* multi-path mechanism (Figure 55), the authors determined the value of kinetic parameters using trial and error in order to find a good fit between the experimental and calculated steady state polarization sweeps and EIS data[6,7]. In this section, an attempt has been made to explain a methodology to calculate the kinetic parameters of the reactions underlying the Keddam, *et al.,* multi-path mechanism at pH 4.0 in strong acid sulfate solution. As shown in Figure 55, there are 20 unknown kinetic parameters, including k_n (reaction rate constant) and b_n (Tafel slop) for the three pathways, which makes it next to impossible to calculate all of them simultaneously. Therefore, instead of considering all three pathways at once, it is necessary to choose experimental conditions at which one of the pathways is dominant. Using this approach there will be

---

(27) The general approach for the derivation of the functions used in this section are based on reference numbers [6–8,21,43].

smaller number of reactions and the associated kinetic parameters to be calculated. In this section, the approach for calculation of the kinetic parameters of path 1 and path 2 of multi-path mechanism in the strong acid sulfate environments is described, as an example.

E.4.3.1. Calculation of Kinetic Parameters of Path 1 in Multi-path Mechanism. Figure 90 shows the experimental Nyquist plot measured at the open circuit potential, in 0.3 M Na_2SO_4 strong acid solution, pH 4.0, and at 25°C, using a pure iron rotating disk electrode. The high frequency capacitive loop is related to the double layer capacitance in parallel with the charge transfer resistance while the low frequency inductive loop is related to relaxation of an adsorbed species. Considering the multi-path mechanism (Figure 55), overall, there are three pathways and four adsorbed species. Since the experimental Nyquist plot at the open circuit potential shows only one inductive loop, therefore, it can be assumed that there is only one adsorbed species on the metal surface related to the dominant pathway at the open circuit potential and active dissolution region.

According to Keddam, *et al.*, in the active dissolution region, path 1 is dominant which is similar to the Bockris mechanism[6,7]. Moreover, it has been shown by several studies that the Bockris mechanism is valid near the open circuit potential. Therefore, it is here accepted that this inductive loop is related to relaxation of $Fe\ (I)$ or $FeOH_{ads}$.[43]

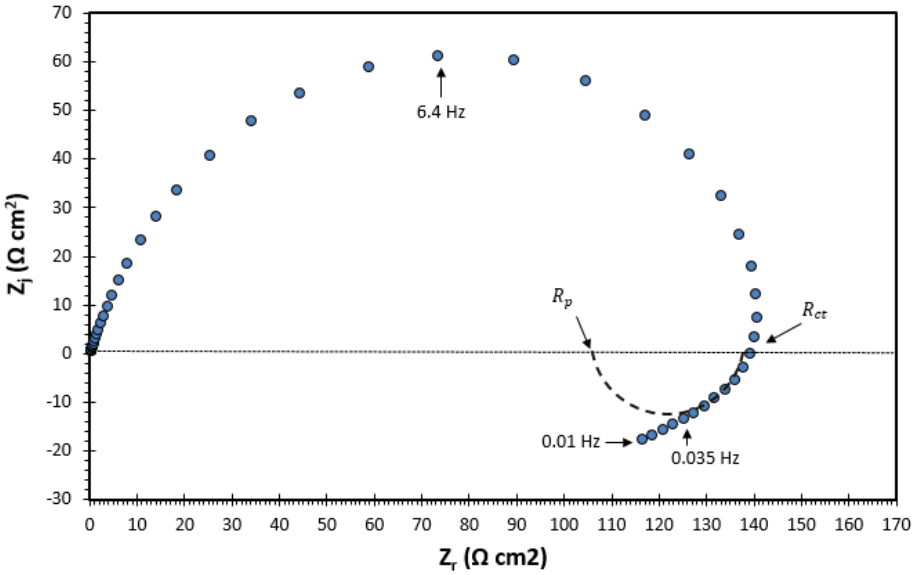

Figure 90

Experimental Nyquist plot at the open circuit potential. Experimental parameters: pure iron RDE, 1600 rpm, pH 4.0, 25°C, 1 bar N_2, 0.3 M Na_2SO_4 supporting electrolyte.

As explained above, both steady state potentiodynamic sweeps and EIS data at the open circuit potential are providing information mostly related to path 1 which can be used to calculate its kinetic parameters. However, at the open circuit potential there is always a contribution from the cathodic reduction of hydrogen ions to the experimental data which must be considered. Therefore, the extent of contribution of the cathodic reaction to the measured impedance data used to calculate the kinetic parameters of the anodic reaction must be investigated and considered as a source of error for the final calculated values. the following section explains the calculation for the percent contribution of the cathodic reaction to the overall impedance measurement.

E.4.3.1.1. Contribution of Cathodic Reduction of Hydrogen Ion to the Measured Impedance Data. This section follows the methodology described in Chapter C of this document in order to calculate the percent contribution of the cathodic reduction of hydrogen ions to the measured impedance data. In the first step a mechanistic model was used to calculate the steady state potentiodynamic sweeps which are shown and compared with the experimental sweep in Figure 91.

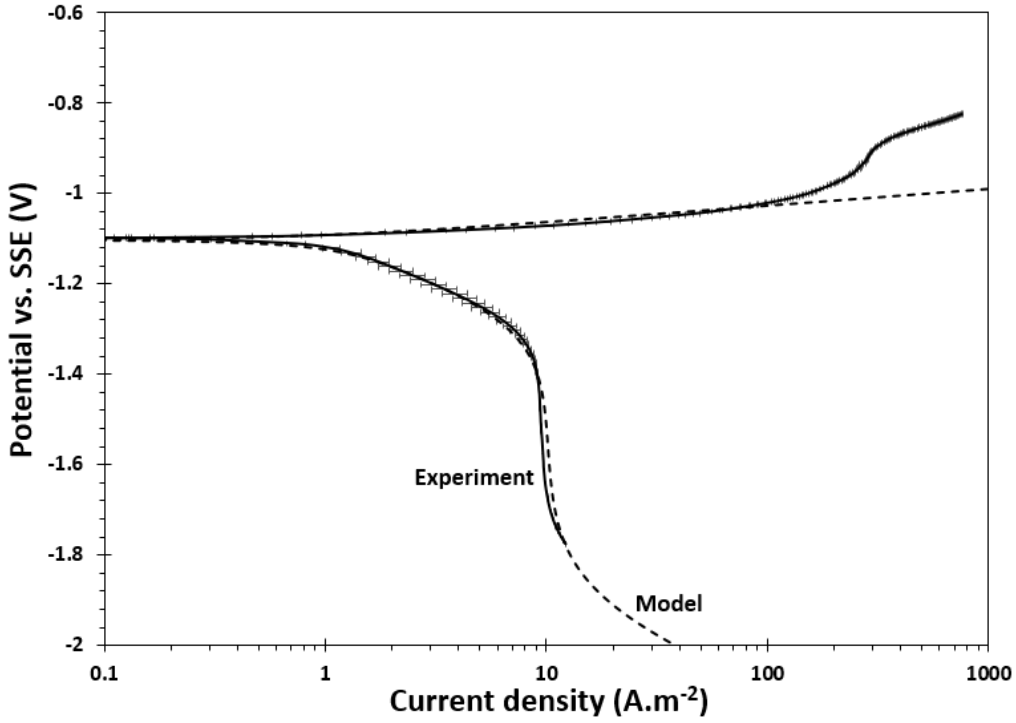

Figure 91

Comparison between measured and calculated steady state potentiodynamic sweep curves. Experimental and modeling parameters: pure iron RDE at 1600 rpm, pH 4.0, 25°C, 1 bar N_2, 0.3 M Na_2SO_4 supporting electrolyte [28].

[28] The potential is converted from Ag/AgCl reference electrode, used during experiment, to saturated sulfate electrode (SSE) considering -457 mV difference.

The modeled potentiodynamic sweep is the summation of current densities generated from the iron dissolution, hydrogen reduction and water reduction reactions as shown in Figure 92. The polarization resistance of each electrochemical reaction was calculated as the first derivative of the potentiodynamic sweeps shown in Figure 92. The polarization resistance of the electrochemical reaction with respect to potential is shown in Figure 93. This shows that, at the open circuit potential, the anodic reaction is the dominant reaction contributing to the overall polarization resistance, while there is 17% contribution from cathodic reduction of hydrogen ion.[29]

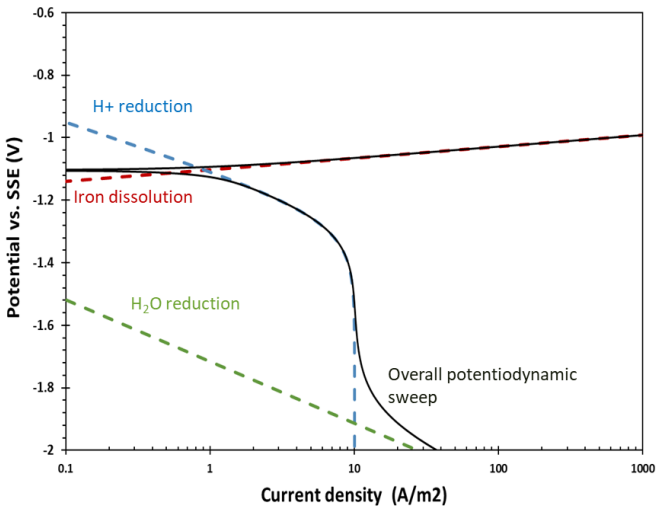

Figure 92

Calculated steady state potentiodynamic sweep of individual reactions underlying the overall potentiodynamic sweep shown in Figure 91. Modeling parameters: pure iron RDE at 1600 rpm, pH 4.0, 25°C, aqueous solution saturated at 1 bar N_2, with 0.3 M Na_2SO_4 supporting electrolyte.

---

[29] This value was considered as one of the sources of error for the calculated kinetic parameters presented here. However, this error was not implemented in the calculations.

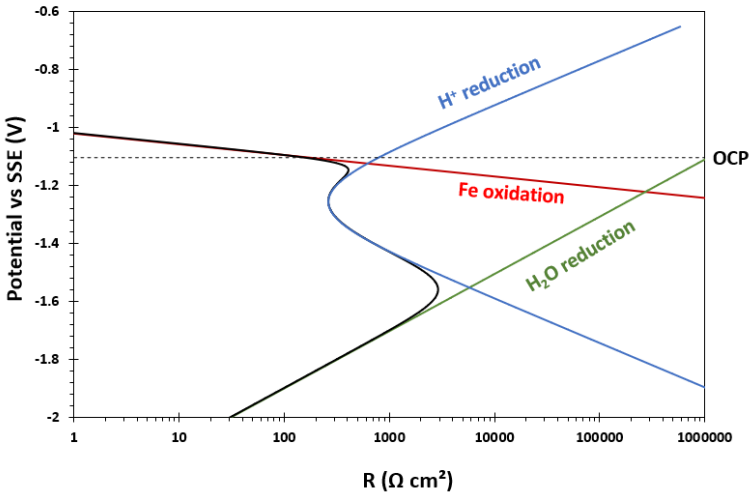

Figure 93

Modeled polarization resistance of H^+ reduction, Fe oxidation, H_2O reduction and overall polarization resistance, derived from the modeled potentiodynamic sweeps shown in Figure 92. Modeling parameters: pure iron RDE at 1600 rpm, pH 4.0, 25°C, aqueous solution saturated at 1 bar N_2, with 0.3 M Na_2SO_4 supporting electrolyte.

E.4.3.1.2. Mathematical Framework for Calculation of the Kinetic Parameters of Path 1. As explained at the beginning of Section E.4.3.1., at open circuit potential, path 1 is the dominant pathway including Reactions (83) and Reaction (84). Therefore, overall, there are four kinetic parameters to be calculated being $\boldsymbol{k_{0,1}}$, $\boldsymbol{k_{0,2}}$, $\boldsymbol{b_1}$ and $\boldsymbol{b_2}$. One of the sources of errors in the calculation of the kinetic parameters originates from the 17% contribution of the cathodic reaction to the impedance data at open circuit potential (Explained in Section E.4.3.1.1.). Moreover, at the open circuit potential there is adsorption of hydrogen ion on the iron surface. These errors are not considered in the calculation discussed in this section.

Calculation of the two unknowns $k_{0,1}$ and $k_{0,2}$ requires two equations as a function of the unknowns. The equation for steady state current density of the anodic reaction at the

open circuit potential (Equations (138)) and the characteristic frequency of the inductive loop shown in Figure 90 (Equation (139)) are the two equations used for the calculation of the unknows. The details regarding the derivation of the two functions considering Equations (140) and (141) are provided in Appendix II.4 based on literature [6–8,21,43]. The steady state current density was determined using the LPR technique and Stern-Geary equation[82] with B value of 26 mV. The characteristic frequency of the inductive loop was estimated by the experimental data shown in Figure 90.

$$\bar{\iota}_{F,total} = \frac{2Fk_1k_2[OH^-]}{k_1[OH^-] + k_2} \quad (138)$$

$$f_{ch,1} = \frac{k_1[OH^-]+k_2}{2\pi\beta} \quad (139)$$

$$k_i = k_{0,i} \exp\left(\frac{V}{b_i}\right) \quad (140)$$

$$b_i = \frac{RT}{\alpha_i nF} \quad (141)$$

The Tafel constants, b_1 and b_2 can be calculated using two equations, polarization resistance (Equation (142)) and the charge transfer resistance (Equation (143)). The details regarding the derivation of the two functions are provided in Appendix II.4 based on literature [6–8,21,43]. The value of the charge transfer resistance was determined by the cross section of the high frequency capacitive with x-axis as shown in Figure 90. Meanwhile, as during the experiment a complete inductive loop could not be achieved, the value of the polarization resistance was determined using the LPR technique. Table 12 and Table 13 shows the parameters for calculation of the kinetic parameters, obtained based on repeated experiments, and the calculated values of kinetic parameters respectively.

$$\frac{1}{R_p} = \frac{1}{R_{ct}} + \frac{(k_2 - k_1[OH^-])\frac{Fk_1k_2[OH^-]}{k_1[OH^-] + k_2}(\frac{1}{b_1} - \frac{1}{b_2})}{k_1[OH^-] + k_2} \quad (142)$$

$$\frac{1}{R_{ct}} = \left(\frac{di_{F,total}}{dV}\right)_{\theta_n} = \frac{Fk_1k_2[OH^-]}{k_1[OH^-] + k_2}\left(\frac{1}{b_1} + \frac{1}{b_2}\right) \quad (143)$$

Table 12

Experimental parameters for calculation of $k_{0,n}$ and b_n of Reactions (83) and (84).

Parameter	Description	Value
$\bar{\iota}_{F,total}$	Anodic faradaic current density at OCP	$2.43 \times 10^{-4} \pm 6.98 \times 10^{-6}$ A /cm^2
$f_{ch,1}$	Characteristic frequency of the Inductive loop shown in Figure 90.	0.036 Hz
$R_{p,OCP}$	Polarization resistance at OCP	106.90 ± 3.16 Ω cm^2
$R_{ct,OCP}$	Charge transfer resistance at OCP	141.57 ± 2.53 Ω cm^2
β	Maximum surface concentration of the intermediate	10^{-5} mol/cm^2
$[OH^-]$	Concentration of hydroxide ion determined based on pH value	10^{-13} mol/cm^3
F	Faradaic constant	96485.33 C/mol
V	Potential (in this case open circuit potential)	-1.099 V vs. SSE
T	Temperature	298.15 K

Table 13

Calculated kinetic values related to Reactions (83) and (84).

Parameter	Description	Value
k_1	Kinetic rate for Reaction (83) at -1.099 V vs. SSE	1.29×10^4
$k_{0,1}$	Kinetic rate constant for Reaction (83)	4.97×10^{22}
b_1	Tafel component of Reaction (83)	0.0257 V
α_1	Symmetric coefficient for Reaction (83)	1.00
k_2	Kinetic rate for Reaction (84) at -1.099 V vs. SSE	5.54×10^{-8}
$k_{0,2}$	Kinetic rate constant for Reaction (84)	79.83
b_2	Tafel component of Reaction (84)	0.0521 V
α_2	Symmetric coefficient for Reaction (84)	0.49

It should be noted that the value of the current density at OCP, 2.43 A/m^2, which was implemented in the calculations, is based on a B value of 26 mV which is frequently used for corrosion current density calculation in an aqueous CO_2 environment. However,

based on Figure 91 and the model potentiodynamic sweeps, the corrosion current density is about 0.92 A/m^2. Considering the current density of 0.92 A/m^2, the calculated b_1 and b_2 are 0.0098 V and 0.0194 V respectively. Consequently, α_1 and α_2 are 2.6 and 1.3 respectively which do not follow the assumption behind the elementary reactions. Although the experimental potentiodynamic sweeps were repeatable with small error bars (Figure 91), there is another study indicating corrosion current density of about 2 A/m^2 at approximately similar test conditions used in the present study[17]. Therefore, it is suspected that there are some errors in the steady state potentiodynamic sweeps obtained in the present study and the corrosion current density obtained based on LPR measurements is more accurate. Another possibility for the source of errors in the calculated results might be the 17% contribution of the cathodic reaction in the measured impedance data at OCP as discussed in Section E.4.3.1.1. In other words, extracted values from the Nyquist plot which were used in the calculations are not purely related to the anodic reaction.

E.4.3.2. Calculation of the Kinetic Parameters of Path 2 in the Multi-path Mechanism. Figure 94 shows the Nyquist plot conducted at more positive potential (*-968.4 mV vs. SSE)* and in the transition region which shows three capacitive loops. The high frequency loop is related to the double layer capacitance in parallel with the charge transfer resistance. According to Keddam *et al,.* [6,7] the second capacitive loop is related to the relaxation of the adsorbed species $\boldsymbol{Fe\,(I)_{ads}}$ $(\boldsymbol{\theta_1})$ while the third capcitive loop at very low frequency is related to the relaxation of $\boldsymbol{Fe(I)^{*}_{ads}}$ $(\boldsymbol{\theta_2})$. Therefore, in the transition region, the EIS data is affected by both path 1 and path 2 shown in Figure 55.

The kinetic constants of path 1 were already calculated as described in Section E.4.3.1. Therefore, the steady state potentiodynamic sweep and EIS data in the transition regions can be used to calculate the kinetic constants of path 2, which are $k_{0,3}$, $k_{0,-3}$, $k_{0,4}$, b_3, b_{-3} and b_4 related to Reaction (85) and (86). Using the Equations for the characteristic frequencies of the loops θ_1 and θ_2 (Equations (144) and (145) respectively), the unknows k_3 and k_{-3} can be calculated. Table 13 and Table 14 show the parameters implemented in the calculations.

In addition, k_4 can be calculated using Equation (146) for the steady state current density at the transition region. The details regarding the derivation of the two functions are provided in Appendix II.4 based on literature [6–8,21,43].

$$f_{ch,1} = \frac{(k_1[OH^-] + k_2 + k_3[OH^-])R_{ct}}{2\pi\beta(R_1 + R_{ct})} \quad (144)$$

$$f_{ch,2} = \frac{k_{-3}(R_{ct} + R_1)}{2\pi\beta(R_{ct} + R_1 + R_2)} \quad (145)$$

$$\bar{\imath}_{F,total} = 2Fk_2\bar{\theta}_1 + 2Fk_4[OH^-]\bar{\theta}_2 \quad (146)$$

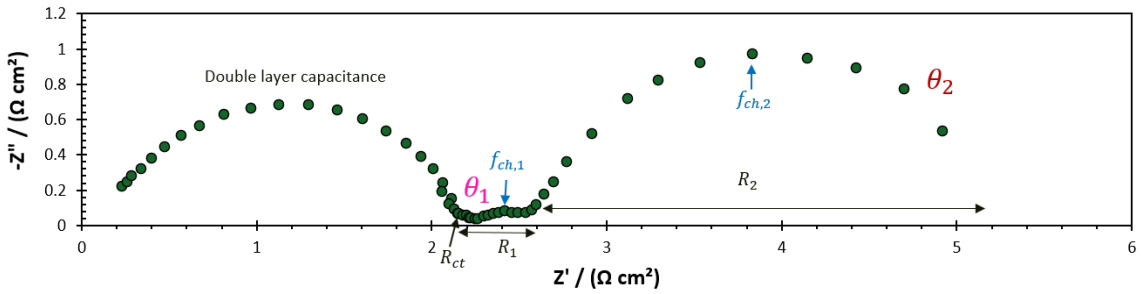

Figure 94

Experimental EIS data performed at the DC potential -968.4 mV vs. SSE shown in Figure 91. Experimental parameters: pure iron RDE at 1600 rpm, pH 4.0, 25°C, 1 bar N_2, 0.3 M Na_2SO_4 supporting electrolyte.

Table 14

Part 1 of the experimental parameters for calculation of $k_{0,n}$ and b_n of Reactions (85) and (86).

Parameter	Description	Value
Experimental results at DC potential -968.5±0.1 mV vs. SSE		
$\bar{\imath}_{F,total}$	Anodic faradaic current density at -0.9684 V vs. SSE	$2.20 \times 10^{-2}\,\mathrm{A/cm^2}$
$\bar{\imath}_{F,total}$	Anodic faradaic current density at -0.9686 V vs. SSE	$2.19 \times 10^{-2}\,\mathrm{A/cm^2}$
$f_{ch,1}$	Characteristic frequency of the second capacitive loop at -0.9684 V vs. SSE	0.63 Hz
$f_{ch,1}$	Characteristic frequency of the second capacitive loop at -0.9686 V vs. SSE	1.12 Hz
$f_{ch,2}$	Characteristic frequency of the third capacitive loop at -0.9684 V vs. SSE	0.015 Hz
$f_{ch,2}$	Characteristic frequency of the third capacitive loop at -0.9686 V vs. SSE	0.015 Hz
R_1	The diameter of the second capacitive loop related to θ_1 at -0.9684 V vs. SSE.	$0.39\ \Omega\,\mathrm{cm^2}$
R_1	The diameter of the second capacitive loop related to θ_1 at -0.9686 V vs. SSE.	$0.40\ \Omega\,\mathrm{cm^2}$
R_2	The diameter of the third capacitive loop related to θ_2 at -0.9684 V vs. SSE.	$2.62\ \Omega\,\mathrm{cm^2}$
R_2	The diameter of the third capacitive loop related to θ_2 at -0.9686 V vs. SSE.	$3.01\ \Omega\,\mathrm{cm^2}$
R_{ct}	Charge transfer resistance at -0.9684 V vs. SSE	$2.18\ \Omega\,\mathrm{cm^2}$
R_{ct}	Charge transfer resistance at -0.9686 V vs. SSE	$2.19\ \Omega\,\mathrm{cm^2}$
Experimental results at DC potential -955.4±0.1 mV vs. SSE		
$\bar{\imath}_{F,total}$	Anodic faradaic current density at -0.9553 V vs. SSE	$2.44 \times 10^{-2}\ \mathrm{A/cm^2}$
$\bar{\imath}_{F,total}$	Anodic faradaic current density at -0.9556 V vs. SSE	$2.43 \times 10^{-2}\ \mathrm{A/cm^2}$
$f_{ch,1}$	Characteristic frequency of the second capacitive loop at -0.9553 V vs. SSE	1.50 Hz
$f_{ch,1}$	Characteristic frequency of the second capacitive loop at -0.9556 V vs. SSE	1.50 Hz
$f_{ch,2}$	Characteristic frequency of the third capacitive loop at -0.9553 V vs. SSE	0.008 Hz
$f_{ch,2}$	Characteristic frequency of the third capacitive loop at -0.9556 V vs. SSE	0.011 Hz
R_1	The diameter of the second capacitive loop related to θ_1 at -0.9553 V vs. SSE.	$0.44\ \Omega\,\mathrm{cm^2}$
R_1	The diameter of the second capacitive loop related to θ_1 at -0.9556 V vs. SSE.	$0.47\ \Omega\,\mathrm{cm^2}$
R_2	The diameter of the third capacitive loop related to θ_2 at -0.9553 V vs. SSE.	$6.16\ \Omega\,\mathrm{cm^2}$
R_2	The diameter of the third capacitive loop related to θ_2 at -0.9556 V vs. SSE.	$4.14\ \Omega\,\mathrm{cm^2}$
R_{ct}	Charge transfer resistance at -0.9553 V vs. SSE	$2.15\ \Omega\,\mathrm{cm^2}$
R_{ct}	Charge transfer resistance at -0.9556 V vs. SSE	$1.89\ \Omega\,\mathrm{cm^2}$

Table 15

Part 2 of the experimental parameters for calculation of $k_{0,n}$ and b_n of Reactions (85) and (86)

Parameter	Description	Value
Experimental results at DC potential -944.6±2.4 mV vs. SSE		
$\bar{\imath}_{F,total}$	Anodic faradaic current density at -0.9422 V vs. SSE	$2.61 \times 10^{-2}\mathrm{A/cm^2}$
$\bar{\imath}_{F,total}$	Anodic faradaic current density at -0.9471 V vs. SSE	$2.56 \times 10^{-2}\mathrm{A/cm^2}$
$f_{ch,1}$	Characteristic frequency of the second capacitive loop at -0.9422 V vs. SSE	2.02 Hz
$f_{ch,1}$	Characteristic frequency of the second capacitive loop at -0.9471 V vs. SSE	2.02 Hz
$f_{ch,2}$	Characteristic frequency of the third capacitive loop at -0.9422 V vs. SSE	0.008 Hz
$f_{ch,2}$	Characteristic frequency of the third capacitive loop at -0.9471 V vs. SSE	0.008 Hz
R_1	The diameter of the second capacitive loop related to θ_1 at -0.9422 V vs. SSE.	$0.44\ \Omega\ \mathrm{cm^2}$
R_1	The diameter of the second capacitive loop related to θ_1 at -0.9471 V vs. SSE.	$0.54\ \Omega\ \mathrm{cm^2}$
R_2	The diameter of the third capacitive loop related to θ_2 at -0.9422 V vs. SSE.	$5.98\ \Omega\ \mathrm{cm^2}$
R_2	The diameter of the third capacitive loop related to θ_2 at -0.9471 V vs. SSE.	$7.23\ \Omega\ \mathrm{cm^2}$
R_{ct}	Charge transfer resistance at -0.9422 V vs. SSE	$1.88\ \Omega\ \mathrm{cm^2}$
R_{ct}	Charge transfer resistance at -0.9471 V vs. SSE	$2.02\ \Omega\ \mathrm{cm^2}$
β	Maximum surface concentration of the intermediate	$10^{-5}\ \mathrm{mol/cm^2}$
$[OH^-]$	Concentration of hydroxide ion determined based on pH value	$10^{-13}\ \mathrm{mol/cm^3}$
F	Faradaic constant	96485.33 C/mol
T	Temperature	298.15 K

Following the approach described above, the values of k_3, k_{-3}, and k_4 were calculated based on steady state current density and impedance data at different potentials shown in Figure 95. Results of calculations are shown in Figure 96 were based on Equation (140) and Equation (147), the slope of the average line is equal to $\frac{1}{b_i}$ while the intercept is

equal to $ln\ (k_{0,i})$. The calculated values of the kinetic constants are summarized in Table 16. [30]

$$ln(k_i) = \frac{V}{b_i} + ln\ (k_{0,i}) \qquad (147)$$

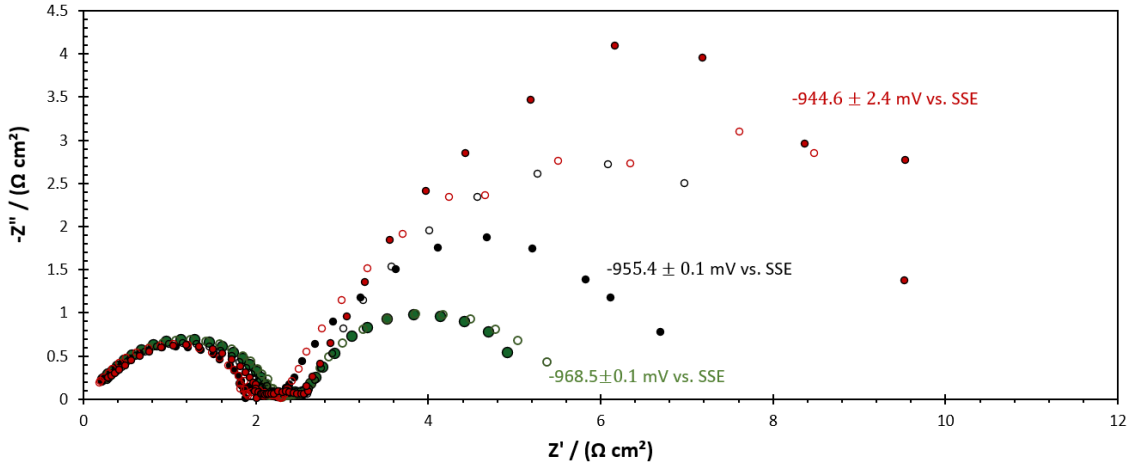

Figure 95

Experimental EIS data performed at transition region of the potentiodynamic sweep shown in Figure 91. Experimental parameters: pure iron RDE at 1600 rpm, pH 4.0, 25°C, 1 bar N_2, 0.3 M Na_2SO_4 supporting electrolyte. The data markers with the same color are related to repeated experiments.

[30] Comparison of the calculated data with the value reported by Keddam et al.,[6] was not possible due to an uncertainty in the reference potential.

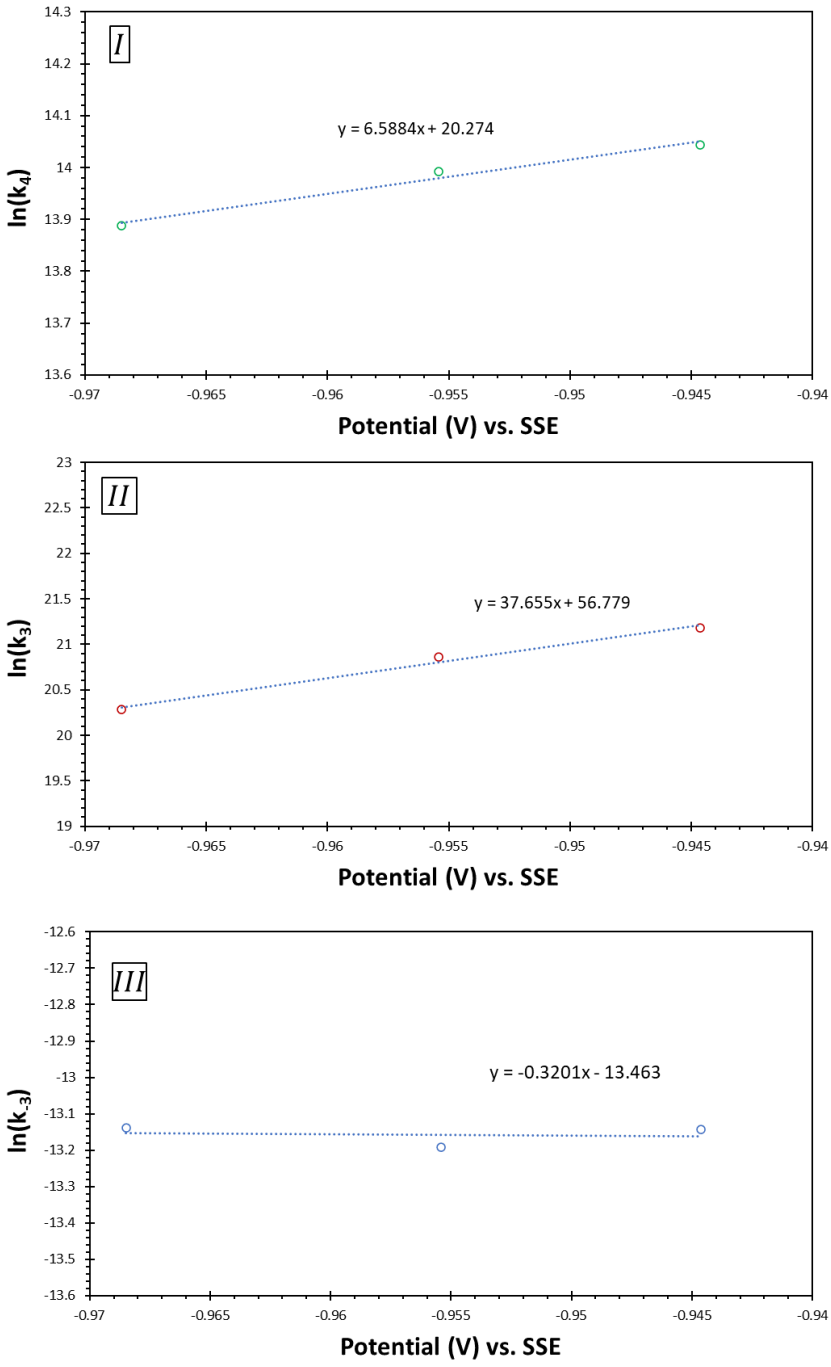

Figure 96

Natural logarithm of the calculated k_3, k_{-3} and k_4 values at different potentials in the transition region shown in Figure 91. Experimental parameters: pure iron RDE at 1600 rpm, pH 4.0, 25°C, 1 bar N_2, 0.3 M Na_2SO_4 supporting electrolyte.

Table 16

Calculated kinetic values related to Reactions (85) and (86).[31]

Parameter	Description	Value
k_3	Kinetic rate for forward Reaction (85) at -968.5±0.1 mV *vs. SSE*	$6.44 \times 10^8 \pm 1.84 \times 10^8$
k_3	Kinetic rate for forward Reaction (77) at -955.4±0.1 mV *vs. SSE*	$1.15 \times 10^9 \pm 2.15 \times 10^7$
k_3	Kinetic rate for forward Reaction (77) at -944.6±2.4 mV *vs. SSE*	$1.57 \times 10^9 \pm 2.15 \times 10^7$
k_{-3}	Kinetic rate for backward Reaction (77) at -968.5±0.1 mV *vs. SSE*	$1.97 \times 10^{-6} \pm 6.74 \times 10^{-8}$
k_{-3}	Kinetic rate for backward Reaction (77) at -955.4±0.1 mV *vs. SSE*	$1.87 \times 10^{-6} \pm 7.77 \times 10^{-8}$
k_{-3}	Kinetic rate for backward Reaction (77) at -944.6±2.4 mV *vs. SSE*	$1.96 \times 10^{-6} \pm 6.42 \times 10^{-8}$
k_4	Kinetic rate for Reaction (86) at -968.5±0.1 mV *V vs. SSE*	$1.07 \times 10^6 \pm 1.56 \times 10^4$
k_4	Kinetic rate for Reaction (86) at -955.4±0.1 mV *vs. SSE*	$1.19 \times 10^6 \pm 2.35 \times 10^3$
k_4	Kinetic rate for Reaction (86) at -944.6±2.4 mV *vs. SSE*	$1.26 \times 10^6 \pm 8.90 \times 10^3$
$k_{0,3}$	Kinetic rate constant for forward Reaction (77) calculated based on Equation (140)	4.56×10^{24}
$k_{0,-3}$	Kinetic rate constant for backward Reaction (77) calculated based on Equation (140)	1.42×10^{-6}
$k_{0,4}$	Kinetic rate for Reaction (86) calculated based on Equation (140)	6.38×10^8
b_3	Tafel component of forward Reaction (77)	0.0266 V
b_{-3}	Tafel component of backward Reaction (77)	3.1240 V
b_4	Tafel component of Reaction (86)	0.1518 V
α_3	Symmetric coefficient for forward Reaction (77)	0.97
α_{-3}	Symmetric coefficient for backward Reaction (77)	0.01
α_4	Symmetric coefficient for Reaction (86)	0.08

[31] The reported value of k_3 , k_{-3} and k_4 are the average of two values calculated based on parameters obtained by repeated experiments at each potential (Table 14 and Table 15).

E.4.3.3. Modeled Anodic Potentiodynamic Sweep by the Multi-path Mechanism. In this section, the multi-path mechanism and the calculated kinetic parameters in Table 13 and Table 16 were used to model the anodic potentiodynamic sweep of pure iron corroding in an aqueous solution at pH 4.0, 25°C, saturated at 1 bar N_2, with 0.3 M Na_2SO_4 supporting electrolyte. The anodic steady state potentiodynamic sweep was calculated up to the pre-passivation region using Equations (148)-(152) (the mathematical derivation of the functions is provided in Appendix II.4 based on literature [6–8,21,43]).

$$\bar{\imath}_{F,total} = \bar{\imath}_{path,1} + \bar{\imath}_{path\ 2} \tag{148}$$

$$\bar{\imath}_{path,1} = 2Fk_2\bar{\theta}_1 \tag{149}$$

$$\bar{\imath}_{path\ 2} = 2Fk_4[OH^-]\bar{\theta}_2 \tag{150}$$

$$\bar{\theta}_1 = \frac{k_1k_{-3}[OH^-]}{k_1k_3[OH^-]^2 + k_1k_{-3}[OH^-] + k_2k_{-3}} \tag{151}$$

$$\bar{\theta}_2 = \frac{k_1k_3[OH^-]^2}{k_1k_3[OH^-]^2 + k_1k_{-3}[OH^-] + k_2k_{-3}} \tag{152}$$

The calculated steady state anodic potentiodynamic sweep and its comparison with the experimental data are shown in Figure 97.I. Overall, there is a good fit between the experimental and calculated data. The discrepancy between the model and experimental data at low anodic potential (near the OCP) is due to the absence of the effect of cathodic reaction, which is not included in the calculations but did affect the measurements. Moreover, Figure 97.II shows the change in surface coverage fraction of adsorbed species $Fe(I)$ *(θ_1)* and $Fe(I)^*$ *(θ_2)* with respect to potential using Equations (151) and (152). As described in Section E.2.3. the transition region of the anodic potentiodynamic sweep is due to surface coverage fraction of $Fe(I)^*_{ads}$ (θ_2) reaching to its maximum followed by a

decrease in the surface coverage fraction of $Fe(I)_{ads}$ (θ_1) . Similar behavior was observed through the calculated data shown in Figure 97.II.

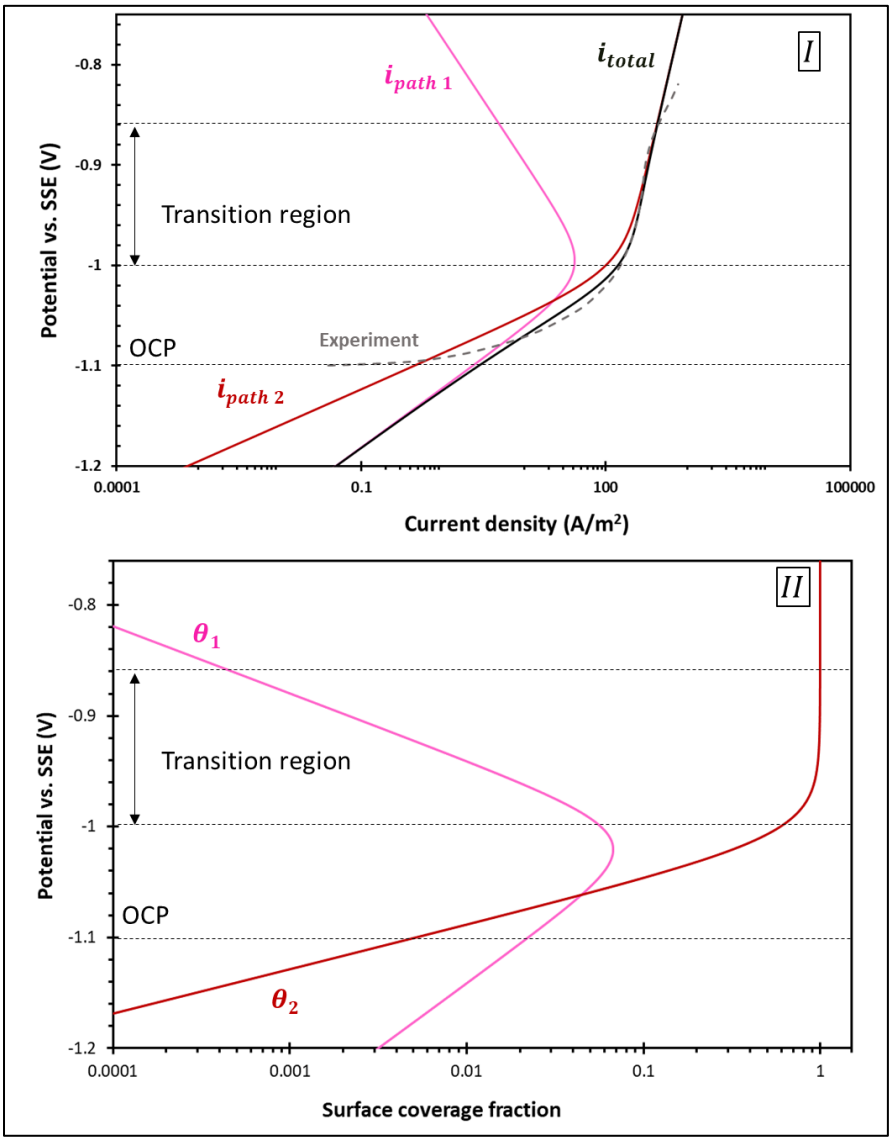

Figure 97

I: Comparison of the experimental steady state potentiodynamic sweep with the modeled data using the multi-path mechanism; II: Calculated surface coverage of adsorbed species $Fe(I)$ (θ_1) and $Fe(I)^*$ (θ_2) with respect to potential at pH 4.0, 25 °C, pure iron RDE, 1600 rpm, 1 bar N_2, 0.3 M Na_2SO_4.

E.5. Summary

The discussion in this chapter showed that the rate of anodic dissolution of iron decreases in presence of chloride ion. In addition, adsorption of chloride ion results in the formation of an additional adsorbed intermediate species which participate in the anodic reaction through a distinct pathway along with pathways 1-3 of the multi-path mechanism.

The EIS data obtained in the strong acid chloride solution were compared with the data obtained in weak acidic chloride solution in the presence of CO_2. Results showed that the presence of CO_2 does not lead to the formation of an additional adsorbate participating in the anodic reaction. Meanwhile, the rate of iron dissolution accelerated in CO_2 environment compared to the strong acid solution. This behavior in the aqueous CO_2 solution was concluded to be due the change in the solution composition at the metal surface, which lead to the change in the nature and chemical composition of the complex adsorbed species, kinetic constants and extent of coverage of the iron surface by different adsorbed intermediate species and ions, which affect the kinetics of the reaction steps and the overall reaction.

Moreover, in the last section of this chapter, a methodology was introduced to calculate the kinetic constants of the multipath mechanism at pH 4.0, in strong acid sulfate solution, using the theory behind steady state current density and EIS data.

Chapter F: Determining Critical Micelle Concentration of Organic Corrosion Inhibitors and its Effectiveness in Corrosion Mitigation [32]

F.1. Introduction

Corrosion inhibitors are frequently used as an economic and effective strategy to mitigate internal corrosion of mild steel pipelines. Consideration of internal pipeline corrosion is critically important to the oil and gas industry, be it for management of asset integrity, safety, environmental protection, and prevention of economic consequences of failure. Much research has been conducted to evaluate the corrosion mechanisms involved in so called "sweet" systems, with aqueous CO_2,[14,16,17], more neglected was research evaluating corrosion mechanisms in the presence of organic corrosion inhibitors, this topic receiving more attention in recent years [24,26,83–86]. Organic corrosion inhibitors have a structure similar to that of amphiphilic surfactants, consisting of a polar/hydrophilic head group, by which they can adsorb to the steel surface, and a non-polar/hydrophobic tail that forms a hydrophobic barrier. When a surfactant inhibitor film forms on a metal surface, this results in decreased corrosion rates [24,86,87]**.** The properties of such surfactant-type inhibitor molecules, their structures, and behavior in aqueous solutions have been investigated for many years in order to understand their behavior, as well as improve their inhibition efficiency. One of the parameters related to the behavior of these inhibitors is their so-called *critical micelle concentration* (CMC), which is the concentration when these surfactant-type molecules begin to aggregate into structures called micelles in the bulk

[32] The text, figures and tables in this chapter are taken from publications of the author: NACE International proceeding paper no. 13004 (2019), and Corrosion 77 (2020): pp. 266–275 (reference numbers [4,5]).

solution. The CMC is one of the frequently used parameters for determining the injection dosage rate of an inhibitor under field conditions [23].

It has been argued that at or above the CMC the corroding metal surface is covered by these adsorbed molecules and will reach a maximum level of corrosion inhibition**.** Moreover, many studies claim that once the CMC has been exceeded, and the maximum decrease in corrosion rate has been achieved, the addition of more surfactant inhibitor would only result in the formation of more micelles in the bulk solution rather than having them increasingly adsorb on the metal surface [23,88,89]. However, there is increasing evidence that the situation is not so simple. For example: an atomic force microscopy (AFM) study using a cationic surfactant, 1-dodecylpyridinium chloride, found that a carbon steel surface was entirely covered by this corrosion inhibitor at 1 CMC with the corresponding inhibition efficiency of about 70%, while at 9 CMC it reached an inhibition efficiency of about 90% [24]. This and some other similar observations suggest that the assumed link between CMC and inhibition efficiency requires further investigation.

The easiest and most common method for determining CMC is via surface tension measurement at the water-air interface [25,90]. The idea is that as a surfactant concentration increases in an aqueous solution, the measured interfacial tension decreases until it reaches a plateau and, at that point, the CMC is found. However, this behavior gives rise to at least two plausible hypotheses, which could explain it:

- **Hypothesis #1: the water-air interface saturates with the surfactant molecules when the surface tension reaches the plateau.** With increasing concentrations of surfactant molecules in a solution, the amount of surfactant molecules at the water-

air interface increases until it reaches saturation and the measured surface tension approaches a plateau, while at the same time the saturation in the bulk solution has not been reached and the micelles did not form.

- **Hypothesis #2**: **the bulk solution reaches saturation with the surfactant molecules and micelles are formed.** The concentration of the surfactants in the bulk solution increases until it becomes saturated when micelles begin to form, while at the same time the saturation of the water-air interface has not been reached.

Both hypotheses are consistent with reaching a plateau in surface tension measurements at some concentration, but only if hypothesis #2 is true can the CMC of the surfactant be determined this way. In that case, any further addition of the surfactant beyond the CMC would result in the formation of more micelles rather than having the surfactant accumulate at the water-air interface. However, hypothesis #1 is a classical explanation that underpins adsorption isotherms and cannot be lightly rejected. Therefore, an alternative, independent method to measure CMC is required, in order to distinguish which hypothesis may be true.[33]

The overall scenario behind the CMC being a critical parameter in corrosion inhibition gives rise to one more hypothesis that can be postulated:

- **Hypothesis #3: the maximum corrosion inhibition efficiency is achieved when the metal surface reaches a certain coverage by the inhibitor, which corresponds to the bulk CMC**. The CMC can be determined by the plateau in the

[33] Here it is assumed that the likelihood of both hypotheses being true is low, *i.e.*, that the water-air interface and the solution become saturated at the same concentration is highly improbable.

surface tension measurements at the water-air interface or by an alternative technique.

In summary, these three hypotheses postulate that the behavior at one interface (corrosion at the metal surface) is related to what is occurring in the bulk (formation of micelles) by measuring what is occurring at another interface (changes in water-air interfacial tension). Whether this is true (or not) can only be determined if the surfactant inhibitor concentrations obtained at the plateau of water-air interfacial tension corresponds to the independently measured CMC in the bulk solution and also corresponds to the independently determined inhibitor concentration at which maximum corrosion inhibition efficiency is found.

Therefore, the primary objective of this research was to evaluate the validity of the surface tension measurement for determining CMC, as a means of identifying optimal corrosion inhibitor concentration. For surface tension measurement, the standard Du Noüy ring method was used; for determination of the CMC of the surfactant inhibitor molecules, amongst the 70+ techniques identified in the open literature [90], one of the most common ones –fluorescence spectroscopy – was used.

F.2. Background

F.2.1. Corrosion Inhibitors

Corrosion can lead to severe, and frequently unrecognized, economic losses. Inhibitors are chemical compounds that can protect a metal surface by the formation of a protective film layer [24,25,87]. Corrosion inhibitors have a charged head group that can adsorb on the metal surface and a hydrophobic tail, which can retard the presence of water

molecules. Generally, the mechanism of corrosion mitigation by organic inhibitors is *via* the formation of a protective film layer by adsorption of the inhibitor molecules on the metal surface that retards the corrosive species from interacting with the metal. The mechanism of protection of inhibitors is more discussed is Section F.2.4.

The efficiency of a corrosion inhibitor is defined by Equation (153).

$$EI = \frac{CR - CR_{inh}}{CR} \times 100 \qquad (153)$$

Where:

EI: Inhibition efficiency (%)

CR: Corrosion rate in the absence of corrosion inhibitor (mm/y)

CR_{inh}: Corrosion rate in the presence of corrosion inhibitor (mm/y)

F.2.2. Structure of Organic Corrosion Inhibitors

A corrosion inhibitor has a structure akin to a surfactant (Figure 98), compounds that diminish interfacial forces (e.g., surface tension). Typically, they possess a polar head group containing nitrogen, oxygen, phosphorus, or sulfur, which can displace water molecules and attach to a metal surface [91]. In addition, such molecules have a hydrophobic tail that repels water from the metal surface and, consequently, decreases the surface area exposed to water, thereby decreasing the corrosion rate. Such molecules are termed amphiphilic.

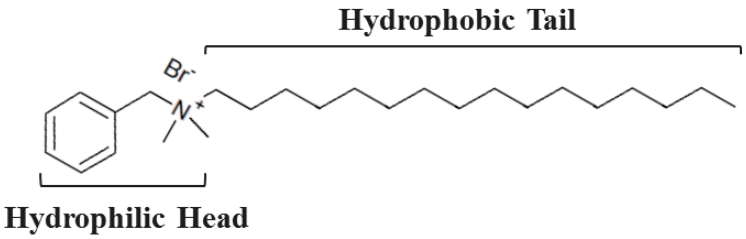

Figure 98

Structure of a quaternary ammonium corrosion inhibitor.

F.2.3. Critical Micelle Concentration (CMC)

Micelle formation is considered as an important measurable property of surfactant corrosion inhibitors. The solubility of surfactant molecules in water at different concentrations is based on the nature of the hydrophobic part of their structure – the non-polar tail. When the alkyl tail length is short, then discrete, unaggregated molecules dissolve in water with a small increase in free energy of solvation, as this just requires reconfiguration of water molecules around the smaller molecule rather than breaking the hydrogen bonds between water molecules [91]. As the tail length of the surfactant increases, the volume that each molecule occupies requires the breaking of the hydrogen bonds (increases in free energy) which eventually results in water molecules being repelled by the hydrophobic part of the surfactant molecules. Therefore, as the concentration of the surfactant having long tail length increases in water, with the smallest interface between water and the hydrophobic part of the molecules being thermodynamically favored, the free energy of the system increases. To reduce the free energy, two different outcomes can be expected [91–93]:

- The surfactant molecules will increasingly migrate to the water-air or water-oil interface [34] oriented with the polar head in the water and the non-polar tail in the air or oil phase until saturation at the interface is approached [92,93].
- The surfactant molecules will start aggregating in the solution once the saturation concentration is exceeded in order to minimize the interface between the non-polar tails of the surfactant and water molecules. The surfactant molecules reorient in a way that the non-polar tails are turned "inwards" (toward each other) and the polar heads face the polar water molecules. This results in the formation of micelles as a thermodynamically favored arrangement with a smaller free energy [91–93] .

F.2.4. Effect of Tail Length and Surface Coverage on Efficiency of Inhibitors

Although coverage of a metal surface by inhibitor molecules is considered as a barrier against corrosive species, the actual mechanism of protection is not akin to a solid, impenetrable layer being present. In contrast with the assumption that surface coverage retards all electrochemical reactions on the surface of a metal, potentiodynamic polarization experiments have shown that the presence of inhibitors on a metal surface does not affect the mass transfer limit of the hydrogen evolution reaction [83]. Moreover, a study using atomic force microscopy (AFM) on a mild steel surface in the presence of an inhibited solution did not seem to correlate with associated corrosion studies using the same mild steel and same inhibitor. Although AFM results had shown surface topography in the nanometer range where the corrosion inhibitor, at 1 CMC value, seemed to fully cover the

---

[34] When it comes to the boundary between water and gas phases, the words *interface* and *surface* are used interchangeably in this paper. That is: *water surface* means the same as the *water-gas interface*. Likewise, *surface tension* means the same as *water-gas interfacial tension*.

surface of the metal, the calculated efficiency in the associated corrosion studies was less than 80% [24].

With continued research, more has been learned about how the alkyl tail length of a corrosion inhibitor influences an inhibitor's efficiency. A more recent study agreed that inhibitor efficiency was proportional to inhibitor alkyl tail length and was able to provide a more fundamental meaning to the mechanistic view of surface coverage [26,27]. This study found that an increase in the alkyl tail length of a model inhibitor increased the activation energy for chemical reactions, such as the dissolution of iron. This is in much better agreement with the fact that an inhibitor is not a solid barrier as it requires the presence of water and the fact that the presence of an adsorbed inhibitor did not influence the mass transfer limit of the hydrogen evolution reaction. Although constrained by the solubility limit of inhibitor components, an increase in the alkyl tail length of an adsorbed inhibitor would increase the activation energy for chemical reactions that occur at the metal surface and, therefore, retard the corrosion rate accordingly.

F.3. Methodology

F.3.1 Synthesis of the Surfactant Inhibitor Model Compounds

Benzyldimethylalkylammonium (BDA) bromide surfactant inhibitor model compounds were synthesized, with systematically increasing alkyl tail lengths, as shown Figure 99 (C# refers to the number of carbon atoms in the alkyl tail of the synthesized molecules) [35].

---

[35] Synthesis of C4 and C16 used in this work were conducted previously by Juan Dominguez Olivo as part of a different study [26].

Table 17 shows the conditions for the synthesis of the model compounds.

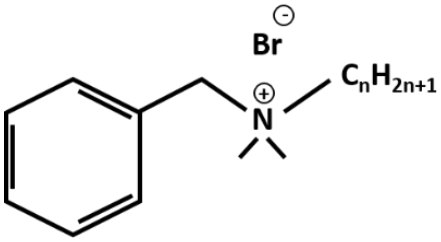

Figure 99

Chemical structure of the benzyldimethylalkylammonium (BDA) bromide inhibitor model compounds (n = 4 –16) [5]. [36]

The experimental setups for synthesis and recovery of the BDA compounds are shown in Figure 100. Initially, N,N-dimethylbenzylamine was mixed with acetonitrile (solvent) in a two-necked round-bottomed flask (24/29 joints) which was then brought to reflux temperature (*ca.* 82°C). Next, the appropriate alkyl bromide reagent was added dropwise to the mixture using an addition funnel. The temperature of the mixture was readjusted to the reflux temperature using a heating mantle connected to a Variac[37]. The fitted condenser, with a steadily maintained flow of water therein, permitted refluxing of the mixture for 24 hours to ensure completion of the amine alkylation reaction (Figure 100.a). The other details related to the syntheses are provided in Table 17. In order to remove the solvent from the final product, rotatory evaporation was used while slowly increasing the temperature of the water bath to 100ºC (Figure 100.b). This along with

[36] Synthesis of C4 and C16 used in this work were conducted previously by Juan Dominguez Olivo as part of a different study[26].
[37] Trade name

vacuum facilitated the complete vaporization of the solvent from the product, as well as any residual reactants.

The structure and purity of the synthesized inhibitor model compounds were confirmed by using ^{1}H-NMR spectra. Melting point measurements were also obtained. BDA-C4 and BDA-C16 used in the experiments were synthesized as described elsewhere.[26]

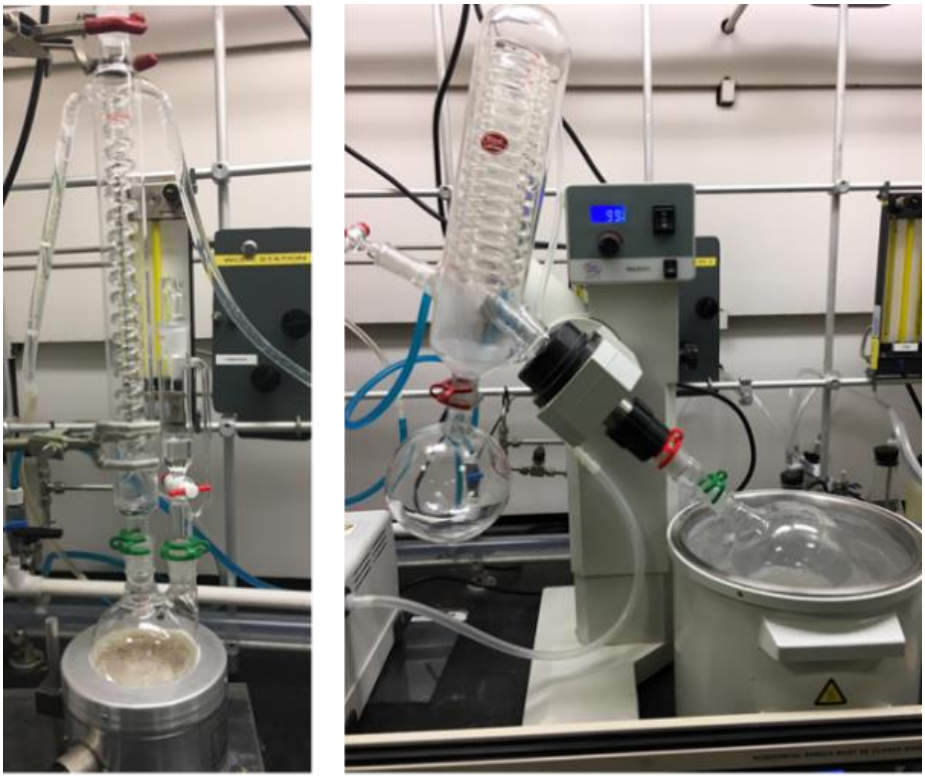

a b

Figure 100

a) Reflux system for amine alkylation. b) Recovery of products by rotary evaporation [4].

Table 17

Test matrix for the synthesis of the BDA inhibitor model compounds [5].

Parameter	Value
Inhibitor Model Compounds Alkyl Tail	C6, C8, C10, C12, C14
N,N-dimethylbenzylamine	0.1 moles
Alkyl bromide	0.1 moles
Acetonitrile	100 ml
Time	24 hours
Reflux Temperature	82°C

F.3.2 Surface Tension Measurements

The surface tension experiments were performed with aqueous solutions at different concentrations of the inhibitor. A concentrated inhibitor solution was dissolved in deionized (DI) water to achieve the desired concentration and at various salinities: 0, 1 and 10 wt.% NaCl concentrations. The temperature of the solutions was adjusted to 30°C using a water bath. For the surface tension measurements, the Du Noüy ring method was used employing a semi-automatic Krüss K20 [38] tensiometer. The Du Noüy ring was decontaminated in between measurements by sequentially cleaning with acetone, deionized water, and a propane flame. To examine if there is any effect of the dissolved CO_2 on the CMC of the inhibitors, for one of the inhibitors (C14) the solution was sparged with CO_2 gas at 1 bar and for 1 hour and surface tension was measured again. All of the measurements were repeated at least three time.

[38] Trade name

F.3.3 Fluorescence Spectroscopy Measurement

In fluorescence spectroscopy, a fluorophore is used which can be excited to emit light more in a non-polar environment compared to a polar environment [94,95]. Nile Red was used as the fluorescence probe in this testing because of its reported accuracy for detecting micelles [96–100]. The emission intensity emitted from a fluorophore molecule is related to the extent of hydrophobicity of its immediate environment. Therefore, the fluorophore molecule is almost nonfluorescent in water or other polar solvents. Below the CMC, when only discrete inhibitor molecules are present in an aqueous solution and hydrophobicity of the medium is low, Nile Red fluoresces to a low extent in this polar solvent. However, when micelles form, the interior part of the micelle becomes a hydrophobic environment from which the fluorophore molecule (Nile Red) will emit light with higher intensity. Therefore, the measurement of the intensity of emitted light can be readily used to detect and quantify the formation of micelles. Meanwhile, the emission intensity of the fluorophore molecules is influenced by several parameters such as solvent polarity, viscosity, temperature, presence of impurities, etc. [101]

The fluorescence spectroscopy measurements were performed at the same conditions as were used for the surface tension measurements and repeated at least twice to confirm the accuracy of the results using a Fluorolog 3-FLC 21[39] spectrofluorometer, manufactured by Horiba [40] Instruments (Edison, NJ). Nile red was purchased from

---

[39] Trade name
[40] Trade name

Molecular Probes[41] or Acros Organics [42]. Dimethyl sulfoxide (DMSO) from Fisher Scientific [43] was used as a non-polar solvent for Nile Red powder. Initially, the Nile Red was dissolved and stirred in DMSO in the ratio of 1 mg/ml in order to be able to add it to water.

F.4. Results and Discussion

F.4.1 Analysis of the Synthesized Inhibitor Model Compounds

The synthesized BDA compounds existed in different forms. BDA-C6, like BDA-C4, was crystalline, while BDA-C8, BDA-C10, and BDA-C12 were ionic liquids as shown in Figure 101. However, BDA-C14, like BDA-C16, existed as a waxy solid. ^{1}H-NMR spectral analysis of the products indicated that the synthesized components are free of unconsumed reactants and acetonitrile solvent. Moreover, it confirmed that the model compounds have the correct structure and are of high purity (+99.5%) as shown elsewhere [4,26]. The range of the melting points for the crystalline model compounds (C4 and C6) and waxy solids model compounds (C14 and C16) are shown in Table 18. Based on the ^{1}H-NMR spectra of the products, it was found that the synthesized components have the desired structure and high purity. Figure 102 shows the ^{1}H-NMR spectra of BDA-C6, BDA -C8, BDA -C10, BDA -C12, BDA -C14 inhibitors in the same manner which the ^{1}H-NMR spectra of BDA -C4 and BDA -C16 have been described elsewhere.[26]

---

[41] Molecular Probes, Inc.
[42] www.acros.com
[43] www.fishersci.com

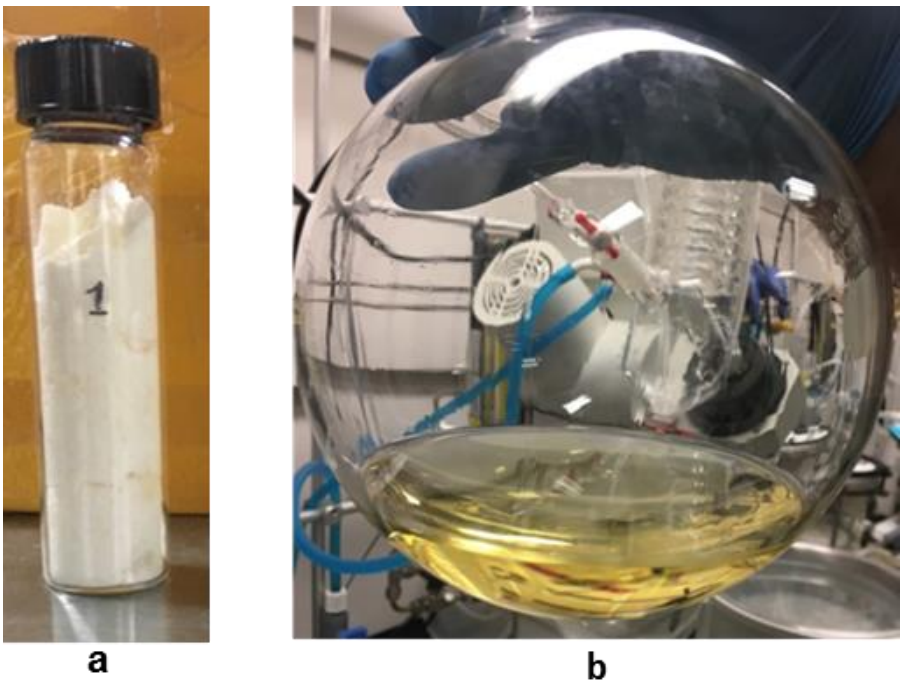

Figure 101

Synthesized inhibitors: a) BDA -C6, crystalline solid; b) BDA -C8, ionic liquid [4].

Table 18

Characterizations of the Synthesized Inhibitor Model Compounds [4].

Compound	State of Mater	Melting Point Range (°C)
BDA -C4	Crystalline solid	148 - 150.5
BDA -C6	Crystalline solid	120.0 - 121.9
BDA -C8	Ionic liquid	-
BDA -C10	Ionic liquid	-
BDA -C12	Ionic liquid	-
BDA -C14	Waxy solid	63.7 - 67.0
BDA -C16	Waxy solid	73.3 - 80

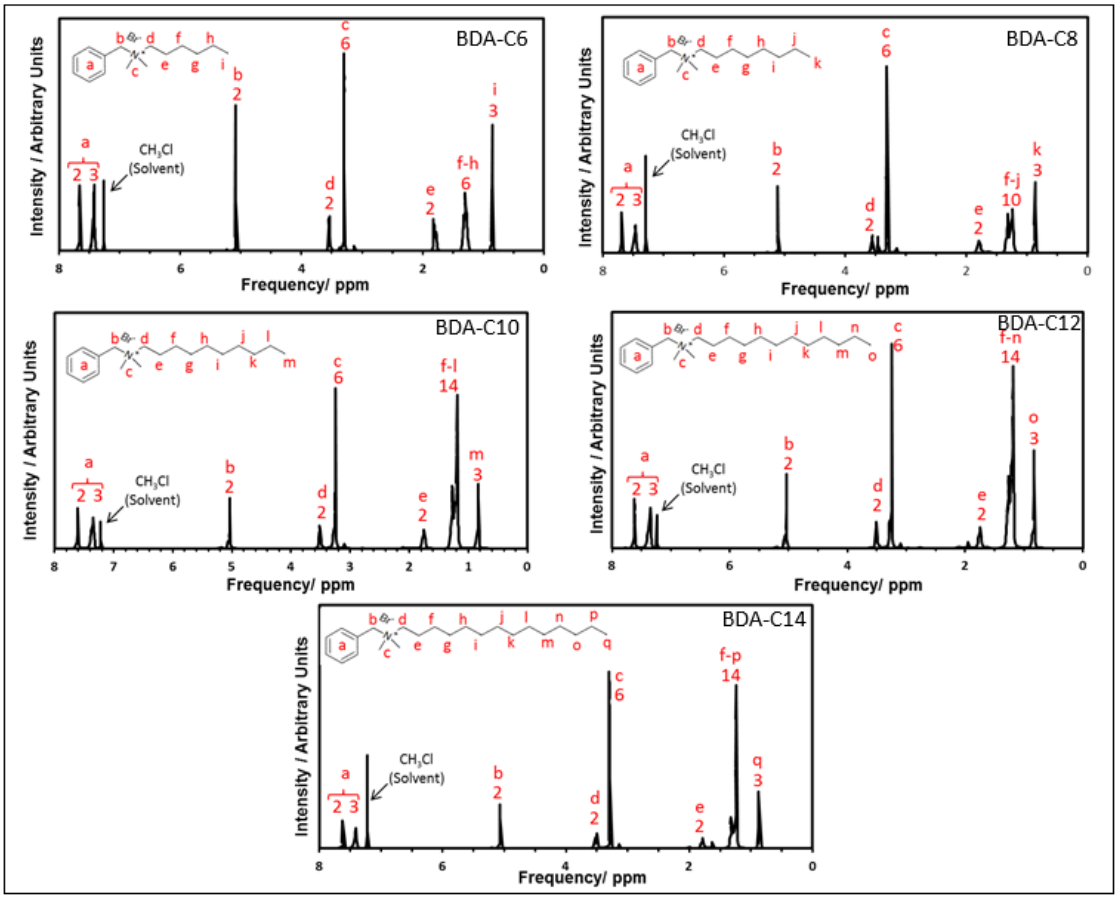

Figure 102

[1]H-NMR spectra of the synthesized BDA inhibitors [4].

F.4.2 Surface Tension Measurements

The first step was to establish if the surface tension measurements were affected by the nature of the dissolved gas, so the effect of the dissolved CO_2 on the CMC of BDA-C14 was examined. The surface tension was measured at progressively higher inhibitor concentrations until an inflection in the curve of surface tension *vs.* inhibitor concentration was observed. As shown in Figure 103, the saturation values for both solutions were approximately the same which indicated that the presence of CO_2 did not affect the

accumulation of the inhibitor molecules at the water-gas interface and all subsequent measurements were done in air, which was much less cumbersome. These measurements were repeated twice with good accuracy, as shown in Figure 103. In the text below, the inhibitor concentration at which the inflection point in the curve of surface tension *vs.* inhibitor concentration is observed will be called the *water-air interfacial saturation concentration* (W-AISC).

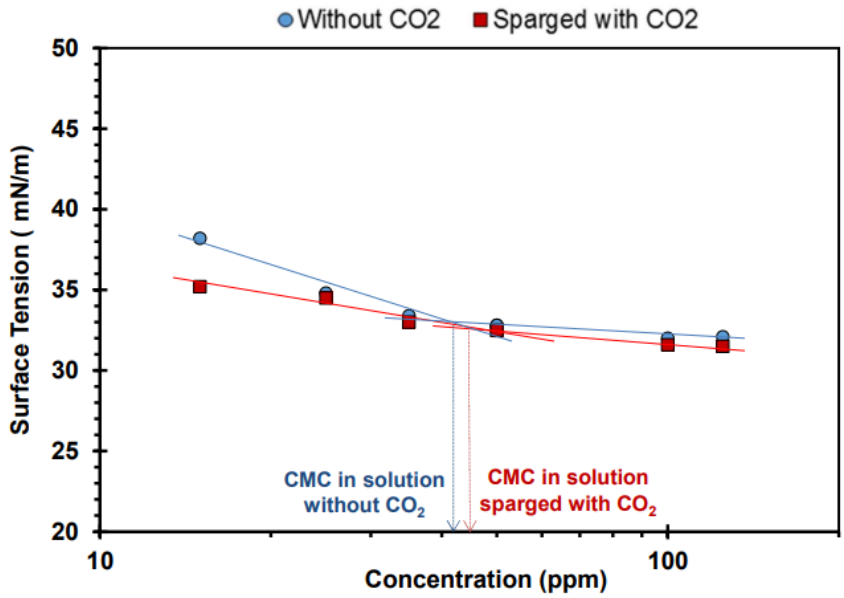

Figure 103

Water-gas interfacial saturation concentration for the BDA-C14 corrosion inhibitor in 1 wt. % NaCl solution with and without dissolved CO_2 gas and at 30°C. Error bars obtained from duplicate measurements are smaller than the data markers [5].

Surface tension measurements of the inhibitor model compounds with different alkyl tail lengths are shown in Figure 104, Figure 105 and Figure 106 for solutions with 0, 1 and 10 wt.% NaCl concentrations, respectively.

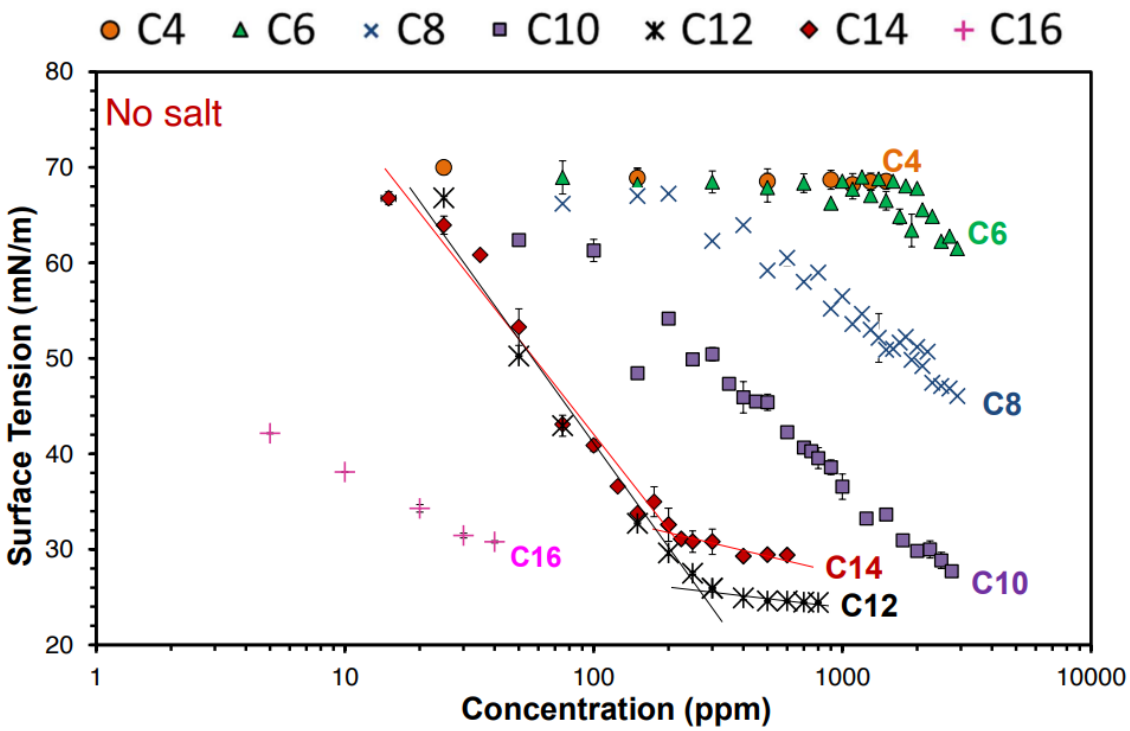

Figure 104

Surface tension vs. concentration curves used for determination of the water-air interfacial saturation concentration (W-AISC) in BDA-Cx solutions without NaCl and at 30°C. Error bars show the minimum and maximum value obtained from multiple measurements [5].

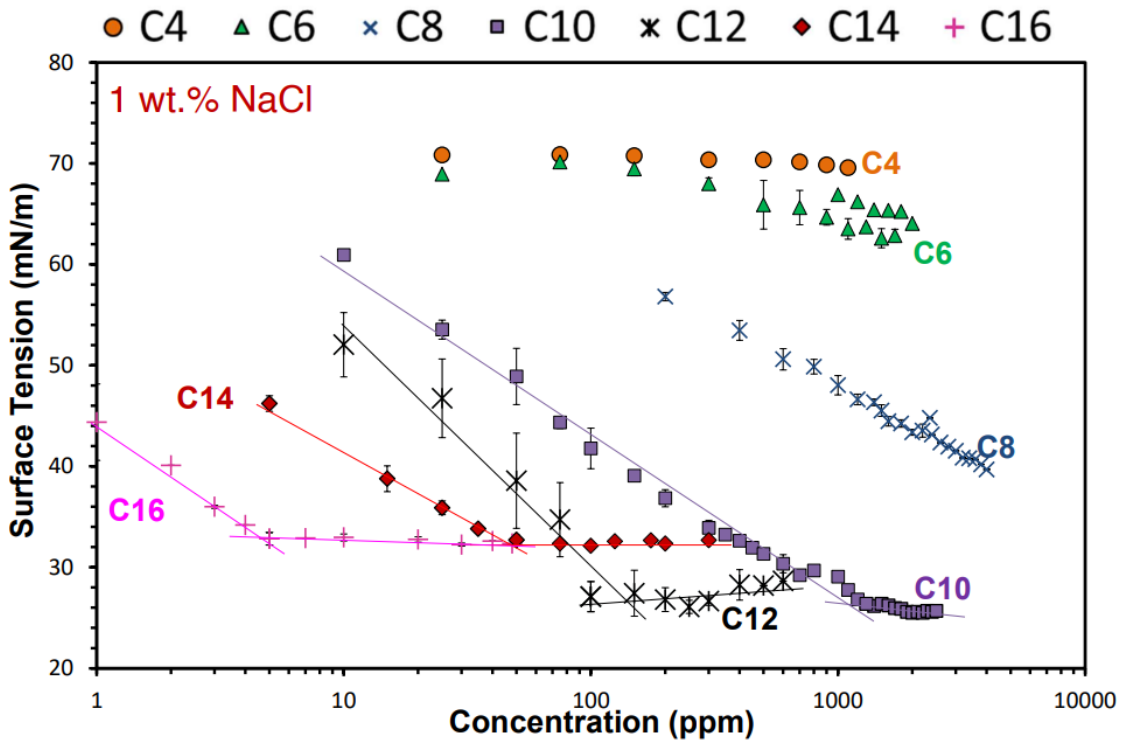

Figure 105

Surface tension vs. concentration curves used for determination of the water-air interfacial saturation concentration (W-AISC) for BDA-Cx inhibitor model compounds in 1 wt. % NaCl aqueous solution and at 30°C. Error bars show the minimum and maximum value obtained from multiple measurements [5].

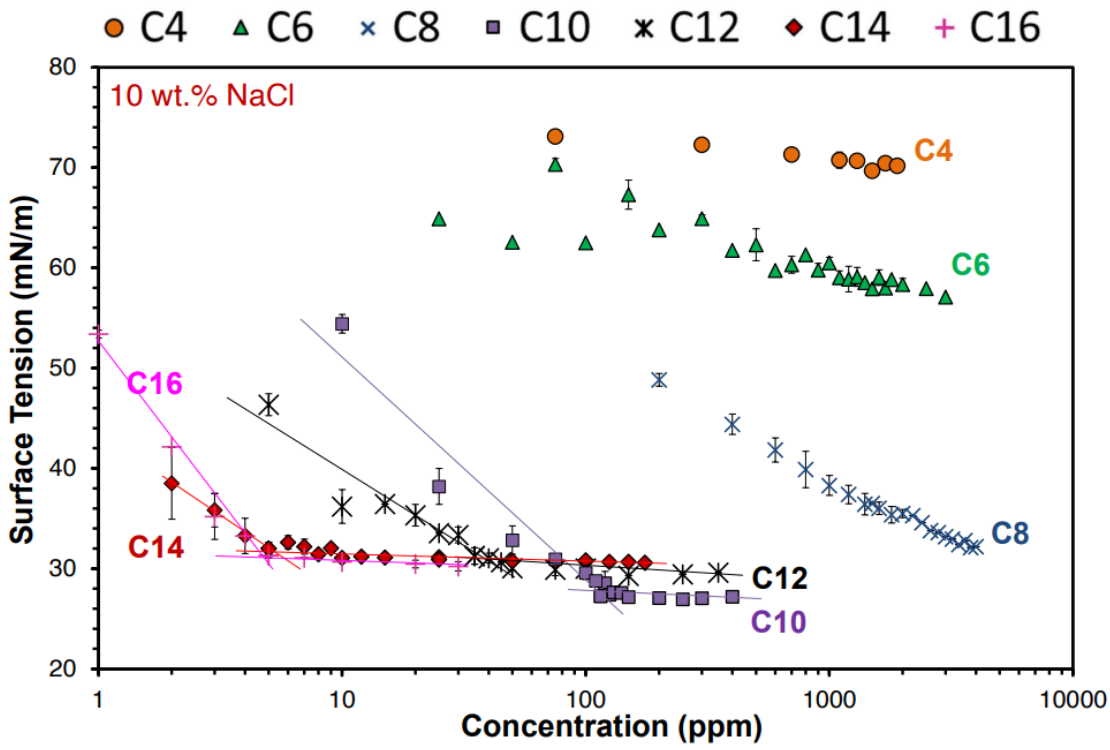

Figure 106

Surface tension vs. concentration curves used for determination of the water-air interfacial saturation concentration (W-AISC) for BDA-Cx inhibitor model compounds in 10 wt. % NaCl aqueous solution and at 30°C. Error bars show the minimum and maximum value obtained from multiple measurements [5].

In a solution without any salt, the presence of BDA-C4 and BDA-C6 inhibitors in concentrations up to 3000 ppm did not significantly change the surface tension of water. This can be explained by the short tail length of these molecules which did not influence the free energy of the system sufficiently to force them to accumulate at the water-air interface in measurable quantities. For larger inhibitor molecules, BDA-C8 and BDA-C10, the surface tension of deionized (DI) water decreased with the increase in inhibitor concentration up to 3000 ppm, but it did not reach a plateau, required to determine the W-

AISC. Larger inhibitor molecules, BDA-C12 and BDA-C14, decreased the surface tension until a plateau was seen and an inflection point could be identified. The largest inhibitor molecule, BDA-C16, has a very low solubility in water, which limited the measurements to concentrations below 50 ppm. In this range, the most dramatic decrease in surface tension was observed at low concentrations, but no clear inflection point in the surface tension curve could be identified.

In addition, the effect of salt concentration on this behavior was investigated. The BDA-C4, BDA-C6, and BDA-C8 inhibitors did not exhibit a plateau at any salt concentration tested here and an inflection point could not be identified. However, the BDA-C10 inhibitor compound which did not show a plateau in a solution without any salt exhibited it at salt concentrations of 1 and 10 wt. %. Moreover, the increase in salt concentration decreased the W-AISC for BDA-C10, BDA-C12, BDA-C14 and BDA-C16 determined by the shift in the position of the inflection point. Figure 107 and Table 19 show the summary of the obtained W-AISC values for different salt concentrations and tail lengths of the inhibitor model compounds.

As is clearly seen in Figure 107, by increasing the tail length of the inhibitor compounds from C4 to C16, the W-AISC decreased. The same is true when it comes to increased salt concentrations which decreased the measured W-AISC.

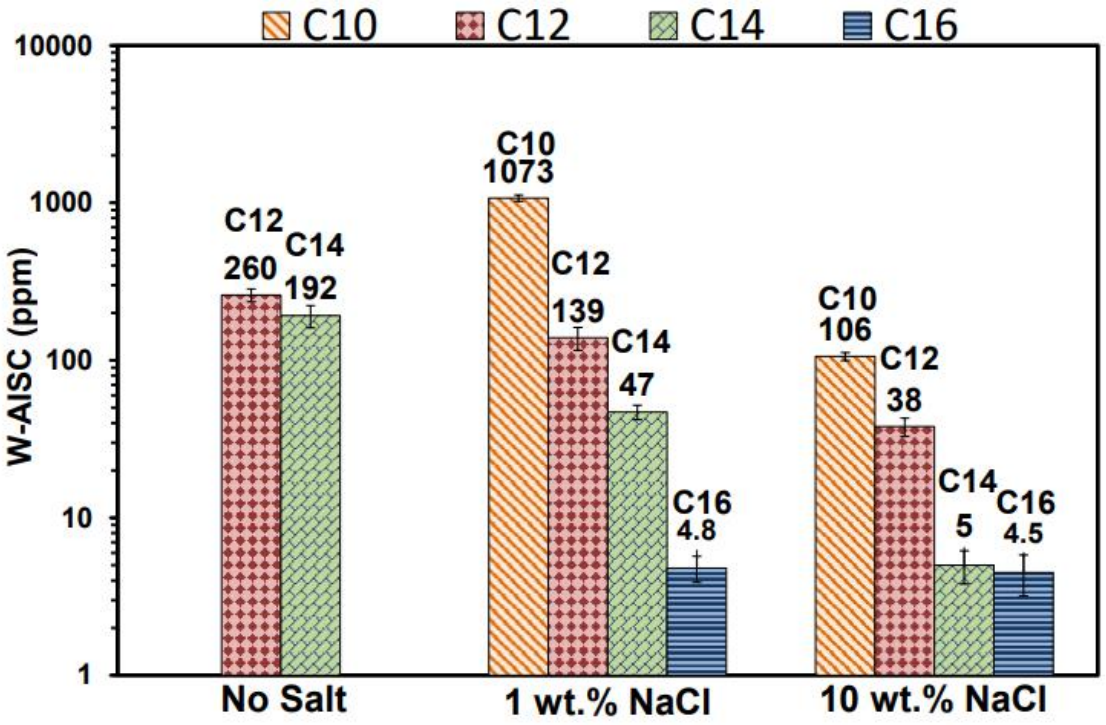

Figure 107

Comparison of water-air interfacial saturation concentration (W-AISC) obtained at different tail lengths of the BDA inhibitor model compounds in solutions with different salinity and at 30°C. Error bars show the variability obtained from multiple experiments[5].

Table 19

Measurement of the critical micelle concentration (CMC) by fluorescence spectroscopy and water-air interfacial saturation concentration (W-AISC) by surface tension measurements, for inhibitor model compounds with different tail lengths dissolved in aqueous solutions with different salinity and at 30°C [5].

Inhibitor Model Compound	Salt Content					
	No salt		1 wt.% NaCl		10 wt.% NaCl	
	W-AISC	CMC	W-AISC	CMC	W-AISC	CMC
BDA-C4	> 1500	Not measured	> 1000	> 5000	> 2000	Not measured
BDA-C6	> 3000	Not measured	> 2000	> 4000	> 3000	Not measured
BDA-C8	> 3000	Not measured	> 4000	> 4000	> 4000	Not measured
BDA-C10	> 3000	> 3000	1073 ± 50	1431 ± 142	106 ± 6	162 ± 24
BDA-C12	260 ± 25	504 ± 25	139 ± 23	345 ± 19	38 ± 5	81 ± 18
BDA-C14	192 ± 31	159 ± 19	47 ± 5	52 ± 5	5 ± 1.2	55 ± 5
BDA-C16	> 50	> 50	4.8 ± 0.9	14.3 ± 0.9	4.5 ± 1.3	8.1 ± 0.3

While the measurements presented above seem to generally fit with the understanding that surface tension should decrease with an addition of a surfactant until a plateau is reached, they do not enable distinguishing between the two possible explanations and therefore neither hypothesis #2 nor hypothesis #1 could be confirmed/rejected. However, one additional observation needs to be emphasized. Irrespective of the tail length, the plateau in the surface tension measurements was always reached at a similar magnitude, somewhere around 30 mN/m. This was true in all inhibitor solutions where the plateau was detected, with or without salt, and indicates a similar state of the water-air interface when it comes to the accumulation of the inhibitor. One can deduce that the most likely explanation for this would be that in all cases the surface became saturated with the inhibitor in more or less the same way, albeit at progressively lower bulk concentrations for larger molecules, which seems to be favoring hypothesis #1. However, the validity of hypothesis #2 and the feasibility of surface tension measurement as an indirect method for the detection of CMC was further tested by comparing the W-AISC with the CMCs obtained by the alternative method, fluorescence spectroscopy.

F.4.3 Fluorescence Spectroscopy Measurements

An example of the raw fluorescence spectroscopy data for BDA-C16 in 1 wt.% NaCl solution is shown in Figure 108.A. Until 15 ppm of inhibitor was added, no peak in emission intensity could be observed. At 15 ppm and higher concentrations, a peak is observed at an emission wavelength of ~640 ± 1 nm. This is clearly indicated in the related graph showing the maximum emission intensity *vs.* concentration in Figure 108.B. Therefore, it can be concluded that somewhere between 10 ppm and 15 ppm of the BDA-

C16 inhibitor concentration in solution micelles started to form and this could be taken as the CMC.

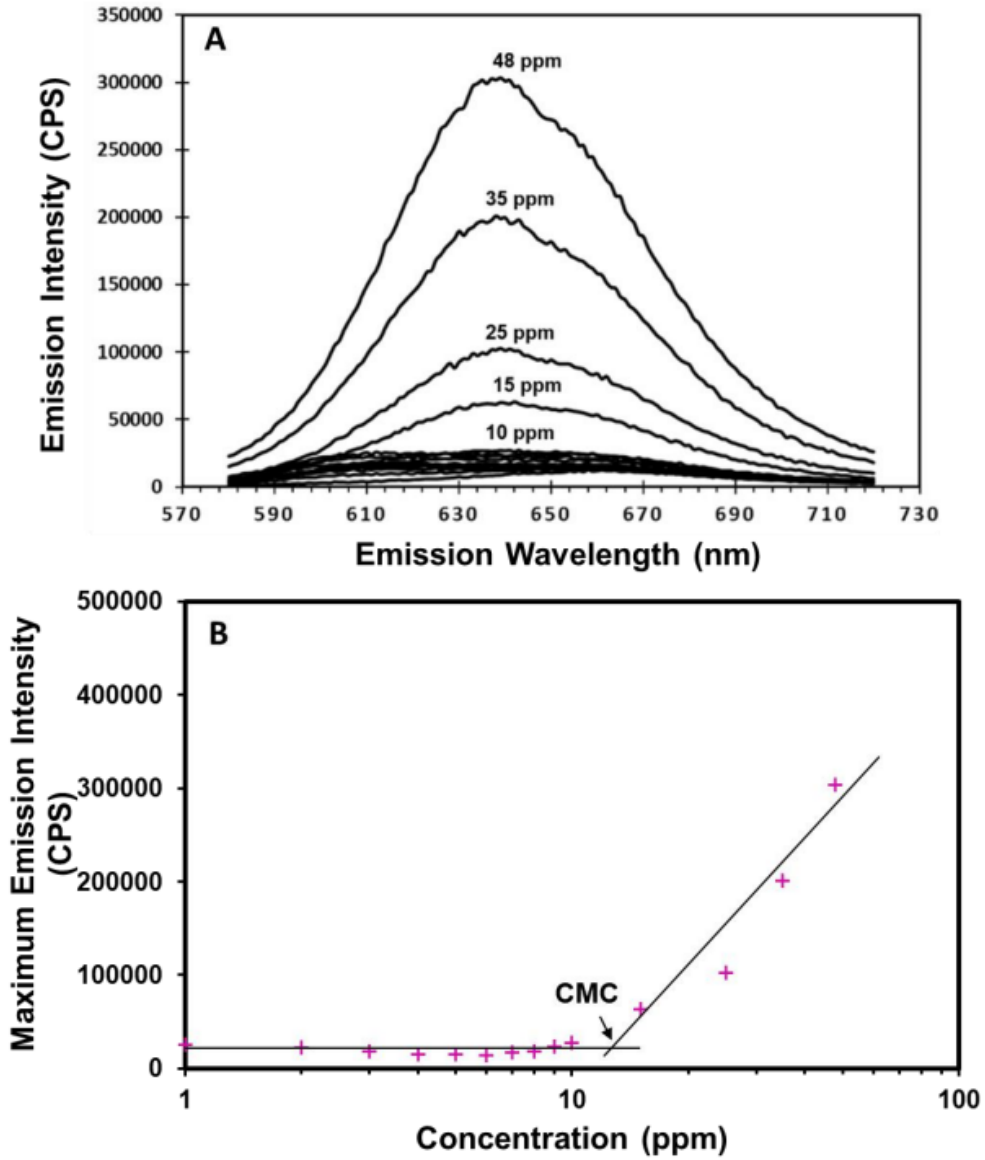

Figure 108

Example of fluorescence spectroscopy results for BDA-C16 inhibitor in a 1 wt.% NaCl aqueous solution and at 30°C. A) raw emission intensity data; B) peak emission intensity as a function of inhibitor concentration [5].

Figure 109 shows the fluorescence spectroscopy results for BDA-C4, BDA-C6, and BDA-C8 in a 1 wt.% NaCl solution. These results show that micelles did not form in these solutions, as no clear increase in peak emission intensity can be observed for any of these inhibitors. There is some increase in peak intensity at around 3000 ppm for BDA-C6 and around 800 ppm for BDA-C8, but this is not conclusive. Overall, these results are in broad agreement with the results of the surface tension measurement technique. Figure 110 shows the fluorescence spectroscopy results for BDA-C10, BDA-C12, BDA-C14 and BDA-C16 in 1 wt. % NaCl, where the CMC value could be found and is reported when the first significant change in emission intensity is measured. The same measurements were performed for solutions having no salt and 10 wt.% NaCl and are shown in Table 19.

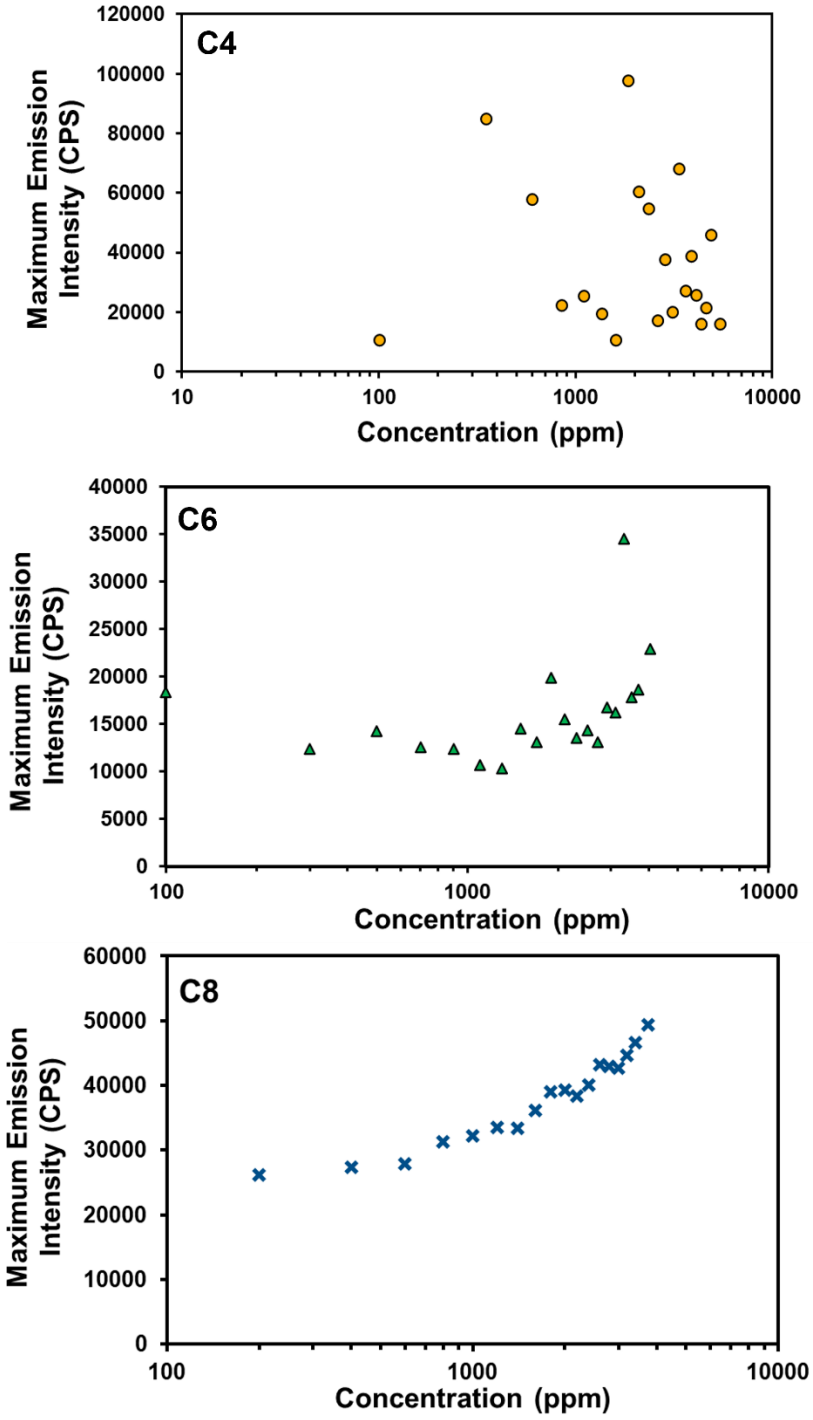

Figure 109

Fluorescence spectroscopy results for BDA-C4, BDA-C6 and BDA-C8 in 1 wt.% NaCl solution and at 30°C [5].

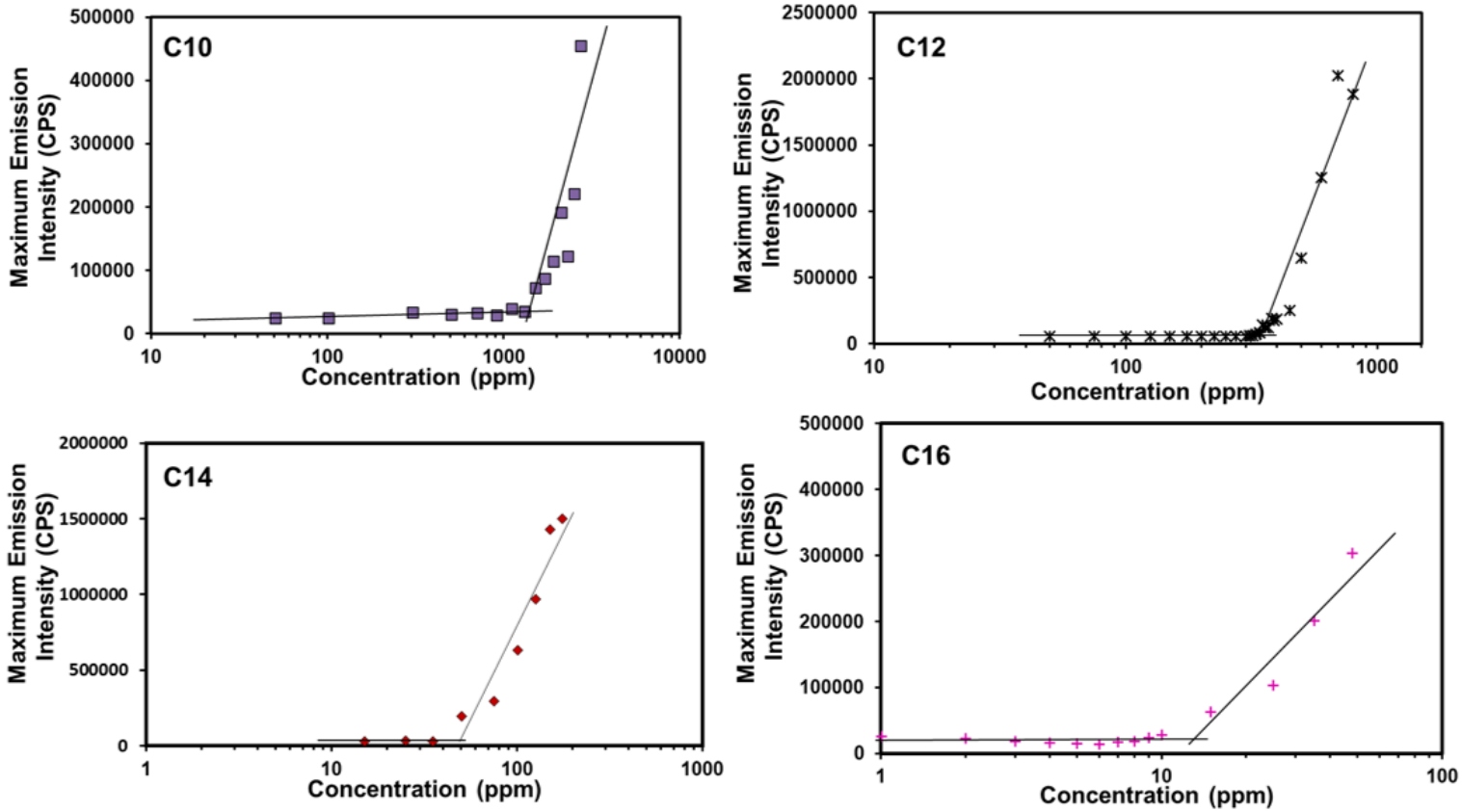

Figure 110

CMC of BDA-C10, BDA-C12, BDA-C14 and BDA-C16 inhibitor aqueous solutions with 1 wt.% NaCl and at 30°C based on fluorescence spectroscopy measurements [5].

F.4.4 Comparison of the W-AISC and CMC

The above data provided us with means to determine whether or not hypothesis #1 or hypothesis #2 are true, i.e., whether CMC can be properly determined by using surface tension measurements. Figure 111 shows the comparisons between W-AISC obtained by surface tension measurements and CMC obtained by fluorescence spectroscopy with respect to the salt concentration and alkyl tail length. It is clear that the concentration values obtained by the two techniques are of the same order of magnitude. Furthermore, both techniques show a decrease in the measured concentration with increased inhibitor tail length, as would be expected. In two of ten cases, the measured W-AISC and CMC are the same, *i.e*., the observed differences are within the range of measurement errors (BDA-C14 in pure water and 1 wt.% NaCl solution). However, for the other eight cases, the CMC measured by fluorescence spectroscopy is higher than the W-AISC determined by surface tension measurements by a large margin – a factor of two or even three. While these observations are not entirely conclusive, they lend more support to hypothesis #1, rather than hypothesis #2. That is, the quaternary ammonium model compounds used in this study first saturate the water-air surface before they saturate the bulk solution leading to micelle formation.

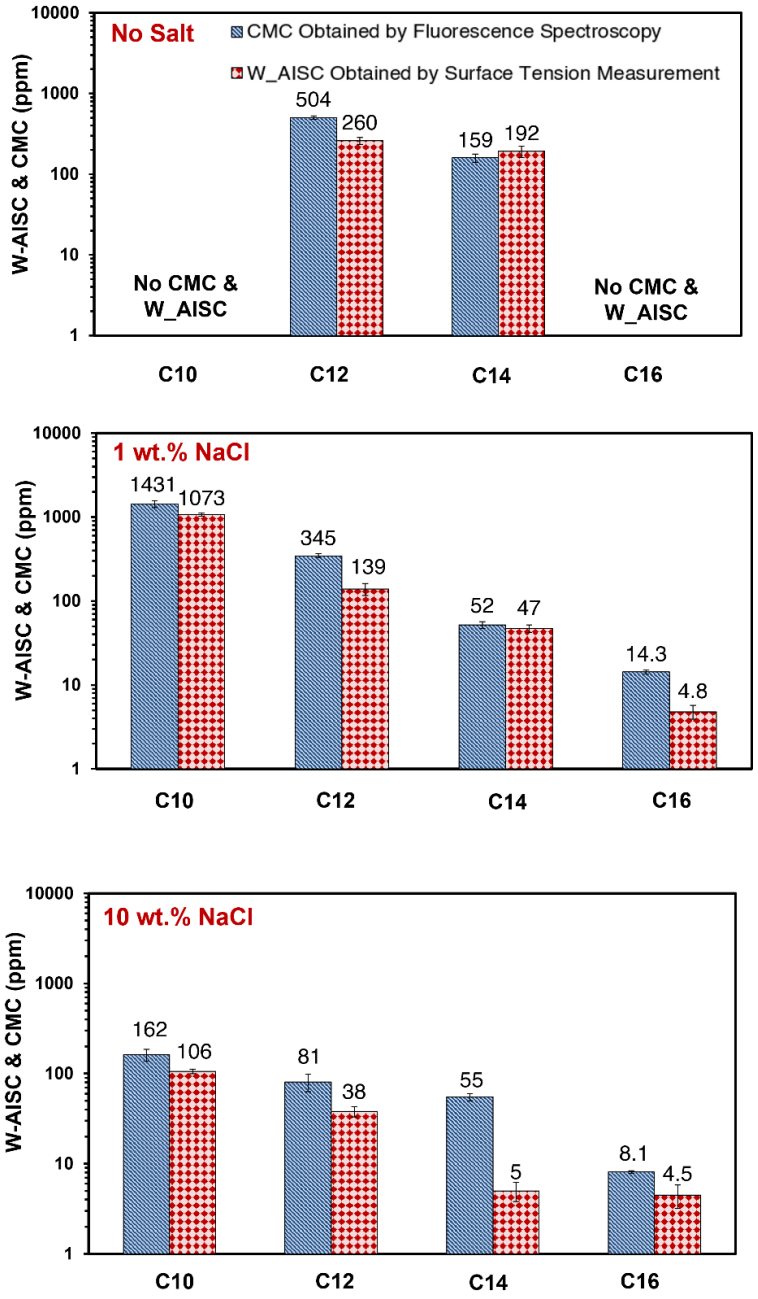

Figure 111

Comparison of CMCs obtained by fluorescence spectroscopy and surface tension measurements in aqueous solutions of BDA-Cx inhibitor model compounds having no salt, 1 wt.% NaCl and 10 wt.% NaCl and at 30°C [5].

The effect of salt also provides support for hypothesis #1, and here is the reasoning behind it. It was already established that the addition of a surfactant inhibitor normally results in the accumulation of the inhibitor molecules on the water-air interface because of the non-polar tails of inhibitor molecules being repelled by the polar aqueous environment; adding salt to the solution does not significantly change this situation, the inhibitor molecules are still repelled from the bulk water towards the water-air interface more or less in the same way. However, at the water-air interface the positive head groups of the inhibitor molecules repel each other, which limits the number of inhibitor molecules that can fit there. Adding NaCl leads to an interaction between the positive head group of the inhibitor and the negative chloride ions what decreases the repulsion forces between the charged inhibitor molecule head groups accumulated at the water-air interface. In other words, in the presence of salt, the inhibitor molecules become more stable near each other at the water-air interface, allowing more of them to be packed there for the same bulk inhibitor concentration. This can be seen by comparing the surface tension of water at a constant bulk concentration of inhibitor and in different salt solutions as shown by the example of BDA-C12 in Figure 112. There, it can be seen that at the same inhibitor concentration, the surface tension is lowered in the presence of salt because more inhibitor molecules are able to accumulate at the water-air interface. For the same reason, the water-air interface saturation occurs at lower bulk inhibitor concentrations [102–104] in the presence of salt and the W-AISC decreases as shown for the example of BDA-C12 in Figure 113. This ability of salt to decrease the repulsion forces between the positive head group of

inhibitors when in close proximity, also helps with formation of micelles, also shown in Figure 113 [103,104].

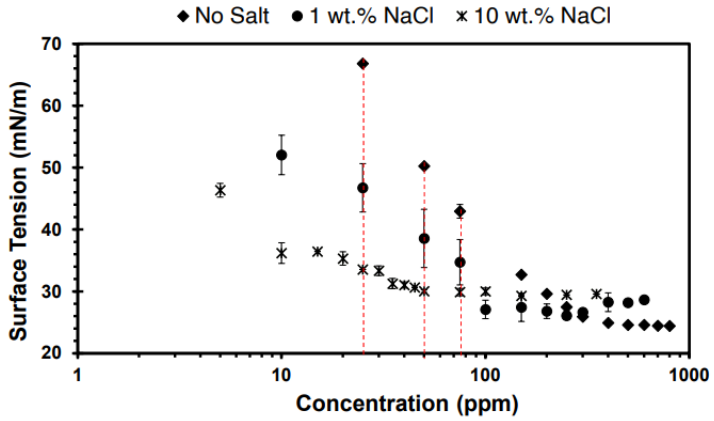

Figure 112

Surface tension measurements of BDA-C12 in aqueous solutions having no salt, 1 wt.% NaCl and 10 wt.% NaCl and at 30°C. Red dotted lines represent locations where surface tensions were measured at the same inhibitor concentration [5].

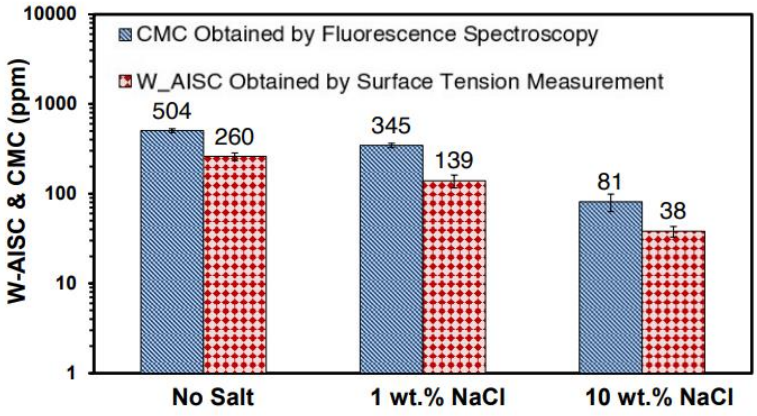

Figure 113

Effect of salt concentration on the CMC and W-AISC of BDA-C12 obtained by the two independent techniques [5].

F.4.5 Corrosion Inhibitor Concentration and Corrosion Mitigation

In addition to the CMC related to bulk saturation, and W-AISC related to water-air surface saturation, another we are now introducing a comparison to a related measure of inhibitor concentration related to corrosion – the so-called *metal surface saturation concentration* (MSSC) [26,105]. It is defined as the corrosion inhibitor concentration at which any further addition of inhibitor to the solution does not decrease the corrosion rate or, in other words, a bulk inhibitor concentration when a maximum coverage by the corrosion inhibitor on the corroding surface is reached [26,105]. It is important to mention that this concentration may or may not correspond to full coverage of the metal surface.

The relationship between the micelle formation in the bulk (at CMC), adsorption of the inhibitors at the water-air interface (W-AISC), and the formation of inhibitor films at the metal surface (at MSSC) is still not understood. Therefore, the MSSC reported in literature was compared with CMC and W-AISC [4,5,26,27] [(44)]. In literates, the MSSC, was obtained by electrochemical corrosion rate measurements performed at different concentrations of the inhibitor model compounds[4,5,26,27]. The concentration beyond which a further decrease in corrosion rate did not occur was considered to be a measure of MSSC, *i.e.*, the concentration at which maximum coverage by the corrosion inhibitor occurred [26]. Based on literatures, all the measurements with the above-mentioned inhibitor model compounds were performed and reported in a CO_2 saturated, 1 wt.% NaCl solution at pH 4.0 and temperature of 30°C [4,5,26,27]. An example of the experimental results and analysis for BDA-C14 is reported elsewhere [4,5] and shown in Figure 114 where it is shown that with

---

[44] The MSCC is obtained by Juan M. Dominguez Olivo and reported elsewhere [4,5,26,27].

an increase in corrosion inhibitor concentration up to 50 ppm the stable corrosion rate is progressively smaller [4,5]. However, above 50 ppm the stable corrosion rate does not change with concentration anymore, which suggests that the adsorbed inhibitor molecules are providing the maximum coverage of the metal surface at bulk concentrations somewhere between 25 ppm and 50 ppm [4,5].

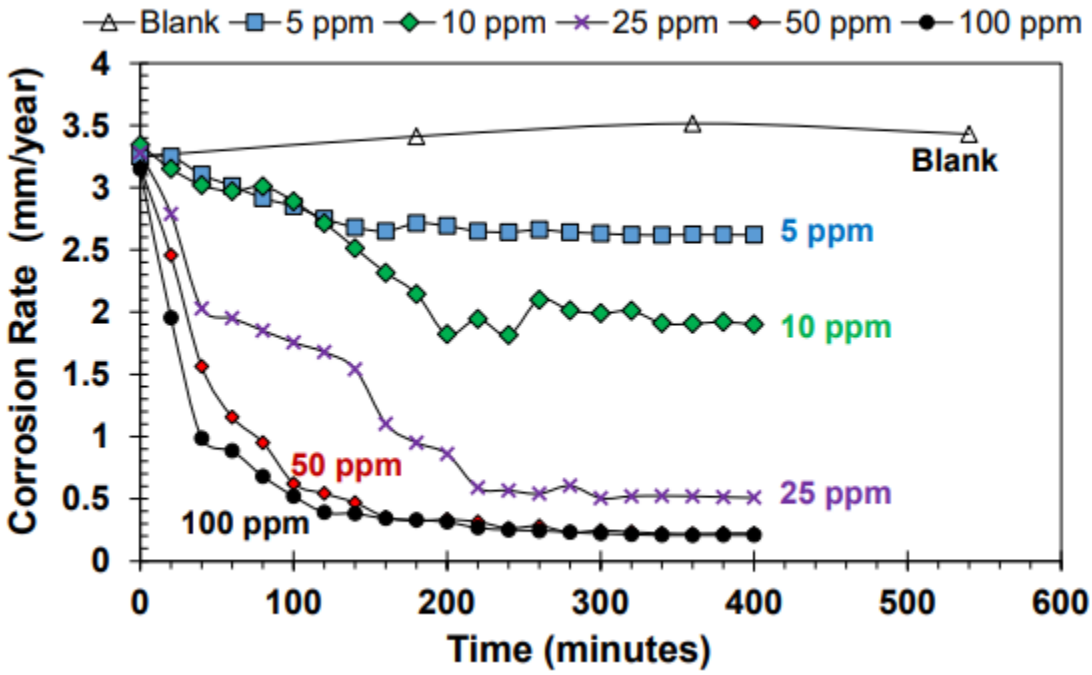

Figure 114

Determining the metal surface saturation by electrochemical corrosion rate measurements with different concentrations of BDA-C14 inhibitor, in a 1 wt.% NaCl aqueous solution, 1 bar CO_2, pH 4 and at 30°C. Experimental data belong to Juan M. Dominguez Olivo and reported elsewhere[4,5]. Figure reconstructed from paper of Moradighadi et al [4,5].

The water-air interfacial saturation concentration (W-AISC), surface tension measurements, the critical micelle concentration (CMC) obtained by fluorescence

spectroscopy and the metal surface saturation concentration (MSSC) reported elsewhere[4,5,26,27] are compared in Figure 115 and summarized in Table 20.

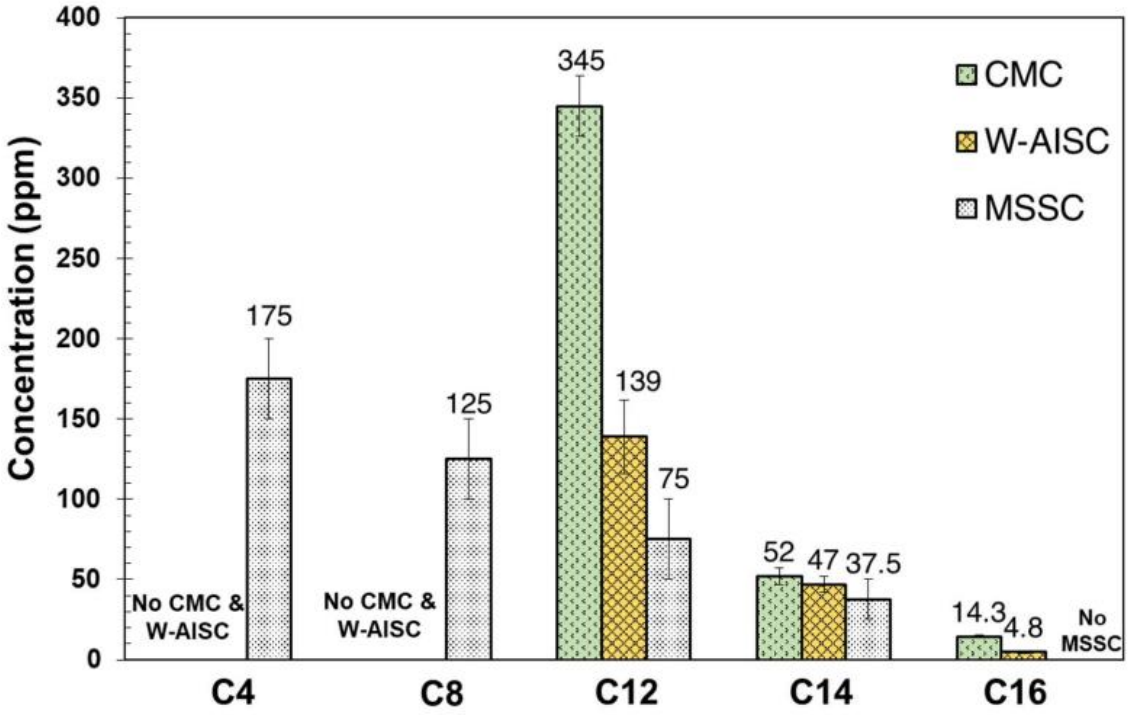

Figure 115

Comparison of the water-air interfacial saturation concentration (W-AISC) obtained by surface tension measurements, the critical micelle concentration (CMC) obtained by fluorescence spectroscopy and the metal surface saturation concentration (MSSC) reported elsewhere[4,5,26,27] for BDA-Cx inhibitor model compounds in an aqueous solution with 1 wt.% NaCl, 1 bar CO_2, pH 4.0 and 30°C.

Table 20

Measured values of the water-air interfacial saturation concentration (W-AISC) obtained by surface tension measurements, the critical micelle concentration (CMC) obtained by fluorescence spectroscopy and the metal surface saturation concentration (MSSC) reported elsewhere[4,5,26,27] *for model inhibitor compounds in an aqueous solution having 1 wt.% NaCl, 1 bar CO_2, pH4 and at 30°C.*

Inhibitor model compound	W-AISC (ppm)	CMC (ppm)	MSSC (ppm)	Stable corrosion rate (mm/year)	Inhibition efficiency
Blank	-	-	-	3.14	-
BDA-C4	> 1000	> 5000	150 - 200	1.15	63%
BDA-C8	> 4000	> 4000	100 - 150	0.69	78%
BDA-C12	139 ± 23	345 ± 19	50 - 100	0.38	88%
BDA-C14	47 ± 5	52 ± 5	25 - 50	0.22	93%
BDA-C16	4.8 ± 0.9	14.3 ± 0.9	> 50	0.15	95%

The following observations can be made:

- For the BDA-C4 and BDA-C8 inhibitors, there was no measurable W-AISC by surface tension measurements and no measurable CMC by fluorescence spectroscopy, *i.e.*, they did not reach saturation either at the metal surface or the bulk solution, yet their MSSC were somewhere in the range 100 – 200 ppm[4,5,26,27].
- For BDA-C12 inhibitor, the CMC was by far the highest (345 ± 19 ppm), the W-AISC was much lower (139 ± 23 ppm), and the MSSC was in the range of 50 – 100 ppm[4,5,26,27]. This suggests that as the concentration of the BDA-C12 inhibitor increases in the bulk solution, the metal surface saturates first, followed by the water-air interface and finally the micelles form in the bulk solution.
- For BDA-C14, the three values are much closer. Again, the metal surface saturates first, somewhere in the range of 25 – 50 ppm[4,5,26,27], while the water-interface and the bulk solution reach saturation somewhere around 47 and 52 ppm, respectively, so all three values are quite similar.
- For BDA-C16, the MSSC was not found within the range of solubility for this inhibitor (0 – 50 ppm) and it was concluded that the metal surface possibly reaches saturation at concentrations higher than 50 ppm[4,5,26,27]. Meanwhile, the saturation of the water-air surface happened in the concentration range 4.8 ± 0.9 ppm while the micelles formed for concentrations more than twice as high, *i.e.*, CMC was in the range 14.3 ± 0.9 ppm. This suggests that the large inhibitor molecule BDA-C16 has a relatively poor affinity for adsorption onto the metal surface when compared

to the propensity to accumulate at the water-air interface and the tendency to form micelles in the bulk solution.

From this, it can be concluded that there is no universal relationship between the A-WISC, the CMC and the MSSC, and that one of those cannot be measured and assumed to be equal to the others. The relationship between the three measure values depends on the inhibitor molecule. The smaller inhibitor molecules (BDA-C4, BDA-C8 and BDA-C12) have shown a stronger tendency to adsorb at the metal surface than to accumulate at the water-air interface or form micelles in the bulk solution. For BDA-C14, this tendency is approximately the same while the large BDA-C16 molecule has shown that it will rather migrate to the water-air interface or form micelles than adsorb onto the metal surface.

Returning to the original hypotheses, the following can be stated:

- **Hypothesis #1 is true.** When the measured surface tension reaches the plateau, this means that the water-air interface is saturated by the surfactant molecules.
- **Hypothesis #2 is false.** When the measured surface tension reaches the plateau, this does not necessary mean that the bulk solution reached saturation with the surfactant molecules and that micelles formed.
- **Hypothesis #3 is also false.** There is no universal relationship between the CMC (the saturation of the bulk solution with the inhibitor) and the maximum corrosion inhibition efficiency achieved at a certain coverage by the adsorbed inhibitor.

The practical implication of this research is the realization that CMC cannot be reliably determined by the surface tension measurements at the water-air interface. Furthermore, when determined by a more suitable alternative technique such as

fluorescence spectroscopy, the CMC cannot be used to find the optimal corrosion inhibitor concentration that will result in maximum protection.

F.5. Summary

- Analyses revealed that for the synthesized inhibitor compounds, first, the water air interface became saturated and then, at higher concentration, micelles started to form in the bulk. Consequently, using surface tension measurement gave information about the concentration at which the water surface became saturated instead of data than can be used for determination of CMC. This means that the surface tension measurement normally used for determining CMC is not an adequate technique. This technique measures the water surface tension which may or may not have a relationship to the formation of micelles in the bulk solution.
- Using fluorescence spectroscopy, for the inhibitors model compounds which form micelles in the tested aqueous solution, it was shown that by increasing the alkyl tail length of the inhibitor or the salt concentration of the bulk solution CMC decreased. Some of the inhibitors with short tail length did not form micelles even in the highly concentrated NaCl aqueous electrolytes.
- Maximum inhibition efficiency reported elsewhere by individual electrochemical corrosion rate experiments at increasing inhibitor concentrations (defined as the metal surface saturation concentration) [4,5,26,27], did not show any specific relationship to the CMC.
- It was shown for the synthesized inhibitor compounds BDA-C4 and BDA-C8, that even if these corrosion inhibitors did not have a measurable CMC value, they provided

corrosion mitigation and had a measurable metal surface saturation concentration as reported elsewhere [4,5,26,27].

Chapter G: Conclusions and Future Work [45]

G.1. Conclusions

This section provides the conclusions regarding the discussions in chapters C-F of this document:

1. At different potentials, the contributions of reactions to the measured impedance might be different compared to their contribution to the measured current density. The experimental data and the relevant analysis in chapter C show that at some specific cathodic potentials, the dominant reaction contributing to the measured current density is due to the cathodic reaction (H^+ reduction) while the dominant reaction contributing to the measured impedance is the anodic reaction (Fe oxidation). Therefore, a model was developed to determine the DC potential at which the EIS data carry more information about the behavior of the desired reactions. The same methodology was used to choose the appropriate DC potential for conducting EIS measurement in order to determine the diffusion coefficients of hydrogen ions in strong acidic solution.
2. The impedance response of cathodic reduction of hydrogen ions, in both strong acid and CO_2 aqueous environments, was modeled which resulted in the development of a new module, LABCORP-AC™, in a corrosion prediction package MULTICORP™. The validity of the model was evaluated considering the effect of

[45] Portions of texts in this chapter appeared in publications of the author: *Electrochimica Acta* 400 (2021): p. 139460, AMPP proceeding paper no. 17900 (2022), AMPP proceeding paper no. 16753 (2021), NACE International proceeding paper no. 13004 (2019), and Corrosion 77 (2020): pp. 266–275 (reference numbers [1–5]).

several variables such as temperature, p_{CO_2}, etc. Moreover, both potentiodynamic sweep and EIS experimental results were predicted reasonably by the model in both strong acid and CO_2 aqueous environments [2].

3. The discussion in chapter E of the current study showed that anions such as Cl^- can displace hydroxide ions from the metal surface, form an additional surface complex, and participate in the anodic reaction parallel to the multi-path mechanism. In weak acidic chloride solution sparged by 1 bar CO_2, the anodic current density increased compared to the strong acidic chloride solutions. However, based on EIS data, there were no additional adsorbed intermediate species in the presence of CO_2, an indication that CO_2 does not directly participate in the anodic reaction and on the bare iron surface. Therefore, Although CO_2 and the associated anions might not displace the hydroxide ions from the metal surface, their presence changes the chemical composition of the adsorbed species, kinetic constants and extent of coverage of the iron surface by different adsorbed intermediated species leading to the change in the kinetics of the underlying reactions.
4. A methodology was introduced to calculate the kinetic constants of the Keddam, *et al.*, multipath mechanism using the theory behind steady state potentiodynamic sweeps and EIS data. The methodology determined the kinetic constants of the mechanism at pH 4 in sulfate strong acidic solution.
5. Analysis of the CMCs of the synthesized inhibitors shows that the values obtained by surface tension measurement in most cases are lower than the CMCs obtained

by fluorescence spectroscopy. Moreover, further analysis revealed that for the synthesized inhibitor compounds, first the water surface becomes saturated, and then at higher concentrations micelles start to form. Consequently, using surface tension measurement for determining CMC gives information about the concentration at which the water surface becomes saturated instead of the formation of micelle. Therefore, using surface tension measurements for determining CMC is not always an adequate technique [5].

6. Using fluorescence spectroscopy, it is shown that by increasing the alkyl tail length of the inhibitor or the salt concentration, CMC decreases. The comparison between metal surface saturation concentration reported elsewhere [4,5,26,27] with the CMC and water surface saturating showed that there is no specific relationship between these values. It is shown in the case of BDA-C4 and BDA-C8, even if the corrosion inhibitors do not have a CMC value, according to other studies [4,5,26,27] they can saturate the metal surface and decrease the corrosion rate [5].

G.2. Future Work

The current work investigated the effect of CO_2 on the mechanism of pure iron dissolution in specific test conditions. Further investigation is required to confirm the conclusions regarding the role of CO_2 on this mechanism as explained below:

- The current study followed the multi-path mechanism to explain the anodic dissolution of pure iron at pH 4.0 and 5.0. However, this mechanism was not investigated at higher pH values, both in this study and the study by Keddam, *et al.*, which is a feature of an aqueous environment related to corrosion of oil and gas

pipelines. Therefore, it is recommended to investigate the same mechanism in the presence and absence of CO_2 in solutions for higher pH values.

- In a weak acidic solution sparged by 1 bar CO_2, the anodic current density increases compared to the strong acidic solution. Although the experimental data showed that CO_2 and the associated anions cannot displace water from the iron surface, they change the chemical composition of the adsorbed species, leading to the change in the kinetic constant of the underlying reactions. However, this conclusion is based on experimental data in solutions sparged by bar CO_2. Based on these findings, it is recommended to study the effect of CO_2 on this mechanism at a higher p_{CO_2}, where the concentration and contribution of the related anions are higher.
- In this work, the mechanism of iron dissolution was investigated in chloride electrolytes in the presence and absence of CO_2 on a fresh iron surface. However, the same mechanism might be affected by the presence of corrosion product layers, such as residual Fe_3C or formed $FeCO_3$ and FeS both in terms of the effect of chemical composition of the surface and mass transfer of anions through the corrosion product layer. Therefore, it is recommended to investigate this mechanism in test conditions where there is the formation of iron carbide, iron carbonate and iron sulfide.

References

1. Moradighadi, N., S. Nesic, and B. Tribollet, *Electrochimica Acta* 400 (2021): p. 139460.
2. Moradighadi, N., Y.S. Choi, and S. Nesic, "Mechanistic Modeling of the Impedance Response of Cathodic Reduction of Hydrogen Ion in Strong Acidic Environments," AMPP, paper no. 17900 (San Antonio, TX: AMPP, 2022).
3. Moradighadi, N., B. Brown, and S. Nesic, "Note on Selecting DC Potentials for EIS Measurements: An Example of Determining the Diffusion Coefficient of Hydrogen Ion in Aqueous Solutions," CORROSION 2021, paper no. 16753 (Virtual: AMPP, 2021).
4. Moradighadi, N., S. Lewis, J.M. Domínguez Olivo, D. Young, B. Brown, and S. Nesic, "Effect of Alkyl Tail Length on CMC and Mitigation Efficiency Using Model Quaternary Ammonium Corrosion Inhibitors," CORROSION 2019, paper no. 13004 (Phoenix, AZ: NACE, 2019).
5. Moradighadi, N., S. Lewis, J.D. Olivo, D. Young, B. Brown, and S. Nešić, *Corrosion* 77 (2020): pp. 266–275.
6. Keddam, M., O.R. Mottos, and H. Takenouti, *J. Electrochem. Soc.* 128 (1981): p. 257.
7. Keddam, M., O.R. Mattos, and H. Takenouti, *J. Electrochem. Soc.* 128 (1981): p. 266.
8. Orazem, M.E., and B. Tribollet, *Electrochemical Impedance Spectroscopy*, 2nd ed. (Hoboken, NJ: John Wiley and Sons, Inc., 2017).
9. "IMPEDANCE | Definition of IMPEDANCE by Oxford Dictionary on Lexico.Com," Lexico Dictionaries, https://www.lexico.com/definition/impedance.
10. Orazem, M.E., N. Pébère, and B. Tribollet, *J. Electrochem. Soc.* 153 (2006): p. B129.
11. Sani, F.M., B. Brown, Z. Belarbi, and S. Nesic, "An Experimental Investigation on the Effect of Salt Concentration on Uniform CO_2 Corrosion" CORROSION 2019, paper no. 13026 (Phoenix, AZ: NACE, 2019).
12. Mansfeld, F., *Electrochimica Acta* 35 (1990): pp. 1533–1544.
13. Lasia, A., *Electrochemical Impedance Spectroscopy and Its Applications,* 1st ed. (New York, NY: Springer, 2014).
14. Kahyarian, A., and S. Nesic, *J. Electrochem. Soc.* 166 (2019): pp. C3048–C3063.
15. Nešić, S., A. Kahyarian, and Y.S. Choi, *Corrosion* 75 (2019): pp. 274–291.
16. Kahyarian, A., M. Singer, and S. Nesic, *Journal of Natural Gas Science and Engineering* 29 (2016): pp. 530–549.
17. Kahyarian, A., "Mechanism and Prediction of Mild Steel Corrosion in Aqueous Solutions Containing Carboxylic Acids, Carbon Dioxide, and Hydrogen Sulfide," PhD dissertation, Ohio University, 2018.
18. Nesic, S., N. Thevenot, J.L. Crolet, and D. Drazic, "Electrochemical Properties of Iron Dissolution in the Presence of CO_2 - Basics Revisited", CORROSION 96, paper no. 96003 (Denver, CO: NACE, 1996).
19. Davies, D.H., and G.T. Burstein, *Corrosion* 36 (1980): pp. 416–422.

20. Kahyarian, A., B. Brown, and S. Nesic, *Corrosion Science* 129 (2017): pp. 146–151.
21. das Chagas Almeida, T., M.C.E. Bandeira, R.M. Moreira, and O.R. Mattos, *Corrosion Science* 120 (2017): pp. 239–250.
22. Almeida, T.C., M.C.E. Bandeira, R.M. Moreira, and O.R. Mattos, *Corrosion Science* 133 (2018): pp. 417–422.
23. Achour, M., and J. Kolts, "Corrosion Control by Inhibition Part I: Corrosion Control by Film Forming Inhibitors," CORROSION 2015, paper no. 5475 (Dallas, TX: NACE, 2015).
24. Pandarinathan, V., K. Lepková, S.I. Bailey, T. Becker, and R. Gubner, *Ind. Eng. Chem. Res.* 53 (2014): pp. 5858–5865.
25. Xiong, Y., B. Brown, B. Kinsella, and S. Nesic, "AFM Studies of the Adhesion Properties of Surfactant Corrosion Inhibitor Films," CORROSION 2013, paper no. 2521 (Orlando, FL: NACE, 2013).
26. Domínguez Olivo, J.M., D. Young, B. Brown, and S. Nesic, "Effect of Corrosion Inhibitor Alkyl Tail Length on the Electrochemical Process Underlying CO_2 Corrosion of Mild Steel," CORROSION 2018, paper no. 11537 (Phoenix, AZ: NACE, 2018).
27. Olivo, D., and J. M, "Electrochemical Model of Carbon Dioxide Corrosion in the Presence of Organic Corrosion Inhibitors," PhD dissertation, Ohio University, 2020.
28. Bockris, J.O., D. Drazic, and A.R. Despic, *Electrochimica Acta* 4 (1961): pp. 325–361.
29. Heusler, K.E., *Zeitschrift Für Elektrochemie, Berichte Der Bunsengesellschaft Für Physikalische Chemie* 62 (1958): pp. 582–587.
30. Linter, B.R., and G.T. Burstein, *Corrosion Science* 41 (1999): pp. 117–139.
31. Baril, G., G. Galicia, C. Deslouis, N. Pébère, B. Tribollet, and V. Vivier, *J. Electrochem. Soc.* 154 (2006): p. C108.
32. Amand, S., M. Musiani, M.E. Orazem, N. Pébère, B. Tribollet, and V. Vivier, *Electrochimica Acta* 87 (2013): pp. 693–700.
33. Musiani, M., M.E. Orazem, N. Pébère, B. Tribollet, and V. Vivier, *Progress in Organic Coatings* 77 (2014): pp. 2076–2083.
34. Gordon, I.A.J., S. Grugeon, H. Takenouti, B. Tribollet, M. Armand, C. Davoisne, A. Débart, and S. Laruelle, *Electrochimica Acta* 223 (2017): pp. 63–73.
35. He, Z., and F. Mansfeld, *Energy and Environmental Science* 2 (2009): pp. 215–219.
36. Roy, S.K., M.E. Orazem, and B. Tribollet, *J. Electrochem. Soc.* 154 (2007): p. B1378.
37. Zhang, S.S., K. Xu, and T.R. Jow, *Electrochimica Acta* 51 (2006): pp. 1636–1640.
38. Nesic, S., J. Postlethwaite, and S. Olsen, *Corrosion* 52 (1996): pp. 280–294.
39. Kahyarian, A., M. Achour, and S. Nesic, "34 - Mathematical Modeling of Uniform CO_2 Corrosion," in Trends in Oil and Gas Corrosion Research and Technologies, ed. A.M. El-Sherik, (Elsevier, 2017), pp. 805–849.
40. Bard, A.J., and L.R. Faulkner, *Electrochemical Methods: Fundamentals and Applications*, 2nd ed. (New York, NY: John Wiley and Sons, Inc., 2001).

41. Levich, V.G., *Physicochemical Hydrodynamics* 1st ed. (Englewood Cliffs, N.J: Prentice-Hall, 1962).
42. Ayagou, M.D.D., M. Tran, B. Tribollet, J. Kittel, E. Sutter, N. Ferrando, C. Mendibide, and C. Duret-Thual, *Electrochimica Acta* 282 (2018): p. 775.
43. Epelboin, I., and M. Keddam, *J. Electrochem. Soc.* 117 (970): p. 1052.
44. Tribollet, B., J. Newman, and W.H. Smyrl, *J. Electrochem. Soc.* 135 (1988): pp. 134–138.
45. Levart, E., and D. Schuhmann, *Journal of Electroanalytical Chemistry and Interfacial Electrochemistry* 28 (1970): pp. 45–47.
46. Newman, J., and K.E. Thomas-Alyea, *Electrochemical Systems,* 3rd ed (Hoboken, NJ: John Wiley and Sons, 2004).
47. Newman, J., *Ind. Eng. Chem. Fundamen*, 7 (1968): pp. 514–517.
48. Woolf, L.A., *J. Phys. Chem.* 64 (1960): pp. 481–484.
49. Farelas, F., M. Galicia, B. Brown, S. Nesic, and H. Castaneda, *Corrosion Science* 52 (2010): pp. 509–517.
50. "MULTICORP - Corrosion Prediction Software", http://www.icmt.ohio.edu/software/multicorp/multicorp%204/index.asp.
51. Harding, M., B. Tribollet, and M.E. Orazem, *Journal of The Electrochemical Society* 164 (2017): pp. E3418–E3428.
52. Nordsveen, M., S. Nešić, R. Nyborg, and A. Stangeland, *Corrosion* 59 (2003): pp. 443–456.
53. De Waard, C., and D.E. Milliams, *Corrosion* 31 (1975): pp. 177–181.
54. Nesic, S., B.F.M. Pots, J. Postlethwaite, and N. Thevenot, *Journal of Corrosion Science and Engineering* 1 (1995).
55. Schmitt, G., and B. Rothmann, *Werkst. Korrosion* 28 (1977): pp. 816–822.
56. Gray, L.G.S., B.G. Anderson, M.J. Danysh, and P.R. Tremaine, "Mechanism of Carbon Steel Corrosion in Brine Containing Dissolved Carbon Dioxide at PH 4," CORROSION 89, paper no. 464 (New Orleans, LA: NACE, 1989).
57. Hurlen, T., S. Gunvaldsen, R. Tunold, F. Blaker, and P.G. Lunde, *Journal of Electroanalytical Chemistry and Interfacial Electrochemistry* 180 (1984): pp. 511–526.
58. Remita, E., B. Tribollet, E. Sutter, V. Vivier, F. Ropital, and J. Kittel, *Corrosion Science* 50 (2008): pp. 1433–1440.
59. T Hurlen, S. Gunvaldsen, and F. Blaker, *Electrochimica Acta* 29 (1984): pp. 1163–1164.
60. Tran, T., B. Brown, and S. Nesic, "Corrosion of Mild Steel in an Aqueous CO_2 Environment – Basic Electrochemical Mechanisms Revisited", CORROSION 2015, paper no. 5671 (Dallas, TX: NACE, 2015).
61. Kahyarian, A., B. Brown, and S. Nesic, "Mechanism of CO_2 Corrosion of Mild Steel: A New Narrative", CORROSION 2018, paper no. 11232 (Phoenix, AZ: NACE, 2018).
62. Kahyarian, A., B. Brown, and S. Nesic, "CO_2 Corrosion, H_2S Corrosion, Organic Acid Corrosion - a Unifying Perspective on Corrosion Mechanisms in Weak Acid Solutions", CORROSION 2019, paper no. 12876 (Nashville, TN: NACE, 2019).

63. Tran, M.T.T., B. Tribollet, V. Vivier, and M.E. Orazem, *Russian Journal of Electrochemistry* 53 (2017): pp. 932–940.
64. Silverman, D.C., *Corrosion* 55 (1999): pp. 1115–1118.
65. Lide, D.R., *CRC Handbook of Chemistry and Physics: A Ready-Reference Book of Chemical and Physical Data,* 75th ed (New York, NY: CRC Press, 1995).
66. Korson, L., W. Drost-Hansen, and F.J. Millero, *Journal of Physical Chemistry* 73 (1969): pp. 34–39.
67. El Miligy, A.A., D. Geana, and W.J. Lorenz, *Electrochemica Acta* 20 (1975): pp. 273–281.
68. Chagas-Almeida, T., O.E. Barcia, R.M. Moreira, M.C.E. Bandeira, and O.R. Mattos, *Electrochimica Acta* 303 (2019): pp. 211–218.
69. Kelly, E.J., *J. Electrochem. Soc.* 112 (1965): p. 124.
70. Dražić, D.M., "Iron and Its Electrochemistry in an Active State," in Modern Aspects of Electrochemistry, eds. B.E. Conway, J.O. Bockris, and R.E. White (Boston, MA: Springer, 1989), pp. 69–192.
71. Heusler, K.E., *Encyclopedia of Electrochemistry of the Elements,* Vol 9. (New York, NY: Marcel Dekker, 1982).
72. Marcus, P., *Corrosion Mechanisms in Theory and Practice,* 3rd ed. (CRC Press, 2012).
73. Aleksanyan, A.Yu., I.I. Reformatskaya, and A.N. Podobaev, *Prot Met* 43 (2007): pp. 125–128.
74. Heusler, K.E., and G.H. Cartledge, *J. Electrochem. Soc.* 108 (1961): p. 732.
75. Barcia, O.E., and O.R. Mattos, *Electrochimica Acta* 35 (1990): pp. 1003–1009.
76. MacFarlane, D.R., and S.I. Smedley, *J. Electrochem. Soc.* 133 (1986): p. 2240.
77. Darwish, N.A., F. Hilbert, W.J. Lorenz, and H. Rosswag, *Electrochimica Acta* 18 (1973): pp. 421–425.
78. Foroulis, Z.A., *J. Electrochem. Soc.* 113 (1966): p. 532.
79. Kuo, H.C., and K. Nobe, *J. Electrochem. Soc.* 125 (1978): p. 853.
80. Schwabe, K., and C. Voigt, *Electrochimica Acta* 14 (1969): pp. 853–869.
81. McCafferty, E., and N. Hackerman, *J. Electrochem. Soc.* 119 (1972): p. 999.
82. Stern, M., and A.L. Geary, *J. Electrochem. Soc.* 104 (1957): p. 56.
83. Olivo, J.M.D., B.A. Brown, and S. Nešić, "Modeling of Corrosion Mechanisms in the Presence of Quaternary Ammonium Chloride and Imidazoline Corrosion Inhibitors" CORROSION 2016, paper no. 7406 (Vancouver, British Columbia, NACE, 2016).
84. Domínguez Olivo, J.M., B. Brown, D. Young, and S. Nesic, "Electrochemical Model of CO_2 Corrosion in the Presence of Quaternary Ammonium Corrosion Inhibitor Model Compounds," CORROSION 2019, paper no. 13392 (Nashville, TN: NACE, 2019).
85. Belarbi, Z., J. Dominguez Olivo, F. Farelas, M. Singer, D. Young, and S. Nešić, *Corrosion* 75 (2019): pp. 1246–1254.
86. Belarbi, Z., F. Farelas, M. Singer, and S. Nešić, *Corrosion* 72 (2016): pp. 1300–1310.

87. Zhu, Y., M.L. Free, R. Woollam, and W. Durnie, *Progress in Materials Science* 90 (2017): pp. 159–223.
88. Malik, Mm.A.A., M.A. Hashim, F. Nabi, S.A. AL-Thabaiti, and Z. Khan, *International Journal of Electrochemical Science* 6 (2011): pp. 1927–1948.
89. Zhao, T., and G. Mu, *Corrosion Science* 41 (1999): pp. 1937–1944.
90. Mukerjee, P., and K.J. Mysels, *Critical Micelle Concentrations of Aqueous Surfactant Systems* (National Standard Reference Data System, 1971).
91. Chandler, D., *Nature* 437 (2005): pp. 640–647.
92. Rosen, M.J., and J.T. Kunjappu, *Surfactants and Interfacial Phenomena*, 4th ed. (Hoboken, NJ: John Wiley and Sons, Inc., 2012).
93. Myers, D., *Surfactant Science and Technology*, 3rd ed. (Hoboken, NJ: John Wiley and Sons, Inc., 2006).
94. Stuart, M.C.A., J.C. van de Pas, and J.B.F.N. Engberts, *Journal of Physical Organic Chemistry* 18 (2005): pp. 929–934.
95. Kurniasih, I.N., H. Liang, P.C. Mohr, G. Khot, J.P. Rabe, and A. Mohr, *Langmuir* 31 (2015): pp. 2639–2648.
96. Chandra, A., J. Vera, W. Durnie, and R. Woollam, "Understanding the Relationship Between Corrosion Inhibitor Adsorption and Surfactant Properties and Micellization: Methodology," CORROSION 2018, paper no. 11467 (Phoenix, AZ: NACE, 2018).
97. Neugebauer, J.M., *Meth. Enzymol.* 182 (1990): p. 239-253.
98. Peterson, A.M., Z. Tan, E.M. Kimbrough, and J.M. Heemstra, *Anal. Methods* 7 (2015): pp. 6877–6882.
99. Liang, Y., Y. Sun, X. Fu, Y. Lin, Z. Meng, Y. Meng, J. Niu, Y. Lai, and Y. Sun, *Artificial Cells, Nanomedicine, and Biotechnology* 48 (2020): pp. 525–532.
100. He, Y., S. Ren, X. Wang, D. Young, M. Singer, Z. Belarbi, M. Mohamed-Saïd, S. Camperos, M.R. Khan, and K. Cimatu, *Corrosion* 78 (2022): pp. 625–633.
101. Lakowicz, J.R., *Principles of Fluorescence Spectroscopy*, 3rd ed. (New York, NY: Springer, 2006).
102. Wan, L.S.C., and P.K.C. Poon, *Journal of Pharmaceutical Sciences* 58 (1969): pp. 1562–1567.
103. Zhou, H., Y. Liang, P. Huang, T. Liang, H. Wu, P. Lian, X. Leng, C. Jia, Y. Zhu, and H. Jia, *Journal of Molecular Liquids* 249 (2018): pp. 33–39.
104. Yu, D., X. Huang, M. Deng, Y. Lin, L. Jiang, J. Huang, and Y. Wang, *The Journal of Physical Chemistry B* 114 (2010): pp. 14955–14964.
105. Murakawa, T., S. Nagaura, and N. Hackerman, *Corrosion Science* 7 (1967): pp. 79–89.

Appendix I: Nomenclature

a	Constant equal to 0.51023 [8,44]
b	Constant equal to -0.61592 [8,44]
b_n	Tafel component
B	Stern-Geary constant (mV)
C_i	Concentration of species i (mol/m^3)
$\bar{C}_i$	Steady state concentration of species i (mol/m^3)
$\tilde{C}_i$	Transient concentration of species i (mol/m^3)
C_{dl}	Double layer capacitance (F/cm^2)
D_i	Diffusion coefficient of species i (m^2/s)
$D_{i,ref}$	Reference diffusion coefficient of species i (m^2/s)
E	Electrode potential (V)
E_a	Activation energy (J/mol)
E_{DC}	Steady state DC potential (V)
F	Faraday constant (C/mol)
f	Frequency (Hz)
$f_{ch,i}$	Characteristic frequency of the loop i
$f_{C_{dl}}$	Characteristic frequency of a double layer capacitance in parallel with a charge transfer resistance
i_T	Total current density (A/m^2)
$\bar{\imath}_F$	Steady state Faradaic current density (A/m^2)
i_F	Faradaic current density (A/m^2)

i_j	Current density of reaction j (A/m^2)
$i_{0,j}$	Exchange current density of reaction j (A/m^2)
$i_{ch,j}$	Charge transfer controlled current density of rection j (A/m^2)
$i_{lim,j}$	Limiting current density of reaction j (A/m^2)
j	Imaginary number
$k_{0,j}$	Rate constant of reaction j
$k_{0,j,ref}$	Reference rate constant of reaction j -
$k_{rds,Fe}$	Rate constant of rate determining step of iron dissolution reaction
k_{f,hy,CO_2}	Rate constant of forward CO_2 hydration reaction (1/s)
k_{b,hy,CO_2}	Rate constant of backward CO_2 hydration reaction (1/s)
K_{hy,CO_2}	Equilibrium constant of CO_2 hydration reaction
K	Dimensionless frequency
n	Number of electrons
p_i	Partial pressure of species i (bar)
p	Dimensionless frequency
R	Universal gas constant (J/ K·mol)
$R_{ct,j}$	Charge transfer resistance of reaction j (ohm·cm^2)
R_{Diff}	Diffusion resistance (ohm cm^2)
R_D	Diffusion resistance (ohm cm^2)
$R_{p,j}$	Polarization resistance of reaction j (ohm·cm^2)
R_s	Solution resistance (ohm·cm^2)

Sc	Schmidt number
t	time (s)
T	Temperature (K)
T_{ref}	Reference temperature (K)
V	Electrode potential (V)
V_{DC}	Steady state DC potential (V)
V_{eq}	Equilibrium potential (V)
y	Distance from the surface (cm)
Z	Impedance (ohm·cm^2)
Z'	Real part of impedance (ohm·cm^2)
$Z^{"}$	Imaginary part of impedance (ohm cm^2)
Z_r	Real part of impedance (ohm cm^2)
Z_J	Imaginary part of impedance (ohm cm^2)
Z_C	Impedance of the double layer capacitance (ohm cm^2)
Z_F	Faradaic impedance (ohm cm^2)
Z_D	Diffusion impedance (ohm cm^2)
Z_{Diff}	Diffusion impedance (ohm cm^2)
α_j	Symmetric coefficient of reaction j
β_i	Maximum surface concentration of the intermediate i
$\boldsymbol{\Gamma}$	Gamma function
δ_i	Characteristic distance for mass transfer of species i (cm)

δ_d	Diffusion layer thickness (m)
δ_r	Reaction layer thickness (m)
λ	Constant (Equation (42))
η	Over potential (V)
μ	Water viscosity (kg/s.m)
μ_{ref}	Reference water viscosity (kg/s.m)
ρ	Density of water (kg/m^3)
ρ_{ref}	Reference density of water(kg/m^3)
ν	Kinematic viscosity (m^2/s)
v_y	Axial velocity (m^2/s)
ξ	Dimensionless position
φ	Phase angle (degrees)
Ω	Rotation speed (rpm)
ω	Angular velocity (rad/s)
θ_i	Dimensionless concentration
θ_i	Surface coverage of species i

Appendix II: Notes on EIS

II.1. Time Constant and Characteristic Frequency [46]

The simple electrochemical cell which can be modeled with an equivalent electrical circuit consists of double layer capacitance in parallel with the charge transfer resistance and all in series with the solution resistance (Figure 116). When the frequency of the applied signal is very high, the DC signal passes through the solution resistance and then the double layer capacitance. But since the frequency is very large, the double layer capacitance becomes similar to a short circuit and almost all the current pass through it. Therefore at large frequency, the impedance shown in the Nyquist plot represents the solution resistance. As the frequency decreases, some of the applied current pass through the double layer capacitance and the rest pass through the parallel charge transfer resistance. Finally, at very low frequency the AC signal becomes similar to a DC signal which only can pass through the charge transfer resistance. Therefore, at low frequency the impedance shown in the Nyquist plot represents the sum of solution resistance and charge transfer resistance.

[46] The general discussion in this section is taken from reference number [8].

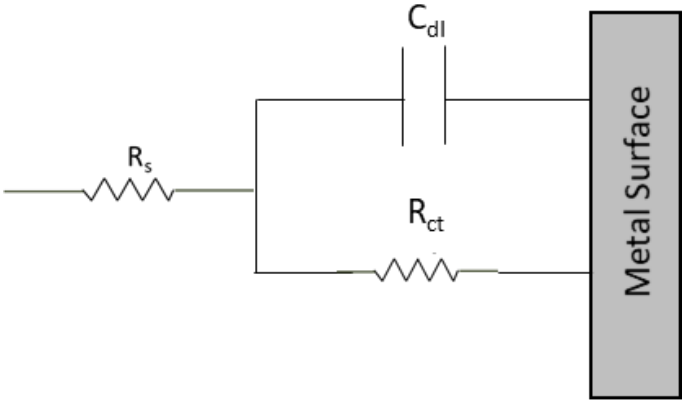

Figure 116

Randles circuit.

The characteristic frequency of an RC and RL circuits is related to the time constants of the circuits. In other words, once the electrode potential is perturbated, the characteristic frequency represents how fast the current reaches to the 63% of its steady state value. The time constant and characteristic frequencies for a system in which there is a resistor in parallel with a capacitor or an inductor in series with a resistor are shown in Equations (154)-(157) [8].

$$\tau_{RC} = RC \tag{154}$$

$$\tau_{RL} = \frac{L}{R} \tag{155}$$

$$\omega_{RC} = 2\pi f_{RC} = \frac{1}{\tau_{RC}} = \frac{1}{RC} \tag{156}$$

$$\omega_{RL} = 2\pi f_{RL} = \frac{1}{\tau_{RL}} = \frac{R}{L} \tag{157}$$

Using the characteristic frequency, the value of the capacitance or inductance can be calculated by Equations (158) and (159) respectively[8].

$$C = \frac{1}{2\pi R f_{RC}} \qquad (158)$$

$$L = \frac{R}{2\pi f_{RL}} \qquad (159)$$

The impedance of an RC circuit shown in Figure 116, can be calculated using Equation (160) which Equations (161) and (162) shows the real and imaginary part of it [8].

$$Z = R_e + \frac{R}{1 + Rj\omega C} \qquad (160)$$

$$Z_r = R_e + \frac{R}{1 + (\omega RC)^2} \qquad (161)$$

$$Z_j = -\frac{\omega C R^2}{1 + (\omega RC)^2} \qquad (162)$$

Therefore, at the characteristic frequency of an RC circuit which is $\omega_{RC} = \frac{1}{RC}$, the real and imaginary parts of the impedance are calculated as shown in Equations (163) and (164) respectively. Consequently, the characteristic frequency of an RC circuit is related to impedance data having maximum imaginary number as shown in Figure 117.

$$Z_r = \frac{R}{2} \qquad (163)$$

$$Z_j = -\frac{R}{2} \qquad (164)$$

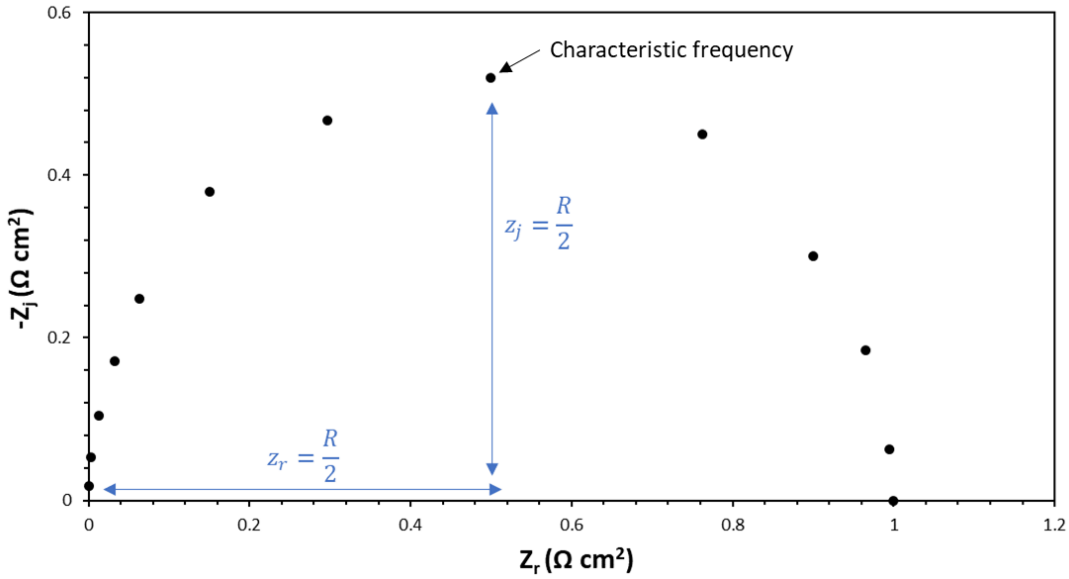

Figure 117

Characteristic frequency of a RC circuit on Nyquist plot.

II.2. Determination of Charge Transfer and Polarization Resistance

Figure 118-Figure 123 show the visual inspection of the Nyquist plots described in Section C.1.3.3 for determining the charge transfer resistance and the polarization resistance. The high frequency loop is related to the double layer capacitance. The charge transfer resistance can be determined at the cross section between the high frequency loop and the x-axis. In addition, the polarization resistance is at the cross section between the lowest frequency loop and the x-axis. This can be further explained by considering an example of an equivalent electrical circuit for the Nyquist plot at OCP+50 mV shown in Figure 118. The Nyquist plot at OCP+50 mV, consists of a high frequency capacitive loop related to the double layer capacitance. Moreover, there are an additional capacitive loop and an inductive loop at low frequency related to adsorbed species.

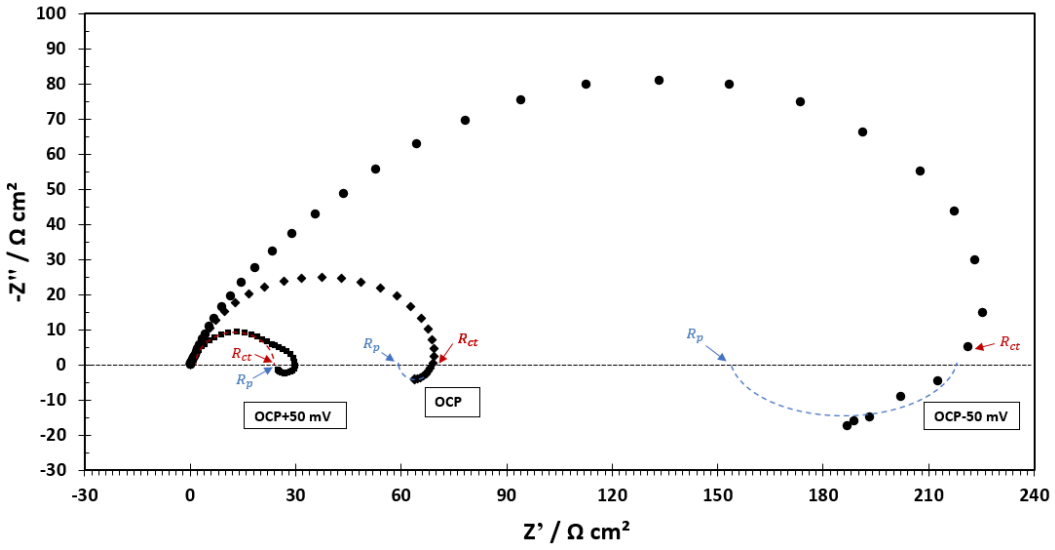

Figure 118

Visual inspection for determining charge transfer and polarization resistances from the Nyquist plots at OCP + 50 mV, OCP, and OCP – 50 mV. Experimental parameters: X65 mild steel RDE, 2000 rpm, pH 4.0, 30°C, aqueous solution saturated at 1 bar CO_2, 0.1 M NaCl supporting electrolyte and frequency range from 10,000 – 0.01 Hz.

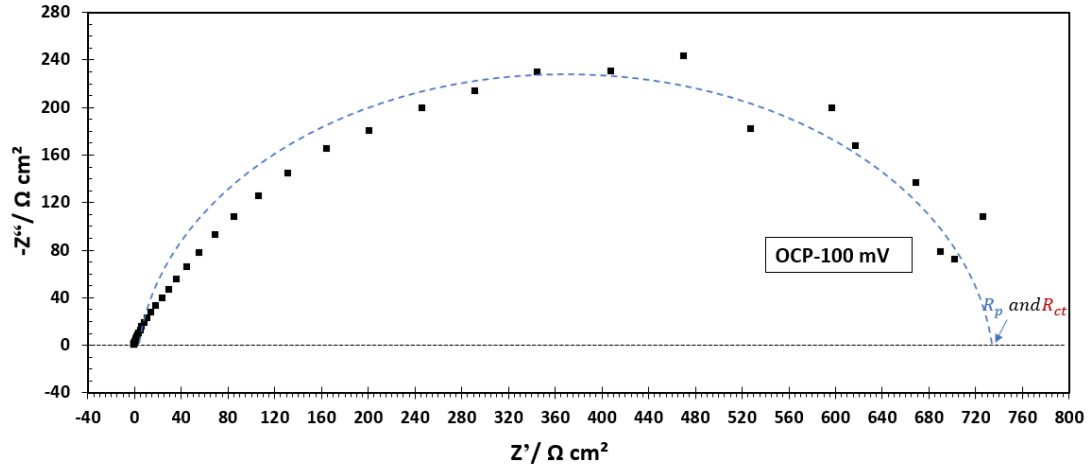

Figure 119

Visual inspection for determining charge transfer and polarization resistances from the Nyquist plot at OCP – 100 mV. Experimental parameters: X65 mild steel RDE, 2000 rpm, pH 4.0, 30°C, aqueous solution saturated at 1 bar CO_2, 0.1 M NaCl supporting electrolyte and frequency range from 10,000 – 0.01 Hz.

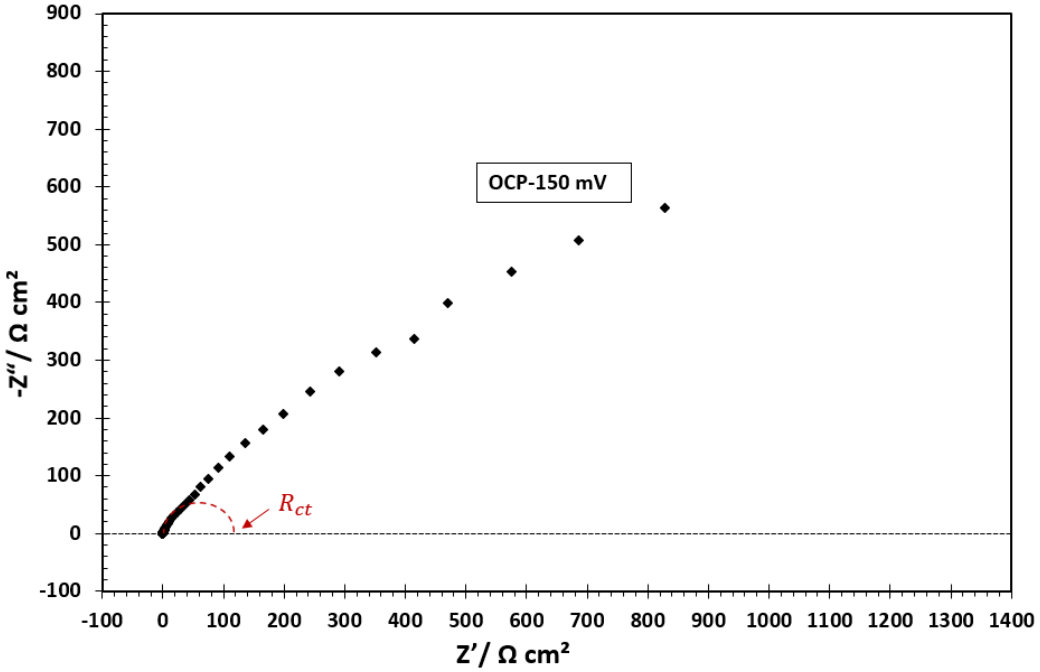

Figure 120

Visual inspection for determining charge transfer resistance from the Nyquist plot at OCP – 150 mV. Experimental parameters: X65 mild steel RDE, 2000 rpm, pH 4.0, 30°C, aqueous solution saturated at 1 bar CO_2, 0.1 M NaCl supporting electrolyte and frequency range from 10,000 – 0.01 Hz.

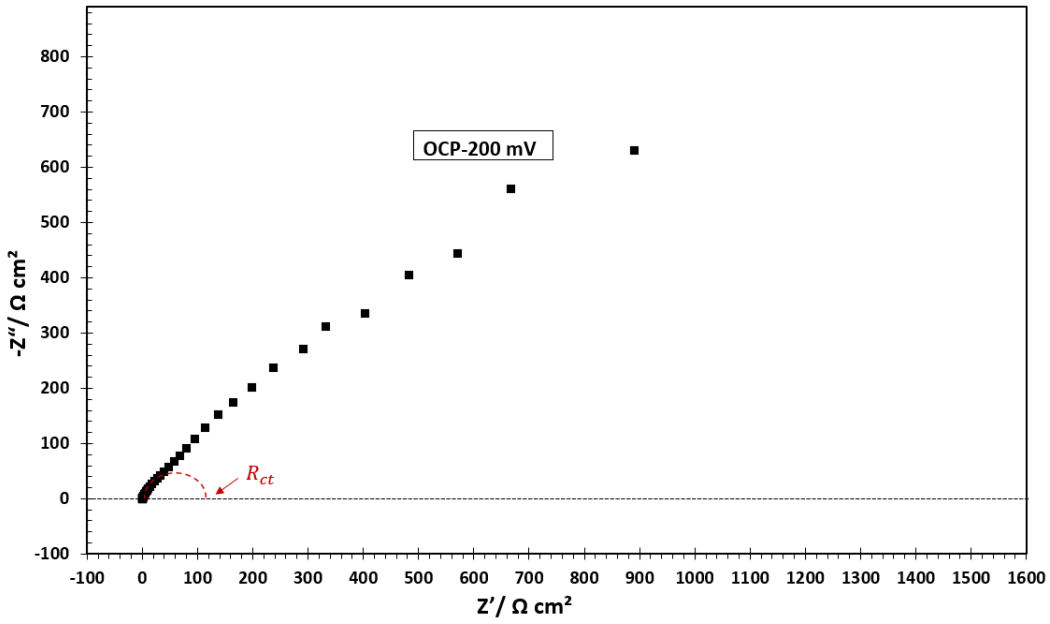

Figure 121

Visual inspection for determining charge transfer resistance from the Nyquist plot at OCP – 200 mV. Experimental parameters: X65 mild steel RDE, 2000 rpm, pH 4.0, 30°C, aqueous solution saturated at 1 bar CO_2, 0.1 M NaCl supporting electrolyte and frequency range from 10,000 – 0.01 Hz.

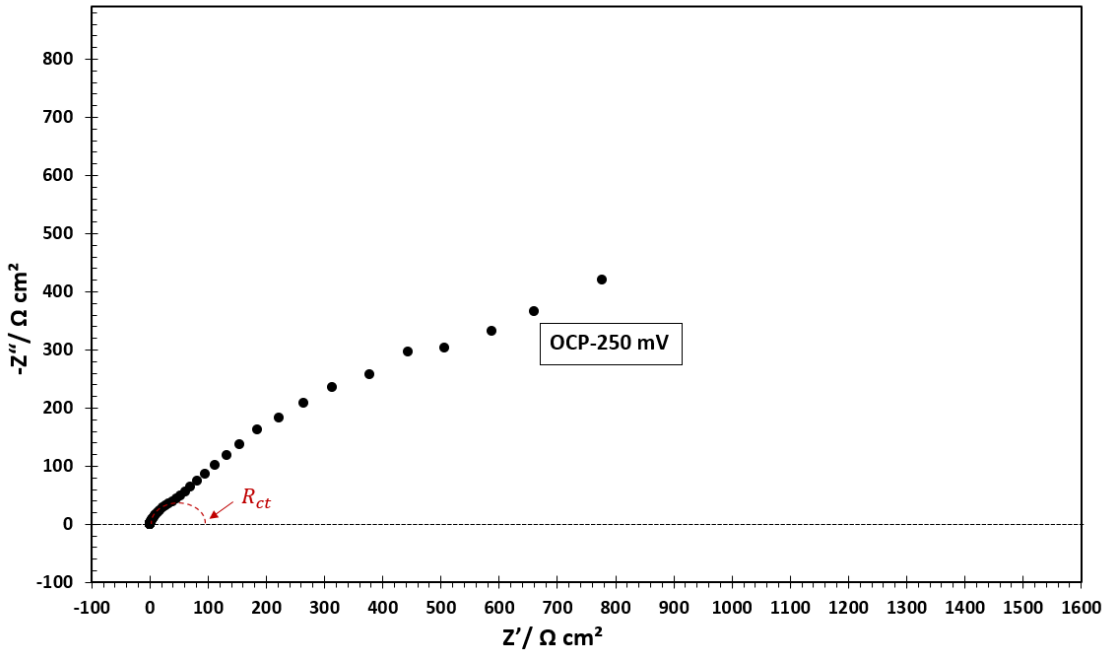

Figure 122

Visual inspection for determining charge transfer resistance from the Nyquist plot at OCP – 250 mV. Experimental parameters: X65 mild steel RDE, 2000 rpm, pH 4.0, 30°C, aqueous solution saturated at 1 bar CO_2, 0.1 M NaCl supporting electrolyte and frequency range from 10,000 – 0.01 Hz.

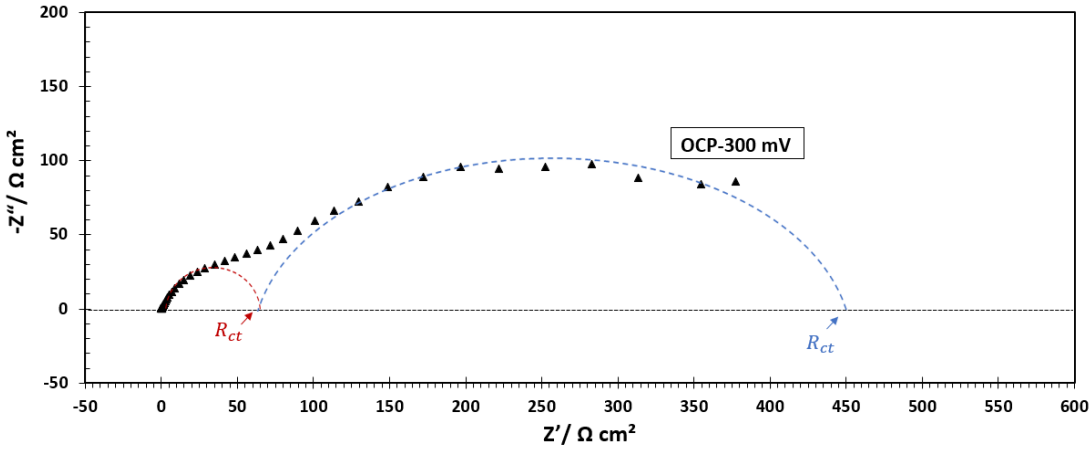

Figure 123

Visual inspection for determining charge transfer and polarization resistances from the Nyquist plot at OCP – 300 mV. Experimental parameters: X65 mild steel RDE, 2000 rpm, pH 4.0, 30°C, aqueous solution saturated at 1 bar CO_2, 0.1 M NaCl supporting electrolyte and frequency range from 10,000 – 0.01 Hz.

Figure 124.a shows the equivalent electrical circuits for the Nyquist plot at OCP+50 mV shown in Figure 118. At very high frequency, the impedance of the double layer capacitance is low, therefore, it can be assumed that it acts similar to a short circuit where all the current path through it as shown in Figure 124.b . Therefore, the impedance is equal to the solution resistance [47].

At relatively lower frequencies range, the impedance of double layer capacitance is high enough, and potential drops across it. Therefore, part of total current path through it, while the rest of it path through the R_{ct} . Meanwhile, as the frequency is relatively high, the impedance of C_1 is very low. Therefore, C_1 acts similar to a short circuit as shown in

[47] Figure 118 shows the corrected Nyquist plot by subtraction of solution resistance from the real part of impedance data.

Figure 124.c. Consequently, at a specific high frequency range, the impedance response is related to double layer capacitance in parallel with a charge transfer resistance as shown in Figure 124.c.

At relatively lower frequency, the impedance of the double layer capacitance is high to an extent that current cannot path through it. At this condition, the double layer capacitance can be assumed to behave similar to an open circuit. Therefore, all the current path through R_{ct} as shown in Figure 124.d. This is the frequency at which the relaxation of the double layer capacitance in parallel with the charge transfer resistance terminates, and the impedance is equal to the summation of the solution resistance and charge transfer resistance shown by the cross resection of the high frequency loop and the x-axis.

The same logic discussed above is also true at lower frequency where the capacitive loop and then inductive loop appear in succession and through the paths shown in Figure 125.E, Figure 125.F, Figure 125.G and Figure 125.H respectively. Note that R_2 and C_2 have negative values representing the low frequency inductive loop.

Finally at very low frequency, where there is almost a direct current, the impedance of the capacitances is so high that they all act similar to an open circuit and the current path through the resistors in the circuit. Therefore, the polarization resistance can be determined using Equation (165) where R_{ct} and R_1 have positive values while R_2 has a negative value. At this frequency, the low frequency inductive loop crosses the x-axis.

$$R_p = R_{ct} + R_1 + R_2 \tag{165}$$

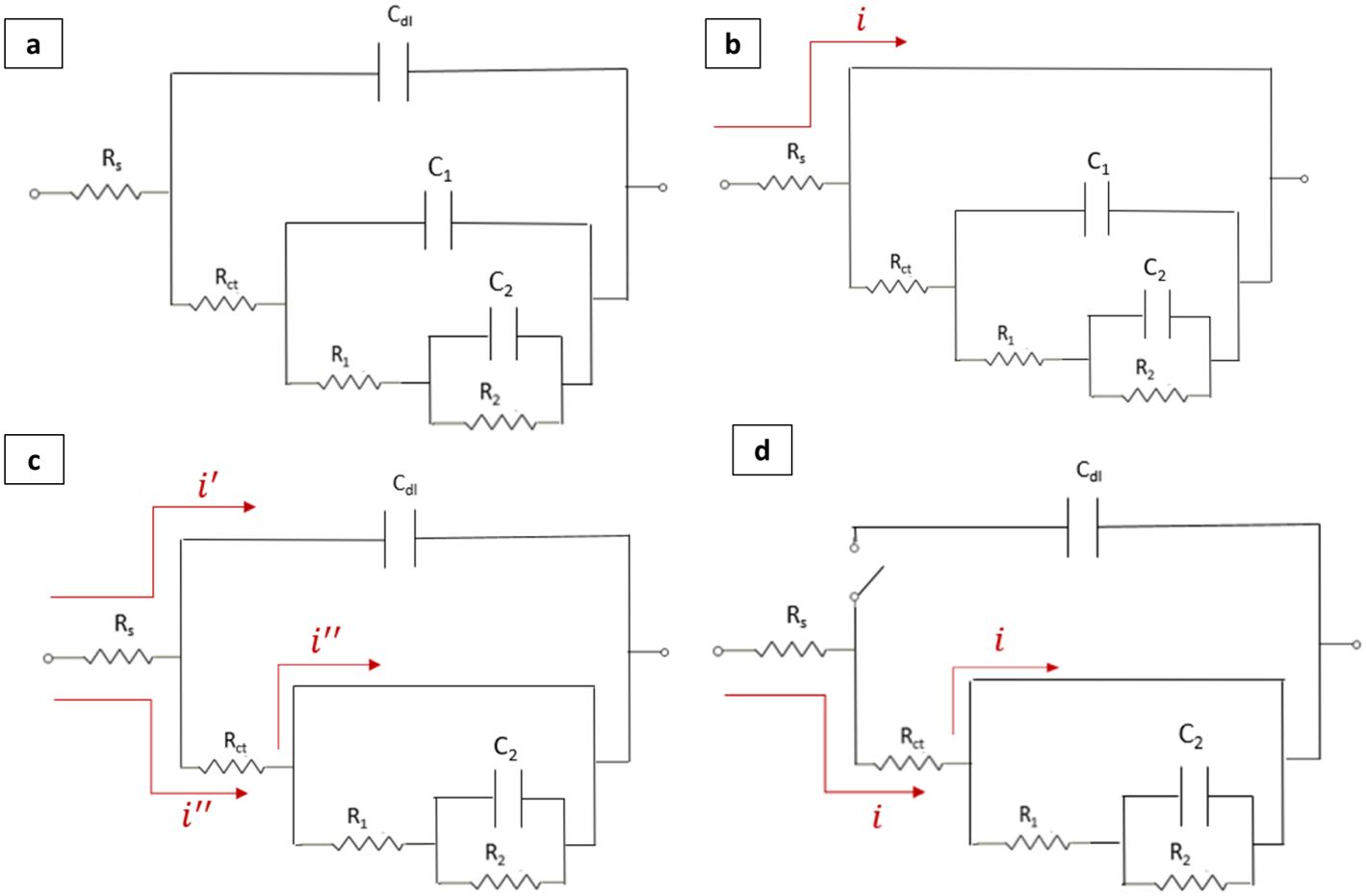

Figure 124

Equivalent electrical circuits for the Nyquist plot at OCP+50 mV shown in Figure 118.Part 1.

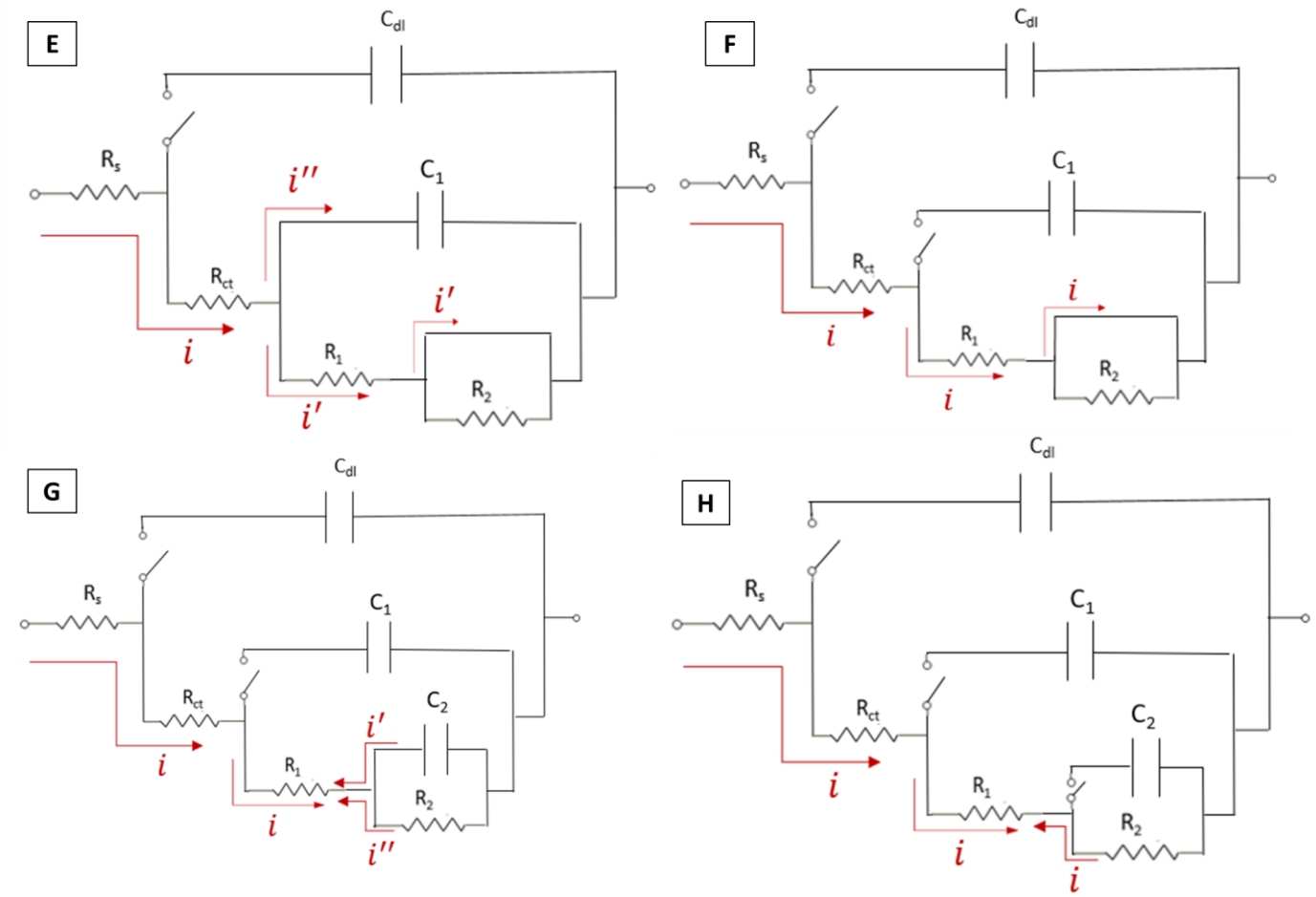

Figure 125

Equivalent electrical circuits for the Nyquist plot at OCP+50 mV shown in Figure 118.Part 2.

The same logic can be applied for the rest of Nyquist plots shown in Figure 118-Figure 123 where the relative electrical equivalent circuits are shown in Figure 126. Equivalent electrical circuit “a” is related to the Nyquist plots at OCP and OCP-50 mV, considering that C_1 and R_1, related to the low frequency inductive loop, have negative values. the same circuit can represent the Nyquist plot at OCP-300 mV considering that all the elements have positive value. Equivalent electrical circuit “b” is valid for the Nyquist plot at OCP-100 mV. In addition, Equivalent electrical circuit “a” and “c” represent the impedance behavior at OCP-150 mV, OCP-200 mV an OCP-250 mV, where R_1 has a large value.

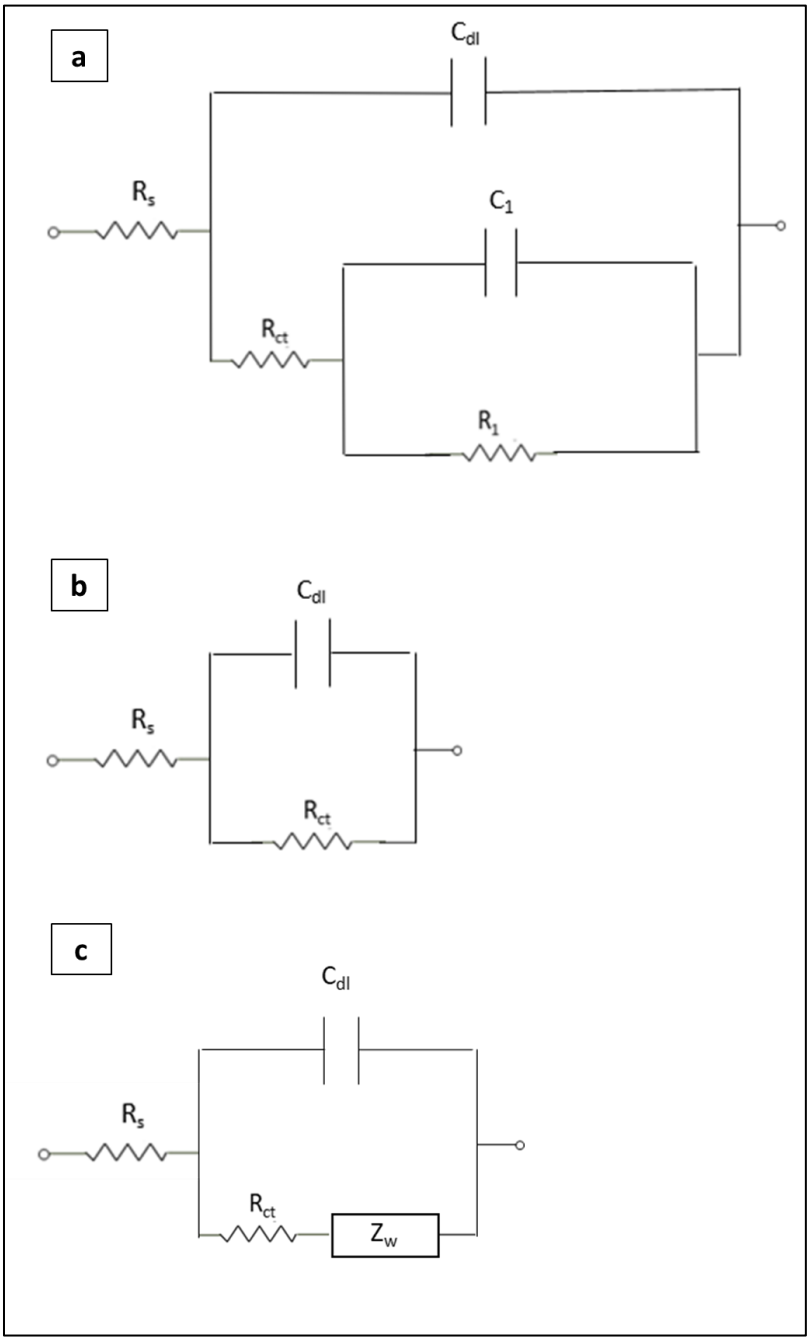

Figure 126

Equivalent electrical circuits for the Nyquist plots shown in Figure 118-Figure 123.(a) related to the Nyquist plots at OCP, OCP-50 mV and OCP-300 mV. (b) related to the Nyquist plot at OCP-100 mV. (c) related to the Nyquist plots at OCP-150 mV, OCP-200 mV and OCP-250 mV.

II.3. Kinetic Models and Diffusion Impedance [48]

The mathematical equations explained in this section is a brief description of the mathematical derivations provided elsewhere[8]. Transient current density of an electrochemical reaction dependent on electrode potential and surface concentration (Reaction (166)) can be shown similar to Equation (167) [8]. A Taylor expansion of the current density at $\bar{\imath}_{AB}$ is expressed in Equations (168) [8].

$$A + B \rightarrow AB^{n+} + ne^{-} \tag{166}$$

$$i = \bar{i} + Re\{\tilde{\imath} e^{j\omega t}\} \tag{167}$$

$$\tilde{\imath}_{AB} = \left(\frac{\partial i_{AB}}{\partial V}\right)_{c_B(0)} \tilde{V} + \left(\frac{\partial i_{AB}}{\partial c_B(0)}\right)_{V} \widetilde{c_B}(0) \tag{168}$$

Equation (169) and (170) shows the steady state current density of Reaction (166) with the kinetic parameter shown in Equations (171) and (172) [8].

$$i_{AB} = K_{AB} c_B(0) \exp\left(\frac{\overline{V}}{b_{AB}}\right) \tag{169}$$

$$i_{AB} = nFD_B \frac{dc_B}{dy} = nFD_B \frac{c_B(\infty) - c_B(0)}{\delta} \tag{170}$$

$$b_{AB} = \frac{RT}{\alpha_{AB} nF} \tag{171}$$

$$K_{AB} = nFk_{AB} \exp\left(\frac{-V_0}{b_{AB}}\right) \tag{172}$$

---

[48] The general discussion in this section is taken from reference number [8].

The surface concentration of species B can be calculated using Equation (173). Consequently, the steady state current density (Equation (169)) can be calculated based on bulk concertation of species B (Equation (174)) [8].

$$\overline{c_B}(0) = \frac{c_B(\infty)}{\frac{K_{AB}\delta}{nFD_B}\exp\left(\frac{\overline{V}}{b_{AB}}\right)+1} \tag{173}$$

$$i_{AB} = K_{AB}\frac{c_B(\infty)}{\frac{K_{AB}\delta}{nFD_B}\exp\left(\frac{\overline{V}}{b_{AB}}\right)+1}\exp\left(\frac{\overline{V}}{b_{AB}}\right) \tag{174}$$

Then first expression in Equation (168) defines the charge transfer resistance (Equation (175)). Therefore, the transient current density can be calculated using Equation (176) which depends on potential and electrode surface concertation of species B [8].

$$\left(\frac{\partial i_{AB}}{\partial V}\right)_{c_i(0),\gamma_k} = \frac{1}{R_{ct}} = \frac{\overline{i}_{AB}}{b_{AB}} \tag{175}$$

$$\tilde{\imath}_{AB} = \frac{1}{R_{ct}}\tilde{V} + K_{AB}\exp\left(\frac{\overline{V}}{b_{AB}}\right)\widetilde{c_B}(0) \tag{176}$$

Divide both side of Equation (176) by Equation (170) ($i_{AB} = nFD_B\frac{dc_B}{dy}$), the impedance response of en electrochemical reaction depending on both potential and surface concentration can be calculated using Equation (177) [8].

$$Z_{AB} = R_{ct} - R_{ct}\frac{K_{AB}\exp\left(\frac{\overline{V}}{b_{AB}}\right)}{nFD_B}\frac{\widetilde{c_B}(0)}{\frac{d\widetilde{c_B}}{dy}} \tag{177}$$

A parameter defined as dimensionless concentration is shown in Equation (178) , where its first derivative with respect to distance is shown in Equation (179). Considering

the dimensionless concentration, Equation (177) is simplified to Equation (180) in which the first term is related to the charge transfer resistance while the second term in called diffusion impedance. The diffusion resistance is defined in Equation (181). Equation (180) shows that at very low frequency, the polarization resistance of the mentioned electrochemical reaction is summation of charge transfer resistance and diffusion resistance[8].

$$\theta_B = \frac{\widetilde{c_B}}{\widetilde{c_B}(0)} \tag{178}$$

$$\acute{\theta}_B = \frac{d(\frac{\widetilde{c_B}}{\widetilde{c_B}(0)})}{d(\frac{y}{\delta})} \tag{179}$$

$$Z_{AB} = R_{ct} + R_{Diff}\left(-\frac{1}{\acute{\theta}_B(0)}\right) = R_{ct} + Z_{Diff} \tag{180}$$

$$R_{Diff} = \frac{\partial V}{\partial c_B(0)}\frac{\delta}{nFD_B} = R_{ct}\frac{K_{AB}\delta\exp\left(\frac{\overline{V}}{b_{AB}}\right)}{nFD_B} \tag{181}$$

II.4. Calculation of Kinetic Constants in Keddam's Multi-Path Mechanism [49]

II.4.1. Calculations of the Kinetic Constant of Path 1

II.4.1.1. Mass Balance in Steady State Condition. The mathematical equations explained in Section II.4.1 and II.4.2 are based on mathematical derivations and approach provided and described elsewhere[6–8,21,43]. Considering path 1 in the Keddam multi-path mechanism [6,7], the surface coverage of the adsorbed species, $\boldsymbol{\theta_1}$ is calculated using the

[49] The general approach for the derivation of the functions used in this section are based on reference numbers [6–8,21,43] .

mass balance equations (182)-(187). In order to make the equations simpler, $\boldsymbol{k_n}$ is defined according to equation (184) in which the surface potential and the Tafel component $\boldsymbol{b_n}$ (Equation (185) are incorporated with the reaction rate constant, $\boldsymbol{k_{n,0}}$, at the equilibrium potential as shown in Equation (186). In steady state condition, the term $\frac{\boldsymbol{d\theta_1}}{\boldsymbol{dt}}$ is equal to zero. Consequently, equations (187) is used to calculate the steady state surface coverage of the adsorbed species.

$$\beta\frac{d\theta_1}{dt} = \frac{i_{F,1}}{F} - \frac{i_{F,2}}{F} \tag{182}$$

$$\beta\frac{d\theta_1}{dt} = k_1[OH^-](1-\theta_1) - k_2\theta_1 \tag{183}$$

$$k_n = k_{n,0}\exp\left(\frac{V}{b_n}\right) \tag{184}$$

$$b_n = \frac{RT}{\alpha_n nF} \tag{185}$$

$$k_{n,0} = k'_{0,n}\exp\left(\frac{-V_{eq}}{b_n}\right) \tag{186}$$

$$\bar{\theta}_1 = \frac{k_1[OH^-]}{k_1[OH^-] + k_2} \tag{187}$$

II.4.1.2. Steady State Current Density. The faradaic current density of the electrochemical reactions in path1 of Keddam's multi-path mechanism can be expressed using Equations (188)- (190).

$$\bar{i}_{F,1} = Fk_1[OH^-](1-\bar{\theta}_1) \tag{188}$$

$$\bar{i}_{F,2} = Fk_2\bar{\theta}_1 \tag{189}$$

$$\bar{i}_{F,total} = \frac{2Fk_1k_2[OH^-]}{k_1[OH^-] + k_2} \tag{190}$$

II.4.1.3. Charge Transfer Resistance. Charge transfer resistance is the resistance related to pure charge transfer current density. In other words, when the change in current density is only related to the change in potential, as shown in Equation (191).

$$\frac{1}{\mathrm{R_{ct}}} = \left(\frac{\mathrm{di_{F,total}}}{\mathrm{dV}}\right)_{\theta_n} = \frac{\mathrm{Fk_1k_2[OH^-]}}{\mathrm{k_1[OH^-] + k_2}}\left(\frac{1}{b_1} + \frac{1}{b_2}\right) \tag{191}$$

II.4.1.4. Mass Balance in Transient Condition. A Taylor expansion at the $\bar{\imath}_{f,n}$ can be expressed in Equations (192). Considering Equation (193), the transient mass balance of the adsorbed species can be obtained as shown in equations (194). Dividing both sides of Equation (194) by $\boldsymbol{\beta j\omega\tilde{V}}$, the first derivative of the transient surface coverage with respect to transient potential can be obtained as shown in Equation (195).

$$\tilde{\mathrm{i}}_n = \left(\frac{\partial \mathrm{i_n}}{\partial \mathrm{V}}\right)_{\theta_n} \tilde{\mathrm{V}} + \sum_n \left(\frac{\partial \mathrm{i_n}}{\partial \theta_n}\right)_{\mathrm{V}} \tilde{\theta}_n \tag{192}$$

$$\theta_n = \bar{\theta}_n + \mathrm{Re}\{\tilde{\theta}_n e^{j\omega t}\} \tag{193}$$

$$\beta j\omega\tilde{\theta}_1 = \left({}^{\mathrm{k_1[OH^-](1-\theta_1)}}\big/_{b_1} - {}^{\mathrm{k_2\theta_1}}\big/_{\mathrm{b_2}}\right)\tilde{\mathrm{V}} + (-\mathrm{k_1[OH^-]} - \mathrm{k_2})\tilde{\theta}_1 \tag{194}$$

$$\frac{\tilde{\theta}_1}{\tilde{\mathrm{V}}} = \frac{\mathrm{k_1[OH^-](1-\theta_1)}/b_1 - \mathrm{k_2\theta_1}/b_2}{\mathrm{k_1[OH^-] + k_2} + \beta j\omega} \tag{195}$$

II.4.1.5. Impedance Calculation. Using Equation (192), the impedance can be calculated using equation (196), in which **m** is defined in Equation (197). The first derivative of the transient surface coverage can also be calculated using Equation (195).

$$\frac{1}{\mathrm{Z}} = \frac{1}{\mathrm{R_{ct}}} + \mathrm{m}\frac{\tilde{\theta}_1}{\tilde{\mathrm{V}}} \tag{196}$$

$$\mathrm{m} = \left(\frac{\partial \mathrm{i}_{f,total}}{\partial \theta_1}\right)_{\mathrm{V}} = \mathrm{Fk_2} - \mathrm{Fk_1[OH^-]} \tag{197}$$

Equation (196) which shows the impedance response of a faradaic reaction in the presence of one adsorbed species can be expressed similar to Equation (198). If the adsorption of a species appears as a capacitive loop, then A_1 which is shown in Equation (199) must have a negative value and if the adsorption of the species appears similar to an inductive loop then A_1 must be a positive value. D_1 always has a positive value which is shown in Equation (200).

$$\frac{1}{Z} = \frac{1}{R_{ct}} + \frac{A_1}{j\omega + D_1} \tag{198}$$

$$A_1 = \frac{\frac{F k_1 k_2 [OH^-]}{k_1 [OH^-] + k_2} (\frac{1}{b_1} - \frac{1}{b_2})(k_2 - k_1 [OH^-])}{\beta} \tag{199}$$

$$D_1 = \frac{k_2 + k_1 [OH^-]}{\beta} \tag{200}$$

Since the adsorption of the of the first adsorbed species at the OCP appears like an inductive loop, then the impedance related of the faradaic reaction can be modeled similar to Figure 127, in which the values of the resistances and inductance can be calculated using Equations (201) and (202). The characteristic frequency of the inductive loop representing the adsorption of the first species can be calculated using in Equation (203).

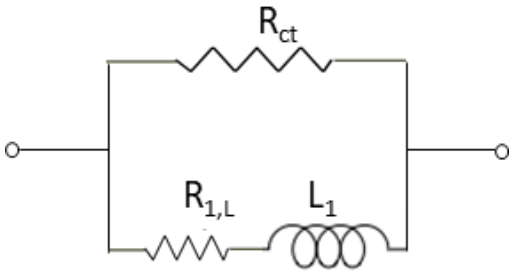

Figure 127

The electrical circuit representing the faradic impedance of coupled reactions including one adsorbed species in path 1 of Keddam multi-path mechanism.

$$\mathrm{R_{1,L}} = \frac{\mathrm{D_1}}{\mathrm{A_1}} \tag{201}$$

$$L_1 = \frac{1}{\mathrm{A_1}} \tag{202}$$

$$\mathrm{f_{ch,1}} = \frac{\mathrm{R_{1,L}}}{2\pi L_1} = \mathrm{D_1} = \frac{\mathrm{k_2} + \mathrm{k_1[OH^-]}}{2\pi\beta} \tag{203}$$

II.4.1.6. Polarization Resistance. The polarization resistance is the resistance of the faradaic reaction at zero frequency. Considering Equation (198) at angular frequency of zero, the equation for the calculation of the polarization resistance can be achieved as shown in Equation (204).

$$\frac{1}{\mathrm{R}_p} = \frac{1}{\mathrm{R_{ct}}} + \frac{(\mathrm{k_2} - \mathrm{k_1[OH^-]})\frac{F\mathrm{k_1k_2[OH^-]}}{\mathrm{k_1[OH^-]} + \mathrm{k_2}}(\frac{1}{b_1} - \frac{1}{b_2})}{\mathrm{k_1[OH^-]} + \mathrm{k_2}} \tag{204}$$

II.4.2. Calculations of the Kinetic Constant of Path 2

II.4.2.1. Mass Balance in Steady State Condition. The surface coverage of the adsorbed species, $\boldsymbol{\theta_1}$ and $\boldsymbol{\theta_2}$ are calculated using the mass balance equations (205)-(207).

Note that $\boldsymbol{\theta_2}$ in the multi-step mechanism is related to a catalytic species that does not consume or produce[6,7].

$$\beta\frac{d\theta_1}{dt} = \frac{i_{F,1}}{F} - \frac{i_{F,2}}{F} - r_3 + r_{-3} \tag{205}$$

$$\beta\frac{d\theta_1}{dt} = k_1[OH^-](1-\theta_1-\theta_2) - k_2\theta_1 - k_3[OH^-]\theta_1 + k_{-3}\theta_2 \tag{206}$$

$$\beta\frac{d\theta_2}{dt} = r_3 - r_{-3} \tag{207}$$

In steady state condition, the terms $\frac{d\theta_1}{dt}$ and $\frac{d\theta_2}{dt}$ are equal to zero. Consequently, equations (208) and (209) are used to calculate the steady state surface coverage of the adsorbed species.

$$\bar{\theta}_1 = \frac{k_1k_{-3}[OH^-]}{k_1k_3[OH^-]^2 + k_1k_{-3}[OH^-] + k_2k_{-3}} \tag{208}$$

$$\bar{\theta}_2 = \frac{k_1k_3[OH^-]^2}{k_1k_3[OH^-]^2 + k_1k_{-3}[OH^-] + k_2k_{-3}} \tag{209}$$

II.4.2.2. Steady State Current Density. The faradaic current density of the electrochemical reactions in path1 and path 2 of Keddam's multi-path mechanism can be expressed using Equations (210)-(212). Considering the surface coverage of the adsorbed species in Equations (208) and (209), Equation (213) is achieved. Replacing Equation (213) in Equation (210), consequently, the total faradic current density generated from path 1 and path 2 can be expressed as Equation (214).

$$\bar{\imath}_{F,1} = Fk_1[OH^-](1-\bar{\theta}_1-\bar{\theta}_2) \tag{210}$$

$$\bar{\imath}_{F,2} = Fk_2\bar{\theta}_1 \tag{211}$$

$$\bar{\imath}_{F,4} = 2Fk_4[OH^-]\bar{\theta}_2 \tag{212}$$

$$k_1[OH^-](1-\bar{\theta}_1-\bar{\theta}_2)=k_2\bar{\theta}_1 \tag{213}$$

$$\bar{\imath}_{F,total}=2Fk_2\bar{\theta}_1+2Fk_4[OH^-]\bar{\theta}_2 \tag{214}$$

II.4.2.3. Charge Transfer Resistance. Similar to previous section the charge transfer resistance can be obtained using the first derivation of the total current density with respect to potential. Considering the expressing in Equation (213), the charge transfer resistance equation (215) is simplifies to Equation (216).

$$\frac{1}{R_{ct}}=\left(\frac{di_{F,total}}{dV}\right)_{\theta_n} = Fk_1[OH^-](1-\bar{\theta}_1-\bar{\theta}_2)/b_1+Fk_2\bar{\theta}_1/b_2 + 2Fk_4[OH^-]\bar{\theta}_2/b_4 \tag{215}$$

$$\frac{1}{R_{ct}}=F(\frac{1}{b_1}+\frac{1}{b_2})k_2\bar{\theta}_1+\frac{2Fk_4[OH^-]\bar{\theta}_2}{b_4} \tag{216}$$

II.4.2.4. Transient Mass Balance. A Taylor expansion at the $\bar{\imath}_{f,n}$ and r_n can be expressed in Equations (192) and (217) respectively. Considering the Equations (192), (193), (205), (207), and (217), the transient mass balance of the adsorbed species can be obtained as shown in equations (218) and (219) where X_1 and X_2 are defined in Equations (220) and (221) respectively.

$$\tilde{r}_n=\left(\frac{\partial r_n}{\partial V}\right)_{\theta_n}\tilde{V}+\sum_n\left(\frac{\partial r_n}{\partial \theta_n}\right)_V\tilde{\theta}_n \tag{217}$$

$$\beta j\omega\tilde{\theta}_1=X_1\tilde{V}+(-k_1[OH^-]-k_2-k_3[OH^-])\tilde{\theta}_1+(-k_1[OH^-]+k_{-3})\tilde{\theta}_2 \tag{218}$$

$$\beta j\omega\tilde{\theta}_2=X_2\tilde{V}+k_3[OH^-]\tilde{\theta}_1-k_{-3}\tilde{\theta}_2 \tag{219}$$

$$X_1=\frac{k_2\theta_1}{b_1}-\frac{k_2\theta_1}{b_2}-\frac{k_3[OH^-]\theta_1}{b_3}-\frac{k_{-3}\theta_2}{b_{-3}} \tag{220}$$

$$X_2 = \frac{k_3[OH^-]\theta_1}{b_3} + \frac{k_{-3}\theta_2}{B_{-3}} \tag{221}$$

Dividing both sides of the Equations (218) and (219) by $\widetilde{V}$, the first derivative of the transient surface coverage with respect to transient potential can be obtained as shown in Equations (222) and (223).

$$\frac{\tilde{\theta}_1}{\widetilde{V}} = \frac{X_1 + (-k_1[OH^-] + k_{-3})\frac{\tilde{\theta}_2}{\widetilde{V}}}{k_1[OH^-] + k_2 + k_3[OH^-] + \beta j\omega} \tag{222}$$

$$\frac{\tilde{\theta}_2}{\widetilde{V}} = \frac{X_2 + k_3[OH^-]\frac{\tilde{\theta}_1}{\widetilde{V}}}{k_{-3} + \beta j\omega} \tag{223}$$

II.4.2.5. Impedance Calculation. Using Equation (192), the impedance can be calculated using equation (224), in which the $\boldsymbol{m}$ and $\boldsymbol{p}$ are defined in equations (225) and (226) respectively. The first derivative of the transient surface coverages can also be calculated using Equations (222) and (223).

$$\frac{1}{Z} = \frac{1}{R_{ct}} + m\frac{\tilde{\theta}_1}{\widetilde{V}} + p\frac{\tilde{\theta}_2}{\widetilde{V}} \tag{224}$$

$$m = \left(\frac{\partial i_F}{\partial \theta_1}\right)_V = Fk_2 - Fk_1[OH^-] \tag{225}$$

$$p = \left(\frac{\partial i_F}{\partial \theta_2}\right)_V = 2Fk_4[OH^-] - Fk_1[OH^-] \tag{226}$$

II.4.2.6. Modeling the Impedance Response of the Adsorbed Species. Equation (224) shows the impedance response of a faradaic reaction in the presence of two adsorbed species which can be expressed similar to Equation (227).

$$\frac{1}{Z} = \frac{1}{R_{ct}} + \frac{A_1'}{j\omega + D_1'} + \frac{A_2}{j\omega + D_2} \tag{227}$$

Since the adsorption of the two species in the transition regions of the anodic reaction appears as two capacitive loops, then A_1' and A_2 must have a negative value. The impedance response of the faradaic reaction can be expressed similar to the electrical circuit shown in Figure 128 [13].

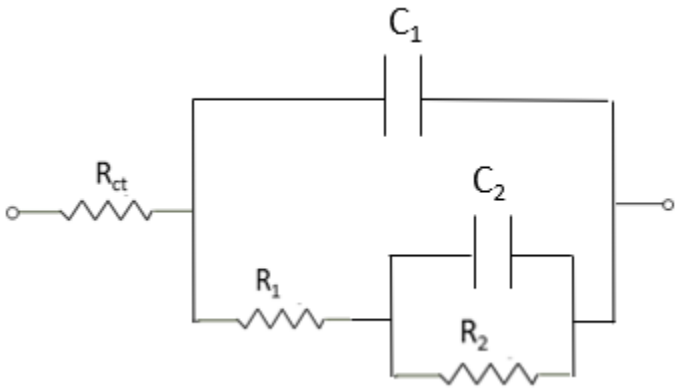

Figure 128

The electrical circuit representing the faradic impedance of coupled reactions including two adsorbed species in the transition region of the anodic reaction.

II.4.2.6.1. Characteristic Frequency of the Capcitive Loop related to the First Adsorbed Species (θ_1). Equation (224) is the general equation for the impedance response of coupled reactions depending on potential and surface coverage of two adsorbed species. In order to calculate the characteristic frequency of the capacitive loop related to the first adsorbed species, θ_1, it is assumed that in the frequency range in which the relaxation of the first species is observed, then there is no relaxation of the second adsorbed species. Following this assumption, Equation (224) is simplified to Equation (228). Equation (228) can be expressed similar to Equation (229) in which A_1' and D_1' can be calculated using

Equations (230) and (231). If the impedance response of the adsorbed species (θ_1) is similar to a capacitive loop, then the equivalent circuit related to the faradaic reactions is shown in Figure 129 in which the electrical components can be calculate using equations (232) and (233).

$$\frac{1}{Z} = \frac{1}{R_{ct}} + m\frac{\tilde{\theta}_1}{\tilde{V}} \tag{228}$$

$$\frac{1}{Z} = \frac{1}{R_{ct}} + \frac{A'_1}{j\omega + D'_1} \tag{229}$$

$$A'_1 = \frac{X_1(Fk_2 - Fk_1[OH^-])}{\beta} \tag{230}$$

$$D'_1 = \frac{k_1[OH^-] + k_2 + k_3[OH^-]}{\beta} \tag{231}$$

$$R_1 = -\frac{A'_1 R_{ct}^2}{D'_1 + A'_1 R_{ct}} \tag{232}$$

$$C_1 = -\frac{1}{A'_1 R_{ct}^2} \tag{233}$$

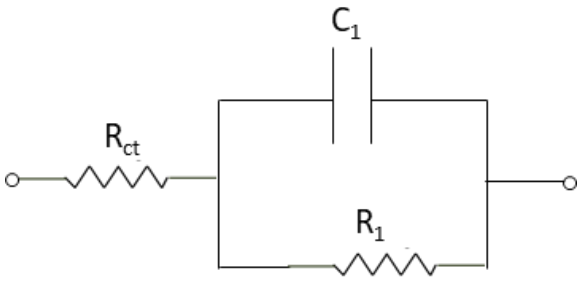

Figure 129

The electrical circuit representing the faradic impedance of coupled reactions in frequency range in which there is relaxation phenomena related to θ_1 in transition region of the anodic reaction.

The characteristic frequency of the capcitive loop representing the adsorption of the first species can be calculated using Equation (234). Considering the relationship between the R_1 (Equations (232) and (235)) and the $f_{ch,1}$(Equation (234)) , the final equation for the calculation of the characteristic frequency is shown in Equation (236).

$$f_{ch,1} = \frac{1}{2\pi R_1 C_1} = \frac{D_1' + A_1' R_{ct}}{2\pi} = \frac{(k_1[OH^-] + k_2 + k_3[OH^-]) + X_1 R_{ct}(Fk_2 - Fk_1[OH^-])}{2\pi\beta} \quad (234)$$

$$R_1 = \frac{X_1(Fk_2 - Fk_1[OH^-])R_{ct}^2}{2\pi\beta f_{ch,1}} \quad (235)$$

$$f_{ch,1} = \frac{(k_1[OH^-] + k_2 + k_3[OH^-])R_{ct}}{2\pi\beta(R_1 + R_{ct})} \quad (236)$$

II.4.2.6.2. Characteristic Frequency of the Capacitive Loop Related to the Second Adsorbed Species (θ_2). In order to calculate the characteristic frequency of the capacitive loop related to the second adsorbed species, θ_2, it is assumed that in the frequency range in which the relaxation of the second species is observed, then there is no relaxation of the first adsorbed species. Following this assumption, Equation (224) is simplified to Equation (237) in which the $A_2$and D_2 can be calculated using Equations (238) and (239). If the impedance response of the adsorbed species (θ_2) is similar to a capacitive loop, then the equivalent circuit related to the faradaic reactions is shown in Figure 130 in which the electrical components can be calculate using equations (240) and (241).

$$\frac{1}{Z} = \frac{1}{R_{ct} + R_1} + \frac{A_2}{j\omega + D_2} \quad (237)$$

$$A_2 = \frac{(2Fk_4[OH^-] - Fk_1[OH^-])X_2}{\beta} \tag{238}$$

$$D_2 = \frac{k_{-3}}{\beta} \tag{239}$$

$$R_2 = -\frac{A_2(R_{ct} + R_1)^2}{D_2 + A_2(R_{ct} + R_1)} \tag{240}$$

$$C_2 = -\frac{1}{A_2(R_{ct} + R_1)^2} \tag{241}$$

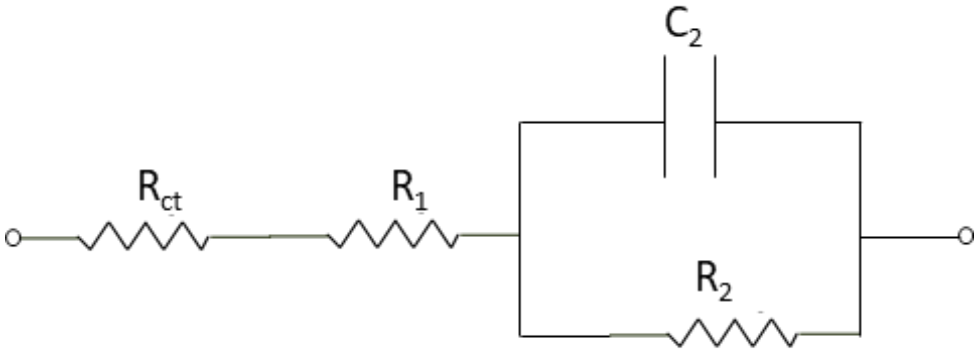

Figure 130

The electrical circuit representing the faradic impedance of coupled reactions in frequency range in which there is relaxation phenomena related to θ_2 in transition region of the anodic reaction.

The characteristic frequency of the capcitive loop representing the adsorption of the second species can be shown in Equation (242). Considering the relationship between the R_2 (Equations (240) and (243)) and the $f_{ch,1}$(Equation (242)) , the final equation for the calculation of the characteristic frequency is shown in Equation (244).

$$f_{ch,2} = \frac{1}{2\pi R_2 C_2} = \frac{D_2 + A_2(R_{ct} + R_1)}{2\pi}$$

$$= \frac{k_{-3} + (2Fk_4[OH^-] - Fk_1[OH^-])X_2(R_{ct} + R_1)}{2\pi\beta} \quad (242)$$

$$R_2 = \frac{-(2Fk_4[OH^-] - Fk_1[OH^-])X_2(R_{ct} + R_1)^2}{2\pi\beta f_{ch,2}} \quad (243)$$

$$f_{ch,2} = \frac{k_{-3}(R_{ct} + R_1)}{2\pi\beta(R_{ct} + R_1 + R_2)} \quad (244)$$

II.5. Repeatability of the Experimental Data for Anodic Dissolution of Iron

This section shows the repeatability of the potentiodynamic sweeps and EIS experiments obtained in one solution. Figure 131 and Figure 132 show the repeatability of potentiodynamic sweeps obtained in fresh solution compared to the experiments performed in the same solution. Figure 133-Figure 138 show the EIS experiments which possibly performed in a fresh solution and compared with experiments performed in the same solution. For EIS data, there are uncertenties if the test number one was perfomed in a fresh solution. Therefore, for next researcher it is recommended to perfomed the EIS experiment in a fresh solution to compared them with the experiments shown in current reserch study. Overall the results show that the presence of Fe^{2+} in the solution might not influence the mechanism of the anodic dissolution of iron.

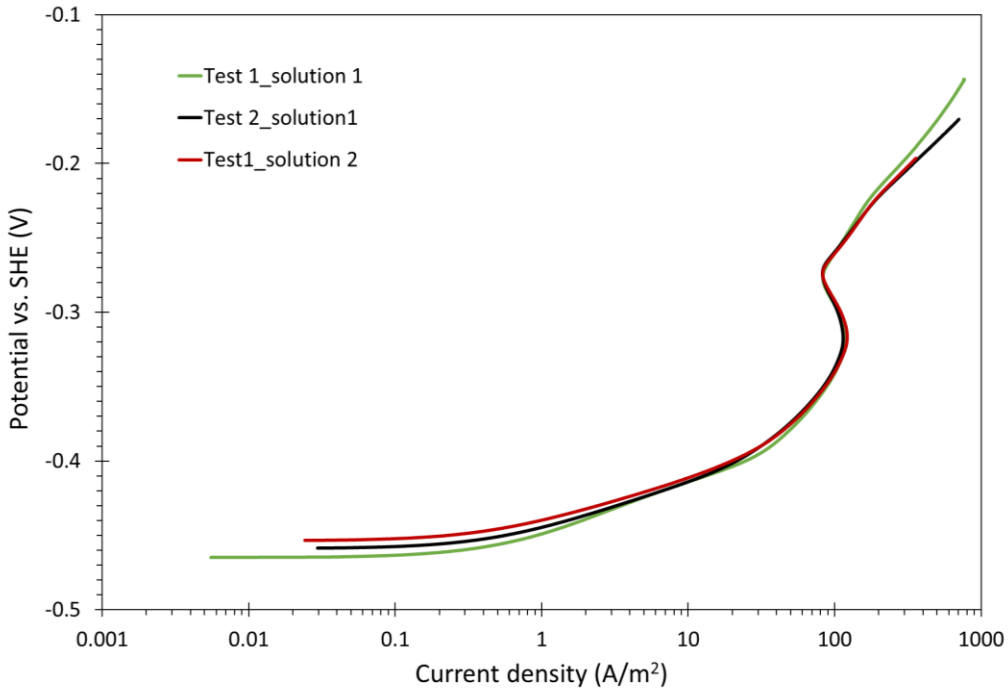

Figure 131

Repeatability of the anodic steady state potentiodynamic sweeps in strong acid chloride solutions measured using a sweep rate of 0.5 mV/s, on pure iron RDE at 1600 rpm, corroding in an aqueous solution at pH 4.0 and 25°C.

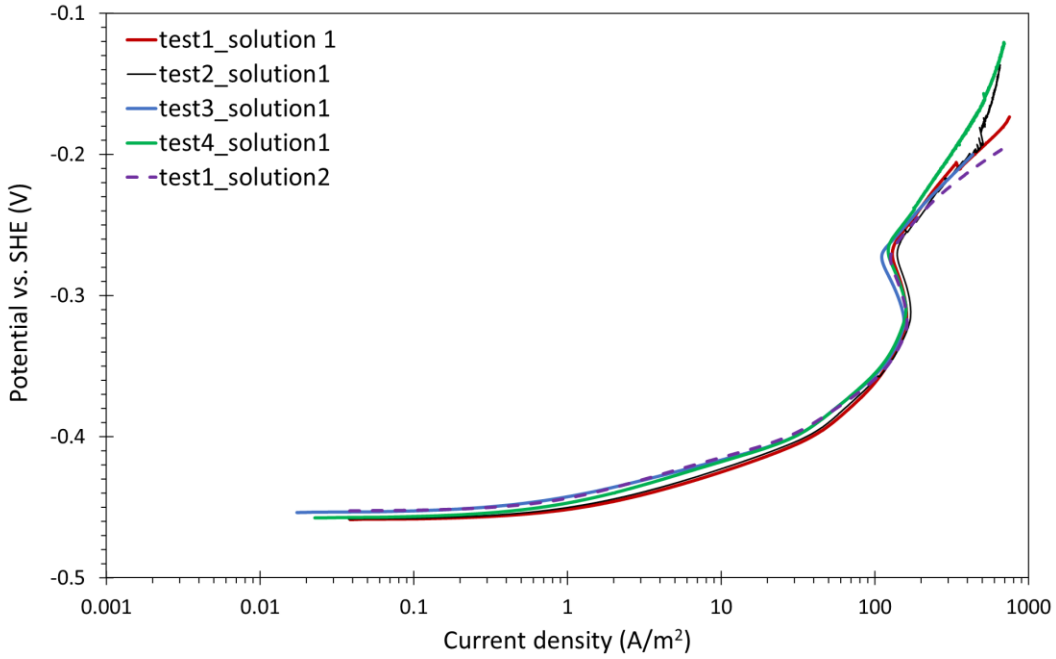

Figure 132

Repeatability of the anodic steady state potentiodynamic sweeps in chloride solution sparged with 1 bar CO_2, measured using a sweep rate of 0.5 mV/s, on pure iron RDE at 1600 rpm, corroding in an aqueous solution at pH 4.0 and 25°C.

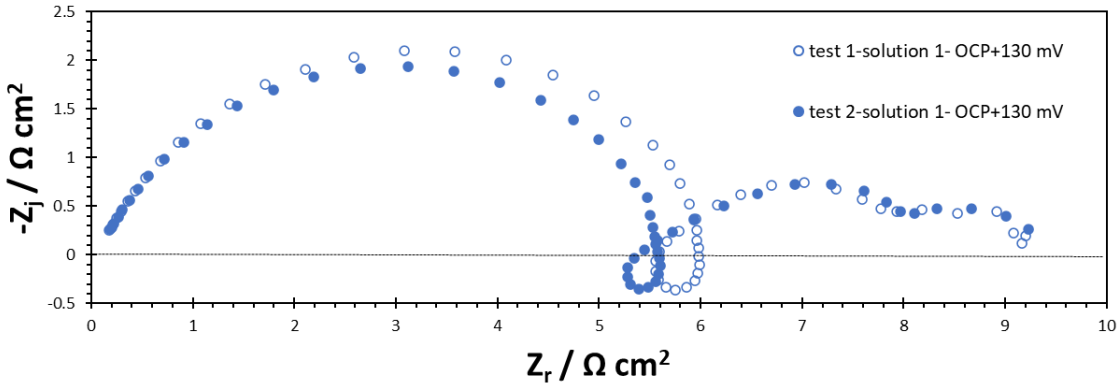

Figure 133

Repeatability of the Nyquist plots at OCP + 130 mV in the active dissolution region Experimental parameters: 1 bar N_2, 0.5 M NaCl, pH 4.0, 25°C, pure iron RDE, 1600 rpm.

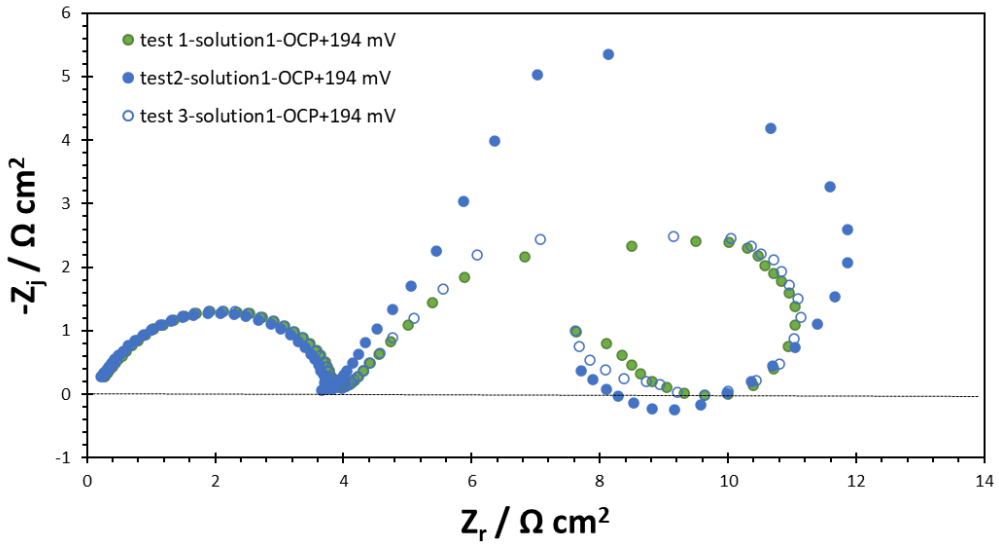

Figure 134

Repeatability of the Nyquist plots at OCP + 194 mV in the transition region Experimental parameters: 1 bar N_2, 0.5 M NaCl, pH 4.0, 25°C, pure iron RDE, 1600 rpm.

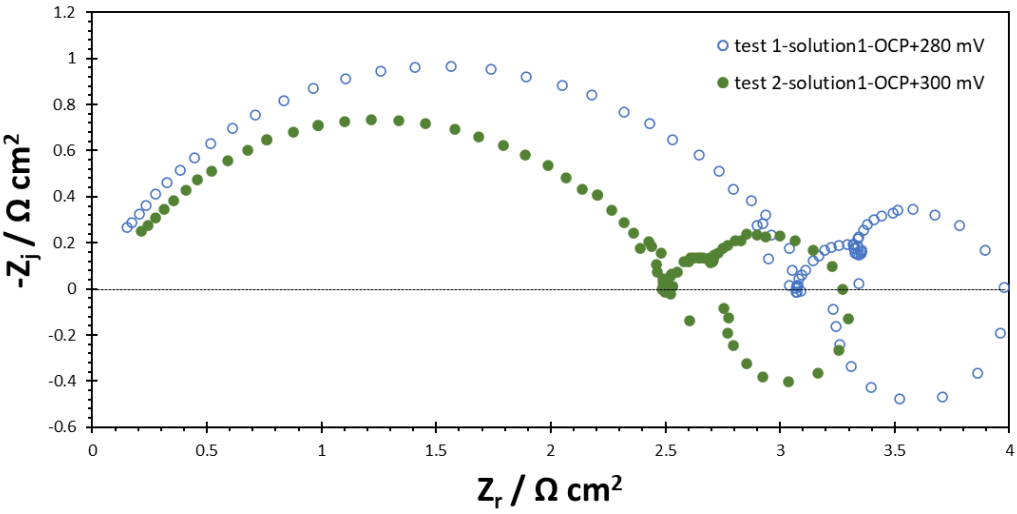

Figure 135

Repeatability of the Nyquist plots in the pre-passivation region. Experimental parameters: 1 bar N_2, 0.5 M NaCl, pH 4.0, 25°C, pure iron RDE, 1600 rpm.

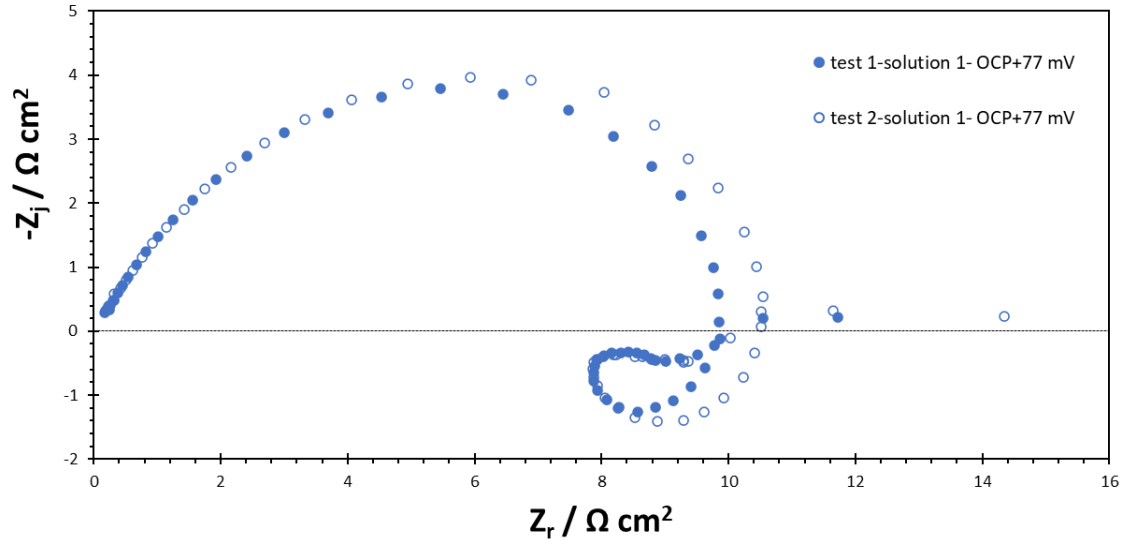

Figure 136

Repeatability of the Nyquist plots at OCP + 77 mV in the active dissolution region Experimental parameters: 1 bar CO_2, 0.5 M NaCl, pH 4.0, 25°C, pure iron RDE, 1600 rpm.

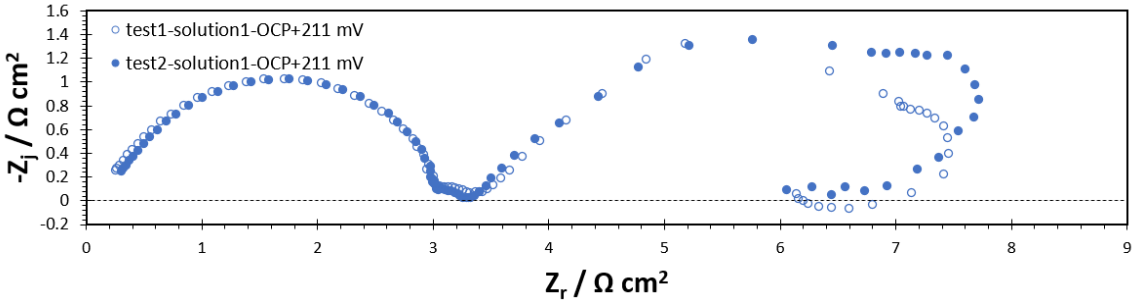

Figure 137

Repeatability of the Nyquist plots at OCP + 211 mV in the transition region Experimental parameters: 1 bar CO_2, 0.5 M NaCl, pH 4.0, 25°C, pure iron RDE, 1600 rpm.

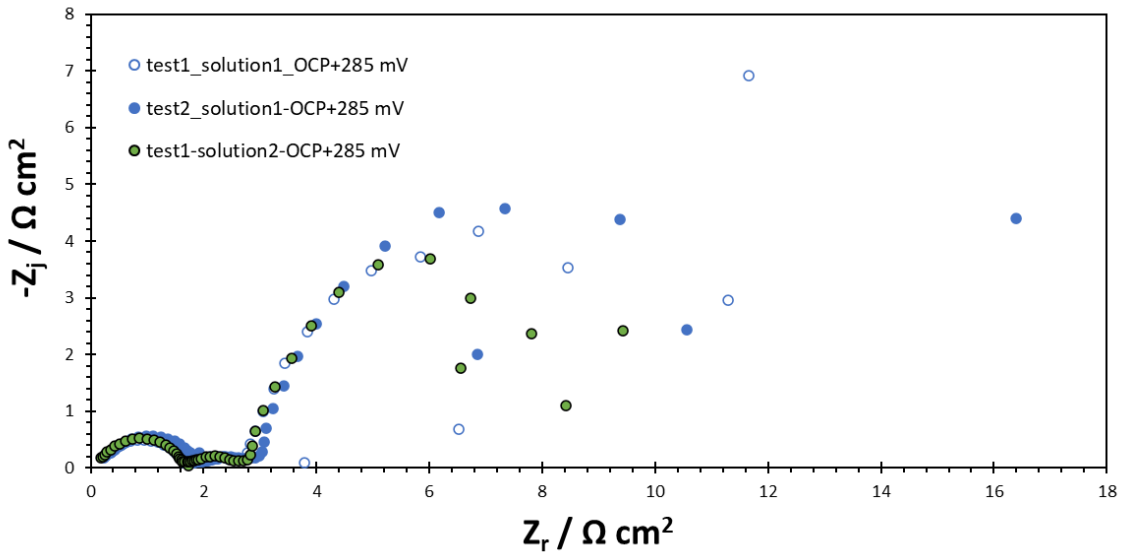

Figure 138

Repeatability of the Nyquist plots at OCP + 285 mV in the transition region Experimental parameters: 1 bar N_2, 0.3 M Na_2SO_4, pH 4.0, 25°C, pure iron RDE, 1600 rpm.

Thesis and Dissertation Services